Enhancing the Sensitivity and Measuring the Deflection of MEMS Microcantilevers

A thesis submitted in fulfilment of the requirements for the degree of Doctor of Philosophy

Sanchitha Nirodha Fernando

BSc.Eng(Hons)

School of Electrical and Computer Engineering

Science, Engineering and Technology Portfolio

RMIT University

March 2008

Declaration

I certify that except where due acknowledgement has been made, the work is that of the author alone; the work has not been submitted previously, in whole or in part, to qualify for any other academic award; the content of the thesis is the result of work which has been carried out since the official commencement date of the approved research program; any editorial work, paid or unpaid, carried out by a third party is acknowledged; and, ethics procedures and guidelines have been followed.

Sanchitha Fernando

12.03.2008

This thesis is dedicated to the loving memory of my father

Acknowledgements

This PhD thesis was made possible by Prof. Ian Bates, Director of the AECM Microtechnology Systems Centre at RMIT University. He offered me the opportunity to join the Centre and pursue a postgraduate research degree, which I gladly accepted. It is entirely due to him that my wife and I are in Australia today. His guidance and support right throughout my candidature has been invaluable. Through him I've learnt that a thorough investigation of the problem is the crucial step to find the best solution. This philosophy has carried me through my PhD, and has transformed my outlook on life. His generous scholarship has helped us to lead a decent life. I thank him from the bottom of my heart for everything he has done for us.

Prof. Michael Austin has been a wonderful supervisor. Despite being somewhat overloaded with work, he always found time to discuss my work whenever I requested. His sharp observations and analytical comments have pushed me to see the broader picture. He has a deep insight on a wide range of subjects, and has an amazing ability to quickly grasp concepts. His critical feedback has been pivotal in helping me reach the end goal. He made every effort to review my thesis chapters promptly. I am eternally grateful for his valuable guidance during my candidature.

In Dr. Jason Chaffey, my second supervisor, I have found a tower of strength. He has taken a very keen interest in my work, right from day one. He has regularly inquired about my progress, even when he was overseas or interstate, and provided valuable feedback. He continuously motivated me right throughout my candidature, and has been a friend through thick and thin. I sincerely thank him for his efforts.

I got to know Prof. Bates through my brother Chiranka. He provided us with accommodation when we first arrived in Australia, and helped us to settle down. Thank you for being such a good brother.

I thank Mrs. Lynda Gilbert, who went out of her way to help me with many administrative matters during my initial days at RMIT.

I take this opportunity to thank all my colleagues at the AECM MSC for their support and help during my studies. Special mention must be made of Mr. Keerthy Silva, Mr. Tim Walker, Mr. Manvinder Singh and Dr. Vijaya Mathe for the many stimulating discussions we've had which helped me to gain a deeper understanding of the problems we were trying to solve.

My sincere gratitude also goes out to Dr. Arnan Mitchell and Dr. Thach Nguyen of SECE, RMIT, for their valuable comments on optics. I also appreciate the untiring efforts of Mr. Sharath Sriram, Ms. Madhu Baskaran and Mr. Paul Jones to get the cantilevers fabricated.

I thank my parents for all the wonderful things they have given me throughout my life. I specially thank my parents and Sevvandi's parents for helping us out at various points in time with household matters and babysitting, which allowed me time to concentrate on my work.

Finally, this brings me to my family. My wife Sevvandi has been my greatest source of inspiration throughout this period. She's always had a listening ear whenever I had a problem, and more importantly, a valuable suggestion to overcome it. We've had many discussions about my work, and your comments have opened up new research avenues. You've always had a positive attitude, and you always believed in me and motivated me. During the last few weeks, I haven't had much time to spend with you and our unborn baby. Yet you never complained, and continued to support me. I appreciate your love and understanding. I thank our little daughter for trying to understand that I'm writing a thesis, and hence doesn't have too much time to spend with her. I love you all, and I am blessed to have you as my family.

Symbols and acronyms

L	Length of the cantilever
b	Width of the cantilever
h	Thickness of the cantilever
E	Young's modulus of the material
I	Moment of area
ν	Poisson's ratio of the material; frequency of optical wave
ρ	Density of the material
t	Deflection of the cantilever
f_0	Fundamental resonant frequency
k	Spring constant of the cantilever; wavenumber $= 2\pi/\lambda$
α	Offset factor of perforation from the fixed end
β	Width factor of perforation
γ	Depth factor of perforation
η	Length factor of perforation
λ	Separation factor between perforations; wavelength of optical wave
N	Number of perforations; number of cantilevers in the array
M	Bending moment
σ	Surface stress
χ	Moment of area factor

ψ_{pl}	Deflection improvement factor under a point load
ψ_{ss}	Deflection improvement factor under a surface stress
ψ_{f}	Resonant frequency improvement factor
θ	Diffraction angle
ϕ	Phase angle
Ψ	Composite phase angle
a	Minimum separation between cantilevers
x_{f}	Position of fixed cantilevers
x_{m}	Position of moving cantilevers

ADC	Analog to Digital Converter
$CMOS$	Complementary Metal Oxide Semiconductor
DFT	Discrete Fourier Transform
FEM	Finite Element Method
FFT	Fast Fourier Transform
FT	Fourier Transform
IDC	Interdigital Cantilevers
LCD	Lowest Common Denominator
$MEMS$	Micro Electro Mechanical Systems
MOA	Moment Of Area
$PSPD$	Position Sensitive Photo Detector

Contents

List of Tables

List of Figures

Abstract

This thesis investigates how the deflection sensitivity of microcantilever sensors can be increased, and how the deflections of an array of these cantilevers can be measured up to a few micrometers, with sub-nanometric resolution, using a simple optical system.

A large number of cantilever-based biochemical sensors have been reported in the literature. Cantilever sensors for some analytes produce deflections of several hundred nanometers, while cantilever sensors for some other analytes only produce deflections in the sub-nanometric range. The cantilever deflection for a given stimulus can be increased by increasing the length or by decreasing the thickness of the beam, but these result in a lower resonant frequency. A lower resonant frequency makes the cantilever susceptible to thermal noise and low-frequency vibrations. Therefore, it is desirable to increase both the deflection and the resonant frequency of cantilevers to improve their sensitivities. While prior research has attempted to enhance the deflection or increase the resonant frequency of cantilevers, a method of simultaneously increasing the deflection and the resonant frequency of cantilevers has not been demonstrated in the literature.

This problem of an inverse relationship between the deflection and the resonant frequency of microcantilevers is investigated in this thesis. It is shown that the deflection and the resonant frequency of cantilevers can be simultaneously increased by creating perforations on the cantilever in a manner that reduces its mass by a larger fraction than the reduction of the spring constant of the cantilever.

Analytical models are developed to describe the deflection and the resonant frequency of perforated microcantilevers. Deflection values obtained from this model are found to be within 6 % of the deflection values obtained using the finite element method software suite *ANSYS*, while resonant frequencies obtained using this model are found to be within 4 % of the simulated values. These results show the validity of the analytical models.

The variations of the deflection and resonant frequency of cantilevers with perforation parameters are characterised using these models. It is shown that the deflection and resonant frequency can be selectively controlled using perforations, enabling cantilevers to be realised with larger deflections as well as higher resonant frequencies compared with standard rectangular cantilevers. This enables the measurement technique to be simplified, since large deflections can be measured in less noise-controlled environments.

Using these analytical models, the optimal profile of a cantilever that combines increased deflection with increased noise immunity is determined. It is established that cantilevers with triangular profiles have a larger deflection×resonant frequency product when compared with standard rectangular cantilevers. These results are compared with values obtained from models available in the literature, as well as with simulations using *ANSYS*. Numerical results obtained from each of these methods show good agreement. The triangular-profiled cantilevers are shown to have a sensitivity to dimensional variations comparable to prismatic cantilevers, and to be relatively insensitive to smoothing effects of fabrication.

The measurement of the deflections of an array of cantilevers using the interdigital interferometric method is investigated in detail. A novel mathematical approach is proposed that decomposes the far-field optical intensity pattern into the sum of several spatial harmonic functions. The relationships between the parameters of the cantilever array, the cantilever deflections and the spatial harmonic functions that determine the observed optical intensity pattern, are established. The spatial frequencies of these harmonic functions are shown to be determined by the distances

between each cantilever of the array, and the phase terms of the spatial harmonic functions are shown to be dependent on the amount of deflection.

The measurement range of the standard interdigital interferometric method is limited to a quarter of the wavelength λ of the optical source. The reason for this limitation is investigated. It is shown that by using the phase terms of the spatial harmonic functions obtained from the Fourier transformation of the far-field diffraction pattern, the measurement range can be extended to $\lambda/2$. It is further established that by making each moving cantilever in an array to have a different deflection for a given stimulus, the measurement range can be increased independent of the half-wavelength limitation. The principles for designing a cantilever array to enable this enhancement are established.

A principle to correct the errors induced by the misalignment of the image sensor with respect to the diffraction envelope of the intensity pattern is established. It is shown that the cantilever array can be designed to correct for large misalignments. Since the requirement of precise optical alignment is eliminated, the proposed method is well suited for automated systems to measure the deflection of cantilevers.

Practical design considerations of a cantilever array and the image sensor are investigated and the principles for determining the cantilever width and the locations of individual cantilevers are established. The requirements of the photo sensor, namely, the maximum allowable pixel spacing, the size of the image sensor and the resolution of the Analog to Digital Converter (ADC) for a given measurement resolution are also determined.

Using these principles, an example array of cantilevers is simulated. Using a basic signal processing algorithm, a measurement resolution of 0.2 nm is demonstrated, which compares with the theoretical resolution of 0.159 nm when using a 10-bit ADC. Deflections up to 3250 nm are shown to be measurable using this array, compared with 162.5 nm for a standard interferometric measurement technique.

Chapter 1

Introduction

The development of a simple, portable, clinical diagnostic device that can perform a comprehensive range of tests, inexpensively, and give results within a few minutes has been a dream of biosensing research groups for many years. A General Practitioner equipped with such a device will be able to make informed diagnoses, monitor critical clinical indicators and tailor treatment accordingly, without the need to wait for laboratory results. Or a volunteer working in a remote village in a third world country will be able to screen hundreds of children in a day for HIV, malaria, hepatitis, nutrition deficiencies and a host of other clinical indicators using a portable test instrument. Since results are available immediately, remedial action can be initiated instantly.

In addition to clinical diagnostics, such an analytical system would be invaluable in areas such as epidemic control, water quality management, environmental monitoring, wine industry, food industry, agriculture and farming where frequent biochemical testing is desirable, yet hitherto impractical due to cost, time or mobility limitations of the tests. The vision of a cheap, compact and simple yet comprehensive test device has been driving the development of Total Analytical Systems (TAS), also known as Lab-on-a-Chip (LOC) devices.

Advances in Micro Electro-Mechanical Systems (MEMS) in general, and in Microflu-

idics in particular, have provided the technological framework to bring us closer to realising this dream. Assays such as ELISA (Enzyme-Linked ImmunoSorbent Assay) are used widely for testing for HIV. Other elements of micro-TAS have been reported, such as a sensor for dengue fever [1], enzymatic analysis of single cells [2], and hepatocyte culture [3]. However, these devices still require that samples be labelled using fluorescent markers, a step that consumes considerable time [4]. When performing a wide range of tests, the samples have to be uniquely tagged for each test, which increases the sample preparation time several-fold. Hence, a rapid TAS has not yet been realised.

MEMS microcantilevers provide an alternative technology that overcomes this limitation. One face of the cantilever is coated with a functionalising layer which is highly specific to a particular analyte. This layer acts as the sensing element. When the cantilever is brought into contact with the corresponding analyte, the interaction between the functionalising layer and the analyte causes a change of free energy, which results in a change of surface stress. The difference between the stresses of the functionalised and non-functionalised layers causes the cantilever to deflect. Thus the cantilever transduces a chemical reaction into a mechanical response [5]. Measurement of this deflection provides a rapid indication of the analyte concentration. The literature is abound with reports of cantilevers being used to detect a myriad range of chemicals [6, 7], proteins [8], antigens [9], DNA [10, 11, 12] as well as a broad range of other biological, chemical and physical phenomena.

The advantages of microcantilever-based sensors are many. Since hundreds of microcantilevers can be fabricated on a single silicon wafer, the cost per unit is low. Cantilever dimensions are generally in the micrometer range, and hence the amount of chemicals required to functionalise the beams are a fraction of what would be required for a macro-scaled device. Further, the forces required to actuate the cantilevers are very small, which make cantilever sensors highly sensitive devices. Due to the high sensitivity, only a minute amount of sample volume, typically a few hundred microliters, is all that is required to perform an accurate test using a cantilever

biosensor.

Several commercial products based on this cantilever technology have been introduced to the market. However, they are either limited to a few, fixed cantilevers [13] or require manual intervention [14]. There is currently no commercial product using cantilevers that can perform automatic tests for a wide range of biochemicals.

If a generic biochemical measurement technology based on microcantilever sensors could be developed, it would help realise the dream of rapid, cheap, in-situ testing in all of the diverse fields mentioned above.

1.1 Motivation

There are a number of technical obstacles that have to be overcome before a microcantilever-based, self-contained biochemical measurement device can be fully developed. For repeatability of tests, the functionalising of cantilevers has to be consistent across all the sensors. The activity, stability and lifetime of functionalised cantilevers have to be characterised. These issues have been investigated in [15].

Some analytes, such as glucose, have been shown to yield stable cantilever deflections within 5 minutes [16]. For clinically significant glucose concentrations, the expected deflections are in the range of 0–40 nm. On the other hand, prostate specific antigens (PSA) have taken 3–4 hours to produce stable cantilever deflections [9] due to low diffusion rates of the molecules in the liquid. It is proposed in [17] that a stable result for PSA can be obtained within 5 minutes by making the sample volume much smaller than that reported in the literature. The drawback is that the cantilever deflections then decrease. If a sample volume of 50 nl is used, the cantilever deflection for clinically significant PSA levels will only be 0.11–2.1 nm [18], which makes measurement difficult.

To be useful in each case, the cantilevers have to be sensitive enough to respond to the smallest analyte concentration of interest. At the same time, the functionalising

layer, and therefore the cantilever surface, has to be large enough to avoid saturation of the sensing layer even at the highest possible analyte concentration.

Another key problem is the measurement of cantilever deflections. Several techniques have been demonstrated in the literature, but each method has its own limitations. The cantilever deflections can range from the sub-nanometric scale up to several micrometers. Thus, the measurement technique has to be able to measure deflections of several hundred nanometers with sub-nanometer resolution. Ideally, the measurement technique should not require any special fabrication of the disposable cantilever sensors, and have non-contact coupling with the cantilevers.

The cantilever dimensions, sample volume size and the requirements of the measurement system are all intrinsically tied together. If a method of arranging an array of cantilevers, functionalised to respond to different analytes can be found, and if the deflection of these cantilevers can be measured using a simple device, then a highly sensitive, rapid, inexpensive diagnostic device can be realised.

1.2 Problem statement

One of the key problems that has prevented the development of a MEMS microcantilever-based, self-contained biochemical measurement device has been the inability to improve the deflection response of cantilevers while maintaining noise immunity. A simple measurement system that can measure deflections of several hundred nanometers with sub-nanometer resolution that does not require manual intervention is not available.

1.3 Objective

The objective of this Thesis is to investigate the basis for achieving an arrangement of cantilevers coupled to a simple measurement system that can be used to

automatically measure deflections of up to several hundred nanometers with sub-nanometric resolution. In order to achieve this objective, the following investigations are undertaken in this thesis.

- Investigate how the deflection of a cantilever can be increased, while maintaining noise immunity.
- Investigate deflection as a function of cantilever geometry.
- Review the measurement techniques to identify the most suitable method to measure the deflection of disposable cantilever sensors.
- Investigate the limitations of the selected measurement methods, and propose methods of overcoming these limitations.

This research takes the state-of-art one step closer to achieving a self-contained, rapid, automated biochemical measurement device.

The problems concerned with functionalisation, saturation, analyte volume, reaction times and other biochemical problems are not addressed in this thesis. Some of these problems are considered in [17].

1.4 Overview of the thesis

The main body of the Thesis is organised into seven Chapters.

Chapter 1 is this Introduction. A broad overview of the problem is presented, and the barriers are stated. The objectives of this Thesis are outlined.

Chapter 2 presents the Literature Review. It covers the state-of-the-art of MEMS cantilever sensors and highlights their problems and limitations. The common techniques available to measure cantilever deflections are reviewed, and their merits and demerits are discussed. From an appraisal of the literature, directions for this research are identified.

Chapter 3 investigates the problem of the inverse relationship between deflection and the resonant frequency of microcantilevers. From these investigations, a principle is established that allows both deflection and resonant frequency to be enhanced simultaneously by introducing structural modifications to the beam. Mathematical models are developed and verified to describe the dynamics of microcantilevers with structural modifications.

Chapter 4 investigates different cantilever structures using the mathematical models developed in Chapter 3. The principles established in the previous chapter are validated. A novel cantilever profile that achieves a larger deflection together with a larger noise immunity compared with standard cantilevers is derived and presented.

Chapter 5 investigates limitations of the standard interferometric method of microcantilever deflection measurement. Several principles are established and proven that allow these limitations to be overcome. A basis for achieving a highly sensitive, automated interferometric measurement method that has a large measuring range is presented.

Chapter 6 uses the principles and the models developed earlier in the thesis to present the basis of a cantilever array which has an adequate deflection, noise immunity and which can be measured in an automated system. It is shown that the system performs as predicted, both at low deflection values as well as at high deflections.

Chapter 7 presents a summary of the work done and the conclusions of the Thesis.

In addition, the thesis is supplemented by two appendices:

Appendix A provides the complete mathematical development of the analytical models described in Chapter 3.

Appendix B lists software scripts written to solve complex equations, and scripts developed to simulate and verify the theories developed in the Thesis.

1.5 Original contributions

This thesis contributes the following to the body of knowledge:

1. A principle to selectively modify the deflection and resonant frequency of microcantilevers using structural modifications.

2. A method to analytically model the surface stress-induced deflection of non-prismatic cantilevers.

3. Simple analytical models to describe the deflection and resonant frequency of non-prismatic cantilevers.

4. A novel cantilever structure that has a higher deflection together with a higher resonant frequency, which gives a higher noise immunity compared with standard rectangular cantilevers.

5. A principle to extend the deflection measurement range of interferometric cantilever arrays beyond the quarter-wavelength limitation.

6. A novel arrangement of an array of cantilevers that facilitates automated measurement of cantilever deflections.

7. A method to overcome the alignment requirement of interferometric measurements.

8. The basis for designing an array of cantilevers whose deflection can be measured using a simple, automated interferometric measurement setup.

1.6 Publications

The research undertaken during the candidature of this thesis has resulted in three publications:

1. S. N. Fernando, M. W. Austin, and J. P. Chaffey, "Improved cantilever profiles for sensor elements", *Journal of Physics D: Applied Physics*, vol. 40, no. 24, pp. 7652–7655, 2007.

2. S. N. Fernando, M. W. Austin, and J. P. Chaffey, "Sensitivity analysis of cantilever biosensors", Proc. SPIE vol. 6035, *Microelectronics: Design, Technology, and Packaging II*, 603514–11, Jan 2006. Proc. SPIE International Symposium on Microelectronics, MEMS and Nanotechnology 2005, Brisbane, Australia, December 11–15, 2005.

3. S. N. Fernando and J. P. Chaffey, "Maximising microcantilever response: an analytical approach using mathematical models", Proc. SPIE vol 5649, *Smart Structures, Devices, and Systems II*, pp. 265–274, Feb 2005. Proc. SPIE International Symposium on Smart Materials, Nano- and Micro-Smart Systems, Sydney, Australia, December 12–15, 2004.

References

[1] A. Baeumner, N. Schlesinger, N. Slutzki, J. Romano, E. Lee, and R. Montagna, "Biosensor for dengue virus detection: Sensitive, rapid, and serotype specific," *Analytical Chemistry*, vol. 74, no. 6, pp. 1442–1448, 2002.

[2] G. Ocvirk, H. Salimi-Moosavi, R. Szarka, E. Arriaga, P. Andersson, R. Smith, N. Dovichi, and D. Harrison, "β-galactosidase assays of single-cell lysates on a microchip: a complementary method for enzymatic analysis of single cells," *Proceedings of the IEEE*, vol. 92, no. 1, pp. 115–125, 2004.

[3] M. Zhang, P. Lee, P. Hung, T. Johnson, L. Lee, and M. Mofrad, "Microfluidic environment for high density hepatocyte culture," *Biomedical Microdevices*, vol. 10, no. 1, pp. 117–121, 2008.

[4] R. McKendry, J. Zhang, Y. Arntz, T. Strunz, M. Hegner, H. P. Lang, M. K. Baller, U. Certa, E. Meyer, H.-J. Guntherodt, and C. Gerber, "Multiple label-free biodetection and quantitative dna-binding assays on a nanomechanical cantilever array," *Proceedings of the National Academy of Sciences*, vol. 99, no. 15, pp. 9783–9788, 2002.

[5] J. Fritz, M. Baller, H. Lang, H. Rothuizen, P. Vettiger, E. Meyer, H.-J. Guntherodt, C. Gerber, and J. Gimzewski, "Translating biomolecular recognition into nanomechanics," *Science*, vol. 288, no. 5464, pp. 316–318, 2000.

[6] F. Battiston, J.-P. Ramseyer, H. Lang, M. Baller, C. Gerber, J. Gimzewski, E. Meyer, and H.-J. Guntherodt, "A chemical sensor based on a microfabricated cantilever array with simultaneous resonance-frequency and bending readout," *Sensors and Actuators, B: Chemical*, vol. 77, no. 1-2, pp. 122–131, 2001.

[7] H. Lang, M. Baller, F. Battiston, J. Fritz, R. Berger, J.-P. Ramseyer, P. Fornaro, E. Meyer, H.-J. Guntherodt, J. Brugger, U. Drechsler, H. Rothuizen, M. Despont, P. Vettiger, C. Gerber, and J. Gimzewski, "The nanomechanical nose," in *Micro Electro Mechanical Systems, 1999. MEMS '99. Twelfth IEEE International Conference on*, pp. 9–13, 1999.

[8] C. Savran, S. Knudsen, A. Ellington, and S. Manalis, "Micromechanical detection of proteins using aptamer-based receptor molecules," *Analytical Chemistry*, vol. 76, no. 11, pp. 3194–3198, 2004.

[9] G. Wu, R. Datar, K. M. Hansen, T. Thundat, R. Cote, and A. Majumdar, "Bioassay of prostrate-specific antigen (PSA) using microcantilevers," *Nature Biotechnology*, vol. 19, no. 9, pp. 856–860, 2001.

[10] J. Thaysen, R. Marie, and A. Boisen, "Cantilever-based bio-chemical sensor integrated in a microliquid handling system," in *Micro Electro Mechanical Systems, 2001. MEMS 2001. The 14th IEEE International Conference on*, pp. 401–404, 2001.

[11] K. M. Hansen, H.-F. Ji, G. Wu, R. Datar, R. Cote, A. Majumdar, and T. Thundat, "Cantilever-based optical deflection assay for discrimination of dna single-nucleotide mismatches.," *Analytical Chemistry*, vol. 73, no. 7, pp. 1567–1571, 2001.

[12] G. Wu, H. Ji, K. Hansen, T. Thundat, R. Datar, R. Cote, M. Hagan, A. Chakraborty, and A. Majumdar, "Origin of nanomechanical cantilever motion generated from biomolecular interactions," *Proceedings of the National Academy of Sciences of the United States of America*, vol. 98, no. 4, pp. 1560–1564, 2001.

[13] Cantion A/S (http://www.cantion.com/cantilever_technology.htm), March 2008.

[14] "Cantisens cantilever arrays for static mode measurements." http://www.concentris.ch, March 2008.

[15] C. Grogan, R. Raiteri, G. M. O'Connor, T. J. Glynn, V. Cunningham, M. Kane, M. Charlton, and D. Leech, "Characterisation of an antibody coated microcantilever as a potential immuno-based biosensor," *Biosensors and Bioelectronics*, vol. 17, no. 3, pp. 201–207, 2002.

[16] X. Yan, H.-F. Ji, and Y. Lvov, "Modification of microcantilevers using layer-by-layer nanoassembly film for glucose measurement," *Chemical Physics Letters*, vol. 396, no. 1-3, pp. 34–37, 2004.

[17] K. Silva, —. Phd, RMIT University, 2008.

[18] K. Silva. (private communication), 2008.

Chapter 2

Literature Review

The quest for the development of simple instruments that analyse bio/chemical samples in real time, in-situ and inexpensively has taken several avenues. Most have embraced Microtechnology and MEMS to deliver cost and speed benefits.

A sensing device consists of three main components: a *detector* which recognises the phenomena of interest; a *transducer* which converts that signal into a measurable form; and a *read-out system* which measures the transduced signal. Microcantilevers have been demonstrated to act both as the detector and as the transducer of bio-chemical interactions. External measurement devices have been used to measure their responses.

In this Literature Review, the principles of using a microcantilever as the transducing element are reviewed. A few relevant examples of MEMS bio/chemical detectors are examined, and their performances are compared. The limitations of cantilever sensors and methods proposed to overcome these limitations are examined. Gaps in the current body of knowledge with regards to cantilever sensors are identified. Then, a range of read-out mechanisms are summarised. Finally, a broad evaluation of the state-of-the-art of MEMS cantilever sensors is performed to identify the problems that this research will investigate.

2.1 Microcantilever sensors

Microcantilevers have been used in Atomic Force Microscopy for many years. Since the early 90's, it has been demonstrated how microcantilevers can be used to transduce many types of phenomena into a mechanical response. Mass, temperature, heat, electromagnetic field, stress etc have been transduced into a mechanical response of microcantilevers [1]. A common application of cantilever sensors is for the detection and measurement of chemical/biochemical species. One face of the cantilever is coated with a layer of molecules that show a high specificity to the analyte of interest. This step is termed as "functionalising" the cantilever. The other face of the cantilever is maintained relatively inert to bio/chemical interactions. When the cantilever is brought into contact with the sample being analysed, the functionalising molecules interact with the target analytes, while being inert to other molecules in the sample. This interaction changes some measurable properties of the cantilever. This response is measured, and is in general proportional to the intensity of the interaction.

Two fundamental principles have been reported in the literature to use a microcantilever as a transducer: the change of resonant frequency method and the deflection method. In the resonant frequency method, also known as the dynamic method, the resonant frequency (natural frequency) of the cantilever shifts as a result of its interaction with the measurand. In the deflection method, sometimes referred to as the static method, the microcantilever deflects as a result of the interaction between the cantilever and the measurand.

2.1.1 The resonant frequency method

When analytes are adsorbed onto the cantilever or when they bind with receptors, the mass of the cantilever increases. This causes a change in resonance frequency,

given by [2, 3]

$$\Delta m = \frac{k}{4\pi^2 n}\left(\frac{1}{f_2^2} - \frac{1}{f_1^2}\right) \tag{2.1}$$

where

Δm : change of mass

k : spring constant of the cantilever

f_1 : initial resonant frequency of the cantilever

f_2 : resonant frequency after adsorption of the analyte

n : a constant, depending on the cantilever type and material

The adsorbed mass Δm can be directly calculated from the shift of resonant frequency $(f_2 - f_1)$. Microcantilever sensors for humidity [4], water vapour, primary alcohols and alkenes [5] and prostate specific antigens (PSA) [6] have been reported which use this principle.

To calculate the adsorbed mass from the shift of resonant frequency using Equation (2.1), the spring constant has to remain unchanged during the biochemical reaction. Experimental results in [2] demonstrated that adsorption of water vapour resulted in an increase in resonant frequency. This suggested that adsorption caused the spring constant to change, in addition to changing the effective mass of the beam. The fact that the frequency increased showed that the effect of adsorption on the spring constant was greater than the change in mass.

It was analytically shown in [7] that tensile surface stresses increase the resonant frequency, while compressive surface stresses decrease the resonant frequency of microcantilevers. When a thin layer of biomolecules is adsorbed, it causes a significant change in the spring constant, but has little effect on the mass [7]. This effect was mathematically analysed in [8]. Since the spring constant does not remain constant, an accurate value of the adsorbed mass cannot always be obtained using Equation (2.1).

It was observed in [9] that the resonant frequency of a microcantilever can be up to 5 times lower in water than in air. It was further observed that the resonant peaks are less prominent in water, due to the damping effect of liquids. This reduces the sensitivity of the device.

Further, the cantilever must be excited to vibrate over a range of frequencies to determine its resonant frequency. The cantilever can be actuated using a piezoelectric crystal [10], an electric field, a magnetic field, or by using a thermal actuating mechanism as reported in [11]. Each of these methods require additional fabrication steps to incorporate the actuation mechanism, or external instruments to excite the beams.

Due to these limitations of the resonant frequency method, the deflection method is more frequently used in cantilever biosensors.

2.1.2 The deflection method

When analytes bind with receptors, there is a change in surface free energy [12]. This change causes a change of surface stress on the functionalised face of the cantilever. Since only one face is functionalised, surface stress changes only in that face. This causes a differential surface stress to develop between the opposite faces of the cantilever. The differential surface stress causes the cantilever to bend [13].

The deflection t of a cantilever as a result of a differential surface stress $\Delta\sigma$ is quantified by the formula commonly referred to as Stoney's Equation:

$$t = \frac{3(1-\nu)L^2\Delta\sigma}{Eh^2} \tag{2.2}$$

where L is the length and h is the thickness of the cantilever; E and ν are the Young's modulus and Poisson's ratio of the cantilever material, respectively.

A large number of sensors have been reported in the literature using this method. Some examples are DNA [14, 15], prostate specific antigens (PSA) [12], glucose [16, 17], and pH [18].

The deflection method does not require the cantilevers to be excited over a range of frequencies in order to take measurements, and the reading is not affected by damping affects of the fluid. Therefore, the deflection method is simpler to implement than the resonant frequency method, and is the more suitable method for biosensors with disposable cantilever sensor elements.

Table 2.1 summarises some features of a few cantilever sensors reported in the literature that use the deflection method.

Table 2.1: Comparison of some common cantilevers from the literature

Sensor	Material	Size (μm)	k (Nm^{-1})	f_0 (kHz)	Type	t (nm)	Ref.
DNA	Si	$500 \times 100 \times 1$	0.02		Rectangular	-50–100	[14]
DNA	Si	180×1	0.26		V-shaped	-10–40	[15]
DNA	Si_xN_y	200×0.5			V-shaped	0–10	[19]
DNA	Si/Si_xN_y	$125 \times 40 \times 0.52$	0.2	60	Rectangular	–	[20]
PSA	Si_xN_y	200×0.5			V-shaped	0–200	[12]
Ethene, N		$500 \times 100 \times 1$			Rectangular	0–2500	[21]
H_2O, OH's	Si	$500 \times 100 \times 0.8$	0.02		Rectangular	$0–10,000$	[22]
H_2O, OH's	Si	$500 \times 100 \times 8.6$		50	Rectangular	0–1000	[5]
H_2O vapour	Si	200	0.06/0.09		V-shaped	–	[2]
Glucose	Si	$350 \times 35 \times 1$	0.03		Rectangular	0–250	[16]
Glucose	Si	180×1			V-shaped	20	[17]
pH	Si_xN_y	200×0.7			V-shaped	30	[18]
Chemical reaction	Si/Al	$400 \times 35 \times 1.5$	0.19	12.2	Rectangular	500	[23]
Proteins	Si_xN_y				Rectangular	0–30	[24]
Cardiac biomarker	Si	$500 \times 100 \times 0.5$			Rectangular	0–1000	[25]
	Si	8×0.06	4	1200	V-Shaped		[26]

Note: The size of microcantilevers are presented as length $\times$ width $\times$ thickness for rectangular beams, and length $\times$ thickness for v-shaped beams. k: spring constant; f_0: resonant frequency; t: deflection.

2.1.3 Limitations and improvements reported

Microcantilevers are subject to background noise. It was reported in [27] that the flow rate, the salt concentration of the medium, and the pH value of the medium caused changes in the deflection. Thus the experiments were conducted with the flow rate, medium salt and temperature carefully controlled. In [12, 19], temperature was controlled to within $\pm 0.05^{\circ}$C, while in [28] experiments were conducted on a vibration-isolated table in a temperature controlled environment, to minimise errors due to thermal and vibrational noise.

It was shown in [9] that the thermal noise was spread from dc up to the fundamental resonant frequency of a cantilever. Thus increasing the resonant frequency spreads the noise over a larger frequency range, making the noise in a given measurement bandwidth smaller. Taking this principle into consideration, the resonant frequency of microcantilevers was increased in [29] by modifying the cantilevers to have thinner legs. It was shown that the noise decreased by the same factor as the increase of the resonant frequency. In [30], the thermal-noise-limited minimum detectable force using a cantilever was determined. It was seen that the minimum detectable force was inversely proportional to the resonant frequency of the cantilever. These investigations highlighted the need to increase the resonant frequency of cantilevers to increase their noise-limited measurement resolution.

There is considerable drift in cantilever deflections when enclosed in liquid environments. The origin of these drifts are twofold. The first is the sudden, large deflection that occurs when the beam is immersed in the liquid medium, as reported in [14, 15, 19, 20]. This phenomena was explained in [30] as being due to the rearrangement of the cantilever surface. The second source of drift is due to the bi-material effect. Since a cantilever sensor is made up of several layers of different materials (for example silicon and gold) having different thermal expansion coefficients, temperature variations can induce a deflection due to the bi-material effect [31].

The effect of thermal drift on cantilevers was studied in [32]. Two identical silicon nitride cantilevers were fabricated side by side. A thin layer of gold was applied on one face of each cantilever to achieve a bimorph. The device was placed in a fluidic cell and cold water was injected. As the water warmed up to ambient temperature, the cantilevers deflected due to the bi-material effect, and the deflections were monitored. It was demonstrated that a 1°C temperature rise induced a 1.4 nm deflection, which is comparable with deflections caused by biochemical reactions, as given in Table 2.1.

There is no consensus among the scientific community as to the origins of the surface stress. Adsorption-induced surface stress has been investigated by many, such as in [19, 33]. Adsorption, electrostatic interactions, changes in the surface hydrophobicity and conformational changes of the adsorbed molecules have been identified as possible reasons for the generation of surface stress [34]. In [35] it was concluded that a cantilever biosensor can deflect due to several phenomena. In addition to specific interactions, non-specific bindings and thermal drifts were identified as factors contributing to the deflection of cantilevers. Thus, the need to make differential measurements with respect to reference cantilevers to eliminate non-specific signals was highlighted in this paper.

In a differential measurement arrangement, one cantilever is functionalised to interact with the analyte, while another is coated with an inert layer, such as gold. Common-mode noise affects both cantilevers in a near-identical manner, and a differential measurement can be used to eliminate this noise. This approach was reported in [14]. It was shown in [32] that differential measurements were nearly 50 times less sensitive to temperature variations than measurements on a single cantilever.

In a further improvement, an array of cantilevers was used in [21, 22]. Four cantilevers were coated with gold on one side; the uncoated side acted as a sensor for water vapour. Another four cantilever were coated with gold on both sides, making them inert to water vapour and acted as reference beams. The sensor cantilevers deflected in the presence of water vapour, while the reference cantilevers showed

no deflection. By taking the average of the sensor cantilevers, random noise effects such as thermal noise and electronic amplifier noise were reduced. The differential measurement between the sensor cantilevers and reference cantilevers reduced common-mode noise such as mechanical vibrations and thermal drift.

In [5], individual cantilevers in an array were functionalised with different polymers. Each polymer interacted with the analyte in a unique manner, giving rise to a range of different responses within the elements of the array. An Artificial Neural Network (ANN) was used to identify patterns and extract information from the response of the array. It was demonstrated that this array could be used to analyse a range of chemicals such as water, alcohols and alkenes.

Another problem of microcantilever biosensors is the long time required to attain stable deflections for some analytes. The time taken to reach a stable deflection of a few cantilever sensors are summarised in Table 2.2.

Table 2.2: Comparison of sample volumes and measurement times

Sensor	Sample volume (μl)	Stabilisation time	Def. range (nm)	Ref.
DNA	0.14	80 s	–	[20]
DNA	250	30 min	-40–10	[15]
DNA	3000	80 mins	-50–100	[14]
Glucose	200	1 hour	0–250	[16]
Glucose	200	20 min	–	[27]
Glucose	2000	5 min	20	[17]
PSA	100	3–4 hours	0–200	[12]

The main reason for the long detection time of cantilever-based DNA sensors is thought to be caused by the slow diffusion of molecules in the reaction chamber [12]. In [15], at least 30 minutes were required to achieve stable cantilever deflections for the detection of DNA-oligonucleotide in a 250 μl fluid chamber. In contrast, a stable deflection for the detection of DNA-oligonucleotide was obtained in just 80 seconds when microchannels having volumes of 0.14 μl were used [20]. It was further shown in [20] that the smaller fluid cells overcame the problems of liquid turbulence and temperature gradients. In the case of glucose sensors, the fast response time in [17]

was achieved by using a novel layer-by-layer nanoassembly technique to functionalise the cantilevers.

It is being shown in [36] that smaller reaction chambers, while achieving fast responses, results in much lower surface stresses. As an example, using the results of [12], the surface stress for the minimum clinically significant PSA level of 1 ng/ml is found to be 4×10^{-3} μN/μm, where the reaction volume was 100 μl. However, when the volume is 50 nl, the surface stress value becomes 48.5×10^{-6} μN/μm [37].

Thus, while fast response times can be achieved using small analyte volumes, the cantilever response must be enhanced accordingly such that the deflections are large enough to be measured using a simple device. It was noted earlier that the resonant frequency of microcantilevers must be increased to improve noise immunity. Thus, to be viable sensor elements, both the deflection and the resonant frequency of cantilevers must be simultaneously increased.

2.2 Enhancing cantilever response

The deflection for a given surface stress value can be increased by selecting a material that has a lower Young's modulus, as evident from Equation(2.2). Cantilevers made of polymers such as PPMA, PMMA and polystyrene have been shown to have Young's moduli in the range 3–6 GPa, compared with a Young's modulus of 165 GPa for silicon [38]. Cantilevers made out of the SU-8 polymer, which has a much lower Young's modulus than silicon, have also been reported [39, 40]. However, immobilizing receptors on polymers is difficult [41], and only a few biosensing applications using polymer cantilevers have so far been demonstrated, such as in [42].

Thin microcantilevers have a greater deflection than thick beams for the same surface stress, as evident from Stoney's equation (2.2). However, thin beams tend to deform in the lateral direction (arching) in addition to deflecting in the longitudinal direction (bending). The arching effect is schematically shown in Figure 2.1(a). Arching increases the section modulus of the cantilever, making longitudinal bending more

difficult [43], thereby reducing the sensitivity of the cantilever. Arching also makes measurement by both piezoresistive and optical methods complicated since different points across the free end of the cantilever will have different displacements, and there will be no single value for the free-end deflection. Thin cantilevers are also susceptible to breakage during fabrication.

Ribbed cantilevers (Refer Figure 2.1(b)) were investigated in [43, 44] as a means of overcoming these problems. Cantilevers having alternate thin and thick sections were simulated using the Finite Element Method (FEM). It was shown that ribbed cantilevers could achieve a deflection comparable to that of a thin beam, while reducing arching to a level comparable to that of a thick beam.

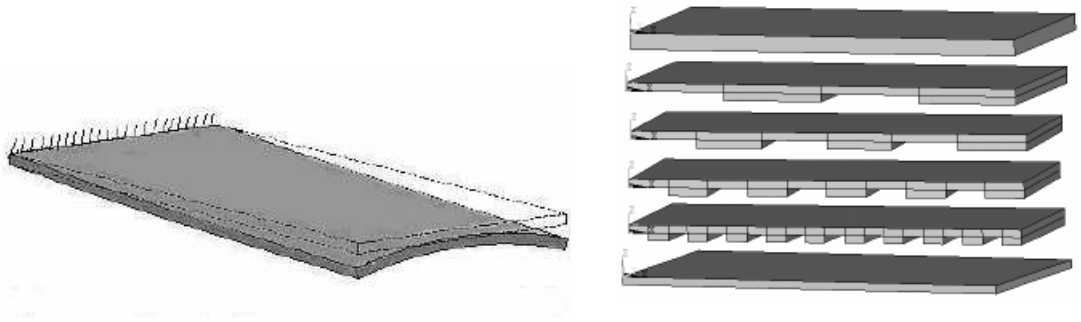

(a) The arching effect (b) Different ribbed cantilevers

Figure 2.1: Arching and ribbed cantilevers [43].

In another similar approach, grooves were milled on the cantilever surface, and an improved response was obtained [13]. Rectangular silicon microcantilevers measuring 200 μm $\times$50 μm$\times$1.5 μm were used in this investigation. Using focused ion beam (FIB) milling, grooves of 200 nm, 400 nm and 600 nm were created on the 100 μm nearest the fixed end of the cantilever. Figure 2.2 shows a portion of a milled cantilever.

After chemical functionalisation and reacting with the analyte, the unmodified beams showed no clear measurable response while measurable deflections were observed in the milled beams. It was also observed that while the grooves increased

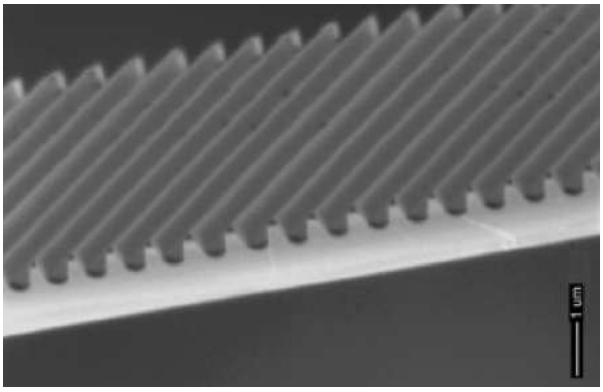

Figure 2.2: Microcantilever with milled grooves [13].

sensitivity, it also made the cantilevers noisier. The resonant frequencies of grooved cantilevers were found to be lower than the unmodified beams, which explains the decrease of noise immunity. The response was also found to depend on the groove dimensions, highlighting the need to optimise the scale of the features.

Increasing the deflection of cantilevers by introducing surface modifications was reported in [45]. Gold nanostructures were formed on the surfaces using two approaches: binding a layer of gold nanospheres with a mean diameter of 20 nm or by forming a granular gold film. These nanostructures achieved a 13-fold increase in surface area, and a 6-fold increase in receptor density. The measured deflection was two orders of magnitude greater than that of microcantilevers with smooth surfaces.

Thus, there have been several different methods reported to increase the deflection of cantilevers. However, when deflections have been increased by making structural modifications to the cantilevers, it has resulted in an increase in noise. No analytical study has been reported to optimise the form of these structural modifications. Currently, no principle is known by which the deflection of cantilevers can be increased while maintaining a high resonant frequency, in order to maintain a high noise immunity.

2.3 Cantilever response detection methods

The read-out system used to measure the deflection of disposable cantilever sensors must meet several conditions. Firstly, it should be possible to couple the read-out system with the disposable cantilevers easily for deflection measurements to be made. The measurement technique must have an adequate resolution to measure the minimum expected deflection, and must have an adequate range to measure the largest deflection. Ideally, the technique must not impose any special fabrication requirements on the cantilevers.

A number of different read-out techniques to measure the response of microcantilevers have been reported in the literature, and the most common ones are summarised below. Their relative merits and demerits are discussed from the viewpoint of meeting the above requirements.

2.3.1 Capacitive

The deflection of cantilevers can be measured by a parallel plate capacitive arrangement [46]. The cantilever is arranged as a moving electrode in the proximity of one or more fixed electrodes, separated by a dielectric. As the beam deflects, the separation between the electrodes changes, which causes its capacitance to change.

Often, a differential capacitive arrangement is used. Three electrodes are used in this configuration, two of which are fixed and the third is movable. The fixed electrodes form one capacitor, while the movable electrode forms a capacitor with a fixed electrode. The differential signal obtained from the two capacitors cancel out common-mode noise effects as discussed earlier.

Capacitive sensors consume less power than optical and piezoresistive methods [47], and are best suited when the sensors can be reused. A separate electronic circuit should be connected to the cantilever to read the capacitance value. Generally an Application Specific Integrated Circuit (ASIC) is fabricated alongside the cantilevers

for this purpose [48]. Several cantilevers can be connected as an array to use the same read-out circuit. Thus it is possible to develop complete sensors in a single package [47].

However, capacitive methods cannot be employed in electrolytic solutions. Further, since the measured capacitance depends on the dielectric constant of the medium between the capacitor plates and the area of the plates, there is a high degree of variability between sensors. Therefore each device has to be calibrated prior to measurements being made. If a capacitive measurement technique is used with disposable cantilever sensors, a physical electrical connection must be established between the cantilevers and the external measurement electronics, properly insulated to avoid any contact with fluidic cells. These requirements make fabrication and packaging expensive, and makes the technique less attractive for disposable sensors.

2.3.2 Piezoresistive

Measuring the deflection of cantilevers using piezoresistive sensors is also widely reported in the literature [20, 49, 50]. A set of piezoresistors is fabricated close to one surface of the cantilever. As the cantilever deflects, the stresses on its surfaces change, which cause the resistances of piezoresistors to change. Using a simple Wheatstone Bridge, the change of resistance can be measured. When the piezoresistive constants are known, the deflection of the microcantilevers can be calculated.

The piezoresistive method is well suited when the entire measurement system needs to be integrated into a single IC. The piezoresistors can be fabricated on the cantilevers, and the bridge circuit can be fabricated on the same chip. Piezoresistive sensors do not require alignment, and are simple to operate. They are not affected by the electrical conductivity nor by the optical properties of the media, and hence can be used in liquids, including opaque ones [20].

Fabricating piezoresistors on a cantilever is a complex process, as can be seen from [20, 51]. This makes fabrication expensive, and is the main limitation of the

piezoresistive measurement technique. If used with disposable sensors, a physical electrical connection must be established between the cantilevers and the external read-out circuitry. Further, when used in liquid environments, these electrical connections have to be insulated. Like the capacitive measurement technique, piezoresistive measurement is unattractive for use in disposable sensors.

2.3.3 Optical lever method

This is the most widely reported technique to measure the deflection of cantilevers. For example [12, 13, 15, 28, 45, 52] employ the optical lever method for measurements. A portion of the cantilever is coated with an optically reflective material, typically gold. A laser beam is focused onto this section, and a Position Sensitive Photo Detector (PSPD) is aligned with the reflected laser beam. When the cantilever deflects, the reflected beam moves in proportion to the deflection of the microcantilever [52]. A schematic diagram of the optical lever method is shown in Figure 2.3. The displacement of the reflected beam can be traced by the PSPD. Sub-nanometer resolutions have been reported using the optical lever method [28].

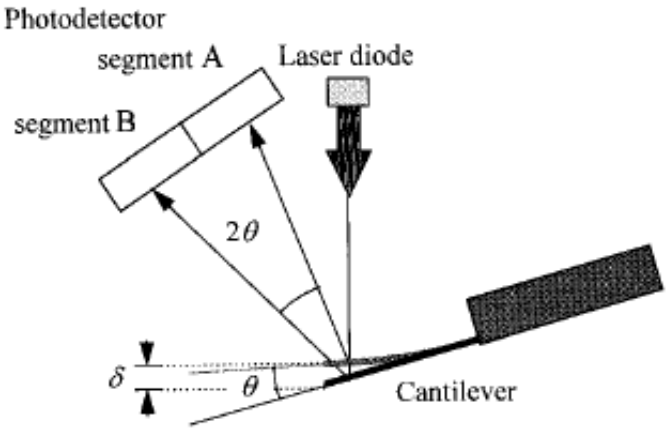

Figure 2.3: Schematic diagram of the optical lever method [53].

The optical level method does not require modifications to the cantilever (apart from a reflective coating if required), nor special circuitry to be fabricated into the

chip. The read-out is not affected by the electrical conductivity of the medium. Further, since the cantilevers and measurement systems are coupled optically, no physical contact between the read-out instrument and the cantilevers is required, greatly simplifying the packaging of sensors.

There are, however, several disadvantages of this method. The optical elements and the alignment instruments are bulky and expensive. Two alignment are required when using this method: the laser has to be precisely focused onto a known position on the cantilever, and PSPD has to be aligned with the reflected beam. These two alignment steps require precise instrumentation, and is difficult to automate. Further, to relate the measurement of the PSPD to the actual deflection of the cantilever, the distance between the cantilever and the PSPD, the incident angle of the laser and the refractive index of the media have to be accurately known. Optical techniques can only be used in transparent media. This method is also unsuitable when the refractive index of the medium is variable.

It is also difficult to make a differential measurement, or monitor an array of cantilevers simultaneously using the optical lever method, as each cantilever requires a laser source and read-out system. In [21, 22] a time multiplexed array of lasers was used, and the responses were measured using a single PSPD as a means of overcoming this problem.

In a variation of this principle, a fibre optic displacement sensor was used to measure displacements [54]. The sensor head consists of a bundle of optical fibres, some of which were connected to a laser source while the others were connected to photodiodes. Light coming from the transmitting fibres was reflected by the cantilever, and was captured by the receiving fibres. As the cantilever deflected, the proportion of light entering each receiving fibre changed, which gave an indication of the deflection.

The diameter of the fibre optic bundle limits the resolution. With a bundle diameter of 150 μm, displacements in the order of 100 μm were measured. This technique lacks the fine measurement resolution needed for MEMS cantilever sensors.

2.3.4 Optical interferometry

The deflection of cantilevers can also be measured by optical interferometry. A reference laser beam interferes with the reflected beam from the cantilever. The resulting interference pattern can be used to determine the deflection of the cantilever, and resolutions in the sub-angstrom range have been reported.

In [55] an interferometric deflection measurement method using an optic fiber is reported. The optic fibre is placed approximately 10 μm above the cantilever. A small fraction of the light is reflected back into the fibre by the glass-air interface at the end of the fibre. The remaining light exits the fibre, gets reflected off the cantilever and re-enters the fibre. These two reflected waves interfere. The optical power at the detector depends on the phase difference between the two waves, which is determined by the gap between the fibre and the cantilever. This arrangement is schematically shown in Figure 2.4.

Using a similar arrangement, displacements of approximately 1 nm were measured in [56], while sub-angstrom resolutions were achieved in [57].

However, the optical fibre needs to be positioned within a few micrometers of the cantilever for measurement, and the fibre has to be properly aligned and oriented. The fine adjustments require precise instruments and microscopic observation during setup. Further, the method loses sensitivity in liquids, limiting its use in biosensors.

A different interferometric technique using an interdigital cantilever (IDC) array for Atomic Force Microscopes was proposed in [58]. This structure consisted of two main cantilevers, each having a set of fingers attached to it. The fingers on one cantilever were arranged in an interdigital pattern with the fingers of the other cantilever. Figure 2.5 shows an image of an IDC. The outer cantilever was movable with an external force, while the inner cantilever remained stationary.

A laser beam was focused on to the interdigital fingers. The diffracted modes were captured by photodiodes. As the outer cantilever deflected, the interdigital fingers formed a phase sensitive diffraction grating. The intensity of the diffracted modes

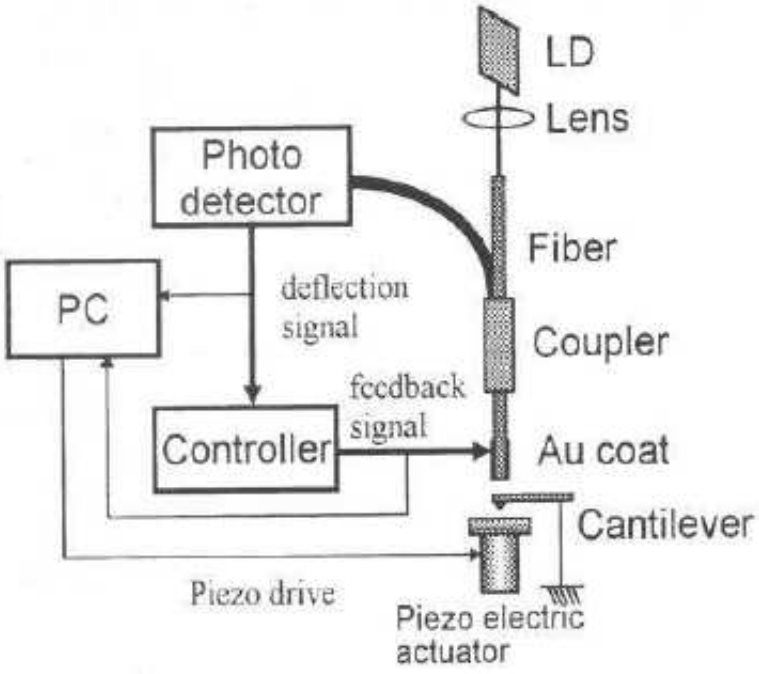

Figure 2.4: Schematic diagram of the fibre-optic interferometric sensor [55].

changed with the deflection.

Further work on the interdigital cantilever was reported in [60], where the noise-limited minimum detectable deflection was calculated to be 0.1 Å. It was shown that this arrangement required only a coarse alignment of the optical devices. It was further demonstrated that since the interdigital arrangement was essentially differential in nature, common-mode noise such as mechanical noise and laser noise were reduced.

An interdigital arrangement of cantilevers was also used in [61]. It was shown that thermal drifts could be eliminated by this technique, as the measurements were inherently differential. Further, the IDC technique requires only a single measurement from a crudely aligned photodiode, while the optical lever method requires the measurement of the deflection of two cantilevers from a precisely aligned optical system to make a differential measurement. A Signal to Noise Ratio (SNR) of 18

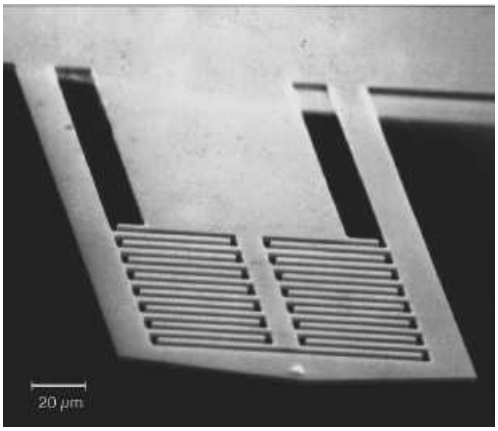

Figure 2.5: Micrograph of an interdigital cantilever [59].

was achieved for an IDC, while the SNR achieved for the optical lever was 3.

Like other optical methods, interferometric methods can only be used in transparent media. If the fluids can be flushed out of the reaction cell before taking deflection measurements, this limitation can be overcome. A further limitation of interferometric methods is the measurement range. Since the interference patterns are cyclic with the wavelength, absolute deflection measurements are limited to a single wavelength. While fringe counting, as used in traditional interferometric arrangements such as the Michelson Interferometer, can be used to measure much larger deflections, it requires continuous monitoring of the cantilever deflections. In a situation where the fluid has to be flushed out before taking measurements, the fringe counting technique becomes unusable.

In order to reduce the cost of optical measurement systems, several groups have investigated the possibility of using optical heads of CD/DVD drives as high resolution, low cost measurement devices. In [62], it was reported that the Focus Error Signal (FES) of commercial CD drives could be used take measurements in the order of 10's of micrometers.

A more comprehensive investigation of using a CD head was reported in [63]. Refer Figure 2.6. When the laser beam is focused on the measured surface, the beam scatters equally on the four quadrants on the photodiode. When the laser is out

of focus, the tilted glass plate creates an astigmatic beam, which is elliptical. The Focus Error Signal (FES) is given by

$$FES = (A + C) - (B + D)$$

where A,B,C and D are the outputs of the four quadrants. This method was shown to have a resolution of 10 nm.

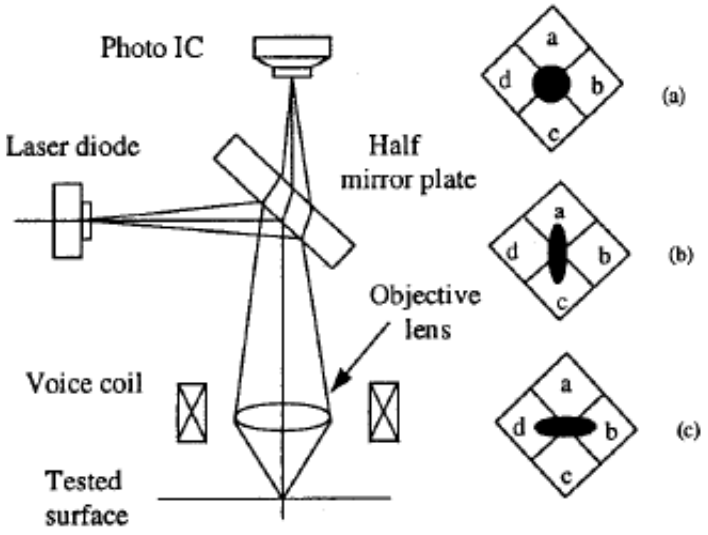

Figure 2.6: Schematic of a CD optical head arrangement, together with (a) in-focus pattern and (b,c) out-of-focus patterns at the photo detector [63].

In [64], a DVD head was used to characterise microcantilevers. Measurement resolutions of 1 nm in air and 2 nm in water were reported.

The advantages and disadvantages of the main methods of cantilever deflection measurement are tabulated in Table 2.3.

From the analysis of the different methods, it can be seen that only the optical methods do not require any specially fabricated cantilevers, which keeps the unit cost low. No physical connection between the cantilevers and the read-out instrument is required, simplifying the packaging of the sensors. Of the different optical methods,

Table 2.3: Comparison of the main deflection measurement techniques

Method	Advantages	Disadvantages
Capacitive	Easy to integrate with on-chip electronics Uses very little power Can measure an array of cantilevers	Can't be used in conductive media Need special fabrication Need to calibrate for dielectric variations Need electrical connection
Piezoelectric	Can integrate with on-chip electronics Unaffected by conductivity and transparency of medium Can measure an array No alignment requirement	Fabrication is complicated and expensive Electrical connections need insulation Need electrical connection with read-out circuit
Optical lever	Sub-angstrom resolutions Simple to implement No special fabrication required Non-contact coupling with read-out circuit	Precise alignment required Difficult to automate Difficult to measure multiple cantilevers Affected by refractive index of medium
Optical interferometry	Inherently differential measurements Only rough alignments required Sub-nanometer resolutions No special fabrication required Non-contact coupling	Measurement range limited to $\lambda/4$ Doesn't work in translucent liquids

the interferometric cantilever array method is the most attractive to measure the deflection of disposable cantilever sensors. It only requires a coarse alignment of the optical elements. It has a high resolution and the measurements are inherently differential in nature. However, its measurement range is limited to a quarter of the wavelength of the optical source. With a 650 nm source, the maximum measurable deflection is 162.5 nm, which is inadequate to measure some of the large deflections presented in Table 2.1. Since this method cannot be used in translucent media, the liquids have to be flushed out of the reaction cells before measurements can be taken.

2.4 Disc-based systems

In addition to using CD heads for optical measurements, interest has been shown in replicating entire biosensing systems on optical disc drive platforms. The optics of a CD/DVD drive can be regarded as a laser-scanning microscope. The centrifugal force generated by the spinning disc can be utilised in centrifugal filtering, microfluidic flow control and fluid mixing. A micro-array of sensors can be implemented on a single disc to conduct a broad range of tests simultaneously. Such a biosensor based on compact discs was reported by Burstein Technologies [65]. A standard CD/DVD reader was used with a custom made BioCompact Disc (BCD) together with special software to identify and quantify biochemical species. The BCD contained a large number of "Array Spots" that capture probes, for example DNA strands, of interest. The sample under test was treated with Biotin that made the target DNA molecules receptive to large Reporter Microspheres. When the sample was brought into contact with the BCD, target DNA strands in the sample hybridized (combine through hydrogen bonding) with the complementary capture probes on the BCD. Reporter Microspheres were then introduced, which bound with the hybridized DNA molecules. Array spots in both hybridized and bound states are shown in Figure 2.7.

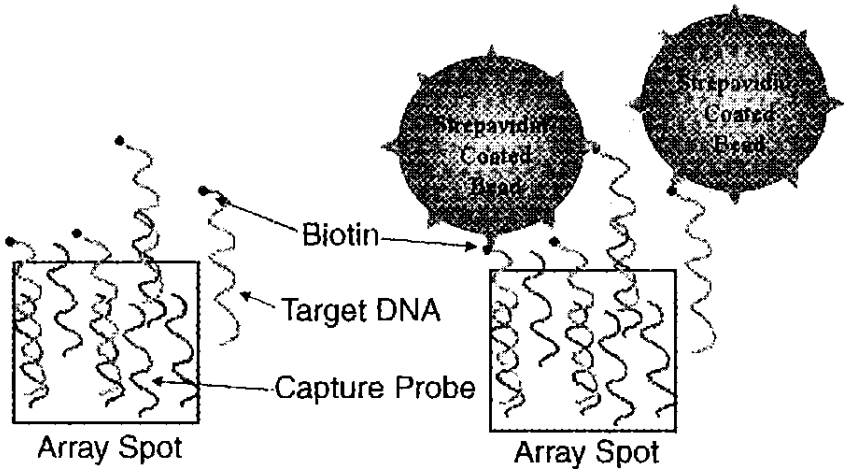

Figure 2.7: Principle of the BioCompact CD [63].

The presence of microspheres was observed optically using the CD/DVD drives. The concentration of the target DNA was determined by quantifying the number of Reporter Microspheres.

A spinning disc platform, similar to a compact disc, was used by Varma et al [59, 66, 67, 68] to address the problem of low-throughput of biosensors. Radial gold spokes were fabricated on a dielectric mirror. The thickness of these spokes was kept at $1/8^{th}$ of the wavelength of the read-out laser. Antibodies were then immobilized on some of the gold ridges. The BioCD, as the disc is called, was then exposed to antigens, that bound with the immobilized antibodies.

The BioCD was mounted on a photo-resist spinner, and an optical measurement system was arranged as in Figure 2.8. When the laser beam fell on the edge of a spoke, the measured intensity reduced by 50 %, since light reflected from the reflective substrate and the gold ridge interfered with a phase difference of $\pi/2$. When the the laser fell on ridges with bound antibodies, the intensity of the reflected light decreased further. It was demonstrated that the reduction in intensity was due to interference, and not scattering of light, by changing the height of the ridges to $3\lambda/8$, in which case the intensity drop was less than 50%.

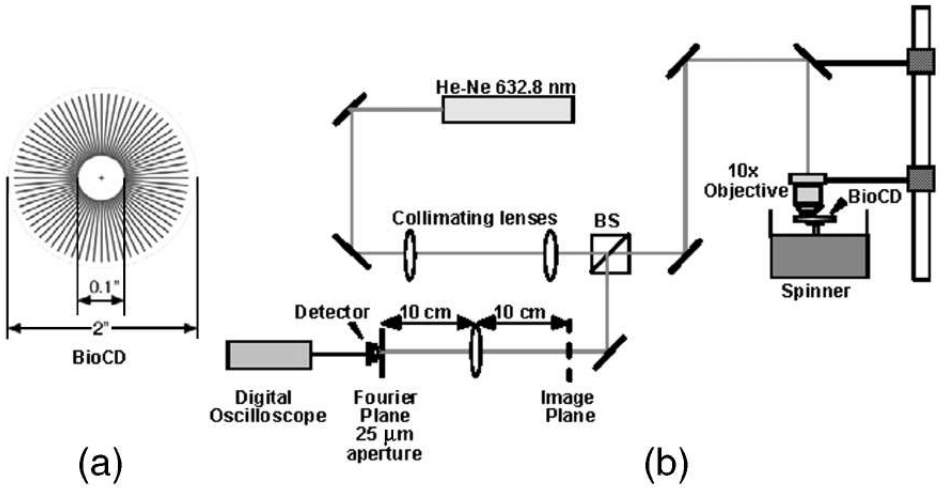

Figure 2.8: (a) Schematic of the gold spokes on the BioCD. (b) Schematic of optical detection system [59].

When the BioCD was spun at a rate of 6000 rpm, sampling rates of 100,000 samples per second were achieved. However, wobbling of the disc caused optical misalignments and induced a DC shift into the measurement. The use of high-stability spinners was suggested as the solution. Further, to measure the concentration of a species, the number of positive signals must be counted. Unlike cantilever–based sensors, a single measurement cannot yield the concentration of the analyte.

Thus, there have been several reports of biosensors being implemented on disc-based platforms. Forces generated by the the spinning discs enable microfluidic operations, while the optics provide a cheap measurement technique.

2.5 Conclusions

In this literature review, a range of cantilever sensors and their performances were presented. Microcantilever sensors based on the deflection method were identified as being more suitable for biosensing applications than sensors based on the resonant frequency method. The analysis of cantilever sensors highlighted that to achieve

stable deflections within a few minutes, the reaction volumes for some analytes should be made smaller. This results in much smaller cantilever deflections than reported in the literature. To enable measurement of these deflections using a simple device, the cantilever deflections should be increased.

It was further noted that the resonant frequency of cantilevers should be increased to achieve higher noise immunities, and thereby higher sensitivities. Several methods reported in the literature to increase the deflection of cantilevers were presented, and these methods were noted to decrease the resonant frequency of cantilevers. A method to achieve larger deflections and larger resonant frequencies simultaneously is currently unknown.

The review of several deflection measurement techniques found the interferometric cantilever array method to be the most suitable method to measure the deflection of disposable cantilever sensors, provided the reagents can be flushed out before measurements are taken. However, the measurement range is limited to about 160 nm, which prevents the measurement of large cantilever deflections.

Disc-based platforms can be used to implement entire sensor arrays with integrated microfluidics and cheap optical read-out devices. However, the inherent vibrations require that the cantilevers have higher resonant frequencies to minimise errors due to vibrational noise.

References

[1] R. Raiteri, M. Grattarola, H.-J. Butt, and P. Skladal, "Micromechanical cantilever-based biosensors," *Sensors and Actuators, B: Chemical*, vol. 79, no. 2-3, pp. 115–126, 2001.

[2] G. Chen, T. Thundat, E. Wachter, and R. Warmack, "Adsorption-induced surface stress and its effects on resonance frequency of microcantilevers," *Journal of Applied Physics*, vol. 77, no. 8, pp. 3618–3622, 1995.

[3] J. Yang, T. Ono, and M. Esashi, "Mechanical behavior of ultrathin microcantilever," *Sensors and Actuators A: Physical*, vol. 82, no. 1-3, pp. 102–107, 2000.

[4] D. Strembicke, A. Robinson, F. Vermeulen, M. Seto, and K. Brown, "Humidity measurement using resonating CMOS microcantilever structures," in *Electrical and Computer Engineering, 1999 IEEE Canadian Conference on*, vol. 3, pp. 1658–1661 vol.3, 1999.

[5] F. Battiston, J.-P. Ramseyer, H. Lang, M. Baller, C. Gerber, J. Gimzewski, E. Meyer, and H.-J. Guntherodt, "A chemical sensor based on a microfabricated cantilever array with simultaneous resonance-frequency and bending readout," *Sensors and Actuators, B: Chemical*, vol. 77, no. 1-2, pp. 122–131, 2001.

[6] J. H. Lee, K. S. Hwang, J. Park, K. H. Yoon, D. S. Yoon, and T. S. Kim, "Immunoassay of prostate-specific antigen (PSA) using resonant frequency shift of piezoelectric nanomechanical microcantilever," *Biosensors and Bioelectronics Selected Papers from the Eighth World Congress on Biosensors, Part II*, vol. 20, no. 10, pp. 2157–2162, 2005.

[7] P. Lu, F. Shen, S. O'Shea, K. Lee, and T. Ng, "Analysis of surface effects on mechanical properties of microcantilevers," *Materials Physics and Mechanics*, vol. 4, no. 1, pp. 51–55, 2001.

[8] Q. Ren and Y.-P. Zhao, "Influence of surface stress on frequency of microcantilever-based biosensors," *Microsystem Technologies*, vol. 10, no. 4, pp. 307–314, 2004.

[9] D. A. Walters, J. P. Cleveland, N. H. Thomson, P. K. Hansma, M. A. Wendman, G. Gurley, and V. Elings, "Short cantilevers for atomic force microscopy," *Review of Scientific Instruments*, vol. 67, no. 10, pp. 3583–3590, 1996.

[10] K. Domanski, P. Grabiec, J. Marczewski, T. Gotszalk, T. Ivanov, N. Abedinov, and I. Rangelow, "Fabrication and properties of piezoresistive cantilever beam

with porous silicon element," *Journal of Vacuum Science and Technology B: Microelectronics and Nanometer Structures*, vol. 21, no. 1 SPEC., pp. 48–52, 2003.

[11] A. V. Grigorov, Z. J. Davis, P. Rasmussen, and A. Boisen, "A longitudinal thermal actuation principle for mass detection using a resonant micro-cantilever in a fluid medium," *Microelectronic Engineering*, vol. 73-74, pp. 881–886, 2004.

[12] G. Wu, R. Datar, K. M. Hansen, T. Thundat, R. Cote, and A. Majumdar, "Bioassay of prostrate-specific antigen (PSA) using microcantilevers," *Nature Biotechnology*, vol. 19, no. 9, pp. 856–860, 2001.

[13] J. J. Headrick, M. J. Sepaniak, N. V. Lavrik, and P. G. Datskos, "Enhancing chemi-mechanical transduction in microcantilever chemical sensing by surface modification," *Ultramicroscopy*, vol. 97, no. 1-4, pp. 417–424, 2003.

[14] J. Fritz, M. Baller, H. Lang, H. Rothuizen, P. Vettiger, E. Meyer, H.-J. Guntherodt, C. Gerber, and J. Gimzewski, "Translating biomolecular recognition into nanomechanics," *Science*, vol. 288, no. 5464, pp. 316–318, 2000.

[15] K. M. Hansen, H.-F. Ji, G. Wu, R. Datar, R. Cote, A. Majumdar, and T. Thundat, "Cantilever-based optical deflection assay for discrimination of DNA single-nucleotide mismatches.," *Analytical Chemistry*, vol. 73, no. 7, pp. 1567–1571, 2001.

[16] J. Pei, F. Tian, and T. Thundat, "Glucose biosensor based on the microcantilever," *Analytical Chemistry*, vol. 76, no. 2, pp. 292–297, 2004.

[17] X. Yan, H.-F. Ji, and Y. Lvov, "Modification of microcantilevers using layer-by-layer nanoassembly film for glucose measurement," *Chemical Physics Letters*, vol. 396, no. 1-3, pp. 34–37, 2004.

[18] H.-F. Ji, K. M. Hansen, Z. Hu, and T. Thundat, "Detection of pH variation using modified microcantilever sensors," *Sensors and Actuators B: Chemical*, vol. 72, no. 3, pp. 233–238, 2001.

[19] G. Wu, H. Ji, K. Hansen, T. Thundat, R. Datar, R. Cote, M. Hagan, A. Chakraborty, and A. Majumdar, "Origin of nanomechanical cantilever motion generated from biomolecular interactions," *Proceedings of the National Academy of Sciences of the United States of America*, vol. 98, no. 4, pp. 1560–1564, 2001.

[20] J. Thaysen, R. Marie, and A. Boisen, "Cantilever-based bio-chemical sensor integrated in a microliquid handling system," in *Micro Electro Mechanical Systems, 2001. MEMS 2001. The 14th IEEE International Conference on*, pp. 401–404, 2001.

[21] H. Lang, M. Baller, F. Battiston, J. Fritz, R. Berger, J.-P. Ramseyer, P. Fornaro, E. Meyer, H.-J. Guntherodt, J. Brugger, U. Drechsler, H. Rothuizen, M. Despont, P. Vettiger, C. Gerber, and J. Gimzewski, "The nanomechanical nose," in *Micro Electro Mechanical Systems, 1999. MEMS '99. Twelfth IEEE International Conference on*, pp. 9–13, 1999.

[22] H. P. Lang, M. K. Baller, R. Berger, C. Gerber, J. K. Gimzewski, F. M. Battiston, P. Fornaro, J. P. Ramseyer, E. Meyer, and H. J. Guntherodt, "An artificial nose based on a micromechanical cantilever array," *Analytica Chimica Acta*, vol. 393, no. 1-3, pp. 59–65, 1999.

[23] J. K. Gimzewski, C. Gerber, E. Meyer, and R. R. Schlittler, "Observation of a chemical reaction using a micromechanical sensor," *Chemical Physics Letters*, vol. 217, no. 5-6, pp. 589–594, 1994.

[24] C. Savran, S. Knudsen, A. Ellington, and S. Manalis, "Micromechanical detection of proteins using aptamer-based receptor molecules," *Analytical Chemistry*, vol. 76, no. 11, pp. 3194–3198, 2004.

[25] Y. Arntz, J. D. Seelig, H. P. Lang, J. Zhang, P. Hunziker, J. P. Ramseyer, E. Meyer, M. Hegner, and C. Gerber, "Label-free protein assay based on a nanomechanical cantilever array," *Nanotechnology*, vol. 14, no. 1, pp. 86–90, 2003.

[26] K. Fukushima, D. Saya, H. Toshiyoki, H. Fujita, and H. Kawakatsu, "Characterization of silicon nanocantilevers," *Seisan Kenkyu*, vol. 53, no. 2, pp. 51–54, 2001.

[27] A. Subramanian, P. Oden, S. Kennel, K. Jacobson, R. Warmack, T. Thundat, and M. Doktycz, "Glucose biosensing using an enzyme-coated microcantilever," *Applied Physics Letters*, vol. 81, no. 2, p. 385, 2002.

[28] N. Lavrik, C. Tipple, M. Sepaniak, and P. Datskos, "Gold nano-structures for transduction of biomolecular interactions into micrometer scale movements," *Biomedical Microdevices*, vol. 3, no. 1, pp. 35–44, 2001.

[29] A. R. Hodges, K. M. Bussmann, and J. H. Hoh, "Improved atomic force microscope cantilever performance by ion beam modification," *Review of Scientific Instruments*, vol. 72, no. 10, pp. 3880–3883, 2001.

[30] A. M. Moulin, S. J. O'Shea, and M. E. Welland, "Microcantilever-based biosensors," *Ultramicroscopy*, vol. 82, no. 1-4, pp. 23–31, 2000.

[31] A.-R. Khaled, K. Vafai, M. Yang, X. Zhang, and C. Ozkan, "Analysis, control and augmentation of microcantilever deflections in bio-sensing systems," *Sensors and Actuators, B: Chemical*, vol. 94, no. 1, pp. 103–115, 2003.

[32] C. Savran, A. Sparks, J. Sihler, J. Li, W.-C. Wu, D. Berlin, T. Burg, J. Fritz, M. Schmidt, and S. Manalis, "Fabrication and characterization of a micromechanical sensor for differential detection of nanoscale motions," *Microelectromechanical Systems, Journal of*, vol. 11, no. 6, pp. 703–708, 2002.

[33] D. Dareing and T. Thundat, "Simulation of adsorption-induced stress of a microcantilever sensor," *Journal of Applied Physics*, vol. 97, no. 4, pp. 043526–1–043526–5, 2005.

[34] S. K. Vashist, "A review of microcantilevers for sensing applications." http://www.azonano.com/Details.asp?ArticleID=1927, November 2007.

[35] M. Alvarez, L. Carrascosa, M. Moreno, A. Calle, A. Zaballos, L. Lechuga, C. Martinez-A, and J. Tamayo, "Nanomechanics of the formation of dna self-assembled monolayers and hybridization on microcantilevers," *Langmuir*, vol. 20, no. 22, pp. 9663–9668, 2004.

[36] K. Silva, —. Phd, RMIT University, 2008.

[37] K. Silva. (private communication), 2008.

[38] M. Palacio, B. Bhushan, N. Ferrell, and D. Hansford, "Nanomechanical characterization of polymer beam structures for biomems applications," *Sensors and Actuators A: Physical*, vol. 135, no. 2, pp. 637–650, 2007.

[39] A. Johansson, M. Calleja, P. Rasmussen, and A. Boisen, "SU-8 cantilever sensor system with integrated readout," *Sensors and Actuators A: Physical Eurosensors XVIII 2004 - The 18th European conference on Solid-State Transducers*, vol. 123-124, pp. 111–115, 2005.

[40] J. Thaysen, A. D. Yalcinkaya, P. Vettiger, and A. Menon, "Polymer-based stress sensor with integrated readout," *Journal of Physics D: Applied Physics*, vol. 35, no. 21, pp. 2698–2703, 2002.

[41] L. Carrascosa, M. Moreno, M. Alvarez, and L. Lechuga, "Nanomechanical biosensors: a new sensing tool," *TrAC Trends in Analytical Chemistry*, vol. 25, no. 3, pp. 196–206, 2006.

[42] M. Calleja, M. Nordstrom, M. Alvarez, J. Tamayo, L. Lechuga, and A. Boisen, "Highly sensitive polymer-based cantilever-sensors for dna detection," *Ultrami-*

croscopy Proceedings of the Sixth International Conference on Scanning Probe Microscopy, Sensors and Nanostructures, vol. 105, no. 1-4, pp. 215–222, 2005.

[43] O. Karhade, S. Chiluveru, and P. Apte, "Novel cantilever for biosensing applications," *Microfluidics, BioMEMS, and Medical Microsystems III; Progress in Biomedical Optics and Imaging - Proceedings of SPIE*, vol. 5718, pp. 48–53, 2005.

[44] O. Karhade, S. Chiluveru, and P. Apte, "Novel cantilever for biosensing applications," in *Advanced Semiconductor Manufacturing, 2004. ASMC '04. IEEE Conference and Workshop*, pp. 409–412, 2004.

[45] N. V. Lavrik, C. A. Tipple, M. J. Sepaniak, and P. G. Datskos, "Enhanced chemi-mechanical transduction at nanostructured interfaces," *Chemical Physics Letters*, vol. 336, no. 5-6, pp. 371–376, 2001.

[46] S. D. Senturia, *Microsystem Design*. Boston ; London: Kluwer Academic, 2001.

[47] D. R. Baselt, B. Fruhberger, E. Klaassen, S. Cemalovic, C. L. Britton, S. V. Patel, T. E. Mlsna, D. McCorkle, and B. Warmack, "Design and performance of a microcantilever-based hydrogen sensor," *Sensors and Actuators B: Chemical*, vol. 88, no. 2, pp. 120–131, 2003.

[48] J. Britton, C.L., R. Warmack, S. Smith, P. Oden, R. Jones, T. Thundat, G. Brown, W. Bryan, J. Depriest, M. Ericson, M. Emery, M. Moore, G. Turner, A. Wintenberg, T. Threatt, Z. Hu, L. Clonts, and J. Rochelle, "Battery-powered, wireless MEMS sensors for high-sensitivity chemical and biological sensing," in *Advanced Research in VLSI, 1999. Proceedings. 20th Anniversary Conference on*, pp. 359–368, 1999.

[49] Y. Ma, A. M. Robinson, R. P. Lawson, K. B. Brown, D. Strembicke, W. Allegretto, and T. Zhou, "Measuring the deflection of CMOS micromachined cantilever devices using a piezoresistive sensor," *Canadian Journal of Electrical and Computer Engineering*, vol. 25, no. 1, pp. 3–7, 2000.

[50] K. Domanski, D. Tomaszewski, P. Grabiec, Z. Gnindowski, A. Kudla, R. Beck, A. Jakubowski, T. Gotszalk, and I. Rangelow, "Silicon piezoresistive cantilever beam with porous silicon element," *Proceedings of the Eleventh International Workshop on the Physics of Semiconductor Devices (SPIE Vol.4746)*, pp. 523–526 Volume 1, 2002.

[51] K. W. Wee, G. Y. Kang, J. Park, J. Y. Kang, D. S. Yoon, J. H. Park, and T. S. Kim, "Novel electrical detection of label-free disease marker proteins using piezoresistive self-sensing micro-cantilevers," *Biosensors and Bioelectronics Selected Papers from the Eighth World Congress on Biosensors, Part II*, vol. 20, no. 10, pp. 1932–1938, 2005.

[52] X. Y. Ye, Z. Y. Zhou, Y. Yang, J. H. Zhang, and J. Yao, "Determination of the mechanical properties of microstructures," *Sensors and Actuators A: Physical*, vol. 54, no. 1-3, pp. 750–754, 1996.

[53] T. Miyatani and M. Fujihira, "Calibration of surface stress measurements with atomic force microscopy," *Journal of Applied Physics*, vol. 81, no. 11, pp. 7099–7115, 1997.

[54] S. Firebaugh, H. Charles Jr., R. Edwards, A. Keeney, and S. Wilderson, "Optical deflection measurement for characterization of microelectromechanical systems (MEMS)," *IEEE Transactions on Instrumentation and Measurement*, vol. 53, no. 4, pp. 1047–1051, 2004.

[55] D. Rugar, H. Mamin, R. Erlandsson, J. Stern, and B. Terris, "Force microscope using a fiber-optic displacement sensor," *Review of Scientific Instruments*, vol. 59, no. 11, pp. 2337–2340, 1988.

[56] N. Kato, I. Suzuki, H. Kikuta, and K. Iwata, "Force-balancing microforce sensor with an optical-fiber interferometer," *Review of Scientific Instruments*, vol. 68, no. 6, pp. 2475–2478, 1997.

[57] D. Rugar, H. J. Mamin, and P. Guethner, "Improved fiber-optic interferometer for atomic force microscopy," *Applied Physics Letters*, vol. 55, no. 25, pp. 2588–2590, 1989.

[58] S. Manalis, S. Minne, A. Atalar, and C. Quate, "Interdigital cantilevers for atomic force microscopy," *Applied Physics Letters*, vol. 69, no. 25, pp. 3944–3946, 1996.

[59] M. Varma, D. Nolte, H. Inerowicz, and F. Regnier, "Spinning-disk self-referencing interferometry of antigen-antibody recognition," *Optics Letters*, vol. 29, no. 9, pp. 950–952, 2004.

[60] G. Yaralioglu, A. Atalar, S. Manalis, and C. Quate, "Analysis and design of an interdigital cantilever as a displacement sensor," *Journal of Applied Physics*, vol. 83, no. 12, pp. 7405–7415, 1998.

[61] T. Sulchek, R. Hsieh, S. Minne, C. Quate, and S. Manalis, "Interdigital cantilever as a biological sensor," *Proceedings of the 2001 1st IEEE Conference on Nanotechnology. IEEE-NANO 2001 (Cat. No.01EX516)*, pp. 562–566, 2001.

[62] T. D. Rowsell, "Remote measurement of small displacements using a cd pickup head," *Medical Engineering and Physics*, vol. 17, no. 6, pp. 459–461, 1995.

[63] J.-H. Zhang and L. Cai, "An auto-focusing measurement system with the piezoelectric translator," in *Robotics and Automation, 1997. Proceedings., 1997 IEEE International Conference on*, vol. 4, pp. 2801–2806 vol.4, 1997.

[64] N. Scuor, P. Gallina, O. Sbaizero, H. V. Panchawagh, and R. L. Mahajan, "Dynamic characterization of mems cantilevers in liquid environment using a low-cost optical system," *Measurement Science and Technology*, vol. 17, no. 1, pp. 173–180, 2006.

[65] R. Barathur, J. Bookout, S. Sreevatsan, J. Gordon, M. Werner, G. Thor, and M. Worthington, "New disc-based technologies for diagnostic and research applications," *Psychiatric Genetics*, vol. 12, no. 4, pp. 193–206, 2002.

[66] M. Varma, H. Inerowicz, F. Regnier, and D. Nolte, "High-speed label-free detection by spinning-disk micro-interferometry," *Biosensors and Bioelectronics*, vol. 19, no. 11, pp. 1371–1376, 2004.

[67] M. Varma, D. Nolte, H. Inerowicz, and F. Regnier, "High-speed label-free multianalyte detection through microinterferometry," *Proceedings of the SPIE - The International Society for Optical Engineering*, vol. 4966, pp. 58–64, 2003.

[68] M. Zhao, D. Nolte, W. Cho, F. Regnier, M. Varma, G. Lawrence, and J. Pasqua, "High-speed interferometric detection of label-free immunoassays on the biological compact disc," *Clinical Chemistry*, vol. 52, no. 11, pp. 2135–2140, 2006.

Chapter 3

Modelling of Non-Prismatic Microcantilevers

3.1 Introduction

The need to be able to selectively modify the deflection of a microcantilever while maintaining noise immunity was mentioned in the Introduction of this thesis. The Literature Review highlighted that noise immunity was directly related to the resonant frequency of microcantilevers. It was also noted that all of these conditions cannot be met simultaneously by simply changing the dimensions of the cantilever.

In the first part of this Chapter, this problem is investigated in detail to understand the cause of the inverse relationship between the deflection and the resonant frequency of cantilever beams. A new metric is proposed to compare the utility value of microcantilevers. From these investigations, a principle is derived by which the deflection and the resonant frequency of a cantilever can be enhanced simultaneously by making structural modifications to the cantilevers. A qualitative proof of the principle is presented.

To analyse and optimise the dynamics of these non-prismatic microcantilevers (ie. those not having a constant cross section throughout their length) for sensor ele-

ments, the actual deflection and resonant frequency needs to be quantified. Analytical expressions to describe the deflection and resonant frequency of prismatic microcantilevers are well known. Methods to determine the deflection of non-prismatic beams due to loading are well established [1]. However, these methods consider loading by forces and moments, and not surface stresses as is the case with MEMS sensors of interest. Analytical modelling of the deflection of microcantilevers due to surface stress has been addressed in the literature [2], but has been limited to uniform or prismatic beams.

Vibrations and resonance of non-prismatic beams have been studied for a long time in structural engineering [3, 4]. General analytical methods are available [5] that can be used to compute the resonant frequency of non-prismatic beams. The resonant frequencies of cantilevers with exponentially varying widths were reported in [6]. In [7], the resonant frequencies of step-cantilevers was determined. However, these methods require the solution of a set of complicated equations. Thus, simple analytical models to describe the dynamics of non-prismatic microcantilevers are not available in the literature.

Therefore, in the second part of this Chapter, modelling of the dynamics of non-uniform microcantilevers is investigated. Three analytical models are developed for non-prismatic microcantilevers that describe the deflection due to a point load, deflection due to a surface stress and the resonant frequency. Numerical results obtained from these models are then compared with results obtained from finite element method (FEM) simulations using the *ANSYS* ® *Multiphysics* ™ software suite. These results are also used to characterise the variations of cantilever dynamics with structural modifications.

3.2 Deflection and resonant frequency of microcantilevers

The deflection t of a rectangular microcantilever of length L, width b and thickness h having a differential surface stress $\Delta\sigma$ across the top and bottom surfaces is given by the following formula, commonly referred to as Stoney's equation:

$$t = \frac{3(1-\nu)\Delta\sigma L^2}{Eh^2} \tag{3.1}$$

where E is the Young's modulus and ν is the Poisson's ratio of the microcantilever material. The fundamental resonant frequency f_0 of a rectangular cantilever is given by

$$f_0 = \frac{1}{2\pi}\sqrt{\frac{E}{\rho}} \cdot \frac{h}{L^2} \tag{3.2}$$

where ρ is the density of the material.

It can be seen from Equations (3.1) and (3.2) that the beam has to be made longer and thinner to increase deflection, but these cause the resonant frequency to decrease. Thus, although it is desirable to have a microcantilever with a large deflection together with a high resonant frequency, both parameters cannot be increased simultaneously by changing the dimensions of the beam.

It was highlighted in the Literature Review that both the deflection and the resonant frequency of microcantilevers should be maximized when used as sensor elements—a large deflection simplifies measurement and the high resonant frequency makes the beam immune to vibrational noise. Thus the real utility value of a microcantilever is best indicated by the product of the deflection t and the resonant frequency f_0, rather than by either parameter individually. It is easy to show from Equations (3.1) and (3.2) that

$$t \cdot f_0 = \frac{3(1-\nu)\Delta\sigma}{2\pi\sqrt{E\rho}} \cdot \frac{1}{h} \tag{3.3}$$

Thus the only dimension of a cantilever that affects its utility factor $t \cdot f_0$ is its thickness h, and the largest utility factor is achieved by using the thinnest possible beam.

As an example, consider a silicon cantilever which has the following properties:

$$L = 100\ \mu\text{m} \qquad b = 20\ \mu\text{m} \qquad h = 2\ \mu\text{m}$$
$$E = 165\ \text{GPa} \qquad \rho = 2330\ \text{kgm}^{-3} \qquad \nu = 0.22$$

Let the surface stress be $\Delta\sigma = 0.04\ \mu\text{N}/\mu\text{m}$. Then from Equations (3.1), (3.2) and (3.3), the following values are obtained:

$$\text{Deflection :} \quad t = 1.42\ \text{nm}$$
$$\text{Resonant frequency :} \quad f_0 = 267\ \text{kHz}$$
$$t \cdot f_0 \text{ value :} \quad t \cdot f_0 = 380\ \text{nm.kHz}$$

Suppose the thickness of the beam is now reduced to 1 μm. Then the deflection quadruples, resonant frequency halves and the $t \cdot f_0$ value doubles:

$$\text{Deflection :} \quad t = 5.67\ \text{nm}$$
$$\text{Resonant frequency :} \quad f_0 = 134\ \text{kHz}$$
$$t \cdot f_0 \text{ value :} \quad t \cdot f_0 = 760\ \text{nm.kHz}$$

This thinner beam has a larger deflection but a lower resonant frequency compared with the thicker beam considered earlier. Since the thinner beam has a larger $t \cdot f_0$ value, its deflection can be traded-off with resonant frequency by changing the length of the beam. The $t \cdot f_0$ value remains unchanged as it is independent of the length of the beam. If, for example, the length L is reduced to 60 μm, the following characteristics are obtained:

$$\text{Deflection :} \quad t = 2.04\ \text{nm}$$
$$\text{Resonant frequency :} \quad f_0 = 372\ \text{kHz}$$
$$t \cdot f_0 \text{ value :} \quad t \cdot f_0 = 760\ \text{nm kHz}$$

Clearly, this beam has a larger deflection as well as a higher resonant frequency compared with the first beam. This example demonstrates the importance of considering the $t \cdot f_0$ value when comparing microcantilever properties.

The largest $t \cdot f_0$ value is obtained by having the minimum possible thickness h for the beam. The minimum achievable thickness of a cantilever is determined by strength, stability and fabrication considerations. When using a uniform cantilever with the minimum possible thickness, the deflection and resonant frequency values can be traded-off with each other by varying the length. But both parameters cannot be enhanced simultaneously and no deflection–frequency combination can be achieved that exceeds the $t \cdot f_0$ value determined by Equation (3.3).

In the following section, the reasons for this interdependency are investigated, with a view of determining a principle that can be used to increase both the deflection and the resonant frequency simultaneously.

3.2.1 Analysis of cantilever dynamics using the spring constant

The problem can be better understood by using the beam's spring constant. By definition, the spring constant is the force required to achieve a unit displacement. Therefore, to achieve a larger deflection, the spring constant of the beam has to be reduced. In the case of microcantilevers, the normal spring constant k is defined when a point load is applied on the free end of the beam. The deflection t of a cantilever with a point load F applied on its free end is given by

$$t = \frac{FL^3}{3EI} \tag{3.4}$$

where L is the length of the beam, E is the Young's modulus and I is the moment of area. It follows from the definition that the spring constant k of the beam is

$$k = \frac{3EI}{L^3} \tag{3.5}$$

For a cantilever having a rectangular cross-section, the moment of area I is given by the standard equation

$$I = \frac{1}{12}bh^3 \tag{3.6}$$

where b is the width and h is the thickness of the beam. Substituting Equation (3.6) in (3.5) gives

$$k = \frac{Ebh^3}{4L^3} \tag{3.7}$$

It can be seen from Equation (3.7) that when either the length L is increased or the thickness h is decreased, the spring constant decreases, and hence the deflection increases, as discussed earlier.

The expression for the resonant frequency of the beam given by Equation (3.2) can be rearranged using Equation (3.7) as

$$f_0 = \frac{1}{\pi}\sqrt{\frac{k}{m}} \tag{3.8}$$

where m is the mass of the beam given by $m = Lbh\rho$. If the length of the beam is increased to achieve a larger deflection, the mass of the beam increases and the spring constant decreases, so the resonant frequency decreases. On the other hand if the thickness of the beam is decreased, the mass decreases proportionately while the spring constant decreases in proportion to h^3 as seen from Equation (3.7). Since the reduction of the spring constant is greater than the reduction in mass, the resonant frequency decreases according to Equation (3.8). This shows why the resonant frequency decreases when the deflection is increased by changing the dimensions of the beam.

Now if both the deflection and the resonant frequency are to be increased simultaneously, the spring constant should be reduced in a manner that reduces the mass by a greater factor. Alternatively, the mass of the cantilever has to be reduced in a manner that reduces the spring constant by a smaller factor. This principle can be used to obtain cantilevers that have larger deflections and higher resonant frequencies compared with uniform cantilevers.

It is more intuitive to alter the mass of a cantilever than to alter its spring constant, so the principle of reducing the mass by a larger factor than the spring constant is followed from this point onwards. The mass of the beam can be reduced by removing material from the cantilever. If this can be done in a manner that reduces the spring constant by a smaller factor, both the deflection and the resonant frequency can be enhanced simultaneously.

It is well known that the free end of a beam contributes little towards its deflection. Suppose a small groove is etched at the free end of the beam to create a step cantilever, as shown in Figure 3.1. Then the mass of the cantilever will be reduced. However, the deflection will remain almost unchanged and hence the spring constant will remain unchanged. As a result, the resonant frequency and hence the $t \cdot f_0$ value of this modified beam will be greater than the original uniform beam.

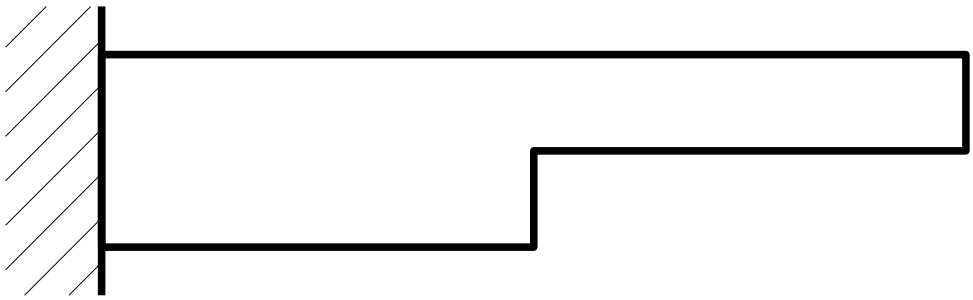

Figure 3.1: A Step Cantilever made by etching a groove at the free end.

The above analysis proposes a mechanism by which the deflection and the resonant frequency can be enhanced simultaneously. It should be noted that the resonant frequency given by Equation (3.8) is valid only for uniform, rectangular beams. While the basic equations presented above are adequate to analyse the dynamics of non-uniform cantilevers qualitatively, they cannot be used for quantitative analyses. Thus, these standard equations cannot be used to estimate the improvement of the $t \cdot f_0$ value nor to determine the optimal form of the groove. In the following sections, new analytical models are developed to quantify the deflection and resonant frequency of cantilevers with grooves.

3.3 Model of a perforated microcantilever

In this analysis, a rectangular, prismatic cantilever is considered. The cantilever is of length L, width b and thickness h. For generality, structural modifications are introduced into the microcantilever in the form of perforations. To keep the analysis simple, the perforations are assumed to be cuboidal. All perforations are assumed to be geometrically identical and their length, width and depth are parametrically defined by ηL, βb and γh respectively. The separation between perforations is denoted by λL and the distance to the first perforation from the fixed end is αL. Figure 3.2 shows a sketch of a beam with a line of such perforations.

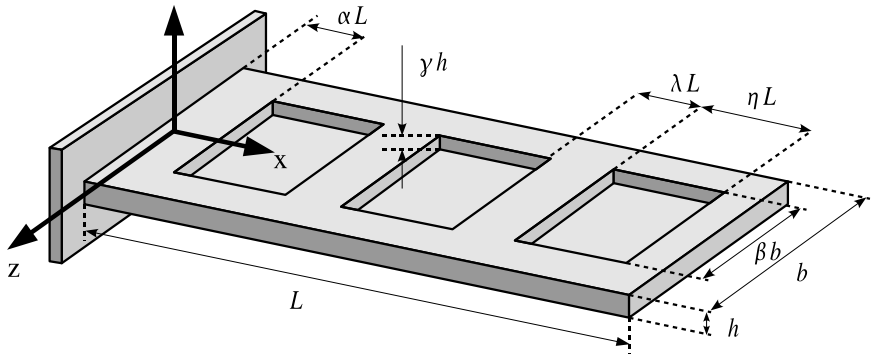

Figure 3.2: Model of a perforated microcantilever.

3.4 Analytical models for cantilever deflection

3.4.1 Moment–Area method

The moment–area method is a semi-graphical approach that can be used to calculate the deflection of cantilever beams [1, 8, 9]. This method is particularly useful when the beam is non-prismatic and is used here to develop analytical models for the deflection of perforated cantilevers.

When loads are applied to cantilevers, internal shear forces and bending-moments develop in the beam. These forces and moments, in general, vary from point to point

along the axis of the cantilever. A moment diagram is a plot of the bending-moment M along the length of the cantilever. An example is shown in Figure 3.3(b).

An M/EI curve (Figure 3.3(c)) is obtained by dividing the internal moment M at every point along the cantilever length by the flexural rigidity EI at that point. E is the Young's modulus of the material and I is the moment of area of the cross-section at that point, and is computed about the neutral axis of that cross-section.

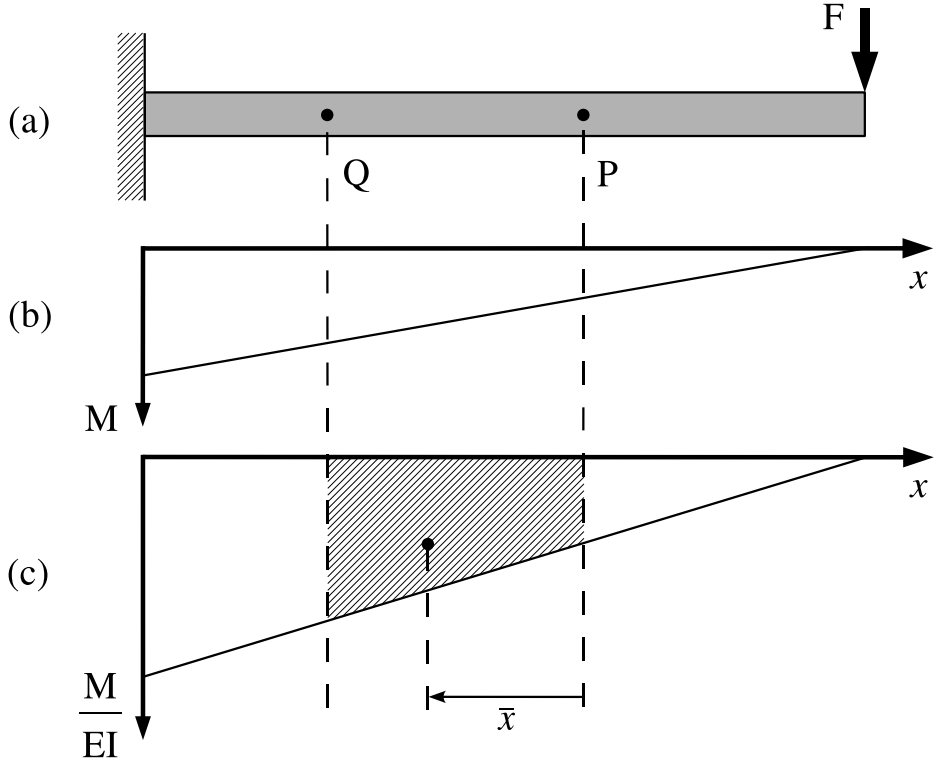

Figure 3.3: (a) A cantilever with a point load at the free end, (b) the bending-moment diagram and (c) the resulting M/EI diagram.

The deflection t of a point P on the microcantilever with respect to a point Q is given by [1, 8, 9]:

$$t_{P/Q} = \overline{x} \int_{P}^{Q} \frac{M}{EI}\, \mathrm{d}x \tag{3.9}$$

The area under the M/EI diagram between points P and Q (the shaded area in

Figure 3.3(c)) represents the integral. $\overline{x}$ is the distance from point P to the centroid of the area under the M/EI diagram between P and Q.

When point P is at the free end and point Q is at the fixed end, Equation (3.9) gives the tip deflection of the microcantilever. Then, $\overline{x}$ is the distance from the free end to the centroid of the M/EI diagram and the integral represents the entire area under the M/EI diagram. This technique is used as the basis to formulate analytical models for the deflection of perforated microcantilevers.

3.4.2 Deflection under a point load

Consider a perforated microcantilever with a point load F acting on its free end. An analytical solution for the deflection t_{pl} of this beam can be obtained using the moment–area method, as detailed in section A.2.2 of Appendix A. When the cantilever has only a single perforation, the following expression is obtained:

$$t_{\mathrm{pl}} = \frac{FL^3}{3EI}\left[1 + 3\eta\left(\frac{1-\chi}{\chi}\right)\left\{(1-\alpha)^2 + \eta\left(\frac{1}{3}\eta + \alpha - 1\right)\right\}\right] \tag{3.10}$$

where χ is given by

$$\chi = \frac{1 - 4\beta\gamma + 6\beta\gamma^2 - 4\beta\gamma^3 + \beta^2\gamma^4}{1 - \beta\gamma} \tag{3.11}$$

When at least one dimension of the perforation (ie, β, γ or η) of Equation (3.10) is made equal to zero, the standard equation for the deflection of a uniform beam under a point load $t_{\mathrm{pl,u}} = FL^3/3EI$ is obtained. Therefore, the deflection of a perforated microcantilever with an end load can be expressed as follows:

$$t_{\mathrm{pl}} = \psi_{\mathrm{pl}} \cdot t_{\mathrm{pl,u}} \tag{3.12a}$$

where,

$$\psi_{\mathrm{pl}} = 1 + 3\eta\left(\frac{1-\chi}{\chi}\right)\left\{(1-\alpha)^2 + \eta\left(\frac{1}{3}\eta + \alpha - 1\right)\right\} \tag{3.12b}$$

and

$$\chi = \frac{1 - 4\beta\gamma + 6\beta\gamma^2 - 4\beta\gamma^3 + \beta^2\gamma^4}{1 - \beta\gamma} \tag{3.12c}$$

In these equations, ψ_{pl} represents the increase in deflection of a perforated microcantilever compared to a prismatic beam having the same dimensions.

3.4.3 Model for deflection with surface stress

When a microcantilever is used as the sensing element in a biological or chemical MEMS device, one face of the beam is functionalised to interact with the analyte. This interaction results in a surface stress developing on that face. The resulting differential surface stress across the functionalised and non-functionalised faces causes the beam to deflect.

A study of modelling surface stresses was reported in [2]. The surface stress σ is a force per unit length, with units Nm^{-1}. Suppose a uniform surface stress σ acts on one face of a microcantilever. Then the resultant tangential force in the axial direction due to the surface stress is $\sigma \cdot b$, where b is the width of the cantilever. Refer Figure 3.4. Since the neutral axis of a rectangular cantilever is at a depth $h/2$, this tangential force can be translated into an equivalent concentrated axial force σb acting along the neutral axis of the beam, and a moment $M = \sigma bh/2$ [2]. This same result is also obtained in [10, 11]. This equivalent bending-moment can be used in the moment–area method to derive an expression for the deflection of perforated microcantilevers.

To keep the surface stress acting on a uniform surface, perforations are introduced on the non-functionalised surface of the beams. Then, it can be shown (section A.2.3, Appendix A) that the deflection is given by

$$t_{\text{ss}} = \frac{3(1-\nu)\Delta\sigma L^2}{Eh^2}\left[1 + \eta\beta\gamma\Big(2(1-\alpha) - \eta\Big)\left(\frac{2 - 5\gamma + 4\gamma^2 - \beta\gamma^3}{1 - 4\beta\gamma + 6\beta\gamma^2 - 4\beta\gamma^3 + \beta^2\gamma^4}\right)\right] \tag{3.13}$$

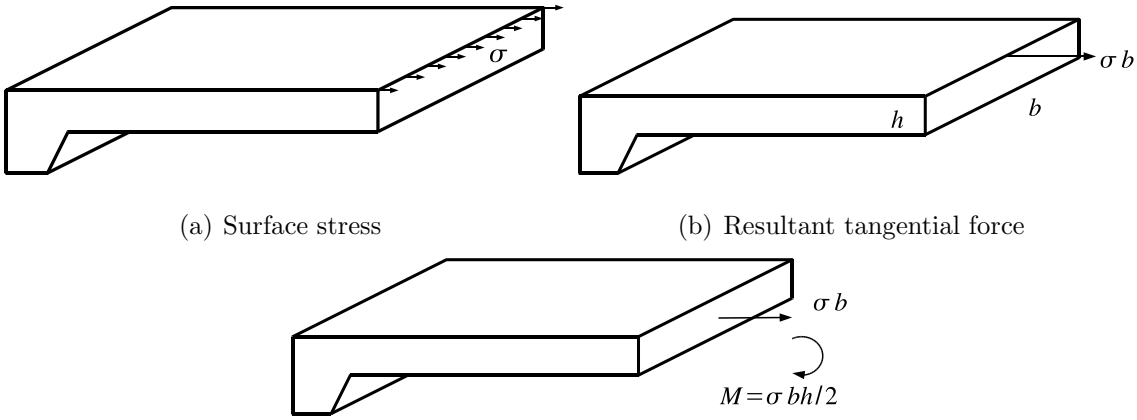

(a) Surface stress

(b) Resultant tangential force

(c) Equivalent axial force and moment

Figure 3.4: Modelling surface stress. (a) The surface stress σ is a force per unit length. (b) The resultant tangential force, that can be translated into (c) an equivalent axial force and a moment.

By making at least one dimension of the perforation (ie, β, γ or η) zero in Equation (3.13), the deflection of a uniform beam due to a differential surface stress $t_{\mathrm{ss,u}}$ is obtained:

$$t_{\mathrm{ss,u}} = \frac{3(1-\nu)\Delta\sigma L^2}{Eh^2}$$

This is the equation commonly known as Stoney's equation. Therefore, the deflection of a perforated microcantilever due to a surface stress can be expressed as follows:

$$t_{\mathrm{ss}} = \psi_{\mathrm{ss}} \cdot t_{\mathrm{ss,u}} \tag{3.14a}$$

where,

$$\psi_{\mathrm{ss}} = \left[1 + \eta\beta\gamma\Big(2(1-\alpha) - \eta\Big)\left(\frac{2 - 5\gamma + 4\gamma^2 - \beta\gamma^3}{1 - 4\beta\gamma + 6\beta\gamma^2 - 4\beta\gamma^3 + \beta^2\gamma^4}\right)\right] \tag{3.14b}$$

Here, ψ_{ss} represents the improvement in deflection of a perforated microcantilever compared to a prismatic beam having the same dimensions.

3.5 Analytical model for resonant frequency

3.5.1 Rayleigh–Ritz method

The Rayleigh–Ritz method [5, 12, 13] can be used to obtain an approximate solution for the resonant frequency of structures with complex geometries. This method is based upon the principle of conservation of energy, and is an extension of Rayleigh's method.

Suppose the deflection curve of a cantilever is given by $Y(x)$. The resonant frequency of the beam is then given by [12]

$$f_0 = \frac{1}{2\pi}\sqrt{\frac{\displaystyle\int_0^L EI\left(\frac{\mathrm{d}^2Y}{\mathrm{d}x^2}\right)^2 \mathrm{d}x}{\displaystyle\int_0^L A\rho Y^2 \,\mathrm{d}x}} \tag{3.15}$$

where A is the cross-sectional area of the cantilever and ρ is the density of the material. As before, E is the Young's modulus, I is the moment of area, and L is the length of the cantilever.

The deflection curve should meet all the boundary conditions of the cantilever. These conditions are that the deflection at the fixed end, the deflection gradient of the fixed end, the bending-moment at the free end and the shear force at the free end are all equal to zero. If x is measured from the fixed end, these boundary conditions can be expressed as [12]:

$$\begin{aligned} (Y)_{x=0} &= 0 & \left(\frac{\mathrm{d}Y}{\mathrm{d}x}\right)_{x=0} &= 0 \\ \left(EI\,\frac{\mathrm{d}^2Y}{\mathrm{d}x^2}\right)_{x=L} &= 0 & \frac{\mathrm{d}}{\mathrm{d}x}\left(EI\,\frac{\mathrm{d}^2Y}{\mathrm{d}x^2}\right)_{x=L} &= 0 \end{aligned} \tag{3.16}$$

The simplest expression for Y that satisfies all of these conditions was found to be

$$Y = \frac{x^4}{L^4} - \frac{4x^3}{L^3} + \frac{6x^2}{L^2} \tag{3.17}$$

Then, the following expression is obtained from the Rayleigh–Ritz method for the resonant frequency of perforated microcantilevers:

$$f_0 = \frac{1}{2\pi}\sqrt{\frac{27E}{26\rho}} \cdot \frac{h}{L^2} \left[\frac{1-(1-\chi)\left[\{(\alpha+\eta)^5-\alpha^5\}-5\{(\alpha+\eta)^4-\alpha^4\}\right.}{1-\frac{45\beta\gamma}{104}\left[\frac{1}{9}\{(\alpha+\eta)^9-\alpha^9\}-\{(\alpha+\eta)^8-\alpha^8\}\right.} \right.$$
$$\left. \left. \frac{+10\{(\alpha+\eta)^3-\alpha^3\}-10\{(\alpha+\eta)^2-\alpha^2\}+5\eta\right]}{+4\{(\alpha+\eta)^7-\alpha^7\}-8\{(\alpha+\eta)^6-\alpha^6\}+\frac{36}{5}\{(\alpha+\eta)^5-\alpha^5\}\left.\right]} \right]^{1/2} \tag{3.18}$$

where χ is given by Equation (3.12c). By making either β, γ or η equal to zero, the cantilever is reduced to a uniform beam. By applying this condition to Equation (3.18), the expression for the resonant frequency of a uniform microcantilever is obtained

$$f_{\mathrm{u}} = \frac{1}{2\pi}\sqrt{\frac{27E}{26\rho}} \cdot \frac{h}{L^2} \tag{3.19}$$

which agrees with the standard equation for the resonant frequency of rectangular cantilevers [5, 12, 13]. Then, the resonant frequency of a perforated microcantilever can be expressed as

$$f_0 = f_{\mathrm{u}} \cdot \sqrt{\psi_{\mathrm{f}}} \tag{3.20a}$$

where ψ_{f} is given by

$$\psi_{\mathrm{f}} = \left[\frac{1-(1-\chi)\left[\{(\alpha+\eta)^5-\alpha^5\}-5\{(\alpha+\eta)^4-\alpha^4\}\right.}{1-\frac{45\beta\gamma}{104}\left[\frac{1}{9}\{(\alpha+\eta)^9-\alpha^9\}-\{(\alpha+\eta)^8-\alpha^8\}\right.} \right.$$
$$\left. \left. \frac{+10\{(\alpha+\eta)^3-\alpha^3\}-10\{(\alpha+\eta)^2-\alpha^2\}+5\eta\right]}{+4\{(\alpha+\eta)^7-\alpha^7\}-8\{(\alpha+\eta)^6-\alpha^6\}+\frac{36}{5}\{(\alpha+\eta)^5-\alpha^5\}\left.\right]} \right] \tag{3.20b}$$

with

$$\chi = \frac{1-4\beta\gamma+6\beta\gamma^2-4\beta\gamma^3+\beta^2\gamma^4}{1-\beta\gamma} \tag{3.20c}$$

The complete derivation of this model is given in section A.3 of Appendix A.

3.6 Validation and characterisation

The analytical models developed above were validated by comparing numerical values obtained using these models with simulated values obtained using Finite Element Method (FEM) software. Using the results of both techniques, variations of microcantilever deflection and resonant frequency with perforation parameters have been characterised.

A nominal cantilever was selected for this analysis, and it was assumed to be made of silicon. The dimensions and material properties of the selected cantilever are presented in Table 3.1.

Table 3.1: Specifications of the cantilever used in the analysis.

Property	Value
Cantilever length, L	100 μm
Cantilever width, b	20 μm
Cantilever thickness, h	2 μm
Young's modulus, E	165 GPa
Density, ρ	2330 kgm^{-3}
Poisson's Ratio, ν	0.22

A nominal perforation having the following parameters was selected for this investigation:

- Perforation location, $\alpha = 0.8$
- Perforation width, $\beta = 0.8$
- Perforation depth, $\gamma = 0.2$

- Perforation length, $\eta = 0.2$

This nominal perforation constitutes $0.8 \times 0.2 \times 0.2 = 0.032 = 3.2\%$ of the volume of the cantilever.

To characterize the effect of perforation parameters on cantilever response, each parameter was varied across its entire range keeping all other parameters at the nominal values listed above. Numerical values for the deflection and resonant frequency of each of these perforated microcantilevers were calculated using the analytical models. These microcantilevers were then simulated using the FEM software package *ANSYS* ® *Multiphysics* ™. Results obtained from these two methods were compared to validate the analytical models.

3.6.1 Range of parameter values

The perforation parameters were defined as fractions of cantilever dimensions in Section 3.3. The maximum width a perforation can take is the width of the cantilever. Thus, the range for the perforation width factor β is $0 \leq \beta \leq 1$. Similarly, the range of the perforation length factor η is $0 \leq \eta \leq 1$. When the perforation depth factor $\gamma = 1$, the perforation becomes a through hole. However, since perforations are made at the free end, this results in the creation of two fingers at the free end. To avoid this condition, the range of perforation depths was taken as $0 \leq \gamma \leq 0.95$.

3.6.2 Modelling in ANSYS

ANSYS Multiphysics is a widely used Finite Element Method (FEM) software suit. It has the capability to model and simulate components as well as entire systems, take different kinds of loads and predict the physical response of those devices. *ANSYS* (Release 11) was used to simulate the dynamics of perforated microcantilevers.

The cantilevers were modelled in three dimensions in *ANSYS*, and the material properties were specified. The fixed end of the cantilever was defined by specifying

all degrees of freedom of the vertical wall on the left edge to be zero. The perforations were created by removing sections from the base cantilever geometry.

Element type *SOLID-98* was used to mesh the model. This is a tetrahedral element with 10 nodes that can be used to mesh complex 3-dimensional shapes. It supports loads at each of the 10 nodes, and has displacement degrees of freedom in all 3 dimensions. A meshed, perforated cantilever is shown in Figure 3.5.

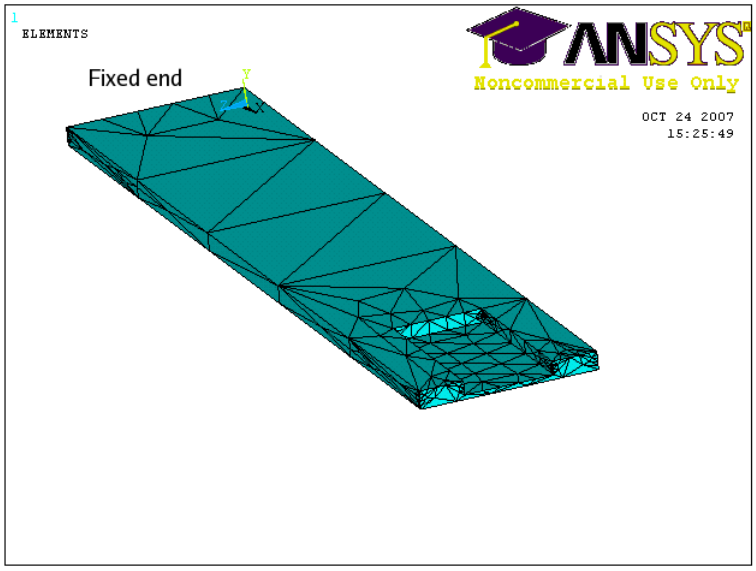

Figure 3.5: A meshed model of a perforated cantilever. A coarse mesh is shown for clarity.

ANSYS does not have the capability to directly model surface stresses. Therefore, the effect of surface stresses was modelled by applying point forces, tangential to the top surface, on the nodes along the top edges of the cantilever [14]. The surface stress was assumed to be 0.04 μN/μm. The force to be applied at each node was determined by multiplying the surface stress by the length of the edge and dividing by the number of nodes along that edge. As an example, the free edge of the cantilever shown in Figure 3.5 is 20 μm in length and has 11 nodes. Therefore, the force on each node is $0.04 \times 20/11 = 0.072\ 727$ μN. The surface stress has to be applied on a uniform surface. Therefore, the surface stress was applied on the

bottom surface. A cantilever with a simulated surface stress acting on its bottom face is shown in Figure 3.6.

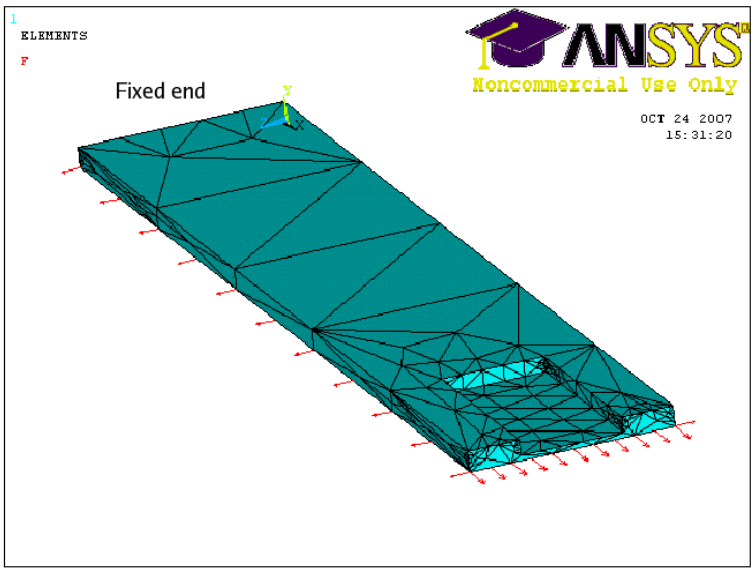

Figure 3.6: A cantilever with a simulated surface stress acting on its bottom surface.

3.7 Validating model for deflection with point load

To validate the analytical model for deflection under a point load, a nominal force of 10 nN was applied at the free end of the cantilever. Figures 3.7–3.9 plot the variations of the calculated cantilever deflections with perforation width, depth and length respectively.

It can be seen from Figures 3.7 and 3.8 that the deflection increases as the perforation width (β) or perforation length (η) is increased. Figure 3.9 shows that the deflection initially increases as the depth of the perforation is increased. However, in the region $0.5 < \gamma < 0.75$, the analytical model predicts a slight decrease in deflection with γ while the FEM results predict a decrease in the rate of increase of deflection.

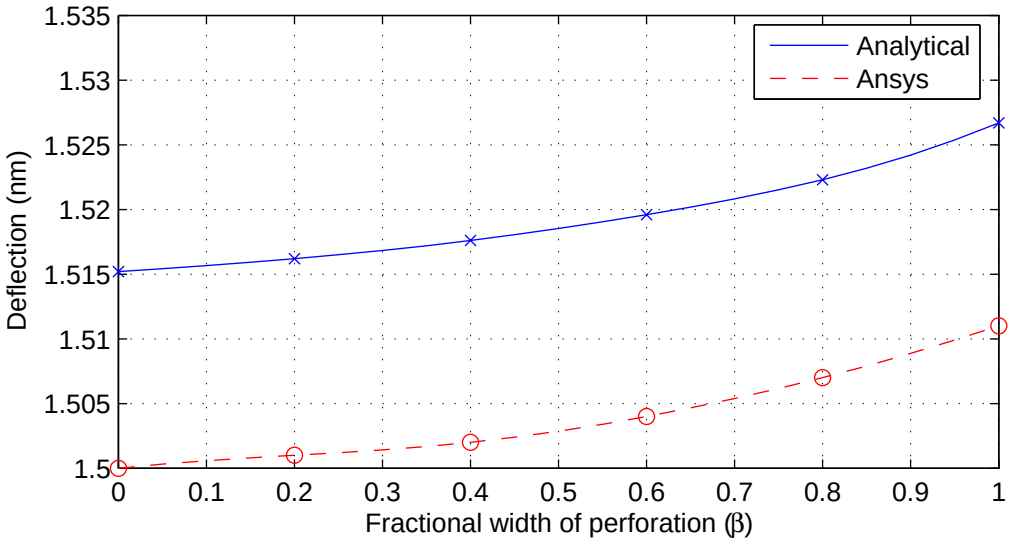

Figure 3.7: Variation of deflection with perforation width (β) for a point loaded beam. [$\alpha = 0.8,\ \gamma = 0.2,\ \eta = 0.2$]

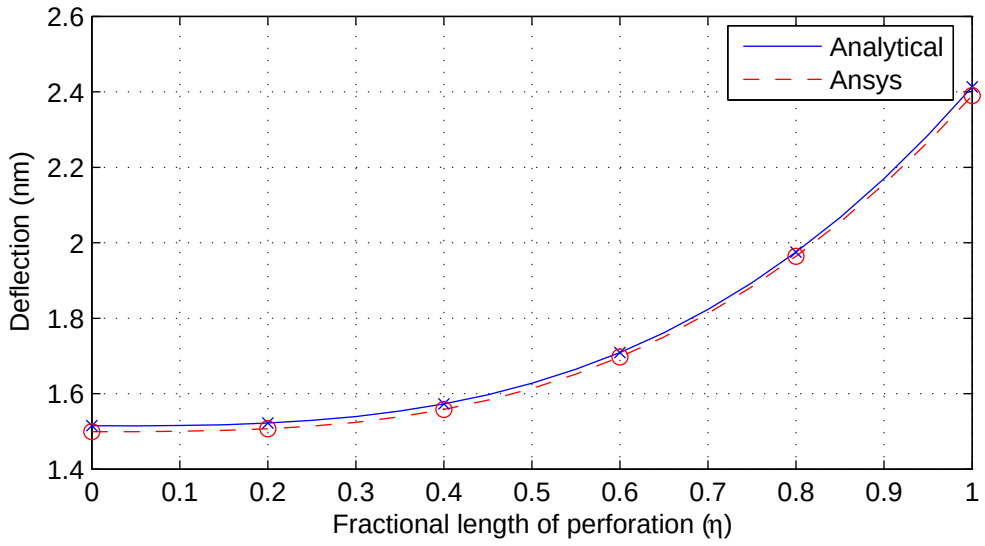

Figure 3.8: Variation of deflection with perforation length (η) for a point loaded beam. [$\alpha = 0.8,\ \beta = 0.8,\ \gamma = 0.2$]

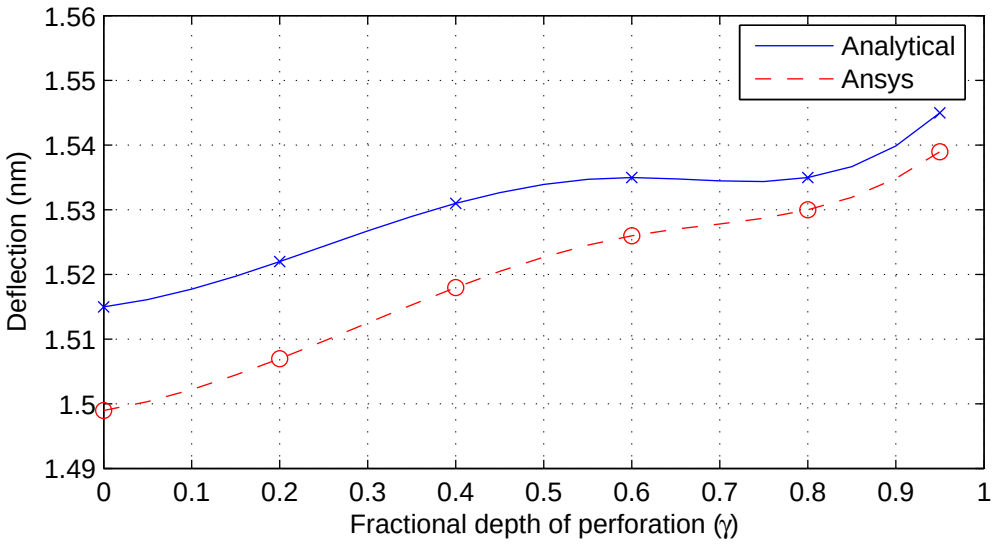

Figure 3.9: Variation of deflection with perforation depth (γ) for a point loaded beam. [$\alpha = 0.8,\ \beta = 0.8,\ \eta = 0.2$]

In each case, the analytical method shows larger deflections than the FEM simulated results. The results obtained from the analytical model were within 1% of the results obtained using *ANSYS*. These results show that the analytical model is in good agreement with the simulations.

The spring constant of a cantilever is inversely proportional to the deflection under a point load. Thus, this analytical model can also be used to obtain accurate estimates of the spring constant of perforated beams.

3.8 Validating model for deflection with surface stress

Variations of deflection with perforation parameters for cantilevers under a surface stress are presented in Figures 3.10–3.12. Figures 3.10 and 3.11 show that the deflection monotonically increases as the perforations are made wider or longer, respectively. As the perforation is made deeper, the deflection initially increases, as

seen from Figure 3.12. In the approximate region $0.55 < \gamma < 0.75$, the deflection slightly decreases as the perforation is made deeper. When the perforation is made deeper than $\gamma \approx 0.75$, the deflection increases sharply.

This observation can be explained as follows. The neutral axis of a prismatic beam is at a depth of $h/2$. When a perforation with $\gamma \ll 1$ is introduced, the neutral axis moves slightly downwards. As γ is increased, the neutral axis moves further down. When $\gamma = 0.5$, the neutral axis reaches its lowest position. With further increases in γ, the neutral axis begins to shift upwards again, and when $\gamma = 1$, reaches $h/2$. The moment of area I is computed about the neutral axis. In the vicinity of $\gamma = 0.6$, the M/EI tends to decrease with increasing γ (refer Figure A.8 in Appendix A), which causes the deflection to decrease.

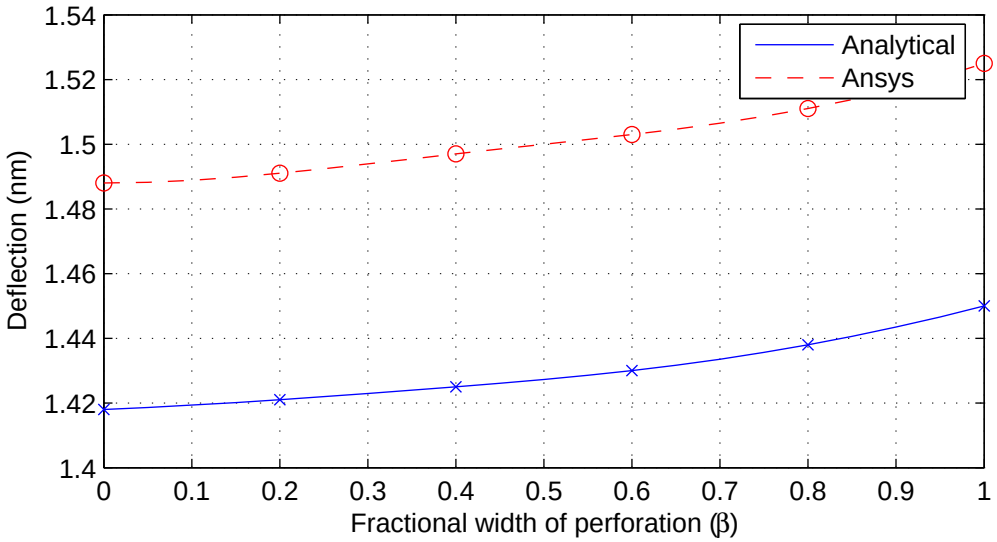

Figure 3.10: Variation of deflection under surface stress with perforation width (β). [$\alpha = 0.8,\ \gamma = 0.2,\ \eta = 0.2$]

In each case, the analytical model predicted a lower deflection than that predicted by the FEM simulation. Both methods produced comparable results, with the maximum difference between the results obtained from the two methods being 6%.

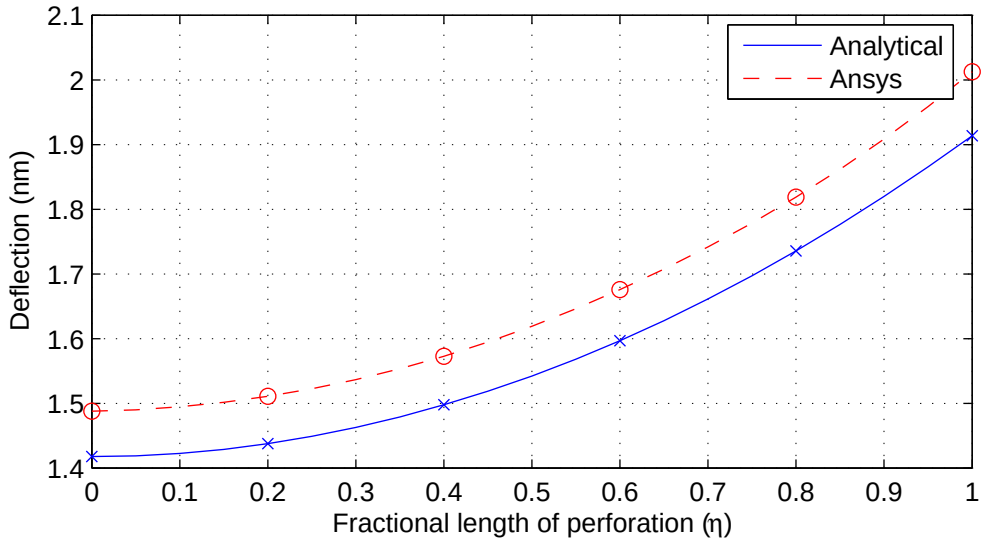

Figure 3.11: Variation of deflection under surface stress with perforation length (η). [$\alpha = 0.8,\ \beta = 0.8,\ \gamma = 0.2$]

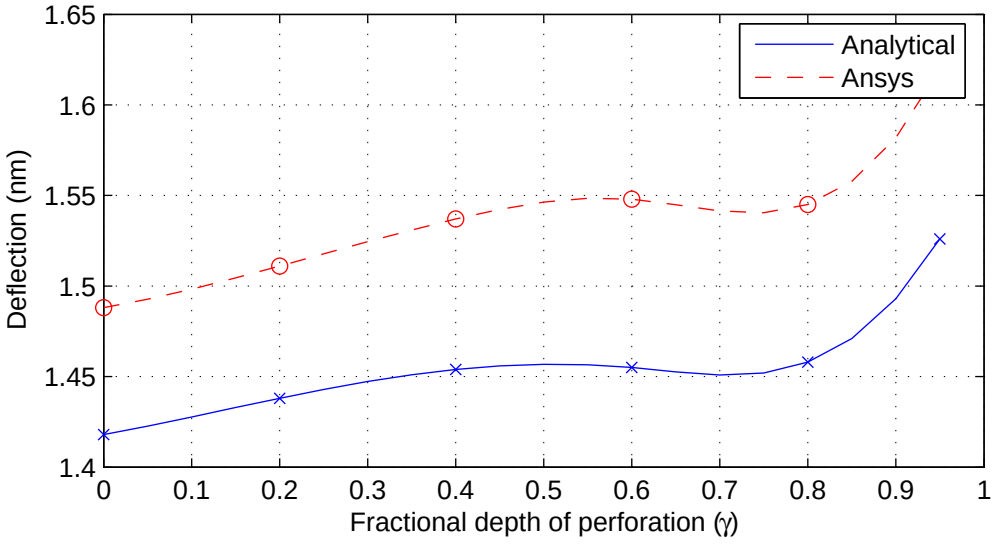

Figure 3.12: Variation of deflection under surface stress with perforation depth (γ). [$\alpha = 0.8,\ \beta = 0.8,\ \eta = 0.2$]

3.9 Validating model for resonant frequency

The variations of resonant frequency with perforation parameters are shown in Figures 3.13–3.15. It can be observed from Figures 3.13 and 3.15 that the resonant frequency increases as the width or depth of a perforation at the free end is increased. Figure 3.14 shows that when a short perforation is made at the free end, the resonant frequency increases. The resonant frequency initially increases with the perforation length and reaches a peak value. A further increase of perforation length causes the resonant frequency to decrease, eventually becoming smaller than the resonant frequency of the original unperforated beam. The analytical model predicts the peak frequency to occur at $\eta \approx 0.5$, while FEM predicts the peak at $\eta \approx 0.4$.

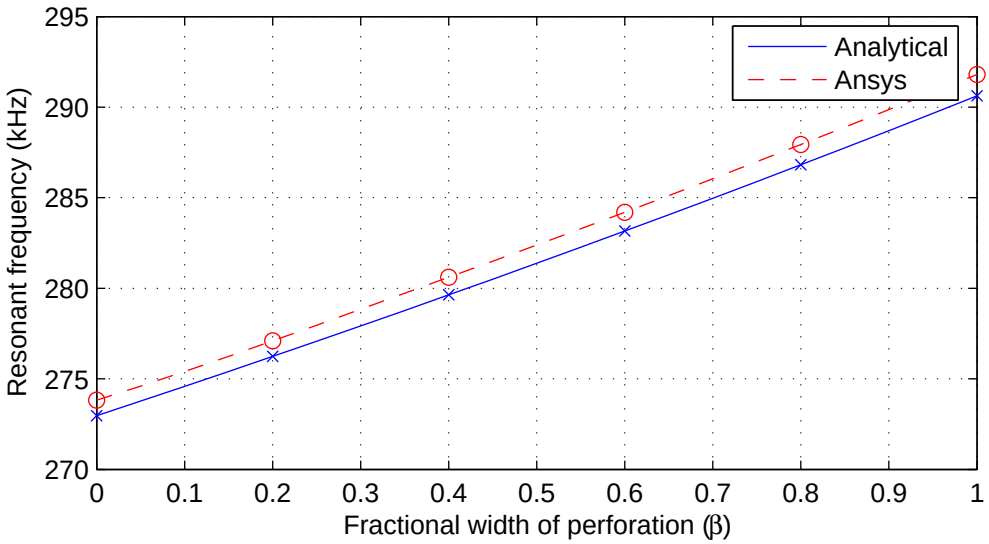

Figure 3.13: Variation of resonant frequency with perforation width (β). [$\alpha = 0.8,\ \gamma = 0.2,\ \eta = 0.2$]

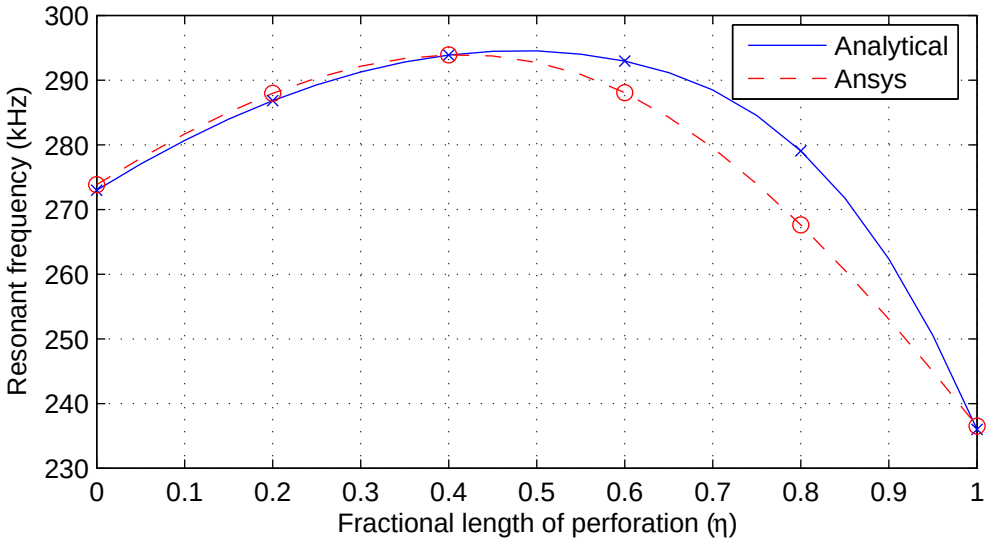

Figure 3.14: Variation of resonant frequency with perforation length (η). [$\alpha = 0.8,\ \beta = 0.8,\ \gamma = 0.2$]

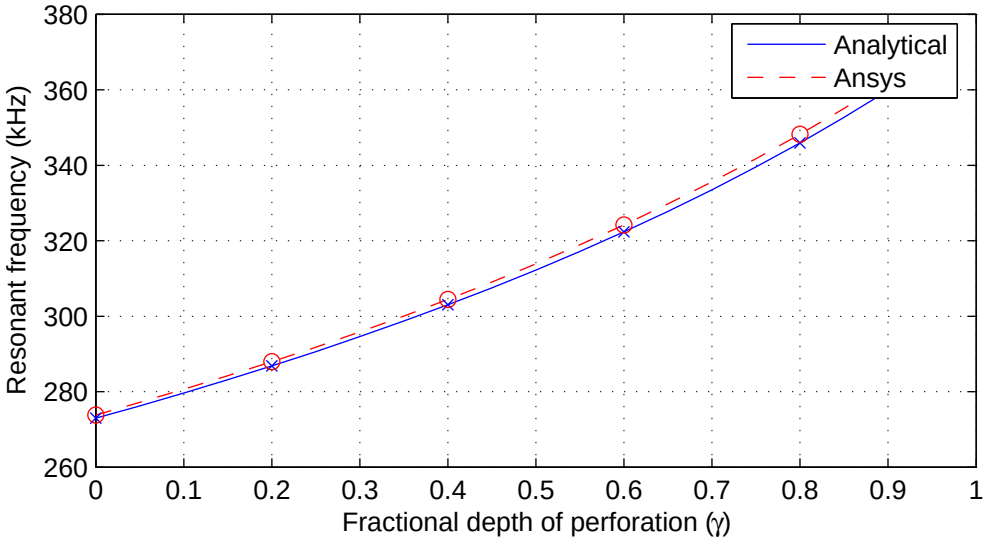

Figure 3.15: Variation of resonant frequency with perforation depth (γ). [$\alpha = 0.8,\ \beta = 0.8,\ \eta = 0.2$]

The differences between the values derived analytically and from the simulations were generally less than 1%, and the FEM simulations predicted higher resonant frequencies than the analytical calculations. The exception was for the variation of the resonant frequency with perforation length η (Figure 3.14), where the maximum difference between the results from the two methods was 4%, and the analytical model predicted a higher resonant frequency for cantilevers with long perforations.

The nominal perforation was 3.2% of the volume of the cantilever, and the largest perforation considered was 16% of the original beam. Results obtained from the analytical models compare well with FEM results for these small perforations. However, if much larger perforations are considered, the microcantilevers will deviate from ideal behaviour which the analytical models assume, and will produce inaccurate results. In general, the techniques used to model microcantilever dynamics, particularly for deflection with surface stress, have been shown to be valid.

3.10 Summary

In this chapter, the dependence of the deflection and the resonant frequency of a microcantilever on its dimensions were investigated. It was shown that the $t \cdot f_0$ value of a cantilever provides a better indication of the beam performance than the deflection or resonant frequency considered individually. It was determined that the the deflection, the resonant frequency and thereby the $t \cdot f_0$ value of a cantilever can be simultaneously increased by reducing the mass of the cantilever in a manner that reduced the spring constant by a smaller factor. Mass can be reduced by creating a perforation on the cantilever.

Three analytical models were developed to describe the deflection due to a point load, the deflection due to a surface stress and the resonant frequency of a perforated microcantilever. Numerical results obtained from these models were then compared with simulated results obtained using the FEM software suite *ANSYS*. It was shown that the analytical models produce results comparable with the simulated results,

which were within 6% of each other.

The analytical models can be used to calculate the spring constant, the deflection and the resonant frequency of perforated microcantilevers. It was also demonstrated that the dynamics of microcantilevers can be accurately modelled using the methods described in this Chapter.

References

[1] R. C. Hibbeler, *Mechanics of Materials*. New York, Toronto: Macmillan College Pub : Maxwell Macmillan International; Maxwell Macmillan Canada, 2nd ed., 1994.

[2] Y. Zhang, Q. Ren, and Y.-P. Zhao, "Modelling analysis of surface stress on a rectangular cantilever beam," *Journal of Physics D: Applied Physics*, vol. 37, no. 15, pp. 2140–2145, 2004.

[3] D. Zhou and Y. K. Cheung, "Vibrations of tapered timoshenko beams in terms of static timoshenko beam functions," *Journal of Applied Mechanics*, vol. 68, no. 4, pp. 596–602, 2001.

[4] R. Jategaonkar and D. S. Chehil, "Natural frequencies of a beam with varying section properties," *Journal of Sound and Vibration*, vol. 133, no. 2, pp. 303–322, 1989.

[5] E. Volterra and E. C. Zachmanoglou, *Dynamics of Vibrations*. Ohio: Charles E Merrill, 1965.

[6] M. C. Ece, M. Aydogdu, and V. Taskin, "Vibration of a variable cross-section beam," *Mechanics Research Communications*, vol. 34, no. 1, pp. 78–84, 2007.

[7] S. K. Jang and C. W. Bert, "Free vibration of stepped beams: Exact and numerical solutions," *Journal of Sound and Vibration*, vol. 130, no. 2, pp. 342–346, 1989.

[8] F. P. Beer, E. R. Johnston, and J. T. DeWolf, *Mechanics of Materials*. New York: McGraw-Hill, 2nd ed., 1992.

[9] J. M. Gere and S. P. Timoshenko, *Mechanics of Materials*. London: Chapman and Hall, 3rd SI ed., 1991.

[10] G. Chen, T. Thundat, E. Wachter, and R. Warmack, "Adsorption-induced surface stress and its effects on resonance frequency of microcantilevers," *Journal of Applied Physics*, vol. 77, no. 8, pp. 3618–3622, 1995.

[11] T. Miyatani and M. Fujihira, "Calibration of surface stress measurements with atomic force microscopy," *Journal of Applied Physics*, vol. 81, no. 11, pp. 7099–7115, 1997.

[12] W. Weaver, S. Timoshenko, and D. H. Young, *Vibration Problems in Engineering*. New York: Wiley, 5th ed., 1990.

[13] W. T. Thomson, M. D. Dahleh, and A. V. Bourmistrova, *Theory of Vibration with Applications*. MIET2124 (Reserve), Upper Saddle River, N.J.: Prentice Hall, 5th ed., 1998.

[14] O. Karhade, S. Chiluveru, and P. Apte, "Novel cantilever for biosensing applications," *Microfluidics, BioMEMS, and Medical Microsystems III; Progress in Biomedical Optics and Imaging - Proceedings of SPIE*, vol. 5718, pp. 48–53, 2005.

Chapter 4

Analysis of Non-Prismatic Cantilevers

4.1 Introduction

In the previous Chapter, it was qualitatively proposed that perforations can be used to simultaneously increase the deflection and resonant frequency of microcantilevers. Analytical models were then derived to quantify the spring constant, deflection and resonant frequency of perforated beams. Results obtained from these models were shown to be in good agreement with results obtained from finite element method (FEM) simulations, which demonstrated the validity of the models and of the techniques used to derive these models.

In this Chapter, these analytical models are used to investigate the dynamics of cantilevers with perforations at the free end. Cantilever profiles are systematically studied that achieve larger deflection–frequency combinations than simple prismatic beams. Improved cantilever profiles are determined from these investigations. Analytical expressions are then derived to describe the dynamics of these improved profiles, and are verified using FEM simulations. From the results of these investigations, a novel cantilever profile for sensor elements is proposed.

4.2 Dynamics of perforated beams

It was reasoned earlier in Chapter 3 that if the mass m of the cantilever can be reduced in a manner that decreases the spring constant k by a smaller factor, then both the deflection and the resonant frequency can be increased simultaneously. It was also noted that this condition can be achieved by removing mass from the free end of the beam.

In this section, the validity of this argument is investigated using the analytical models developed in the previous Chapter. A silicon cantilever with dimensions $100 \times 20 \times 2$ μm is considered. This beam has a mass of $m = Lbh\rho = 9.32$ pg, and a spring constant of $k = Ebh^3/4L^3 = 6.6$ Nm^{-1}. Mass is removed from the beam using perforations. It was seen in the previous Chapter that both the deflection (Figure 3.10) and the resonant frequency (Figure 3.13) are maximized when the perforation width is equal to the beam width (ie. $\beta = 1$). When such a perforation is at the free end, it becomes a rabbet, and the cantilever becomes a step cantilever. Figure 4.1 shows a cantilever with a rabbet.

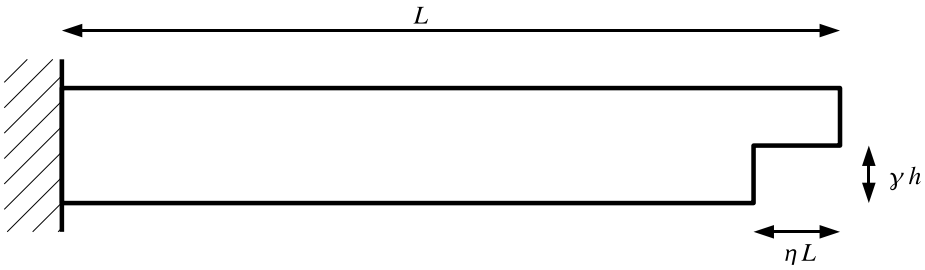

Figure 4.1: A rabbeted cantilever.

4.2.1 Effect of rabbet length on mass and spring constant

Suppose a rabbet of length ηL is made at the free end of the cantilever. The thickness of the rabbet is taken as 0.2 μm ($\gamma = 0.1$). The mass of the cantilever will vary in direct proportion to the volume of the rabbet. The dashed line of Figure 4.2 plots the fractional change of mass with the rabbet length.

The spring constant of a rabbeted cantilever can be obtained from the analytical model for deflection with a point load, given by Equation (3.12). The fractional variation of the spring constant with the rabbet length is shown by the solid line of Figure 4.2. When the rabbet is short, the spring constant changes very little, as modifications to the free end of a cantilever have little effect on the deflection. As the rabbet is made longer, the spring constant decreases sharply. It is evident from Figure 4.2 that the spring constant of a rabbeted beam is always lower than that of the simple prismatic beam. Therefore, a rabbeted beam will have a larger deflection.

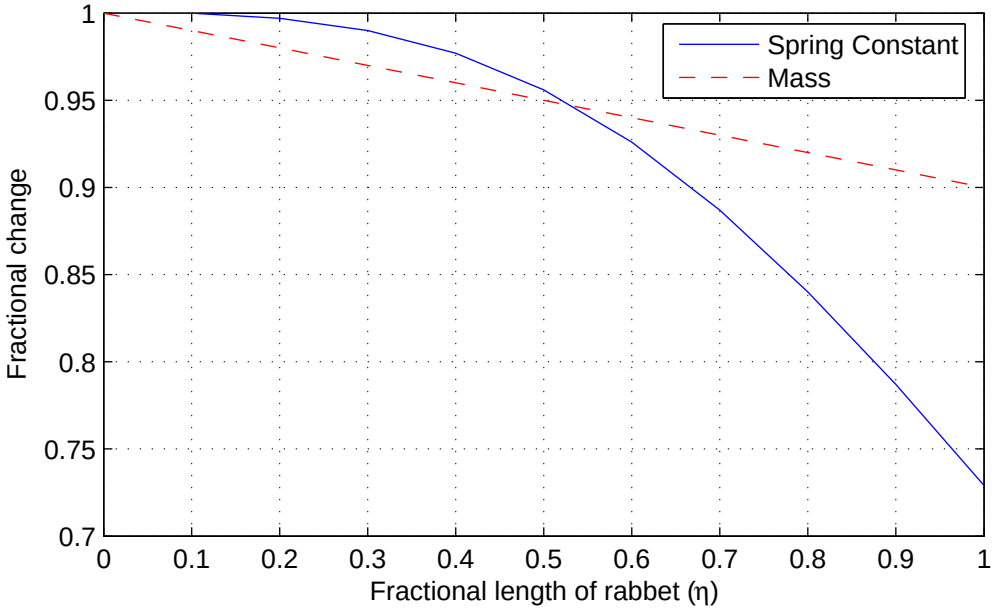

Figure 4.2: Fractional variation of mass and spring constant with rabbet length.

It can be seen from Figure 4.2 that when the rabbet is less than half the length of the beam ($\eta < 0.528$), the fractional change of mass is greater than the fractional change of the spring constant. Therefore, by introducing a rabbet having $0 < \eta < 0.5$ it will be possible to achieve a larger resonant frequency than the original beam. Such a rabbeted beam will also have a larger deflection, due to its lower spring constant.

The above investigations demonstrate that the mass of a microcantilever can be made to decrease by a larger factor than the reduction of the spring constant. In

the following section, the analytical models are used to obtain numerical results to demonstrate the concept of increasing the deflection and resonant frequency simultaneously.

4.2.2 Deflection and resonant frequency of a rabbeted microcantilever

Suppose a differential surface stress $\Delta\sigma = 0.04$ μN/μm develops across the faces of the microcantilever. The variation of deflection of the beam as the rabbet length η is varied can be obtained using the analytical model given by Equation (3.14) of the previous Chapter, and is shown in Figure 4.3.

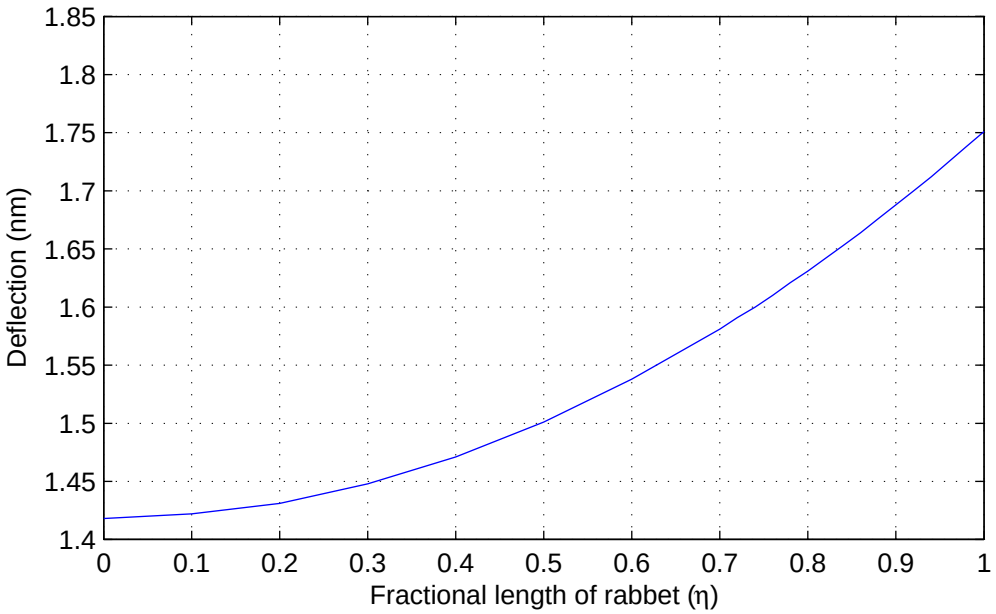

Figure 4.3: Variation of deflection with rabbet length. [$\beta=1,\ \gamma=0.1,\ \alpha+\eta=1$]

When $\eta = 0$, there is no rabbet, and the cantilever is a simple prismatic beam having a thickness of 2 μm. As the value of η is increased, the rabbet becomes longer. Accordingly, the spring constant of the beam decreases, and the deflection increases, as can be seen from Figure 4.3. When $\eta = 1$, the rabbet spans the entire

length of the cantilever. In effect this is a thin beam with a thickness of 1.8 μm. The maximum deflection is observed at this point.

The variation of the resonant frequency as the length of the rabbet is increased can be obtained from Equation (3.20). This is shown in Figure 4.4.

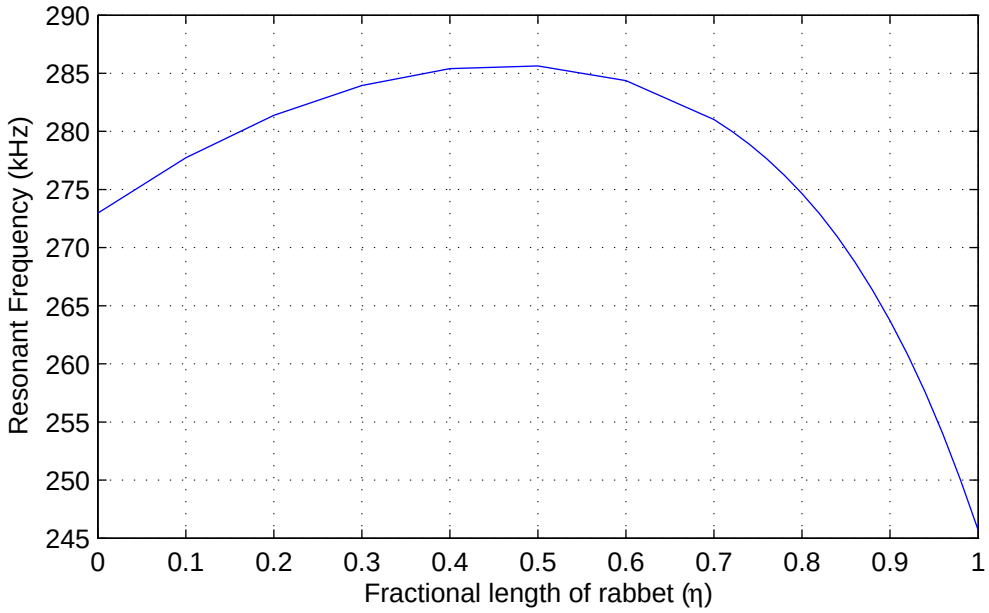

Figure 4.4: Variation of resonant frequency with rabbet length. [$\beta = 1,\ \gamma = 0.1,\ \alpha + \eta = 1$]

When $\eta = 0$, there is no rabbet, and the cantilever is a simple prismatic beam. When η is very small, a small rabbet is made on the free end of the beam. Then the mass of the beam is reduced by a small factor, but the spring constant remains nearly unchanged, as seen earlier in Figure 4.2. This results in the resonant frequency increasing. As the rabbet is made longer, the mass of the beam decreases proportionately, but the spring constant begins to decrease sharply. This causes the rate of increase of the resonant frequency to decrease, and at a value $\eta \approx 0.5$, the resonant frequency reaches its maximum value. When the rabbet is made even longer, the resonant frequency decreases. It can be seen from Figure 4.4 that the resonant frequency of a cantilever can be made greater than that of the original thick beam, by introducing a rabbet at the free end.

4.2.3 Validity of the results and model limitations

It was noted in the previous Chapter that when perforations having a small depth were introduced to the cantilevers, the analytical model for deflection predicted smaller values than the FEM simulations, but within a 6% variation. The model for resonant frequency predicted a lower value, but within 4% of the value given by FEM simulations. It was also noted that the models, particularly the model for resonant frequency, are most accurate when the perforations are small.

When η is very small, the cantilever is a thick beam with a very small rabbet, and hence the models will be accurate. Therefore, the left-hand ends of Figures 4.3 and 4.4 should be valid. When $\eta \rightarrow 1$, the beam can be regarded as a *thin* cantilever with a small section *added* to its fixed end. Hence the models should be valid, and the gradients of the right-hand ends of Figures 4.3 and 4.4 should also be valid. Since Figure 4.4 has a positive gradient at the left end and a negative gradient at the right end, it follows that there must be at least one maxima between the two ends. Hence, the general shape of these figures should be valid, although the numerical values may have inaccuracies due to limitations in the models.

4.2.4 $t \cdot f_0$ value of a rabbeted microcantilever

The variation of the $t \cdot f_0$ value with rabbet length can be obtained from the analytical models, and is plotted in Figure 4.5.

Initially the $t \cdot f_0$ value of rabbeted beams increases nearly linearly with η. The $t \cdot f_0$ value reaches its maximum at $\eta \approx 0.8$, and then begins to decrease. When $\eta = 1$, the beam is a thin prismatic cantilever. It was noted in Chapter 3 that among prismatic beams, thin beams have the largest $t \cdot f_0$ value. Figure 4.5 shows that rabbeted beams can achieve an even larger $t \cdot f_0$ value than a thin beam having a uniform thickness of 1.8 μm.

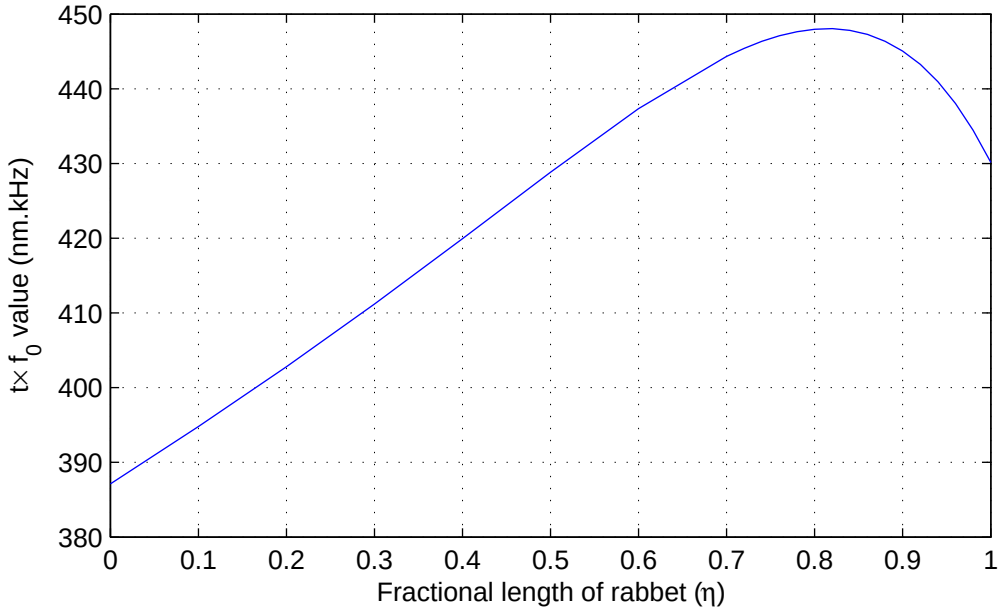

Figure 4.5: Variation of the $t \cdot f_0$ value with rabbet length. [$\beta = 1$, $\gamma = 0.1$, $\alpha + \eta = 1$]

4.2.5 Increasing the rabbet thickness

In the above analyses, the rabbet thickness factor was taken as $\gamma = 0.1$, making the rabbet 0.2 μm thick. The variations of deflection, resonant frequency and $t \cdot f_0$ values at different values of γ are plotted in Figures 4.6, 4.7 and 4.8 respectively.

It can be seen from Figures 4.6 and 4.7 that the deflection and resonant frequency are increased by larger factors when the rabbet is made deeper. Figure 4.8 shows that when deeper rabbets are used, large increases in the $t \cdot f_0$ values compared with simple prismatic beams are obtained. As the rabbet is made deeper, the rabbet length at which the peak $t \cdot f_0$ value is observed shifts slightly to the right. When $\gamma = 0.1$, the peak is observed at $\eta \approx 0.8$, while when $\gamma = 0.7$, the peak value of $t \cdot f_0$ is observed at $\eta \approx 0.85$.

From the above investigations, it can be observed that a rabbeted beam with a thinner free end can achieve a higher resonant frequency than a thick beam, and a higher deflection and a higher $t \cdot f_0$ value than a thin beam. The largest $t \cdot f_0$ value

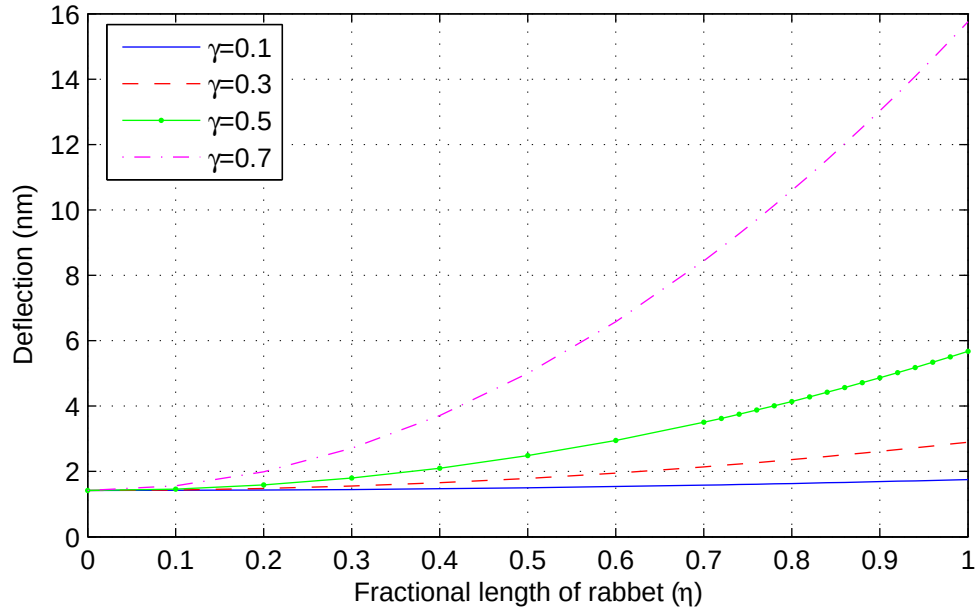

Figure 4.6: Variation of deflection with rabbet length at different rabbet thicknesses.

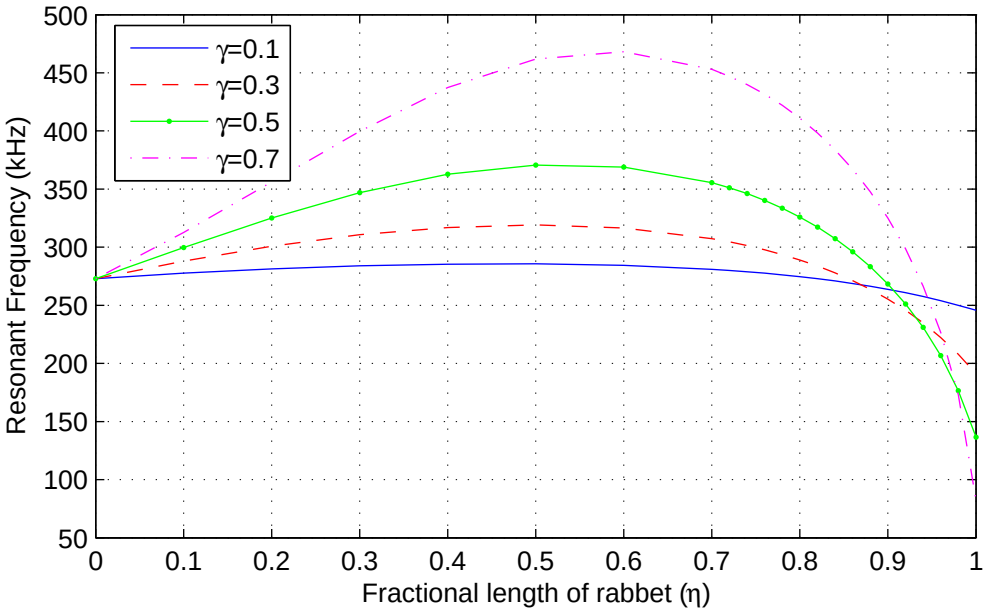

Figure 4.7: Variation of resonant frequency with rabbet length at different rabbet thicknesses.

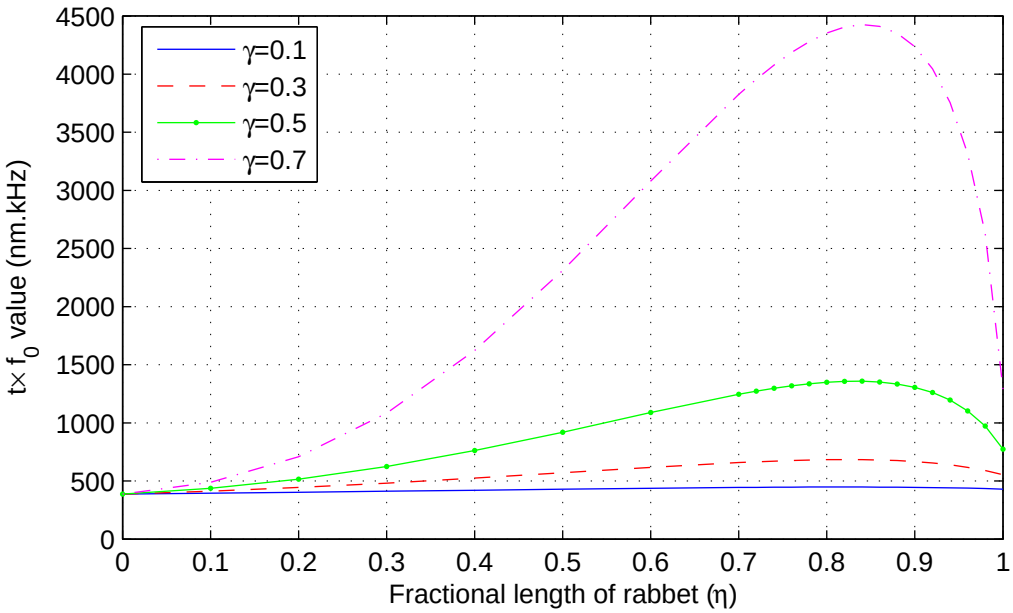

Figure 4.8: Variation of the $t \cdot f_0$ value with rabbet length at different rabbet thicknesses.

is achieved by making the free end as thin as possible.

The deflection of a rabbeted beam cannot be made greater than that of the thin beam. However since the $t \cdot f_0$ value of a rabbeted beam is greater than that of the thin beam, the resonant frequency can be traded-off for deflection by increasing the length of the beam, to achieve a deflection–frequency combination not possible with simple beams. These results also demonstrate the validity of the principle that both the deflection and the resonant frequency can be increased simultaneously when the mass is decreased by a greater factor than the reduction of the spring constant.

From these results, it can be concluded that non-prismatic microcantilevers with a step profile will have better deflection–frequency characteristics compared with prismatic beams with rectangular profiles.

4.3 Improving the cantilever profile

In this section, the results of the previous sections are used to improve the cantilever profile further so that even larger deflection–frequency combinations can be achieved.

4.3.1 The rabbeted beam as a composite beam

Suppose the rabbet is 1 μm thick, and spans 80% of the beam such that nearly the largest possible $t \cdot f_0$ value is observed. Further insight can be obtained by considering this beam as a composite of a thick short stub and a thin long plank, as shown in Figure 4.9. The deflection, resonant frequency and $t \cdot f_0$ values of these

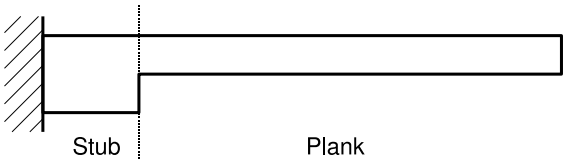

Figure 4.9: The rabbeted beam as a composite of two elements.

elements and the composite beam are tabulated in Table 4.1.

Table 4.1: Mechanical properties of a rabbeted beam and its composite parts.

Element	Sketch	t (nm)	f_0 (kHz)	t· f_0 (nm.kHz)
Composite		4.14	326	1350
Stub		0.057	6824	387
Plank		3.63	213	774

It can be seen from the table that the deflection and resonant frequency of the composite beam are dominated by the corresponding values of the thin plank. The main effect of the thick stub, which has a resonant frequency an order of magnitude greater than the plank, is to cause the resonant frequency of the composite beam

to increase. It also contributes towards the deflection of the composite beam. Note that the deflection of the composite beam is greater than the sum of the deflections of the individual elements.

4.3.2 The plank section as an independent cantilever

The deflection of the thin plank section is two orders of magnitude larger than the thick stub. One end of the plank is fixed to the stub, which can be considered stationary with respect to the plank. Therefore, the plank section can be viewed as a simple prismatic cantilever by itself. While the deflection and $t \cdot f_0$ value of the plank can be increased by making it thinner, an even larger $t \cdot f_0$ value can be achieved by making the free end of the plank thinner compared to its fixed end, as shown earlier. Thus, rather than making the plank section uniformly thinner, if the plank is made into a step beam, a larger $t \cdot f_0$ value can be obtained.

Following in this manner, it can be reasoned that a staircase cantilever (see Figure 4.10) will achieve a larger $t \cdot f_0$ value than a single-step cantilever.

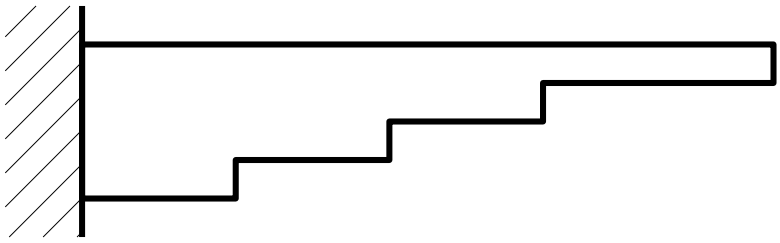

Figure 4.10: A cantilever with a staircase profile.

4.4 Optimizing the cantilever profile

The thickness of a staircase cantilever decreases in discrete steps from the fixed end to the free end. Segments close to the free end could be several times thinner than the fixed end, and give the composite beam large deflection and $t \cdot f_0$ values. The

thicker fixed end gives the beam a high resonant frequency. From this argument it can be inferred that a cantilever having a tapering profile achieves the best $t \cdot f_0$ value.

There are many profiles that meet these requirements, such as triangular and exponential shaped profiles. It is possible to obtain reasonably accurate analytical models to describe the deflection due to surface stress of all such non-prismatic beams, using the moment–area method described in the previous Chapter. However, it is far more difficult, if not impossible, to obtain accurate analytical solutions for the resonant frequency. However, numerical models are available in the literature that can be used to calculate the resonant frequency of tapering cantilevers. In the following section, dynamics of tapering cantilevers are investigated through analytical models and numerical methods. Results are compared with finite element method simulations using the *ANSYS Multiphysics* software.

4.4.1 Modelling tapering cantilevers

The simplest profile that has a gradually diminishing thickness is triangular. Trapezoidal and exponential profiles also have gradually reducing thicknesses. In general, the thickness function $h(x)$ of a cantilever with a gradually diminishing thickness can be expressed by the polynomial function

$$h(x) = h_b + (h_a - h_b)(x/L)^n \tag{4.1}$$

where h_a and h_b are the thicknesses of the fixed and free ends respectively, x is measured from the free end, L is the length of the cantilever and n is the order of the polynomial. Refer Figure 4.11.

When $n = 1$, a trapezoidal profile is obtained. A sketch of this beam is given in Table 4.2. Using the moment–area method, the following expression can be obtained for its deflection due to a surface stress σ (Refer section A.4.1 of Appendix A):

$$t = \frac{6\sigma(1-\nu)L^2}{E(h_a - h_b)^2}\left[\ln\left(\frac{h_a}{h_b}\right) + \frac{h_b}{h_a} - 1\right] \tag{4.2}$$

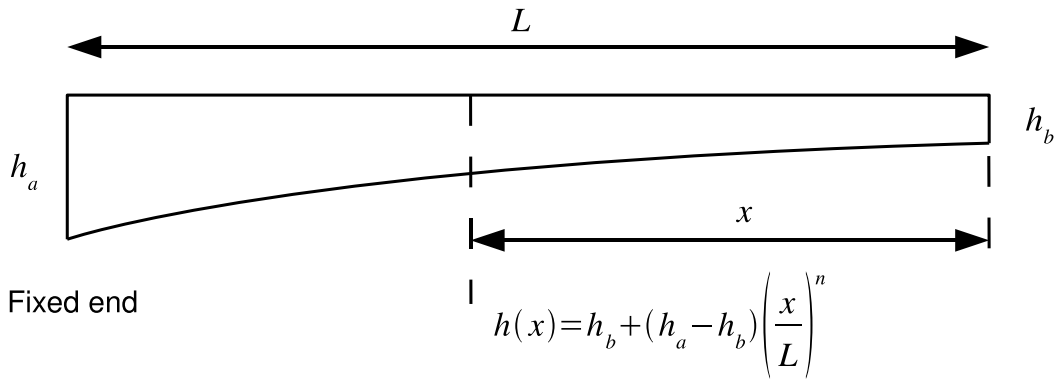

Figure 4.11: The general form of a tapering cantilever.

A triangular beam is obtained when $h_b = 0$ of a trapezoidal beam. However, it can be noted that Equation (4.2) is undefined for $h_b = 0$. Hence, it is not possible to obtain an analytical solution for the deflection of a triangular beam. The same difficulty is encountered even if the differential equation of the deflection curve is solved to find the deflection. Therefore, a triangular beam was approximated by a trapezoidal beam having a very small but non-zero value for h_b.

A cantilever having a quadratic profile is obtained when $n = 2$ is used in Equation (4.1). Its deflection due to a surface stress σ is found to be given by (Appendix A, section A.4.2)

$$t = \frac{3(1-\nu)\sigma L^2}{E(h_a - h_b)}\left[\frac{1}{h_b} - \frac{1}{h_a}\right] \tag{4.3}$$

This equation too is undefined for $h_b = 0$, so a small but non-zero value was considered for h_b.

As the order of the polynomial increases, the rate of change of the cantilever thickness increases, and larger sections of the beam gets thinner. For example when $n = 3$, 25 % of the beam has a thickness of less than 1.6 % of the fixed end thickness. Such a beam may be structurally unrealistic. In the limit when the exponent tends to infinity, the cantilever practically has zero thickness throughout, except at the fixed end where the thickness remains at h_a. Thus, there is no practical value in studying beams with profiles fitting polynomials of the third order and above.

The analytical solution for the resonant frequency of a triangular cantilever is given in [1] as

$$f_0 = \frac{2.6575}{2\pi}\sqrt{\frac{E}{3\rho}} \cdot \frac{h}{L^2} \tag{4.4}$$

It is possible to determine an approximate solution for the resonant frequency of a trapezoidal cantilever using the Rayleigh–Ritz method:

$$f_0 = \frac{1}{2\pi}\sqrt{\frac{E}{\rho}} \cdot \frac{1}{L^2}\left[\frac{27}{16} \cdot \frac{35h_a^3 + 15h_a^2h_b + 5h_ah_b^2 + h_b^3}{18h_a + 73h_b}\right]^{1/2} \tag{4.5}$$

However, it is not possible to determine an analytical solution for the resonant frequency of a cantilever with a quadratic profile using the Rayleigh–Ritz method.

The derivations of the above model is given in section A.5 of Appendix A.

4.4.2 Simulating non-prismatic cantilevers

ANSYS does not have a direct method to construct exponential curves. Therefore to construct an exponential profiled beam, keypoints were defined using coordinates to represent the cross-section of the beam. These keypoints were connected to construct lines, and an area was defined using these lines. This planar model was then extruded to obtain a three-dimensional beam. Once the beam is thus defined, the response of non-prismatic cantilevers can be simulated using the same approach taken in Chapter 3. The cantilevers were assumed to be made of silicon, and the surface stress was again considered to be 0.04 μN/μm.

4.5 Results

Using the analytical models for perforated beams and tapering beams, numerical values for the deflection and resonant frequency of non-prismatic cantilevers considered were computed. These values are compared in this section to determine the optimal cantilever profile for sensor elements. For this investigation, cantilever

beams 100 μm long, 20 μm wide and having a surface stress of 0.04 μN/μm were considered. The thickness of the fixed end of all beams was taken as $h_a = 2$ μm. The perforations of the step cantilevers were assumed to be 1 μm deep. The free ends of the triangular and quadratic cantilevers were considered to be 0.1 μm thick.

Since analytical solutions cannot be obtained to calculate the resonant frequency of all the cantilevers investigated, resonant frequencies were obtained using the numerical model described in [2]. Where possible, resonant frequencies calculated using the analytical solutions were also evaluated. For comparison, all cantilevers were then simulated using *ANSYS*. Results of these investigations are summarized in Table 4.2.

It was noted in the previous Chapter that of the uniform cantilevers, the thinnest beam gives the largest $t \cdot f_0$ value. To generalize the results to any cantilever dimension and surface stress value, all numerical values were normalized with respect to the thin rectangular cantilever having a uniform thickness of 1 μm (cantilever #2). Thus the deflection t, resonant frequency f_0 and the $t \cdot f_0$ product of cantilever #2 are all unity. Of the simple prismatic beams, the thick cantilever (#1) has the highest resonant frequency while the thin beam (#2) has the largest deflection and the largest $t \cdot f_0$ value, as discussed earlier.

Normalized deflection values obtained from the analytical and numerical methods are consistent with FEM results, as can be seen from Table 4.2. The theoretical methods predict larger resonant frequencies than FEM, and there is a large discrepancy for cantilever #9. This could be due to the omission of the effect of rotary inertia.

The step cantilevers #3, #4 and #5 have larger deflections and higher resonant frequencies compared with the thick cantilever (#1), in agreement with the arguments presented previously. However, the FEM results show that the $t \cdot f_0$ value of cantilever #3 is smaller than that of the thin beam (#2). This means that a prismatic thin cantilever can be found that has a higher deflection–frequency combination than the step beam #3.

Table 4.2: Normalized values of deflection, resonant frequency and $t \cdot f_0$ values, together with sketches of the different profiles investigated.

ID	Profile	Theoretical			FEM			Anal.	Sketch
		t	f_0	$t \cdot f_0$	t	f_0	$t \cdot f_0$	f_0	
#1	Rectangular	0.25	2.0	0.50	0.25	2.0	0.50	2.0	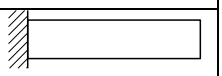
#2	Rectangular	1.0	1.0	1.0	1.0	1.0	1.0	1.0	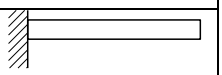
#3	Step ($\eta = 0.5$)	0.44	2.70	1.18	0.36	2.38	0.86	2.72	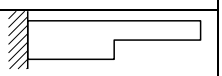
#4	Step ($\eta = 0.6$)	0.52	2.66	1.38	0.52	2.10	1.09	2.70	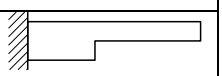
#5	Step ($\eta = 0.8$)	0.73	2.28	1.66	0.72	1.47	1.06	2.34	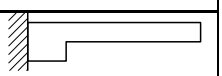
#6	Staircase	—	—	—	0.67	2.74	1.84	—	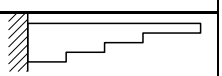
#7	Trapezoidal	0.39	2.25	0.87	0.33	2.16	0.71	2.30	
#8	Triangular	1.13	3.19	3.61	1.18	2.76	3.26	3.04	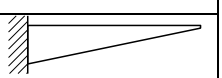
#9	x^2	5.0	3.94	19.71	5.08	1.92	9.76	—	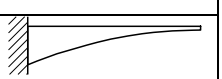

The $t \cdot f_0$ values of cantilevers #4 and #5 are greater than that of the thin beam (#2). Thus, these step beams have high deflection–frequency product combinations that cannot be achieved using simple prismatic cantilevers.

Note that in section 4.2.4 it was established using the analytical models that a cantilever having a rabbet spanning 80 % of its length (ie $\eta = 0.8$) will achieve the highest $t \cdot f_0$ value. However, the results obtained from FEM simulations presented in Table 4.2 show that cantilever #4 which has a rabbet spanning 60 % of the beam length achieves a larger $t \cdot f_0$ value than cantilever #5 that has a rabbet spanning 80 % of the beam length. This discrepancy is due to the limitations of the analytical models. Referring to Figure 3.14 of the previous Chapter, it can be seen that while

the analytical model predicts the highest resonant frequency at $\eta = 0.5$, the FEM results show that the largest resonant frequency is achieved at $\eta = 0.4$. Nevertheless, results from both the analytical method and the FEM simulations show that the $t \cdot f_0$ value of a cantilever can be increased by making the free end of the beam thinner compared with the fixed end.

Only FEM simulations were available to investigate the response of the staircase cantilever. It can be seen that it achieves a $t \cdot f_0$ value 1.84 times greater than the thin cantilever.

The trapezoidal cantilever (#7) has deflection and resonant frequency values similar to cantilever #3, and has no advantage over a simple thin beam.

Both the analytical methods and the FEM simulations show that the triangular-profiled cantilever (#8) will have a deflection larger than the thin rectangular beam (#2), and a resonant frequency greater than the thick rectangular beam (#1). The triangular beam achieves a $t \cdot f_0$ value at least 3.26 times larger than the thin prismatic cantilever. This means that a triangular cantilever will have thrice the deflection of a thin rectangular cantilever, while having the same resonant frequency of the thin beam; alternatively, a triangular cantilever having the same deflection as a thin rectangular beam will have a resonant frequency thrice as large as the thin beam; or both the deflection and the resonant frequency of a triangular cantilever can be made greater than the corresponding values of a thin rectangular cantilever. Thus a triangular cantilever will have deflection and resonant frequency values in combinations that are unattainable using prismatic rectangular cantilevers. Clearly, the triangular beam will have a higher sensitivity than simple prismatic beams.

The quadratic cantilever (#9) has an even higher $t \cdot f_0$ value. However, this beam could be structurally unrealistic.

Triangular beams were shown to have a larger deflection than rectangular beams when actuated by a static electric field in [3]. The above analysis demonstrated that triangular cantilevers will achieve a higher deflection due to a surface stress, as well

as having a higher resonant frequency compared with prismatic cantilevers.

It is difficult to fabricate cantilevers having a variable thickness since microfabrication is a planar technology. In [3], triangular cantilevers were fabricated sideways. The profile of the cantilevers were defined photolithographically, and a novel double-exposure method was proposed to achieve a sharp tip. The beams were then etched using standard micromachining techniques. The width of the cantilevers was limited to about 5 μm. In [4] for example, vertical silicon walls 0.3 μm in thickness and 15 μm in height were realized using deep reactive ion etching (DRIE), with a maximum surface roughness of 20 nm. Using these two techniques, triangular cantilevers having larger widths can be fabricated.

4.6 Analysis of variations

Investigations of the preceding sections considered cantilevers having specific dimensions and shapes. However, standard fabrication techniques will introduce variations into the dimensions and shape of cantilevers which will affect the response and the measurements taken using these cantilevers. The effects of dimensional and shape variations on the response of cantilevers having uniform, step and triangular profiles are investigated in this section.

4.6.1 Effect of dimensional variations on cantilever response

The maximum relative error of a function $y = f(x_1, x_2, x_3, \ldots)$ is given by

$$\left|\frac{\Delta y}{y}\right| = \left|\frac{\partial y}{\partial x_1}\right|\left|\frac{\mathrm{d}x_1}{y}\right| + \left|\frac{\partial y}{\partial x_2}\right|\left|\frac{\mathrm{d}x_2}{y}\right| + \left|\frac{\partial y}{\partial x_3}\right|\left|\frac{\mathrm{d}x_3}{y}\right| + \ldots \tag{4.6}$$

The deflection of step cantilevers can be determined by substituting $\alpha = 1 - \eta$ and $\beta = 1$ into Equation (3.13):

$$t = \frac{3(1-\nu)\Delta\sigma L^2}{Eh^2}\left[1 + \eta^2\gamma\frac{(2-\gamma)}{(1-\gamma)^2}\right] \tag{4.7}$$

This expression is a function of four dimensional parameters, L, h, η and γ. Then the maximum relative error of deflection due to dimensional variations is given by

$$\left|\frac{\Delta t}{t}\right|_{\text{step}} = \left|\frac{\partial t}{\partial L}\right|\left|\frac{\mathrm{d}L}{t}\right| + \left|\frac{\partial t}{\partial h}\right|\left|\frac{\mathrm{d}h}{t}\right| + \left|\frac{\partial t}{\partial \eta}\right|\left|\frac{\mathrm{d}\eta}{t}\right| + \left|\frac{\partial t}{\partial \gamma}\right|\left|\frac{\mathrm{d}\gamma}{t}\right| \tag{4.8}$$

By taking the necessary partial derivatives of Equation (4.7) and substituting the optimal values $\eta = 0.6$ and $\gamma = 0.5$, the expression for the maximum relative error of deflection is obtained.

$$\left|\frac{\Delta t}{t}\right|_{\text{step}} = 2\left|\frac{\mathrm{d}L}{L}\right| + 2\left|\frac{\mathrm{d}h}{h}\right| + 1.04\left|\frac{\mathrm{d}\eta}{\eta}\right| + 1.38\left|\frac{\mathrm{d}\gamma}{\gamma}\right| \tag{4.9}$$

Thus, variations in the length and thickness of the beam have the greatest effect on the deflection of the cantilever, followed by the fractional thickness and the fractional length of the perforation, respectively. As an example, if there is a 5% variation of each of the parameters L, h, η and γ, the deflection could deviate from the ideal value by up to 32% according to Equation (4.9).

The variation of deflection due to dimensional variations of uniform cantilevers can be determined from Equation (4.9) by omitting the final two terms of the expression. Thus for example if the length L and thickness h of a uniform cantilever varied by 5%, the deflection could deviate from the predicted value by up to 20%.

The deflection of a cantilever having a triangular profile is given by Equation (4.2), from which the maximum relative error can be derived. When $h_a = 2$ μm and $h_b = 0.1$ μm, the error is given by

$$\left|\frac{\Delta t}{t}\right|_{\text{trig}} = 2\left|\frac{\mathrm{d}L}{L}\right| + 1.6\left|\frac{\mathrm{d}h_a}{h_a}\right| + 0.36\left|\frac{\mathrm{d}h_b}{h_b}\right| \tag{4.10}$$

Thus variations of the length L has the greatest effect on the deflection of triangular cantilevers, followed by the thickness of the fixed and free ends, respectively. As an example, if L, h_a and h_b varied by 5% from the specified value, the deflection could deviate from the predicted value by up to 20%.

Comparing with the step beam, the deflection of the triangular-profiled beam is less sensitive to dimensional variations. This is partly due to the fact that while there are

four parameters L, h, γ and η in step cantilevers which are sensitive to dimensional variations, there are only three parameters L, h_a and h_b in triangular-profiled beams.

The variations of resonant frequency due to dimensional variations can be determined in a similar manner. The resonant frequency of step cantilevers can be determined from Equation (3.20) by substituting $\alpha = 1 - \eta$ and $\beta = 1$. Then, the maximum relative error of the resonant frequency due to dimensional variations is found to be given by

$$\left|\frac{\Delta f_0}{f_0}\right|_{\text{step}} = 2\left|\frac{\mathrm{d}L}{L}\right| + \left|\frac{\mathrm{d}h}{h}\right| + 0.11\left|\frac{\mathrm{d}\eta}{\eta}\right| + 0.46\left|\frac{\mathrm{d}\gamma}{\gamma}\right| \tag{4.11}$$

The error of the resonant frequency of triangular-profiled cantilevers due to dimensional variations can be determined from Equation (4.5).

$$\left|\frac{\Delta f_0}{f_0}\right|_{\text{trig}} = 2\left|\frac{\mathrm{d}L}{L}\right| + 1.07\left|\frac{\mathrm{d}h_a}{h_a}\right| + 0.07\left|\frac{\mathrm{d}h_b}{h_b}\right| \tag{4.12}$$

The maximum relative errors of deflection and resonant frequency due to dimensional variations of the cantilevers considered above are summarised in Table 4.3.

Table 4.3: Maximum relative errors of cantilever responses due to dimensional variations of 5%.

	% Variation	
Cantilever profile	t	f_0
Uniform	20%	15%
Step	32%	18%
Triangular	20%	16%

It can be seen from Table 4.3 that the deflection of each of the three cantilever types considered are very sensitive to dimensional variations, with the sensitivity of uniform cantilevers and triangular-profiled cantilevers being of similar value. This

analysis highlights that even though triangular-profiled cantilevers have greater $t \cdot f_0$ values when compared with uniform cantilevers, they are equally sensitive to dimensional variations. These investigations assumed 5% variations of all dimensions. However, the lateral features of cantilevers are defined photolithographically, and hence can be fabricated with higher precision. All dimensions of cantilevers have to be carefully controlled during fabrication to ensure the variations are within acceptable limits.

4.6.2 Effect of filleting and smoothing

In the theoretical analysis, the cantilevers were assumed to have sharp edges. In practice however, the edges are smooth and filleted. The effect of filleting and rounding on the response of step cantilevers and triangular cantilevers was investigated using FEM simulations using ANSYS. The cantilever specifications were the same as those given in Section 4.5 above. The fillet radii were assumed to be 1 μm, while the edges of the free end were assumed to have been rounded having radii of 5 μm. Schematic diagrams showing these dimensions are given in Figure 4.12.

The effect of rounding and filleting on the deflection, resonant frequency and the $t \cdot f_0$ value of cantilevers are given below in Table 4.4.

As can be seen from Table 4.4, the deflection, resonant frequency and the $t \cdot f_0$ value of cantilevers with a step profile decrease due to the smoothing of edges. For the smoothing effects considered, the deflection of step cantilevers decreases by 1.8 %. In the case of cantilevers with triangular profiles, the smoothing effects result in an increase of the deflection, resonant frequency and the $t \cdot f_0$ value, which is beneficial from a sensor point of view. Further, the variation of deflection for the smoothing effects considered is only 0.05 %, which can be considered as a negligible variation in most cases. These results show that cantilevers having a triangular profile are far less sensitive to shape variations due fabrication imperfections than cantilevers having a step profile.

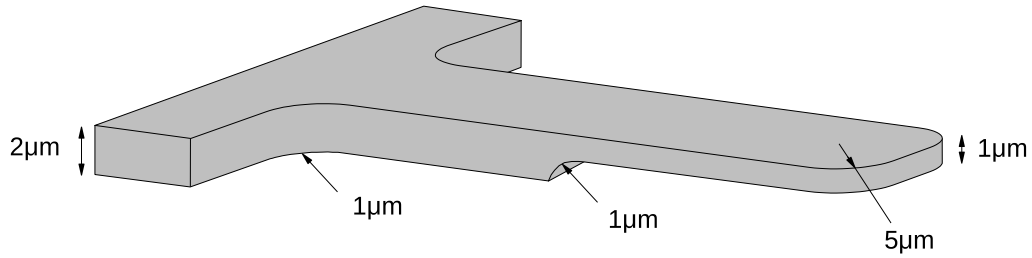

(a)

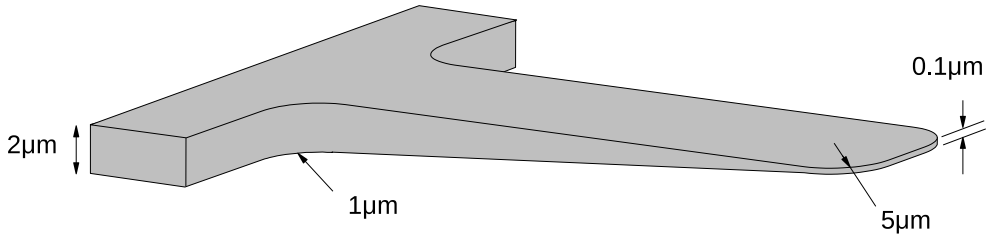

(b)

Figure 4.12: Schematic diagrams of (a) a step cantilever and (b) a triangular-profiled cantilever with filleted edges. The cantilevers are 100 μm in length and 20 μm in width.

4.7 Conclusions

It was demonstrated that cantilevers having larger deflection and resonant frequency values compared with uniform beams can be obtained by making the free end of the beam thinner compared to the fixed end. Rabbeted beams can achieve deflection–frequency combinations not possible with prismatic beams. By using cantilevers with tapering profiles, even greater improvements in the $t \cdot f_0$ values compared with simple rectangular beams can be achieved.

Cantilevers having a triangular profile achieve larger deflections and larger resonant frequencies compared with simple beams. The sensitivity of the response of triangular-profiled cantilevers to dimensional variations are comparable to prismatic cantilevers, and are almost insensitive to smoothing effects of fabrication. Using beams with triangular profiles instead of prismatic rectangular beams will enable microcantilevers to have a higher sensitivity for sensor applications.

Table 4.4: The simulated effects of rounding and filleting on the responses of cantilevers.

Step Cantilever			
	t	f_0	$t \cdot f_0$
Ideal cantilever	2.65 nm	349 kHz	923 nm.kHz
Cantilever with smooth edges	2.60 nm	332 kHz	863 nm.kHz
Percentage variation	-1.8 %	-4.8 %	-6.5 %
Triangular Cantilever			
	t	f_0	$t \cdot f_0$
Ideal cantilever	7.56 nm	381 kHz	2879 nm.kHz
Cantilever with smooth edges	7.57 nm	382 kHz	2893 nm.kHz
Percentage variation	0.05 %	0.5 %	0.5 %

References

[1] S. Timoshenko, *Vibration Problems in Engineering.* N.Y: Van Nostrand, 2nd ed., 1937.

[2] R. Jategaonkar and D. S. Chehil, "Natural frequencies of a beam with varying section properties," *Journal of Sound and Vibration*, vol. 133, no. 2, pp. 303–322, 1989.

[3] Y. Hirai, Y. Marushima, S. Soda, D. Jin, H. Kawata, K. Inoue, and Y. Tanaka, "Electrostatic actuator with novel shaped cantilever," in *Micromechatronics and Human Science, 2000. MHS 2000. Proceedings of 2000 International Symposium on* (Y. Marushima, ed.), pp. 223–227, 2000.

[4] F. Marty, L. Rousseau, B. Saadany, B. Mercier, O. Francais, Y. Mita, and T. Bourouina, "Advanced etching of silicon based on deep reactive ion etching for silicon high aspect ratio microstructures and three-dimensional micro- and nanostructures," *Microelectronics Journal European Micro and Nano Systems - EMN 2004*, vol. 36, no. 7, pp. 673–677, 2005.

Chapter 5

Novel Optical Measurement Method

5.1 Introduction

An analysis of the different methods that have been reported to measure the deflection of microcantilevers was presented in the literature review in Chapter 2. The interdigital interferometric measurement method was shown to be the most viable technique to measure the deflection of disposable cantilever sensors for an automated system. While sub-nanometer resolutions have been reported, it was highlighted that the maximum measurable deflection was limited to $\lambda/4$, where λ is the wavelength of the optical source.

In this Chapter, the interdigital interferometric measurement technique is analysed using a novel approach that has not been reported in the literature. From this analysis, the reason for the limitation in the measurement range is identified. Techniques are then proposed that can overcome this limitation and extend the measurement range. Principles are established and proved to make this technique applicable to an automated measurement system.

5.2 Theoretical background

The use of interdigital cantilevers as a method to determine the deflection of cantilevers was first proposed in [1]. The arrangement proposed was to have interdigital fingers attached to a moving cantilever and a fixed cantilever. These digits formed a phase sensitive diffraction grating. An incident coherent beam of light was diffracted into many orders by the grating. The intensities of these orders depends on the deflection of the moving set of digits and was used to measure the relative deflection between the two cantilevers.

The same principles can be used to measure the deflection of an array of cantilevers, if the array is arranged such that alternate cantilevers are free to deflect, while the others remain stationary. A detailed theory of operation of interdigital cantilevers is available in [2], where Fourier optics is used to analyse the behaviour. In the following section, cantilever array gratings are analysed as lamellar gratings using first principles, which provides a unique insight of the problem. A similar technique was used in [3] to explain the diffraction patterns observed in x-ray diffraction crystallography.

Consider Figure 5.1 which shows a cross section of the cantilever array. Let there be $2N$ cantilevers, at locations $x = x_0$, $x = x_1$, $x = x_2$, ..., $x = x_{2N-1}$. Let x_f denote the location of fixed cantilevers, and let x_m denote the location of moving cantilevers. The fixed cantilevers are at the reference level, while the moving cantilevers have been displaced by a distance t. An incident coherent optical beam of light is reflected by the grating into several orders, which forms an optical diffraction pattern in the far-field.

The diffracted wave amplitude in the far field E_{far} can be expressed by [4]

$$E_{\text{far}} = E_{\text{s}} \cdot F \tag{5.1}$$

where E_{s} is the diffracted wave amplitude of a single cantilever, and F is the interference effect of the $2N$ cantilevers.

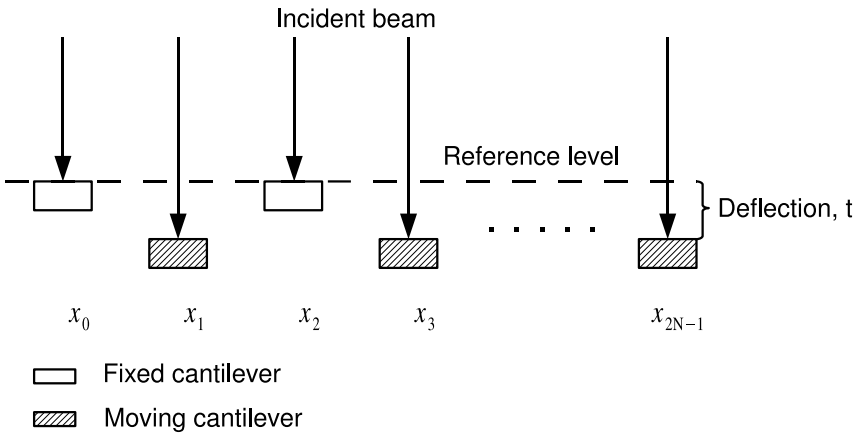

Figure 5.1: Cross sectional view of an array of cantilevers. Also shown is the incident optical beam.

The diffracted wave amplitude of a single rectangular optical aperture, in this case a cantilever, is well known and is given by [5]

$$E_{\mathrm{s}} \propto \operatorname{sinc}\left(\frac{1}{2}kb\sin\theta\right) \tag{5.2}$$

where $k = 2\pi/\lambda$ is the wavenumber and b is the width the cantilever.

The interference term F can be determined using first principles as follows. The field strength of a monochromatic wave at position $\mathbf{r}$ at time t is given by the wavefunction [6]

$$u(\mathbf{r}, t) = A(\mathbf{r})\cos(2\pi\nu t + \phi(\mathbf{r})) \tag{5.3}$$

where $A(\mathbf{r})$ is the amplitude, $\phi(\mathbf{r})$ is the phase and ν is the frequency of the optical wave. When a plane wave is considered, the amplitude $A(\mathbf{r})$ is independent of the position, and is a constant. It is convenient to express the wavefunction of Equation (5.3) in complex notation, which for a plane wave becomes

$$U(\mathbf{r}, t) = A\,\mathrm{e}^{j\phi(\mathbf{r})}\,\mathrm{e}^{j2\pi\nu t} \tag{5.4}$$

from which the complex amplitude is defined as

$$U(\mathbf{r}) = A\,\mathrm{e}^{j\phi(\mathbf{r})} \tag{5.5}$$

When an optical beam is reflected off a grating, each grating element gives rise to a separate wave. The resultant wave F is given by the superposition of the individual complex amplitudes of the waves

$$F = U_0(\mathbf{r}) + U_1(\mathbf{r}) + U_2(\mathbf{r}) + \ldots \tag{5.6}$$

where $U_i(\mathbf{r})$ is the complex amplitude of the wave reflected off the i^{th} grating element. With reference to the array of cantilevers defined above, Equation (5.6) can be rearranged as

$$\begin{aligned} F &= \underbrace{(U_0 + U_2 + U_4 + \ldots + U_{2N-2})}_{\text{fixed cantilevers}} \quad + \quad \underbrace{(U_1 + U_3 + U_5 + \ldots + U_{2N-1})}_{\text{moving cantilevers}} \\ F &= A\left[\mathrm{e}^{j\phi_0} + \mathrm{e}^{j\phi_2} + \ldots + \mathrm{e}^{j\phi_{2N-2}}\right] + A\left[\mathrm{e}^{j\phi_1} + \mathrm{e}^{j\phi_3} + \ldots + \mathrm{e}^{j\phi_{2N-1}}\right] \\ &= A\left[\sum_{\substack{f \text{ even} \\ f=0}}^{2N-2} \mathrm{e}^{j\phi_f} \quad + \quad \sum_{\substack{m \text{ odd} \\ m=1}}^{2N-1} \mathrm{e}^{j\phi_m}\right] \end{aligned} \tag{5.7}$$

Taking the wave reflected off the cantilever at $x = x_0$ as the reference, the phase terms of the reflected waves can be determined from Figure 5.2. For a wave reflected off a fixed cantilever at location $x = x_f$, the optical path difference δ_f with respect to the reference wave is given by l_{12} of Figure 5.2(a):

$$\delta_f = x_f \sin\theta \tag{5.8}$$

The optical path difference δ_m between a wave reflected off a moving cantilever at location $x = x_m$ and the reference wave is given by $l_{34} - (l_{56} + l_{67})$ of Figure 5.2(b):

$$\delta_m = x_m \sin\theta - t_m(1 + \cos\theta) \tag{5.9}$$

where t_m is the deflection of the m^{th} cantilever. The phase differences can then be calculated by multiplying the path differences by the wavenumber k. Substituting the phase terms in Equation (5.7) gives

$$F = A\left[\sum_{\substack{f \text{ even} \\ f=0}}^{2N-2} \mathrm{e}^{jkx_f \sin\theta} \quad + \quad \sum_{\substack{m \text{ odd} \\ m=1}}^{2N-1} \mathrm{e}^{jk\{x_m \sin\theta - t_m(1+\cos\theta)\}}\right] \tag{5.10}$$

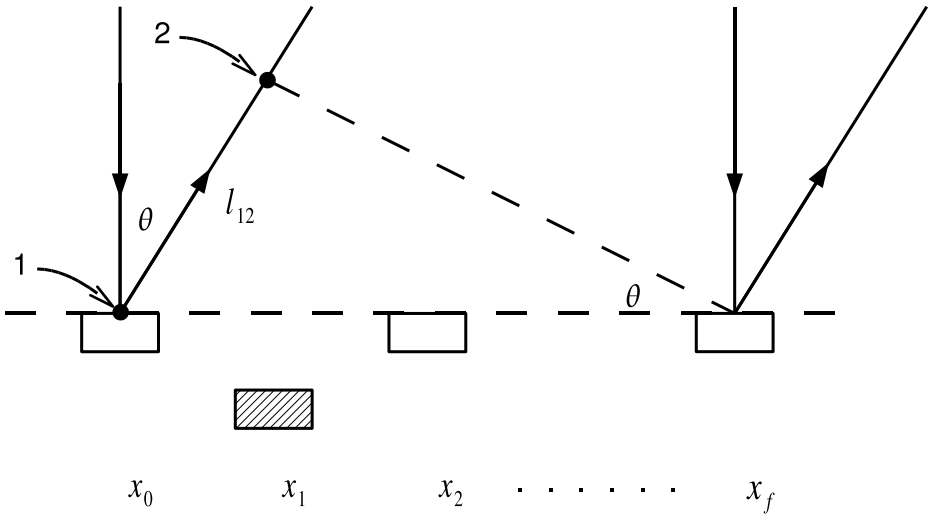

(a) fixed cantilever

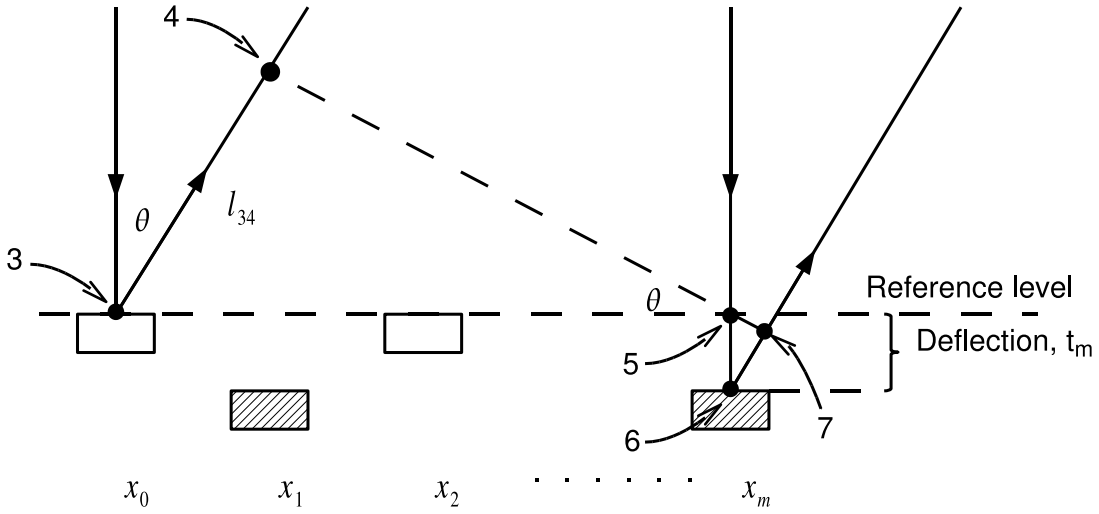

(b) moving cantilever

Figure 5.2: Optical path length differences of (a) fixed cantilever at x_f and (b) moving cantilever at x_m.

By substituting Equations (5.2) and (5.10) in (5.1), the complete expression for the far-field wave E_{far} can be obtained. The optical intensity in the far-field I_{far} is given by

$$I_{\text{far}} = E_{\text{far}} \cdot E_{\text{far}}^{*} \tag{5.11}$$

where * denotes the complex conjugate. Using Equation (5.1) this becomes

$$I_{\text{far}} = E_s^2 (F \cdot F^{*}) \tag{5.12}$$

FF^{*} can be derived using Equation (5.10)

$$\begin{aligned} FF^{*} = A & \left[\sum_{\substack{f \text{ even} \\ f=0}}^{2N-2} \mathrm{e}^{jkx_f \sin\theta} \quad + \quad \sum_{\substack{m \text{ odd} \\ m=1}}^{2N-1} \mathrm{e}^{jk\{x_m \sin\theta - t_m(1+\cos\theta)\}} \right] \\ & \times A \left[\sum_{\substack{f' \text{ even} \\ f'=0}}^{2N-2} \mathrm{e}^{-jkx_{f'} \sin\theta} \quad + \quad \sum_{\substack{m' \text{ odd} \\ m'=1}}^{2N-1} \mathrm{e}^{-jk\{x_{m'} \sin\theta - t_{m'}(1+\cos\theta)\}} \right] \end{aligned} \tag{5.13}$$

$$\begin{aligned} \propto & \left[\sum_{\substack{f \text{ even} \\ f=0}}^{2N-2} \sum_{\substack{f' \text{ even} \\ f'=0}}^{2N-2} \mathrm{e}^{jk(x_f - x_{f'}) \sin\theta} + \sum_{\substack{f \text{ even} \\ f=0}}^{2N-2} \sum_{\substack{m' \text{ odd} \\ m'=1}}^{2N-1} \mathrm{e}^{jk(x_f - x_{m'}) \sin\theta} \, \mathrm{e}^{jkt_{m'}(1+\cos\theta)} \right. \\ & + \sum_{\substack{m \text{ odd} \\ m=1}}^{2N-1} \sum_{\substack{f' \text{ even} \\ f'=0}}^{2N-2} \mathrm{e}^{jk(x_m - x_{f'}) \sin\theta} \, \mathrm{e}^{-jkt_m(1+\cos\theta)} \\ & \left. + \sum_{\substack{m \text{ odd} \\ m=1}}^{2N-1} \sum_{\substack{m' \text{ odd} \\ m'=1}}^{2N-1} \mathrm{e}^{jk(x_m - x_{m'}) \sin\theta} \, \mathrm{e}^{-jk(t_m - t_{m'})(1+\cos\theta)} \right] \end{aligned} \tag{5.14}$$

In a regular array, the cantilevers are equally spaced at intervals a. Further, the deflection of all moving cantilevers are equal, $t_m = t$ for every m. Then, Equa-

tion (5.14) can be written as

$$FF^* \propto \left[\sum_{\substack{f \text{ even} \\ f=0}}^{2N-2} \sum_{\substack{f' \text{ even} \\ f'=0}}^{2N-2} \mathrm{e}^{jk(f-f')a\sin\theta} + \mathrm{e}^{jkt(1+\cos\theta)} \sum_{\substack{f \text{ even} \\ f=0}}^{2N-2} \sum_{\substack{m \text{ odd} \\ m=1}}^{2N-1} \mathrm{e}^{jk(f-m)a\sin\theta} \right.$$
$$\left. + \mathrm{e}^{-jkt(1+\cos\theta)} \sum_{\substack{m \text{ odd} \\ m=1}}^{2N-1} \sum_{\substack{f \text{ even} \\ f=0}}^{2N-2} \mathrm{e}^{jk(m-f)a\sin\theta} + \sum_{\substack{m \text{ odd} \\ m=1}}^{2N-1} \sum_{\substack{m' \text{ odd} \\ m'=1}}^{2N-1} \mathrm{e}^{jk(m-m')a\sin\theta} \right] \tag{5.15}$$

This expression can be simplified to give

$$FF^* \propto \frac{\sin^2(Nka\sin\theta)}{\sin^2(ka\sin\theta)} \cdot \cos^2\left(\frac{ka\sin\theta - kt(1+\cos\theta)}{2}\right) \tag{5.16}$$

From Equations (5.2), (5.12) and (5.16) the optical intensity can be obtained

$$I_{\text{far}} \propto \operatorname{sinc}^2\left(\frac{kb\sin\theta}{2}\right) \cdot \frac{\sin^2(Nka\sin\theta)}{\sin^2(ka\sin\theta)} \cdot \cos^2\left(\frac{ka\sin\theta - kt(1+\cos\theta)}{2}\right) \tag{5.17}$$

Equation (5.17) is consistent with the expression derived for lamella gratings in [4]. It is evident from this expression that the intensity pattern is dependent on the deflection t.

For any diffraction angle θ, the value of the $\cos^2$ term of Equation (5.17) depends on the deflection t. Plots of cosine and $\cos^2$ functions are given in Figure 5.3. It can be seen that the $\cos^2$ curve is cyclic with a period π. However, distinct values of $\cos^2$ are observed only within a range of $\pi/2$ radians. Thus distinct intensity values are observed only within this range. A wavelength λ corresponds to 2π radians. Therefore, the range of deflections giving distinct intensity values is limited to $\lambda/4$. This is a fundamental limitation of interferometric measurement methods.

Changes in the far-field intensity pattern with deflection are illustrated in Figure 5.4. An array of 7 cantilevers was used in this calculation, with 3 of them moving and the rest stationary. Each cantilever was 2 μm wide, and the center-to-center distance

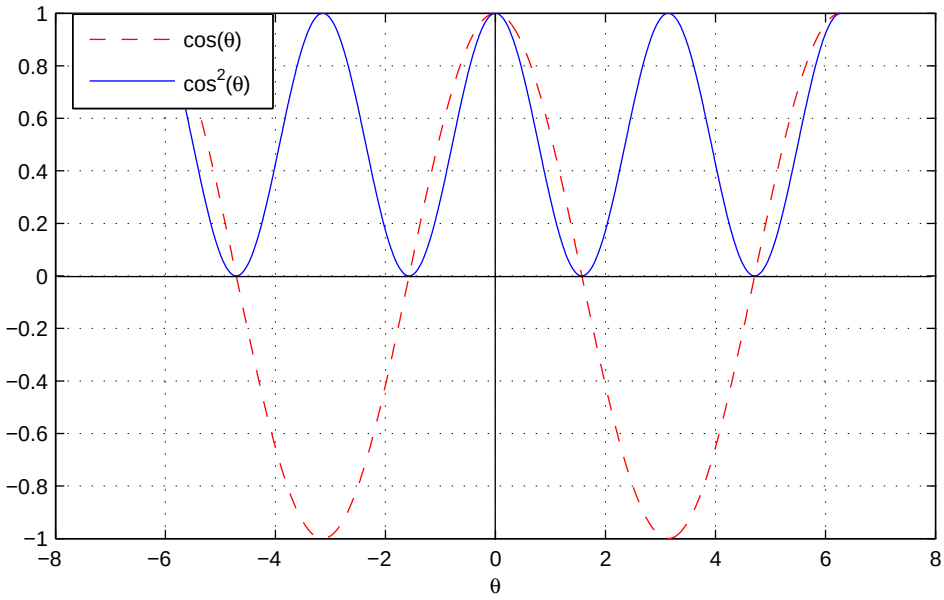

Figure 5.3: Plots of $\cos\theta$ and $\cos^2\theta$.

between them was 4 μm, giving a spatial frequency of $f_g = 2.5 \times 10^5$ m^{-1} for the grating. A diode laser having a wavelength of 650 nm was considered as the optical source. The intensity pattern at zero deflection is shown in Figure 5.4(a), while 5.4(b) shows the intensity pattern when the deflection is $\lambda/4 = 162.5$ nm. This figure is consistent with Figure (5) of [2].

In interferometric arrangements of interdigital cantilevers such as in [1, 7, 8, 9], the intensities of one or more diffraction orders are measured, and the deflection is interpreted from these measurements. Figure 5.5 plots the calculated variations of the intensities of the 0^{th} and 1^{st} orders of the diffraction pattern with cantilever deflection. This figure is consistent with Figure (10) of [2]. There is a direct relationship between the optical intensity of a diffraction order and the deflection. This is the basis of interdigital interferometric measurement systems.

It can be seen from Figure 5.5 that the intensity variations are cyclic over 325 nm, which corresponds to $\lambda/2$. It can also be noted that distinct intensity values are observable only within a deflection range of 162.5 nm, as predicted earlier. This figure

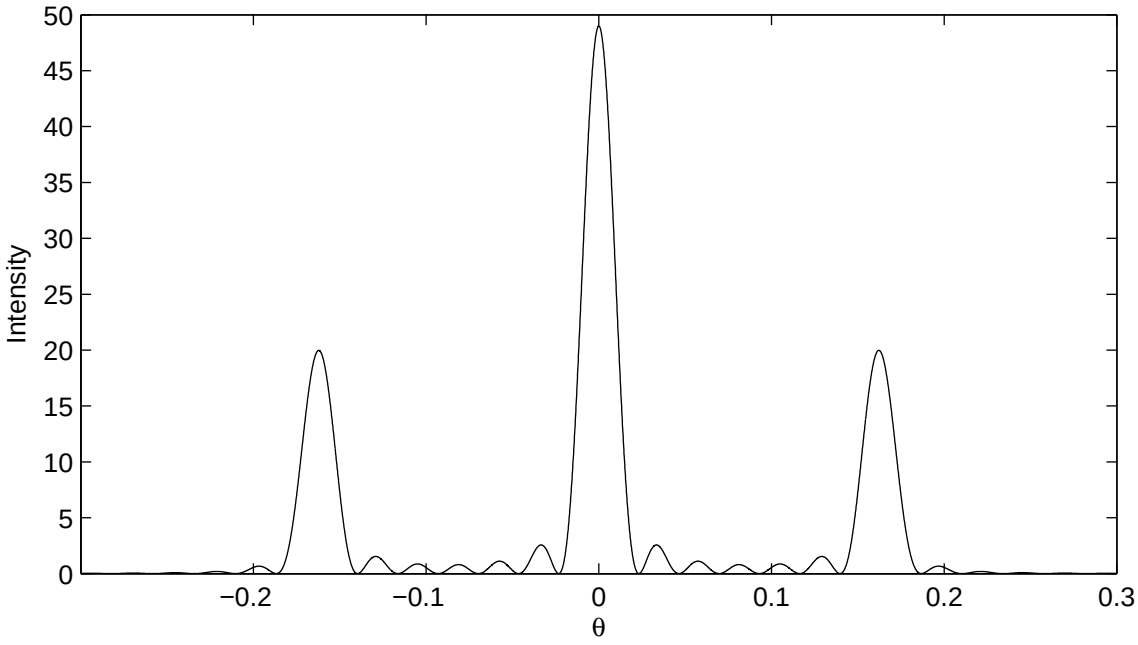

(a) $t = 0$

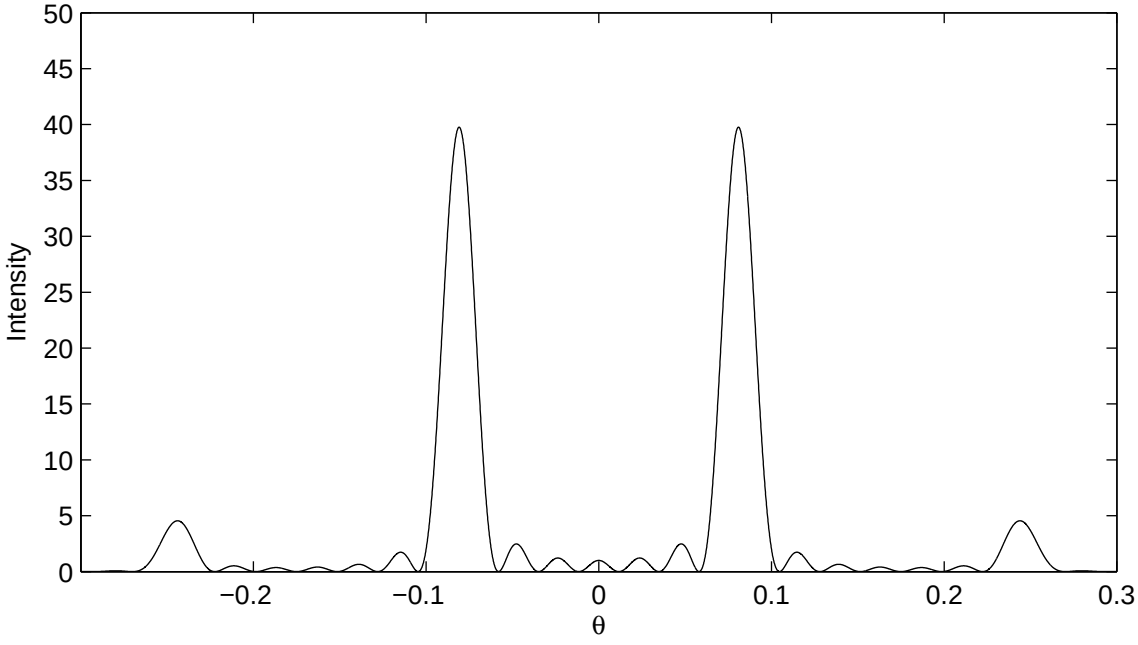

(b) $t = \lambda/4$

Figure 5.4: Intensity pattern at (a) zero deflection and (b) deflection = $\lambda/4$. The array has 3 moving and 4 fixed cantilevers, each 2 μm wide, and the spatial frequency of the grating is $f_g = 5 \times 10^5$ m^{-1}.

highlights the limitation of the measurement range of an interferometric cantilever array.

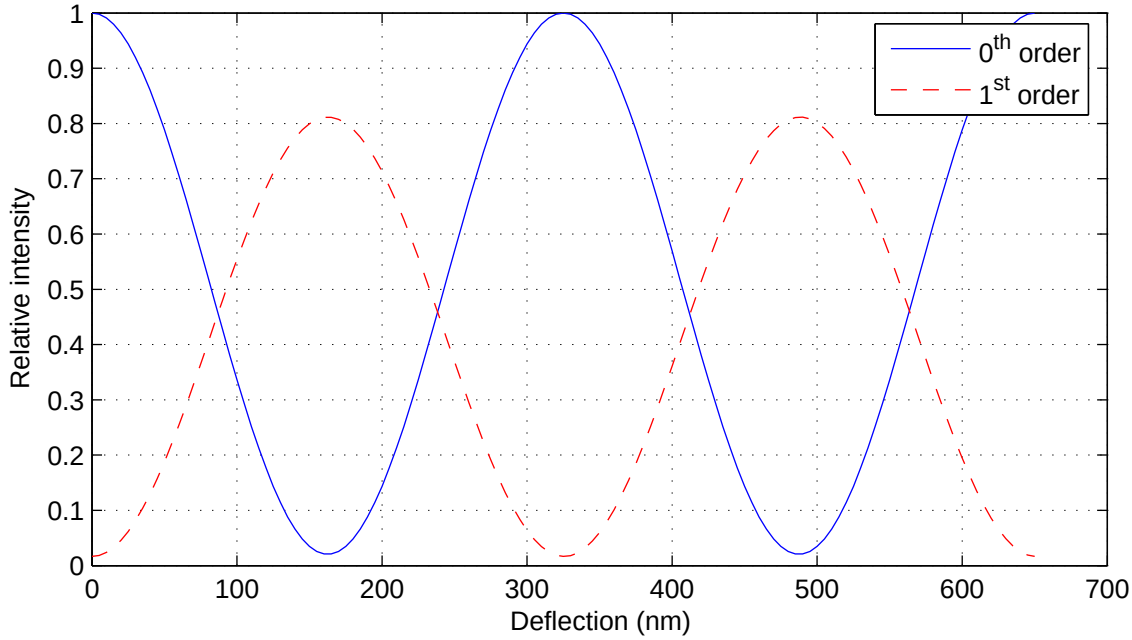

Figure 5.5: Variations of intensities of the 0^{th} and 1^{st} diffraction orders with deflection.

5.3 Alternate representation

Deeper insight into the problem can be obtained by rearranging the expression of the intensity pattern given by Equation (5.14). The first summation term of Equation (5.14) gives the interference effect of waves reflected off fixed cantilevers:

$$
\begin{aligned}
S_{\text{ff}} &= \sum_{\substack{f \text{ even} \\ f=0}}^{2N-2} \sum_{\substack{f' \text{ even} \\ f'=0}}^{2N-2} \mathrm{e}^{jk(x_f - x_{f'})\sin\theta} \\
&= \sum_{\substack{f \text{ even} \\ f=0}}^{2N-2} \sum_{f'=f} \mathrm{e}^{jk(x_f - x_{f'})\sin\theta} + \sum_{\substack{f \text{ even} \\ f=0}}^{2N-2} \sum_{\substack{f' \neq f \\ f' \text{ even} \\ f=0}}^{2N-2} \mathrm{e}^{jk(x_f - x_{f'})\sin\theta}
\end{aligned}
$$

This expression simplifies to

$$S_{\text{ff}} = N + 2 \sum_{\substack{f \text{ even} \\ f=2}}^{2N-2} \sum_{\substack{f' \text{ even} \\ f'<f}}^{2N-4} \cos\left\{k(x_f - x_{f'}) \sin\theta\right\}$$

Substituting $k = 2\pi/\lambda$, this becomes

$$S_{\text{ff}} = N + 2 \sum_{\substack{f \text{ even} \\ f=2}}^{2N-2} \sum_{\substack{f' \text{ even} \\ f'<f}}^{2N-4} \cos\left\{2\pi \cdot \left(\frac{x_f - x_{f'}}{\lambda}\right) \cdot \sin\theta\right\} \tag{5.18}$$

The second and third summations of Equation (5.14) give the interference effect of waves reflected off the fixed cantilevers and the moving cantilevers:

$$\begin{aligned} S_{\text{fm}} &= \sum_{\substack{f \text{ even} \\ f=0}}^{2N-2} \sum_{\substack{m \text{ odd} \\ m=1}}^{2N-1} \mathrm{e}^{jk(x_f - x_m)\sin\theta}\, \mathrm{e}^{jkt_m(1+\cos\theta)} \\ &\quad + \sum_{\substack{m \text{ odd} \\ m=1}}^{2N-1} \sum_{\substack{f \text{ even} \\ f=0}}^{2N-2} \mathrm{e}^{jk(x_m - x_f)\sin\theta}\, \mathrm{e}^{-jkt_m(1+\cos\theta)} \\ &= 2 \sum_{\substack{f \text{ even} \\ f=0}}^{2N-2} \sum_{\substack{m \text{ odd} \\ m=1}}^{2N-1} \cos\left\{k(x_f - x_m)\sin\theta + kt_m(1+\cos\theta)\right\} \\ &= 2 \sum_{\substack{f \text{ even} \\ f=0}}^{2N-2} \sum_{\substack{m \text{ odd} \\ m=1}}^{2N-1} \cos\left\{2\pi \cdot \left(\frac{x_f - x_m}{\lambda}\right) \cdot \sin\theta + 2\pi \cdot t_m \cdot \left(\frac{1+\cos\theta}{\lambda}\right)\right\} \end{aligned} \tag{5.19}$$

The final summation of Equation (5.14) gives the interference effect of waves reflected off the moving cantilevers:

$$\begin{aligned} S_{\text{mm}} &= \sum_{\substack{m \text{ odd} \\ m=1}}^{2N-1} \sum_{\substack{m' \text{ odd} \\ m'=1}}^{2N-1} \mathrm{e}^{jk(x_m - x_{m'})\sin\theta}\, \mathrm{e}^{-jk(t_m - t_{m'})(1+\cos\theta)} \\ &= N + 2 \sum_{\substack{m \text{ odd} \\ m=3}}^{2N-1} \sum_{\substack{m' \text{ odd} \\ m'<m}}^{2N-3} \cos\left\{k(x_m - x_{m'})\sin\theta - k(t_m - t_{m'})(1+\cos\theta)\right\} \\ &= N + 2 \sum_{\substack{m \text{ odd} \\ m=3}}^{2N-1} \sum_{\substack{m' \text{ odd} \\ m'<m}}^{2N-3} \cos\left\{2\pi \cdot \left(\frac{x_m - x_{m'}}{\lambda}\right) \cdot \sin\theta - 2\pi(t_m - t_{m'}) \left(\frac{1+\cos\theta}{\lambda}\right)\right\} \end{aligned} \tag{5.20}$$

Each of the cosines in Equations (5.18)–(5.20) can be viewed as spatial harmonic functions of the form $\cos(2\pi\nu x + \phi)$, with the spatial frequency ν being given by terms of the form $(x_p - x_q)/\lambda$. Then the phase terms of the cosines generated by S_{fm} and S_{mm} are given by $2\pi t_m(1+\cos\theta)/\lambda$ and $-2\pi(t_m - t_{m'})(1+\cos\theta)/\lambda$ respectively.

The far-field interference pattern is then given by $FF^* = S_{\text{ff}} + S_{\text{fm}} + S_{\text{mm}}$. It can therefore be seen that the far-field intensity pattern of an array of cantilevers can be expressed as the sum of a series of spatial harmonic functions, which define the spatial characteristics of the intensity pattern. Recall that x_f and x_m denote the locations of fixed and moving cantilevers respectively. Thus the frequencies of the spatial harmonic functions are determined by the distances between each cantilever of the array. The phase terms are determined by the deflections of the cantilevers.

5.4 Measuring the deflection using phase angles

Consider again an array of cantilevers placed at regular intervals a, and each moving cantilever having the same deflection t. Then, S_{ff}, S_{fm} and S_{mm} can be written as

$$S_{\text{ff}} = N + 2\sum_{\substack{f \text{ even} \\ f=2}}^{2N-2}\sum_{\substack{f' \text{ even} \\ f'<f}}^{2N-4} \cos\left\{2\pi\cdot\left(\frac{f-f'}{\lambda}\right)a\cdot\sin\theta\right\} \tag{5.21}$$

$$S_{\text{fm}} = 2\sum_{\substack{f \text{ even} \\ f=0}}^{2N-2}\sum_{\substack{m \text{ odd} \\ m=1}}^{2N-1} \cos\left\{2\pi\cdot\left(\frac{f-m}{\lambda}\right)a\cdot\sin\theta + 2\pi t\left(\frac{1+\cos\theta}{\lambda}\right)\right\} \tag{5.22}$$

$$S_{\text{mm}} = N + 2\sum_{\substack{m \text{ odd} \\ m=3}}^{2N-1}\sum_{\substack{m' \text{ odd} \\ m'<m}}^{2N-3} \cos\left\{2\pi\cdot\left(\frac{m-m'}{\lambda}\right)a\cdot\sin\theta\right\} \tag{5.23}$$

where f and m are real numbers which determine the locations of the fixed and moving cantilevers respectively. The phase term of S_{mm} is zero since $t_m = t_{m'} = t$. Referring to Equation (5.22), it can be seen that when the deflection t is an integer multiple of $\lambda/(1+\cos\theta)$, the phase terms of the harmonic functions are zero. Thus, the harmonic functions of S_{fm} are cyclic with deflection over a range

$\lambda/(1+\cos\theta)$. The minimum of this expression is obtained when $\theta = 0$, giving the harmonic functions of S_{fm} a period of $\lambda/2$.

Therefore, instead of measuring the intensities of the diffraction orders, if the phase terms of the harmonic functions of Equation (5.22) can be determined, the deflections can be measured up to a limit of $\lambda/2$. Let the phase term of a spatial cosine function of Equation (5.22) be denoted by ϕ

$$\phi = 2\pi t \left(\frac{1+\cos\theta}{\lambda}\right)$$

Then, assuming the diffraction angle θ to be small, $\cos\theta \approx 1$, and the deflection can be calculated using the measured phase from

$$t \approx \frac{\phi\lambda}{4\pi} \tag{5.24}$$

Since the range of unique phases is $0 \leq \phi \leq 2\pi$, the range of measurable deflections is $0 \leq t \leq \lambda/2$. This is a two-fold increase of the measurement range compared with the intensity-based interferometric methods.

It was shown above that the far-field intensity pattern is a composite of harmonic functions. If the Fourier transform of the intensity pattern is taken, it will be possible to determine the phase terms of all the harmonic functions. The method of extracting these phase terms from the FT of the far-field intensity pattern is investigated in the following section.

Suppose there are 5 fixed cantilevers and 5 moving cantilevers in the regular array. The fixed cantilevers will be at locations 0, $2a$, $4a$, $6a$ and $8a$, giving $f = 0$, 2, 4, 6 and 8. Similarly, the values of m will be 1, 3, 5, 7 and 9. Then the frequencies of the harmonic functions generated by S_{ff}, S_{fm} and S_{mm} can be obtained using Equations (5.21)–(5.23). Tables 5.1(a)–(c) show all the possible values of $(f-f)$, $(f-m)$ and $(m-m)$.

Referring to Equations (5.21) and (5.23), and Tables 5.1(a) and 5.1(c), it can be seen that the harmonic functions generated by S_{ff} and S_{mm} will have spatial frequencies

Table 5.1: Values of $(f - f)$, $(f - m)$ and $(m - m)$ for a regular array.

(a) All possible $(f - f)$ values

f \ f	0	2	4	6	8
0	–	2	4	6	8
2	–	–	2	4	6
4	–	–	–	2	4
6	–	–	–	–	2
8	–	–	–	–	–

(b) All possible $(f - m)$ values

m \ f	0	2	4	6	8
1	-1	1	3	5	7
3	-3	-1	1	3	5
5	-5	-3	-1	1	3
7	-7	-5	-3	-1	1
9	-9	-7	-5	-3	-1

(c) All possible $(m - m)$ values

m \ m	1	3	5	7	9
1	–	2	4	6	8
3	–	–	2	4	6
5	–	–	–	2	4
7	–	–	–	–	2
9	–	–	–	–	–

of $2a/\lambda$, $4a/\lambda$, $6a/\lambda$ and $8a/\lambda$. None of these spatial cosines have a phase term. The spatial frequencies of the harmonic functions of S_{fm} can be determined from Table 5.1(b).

When $(f-m) > 0$, the spatial cosine will take the form $\cos\left\{2\pi(f-m)(a/\lambda)\sin\theta + 2\pi t(1+\cos\theta)/\lambda\right\}$, while when $(f - m) < 0$ the spatial cosines will have the form $\cos\left\{2\pi(f - m)(a/\lambda)\sin\theta - 2\pi t(1+\cos\theta)/\lambda\right\}$. Thus, S_{fm} will consist of spatial harmonic functions having frequencies of a/λ, $3a/\lambda$, $5a/\lambda$, $7a/\lambda$ and $9a/\lambda$, each

having a phase term $\pm 2\pi t(1+\cos\theta)/\lambda$. It can be noted that the spatial frequencies of the cosines of S_{fm} are distinct from the spatial frequencies of the harmonic functions of S_{ff} and S_{mm}. Thus, the far-field intensity pattern will be a composition of 5 spatial harmonic functions containing phase terms corresponding to the deflection, and 4 other spatial harmonic functions with no phase terms.

Now, referring to Table 5.1(b) again, it can be seen that there are 9 instances of $|f-m|=1$, and hence there will be 9 cosines with spatial frequency a/λ. Four of these will have a phase of $\phi = 2\pi t(1+\cos\theta)/\lambda$ and the other 5 will have a phase of $\phi = -2\pi t(1+\cos\theta)/\lambda$. These 9 cosines will result in a single spatial harmonic function of frequency a/λ, and its resultant phase can be calculated using standard phasor analysis techniques as described below. Similarly, the other spatial harmonic functions of S_{fm} will be composites of several cosines.

For generality, let there be A harmonic functions of frequency ν having a positive phase ϕ and B harmonic functions of the same frequency having a negative phase $-\phi$. Then the resultant harmonic function y is given by

$$y = A\cos(\nu+\phi) + B\cos(\nu-\phi)$$

In complex notation this becomes

$$\begin{aligned} Y &= A\,\mathrm{e}^{j(\nu+\phi)} + B\,\mathrm{e}^{j(\nu-\phi)} \\ &= \mathrm{e}^{j\nu}\left(A\,\mathrm{e}^{j\phi} + B\,\mathrm{e}^{-j\phi}\right) \end{aligned}$$

The resultant phase Ψ is given by the argument of this complex number

$$\Psi = \tan^{-1}\left[\frac{(A-B)}{(A+B)}\tan\phi\right] \tag{5.25}$$

In the example considered above, where $A=4$ and $B=5$, the phase of the composite spatial harmonic function having a frequency of a/λ will be $\Psi = \tan^{-1}[(-\tan\phi)/9]$.

Referring to Table 5.1(b) and Equation (5.25), it can be noted that the phase terms of the cosines of S_{fm} get cancelled out if the number of fixed cantilevers is greater by one than the number of moving cantilevers.

Thus, the far-field intensity pattern will consist of 9 spatial harmonic functions. Those having frequencies of $2a/\lambda$, $4a/\lambda$, $6a/\lambda$ and $8a/\lambda$ will have a zero phase. The spatial harmonic functions having frequencies of a/λ, $3a/\lambda$, $5a/\lambda$, $7a/\lambda$ and $9a/\lambda$ will be composites of several constituent harmonic functions of the same frequencies, and their resultant phases will be given by Equation (5.25).

The phase spectrum of the Fourier transform of the intensity pattern will give the resultant phase Ψ given by Equation (5.25). To calculate deflection, the constituent phase $\phi = 2\pi t(1 + \cos\theta)/\lambda$ needs to be determined. The constituent phase ϕ can be extracted from the composite phase Ψ using Equation (5.25)

$$\phi = \tan^{-1}\left[\frac{(A+B)}{(A-B)}\tan\Psi\right] \tag{5.26}$$

The deflection can then be calculated from Equation (5.24). The formulas to extract the constituent phase ϕ from the phases of the harmonic functions having spatial frequencies of a/λ, $3a/\lambda$, $5a/\lambda$, $7a/\lambda$ and $9a/\lambda$ obtained from the FT are presented in Table 5.2. Since there is only one harmonic function with a spatial frequency of $9a/\lambda$, the phase ϕ can be directly obtained from the Fourier transform.

Table 5.2: Phase terms of the cosines of S_{fm}.

Spatial frequency	No. of $+\phi$ terms	No. of $-\phi$ terms	Phase
a/λ	4	5	$\tan^{-1}(-9\tan\Psi_1)$
$3a/\lambda$	3	4	$\tan^{-1}(-7\tan\Psi_3)$
$5a/\lambda$	2	3	$\tan^{-1}(-5\tan\Psi_5)$
$7a/\lambda$	1	2	$\tan^{-1}(-3\tan\Psi_7)$
$9a/\lambda$	0	1	$-kt(1+\cos\theta)$

The inverse tangent function provides angles in the range $\pm\pi/2$. Therefore, even though the composite phase angles Ψ obtained from the phase spectrum of the FT will have values between $\pm\pi$, the constituent phase terms ϕ calculated using the

formulas of Table 5.2 will be between $\pm\pi/2$. Thus, the phases of the harmonic functions having spatial frequencies of a/λ, $3a/\lambda$, $5a/\lambda$ and $7a/\lambda$ will only allow measurement of deflections up to $\lambda/4$. The phase of the cosine having a spatial frequency of $9a/\lambda$ can be used to measure deflections up to $\lambda/2$.

Now, the method of obtaining the composite phases Ψ using the Fourier transformation of the far-field intensity pattern is investigated. The mathematical expression for the intensity pattern is given by Equation (5.12). Thus the FT of the intensity pattern is

$$\mathscr{F}[I_{\text{far}}] = \mathscr{F}[E_{\text{s}}^2 \cdot FF^*] \tag{5.27}$$

$$= \mathscr{F}[E_{\text{s}}^2] \otimes \mathscr{F}[FF^*] \tag{5.28}$$

where $\otimes$ denotes convolution. The Fourier transform of sinc^2, from the expression for E_{s}^2 given by Equation (5.2), is a triangular pulse. The far-field interference pattern FF^* was shown to be a sum of spatial harmonic functions. The Fourier transform of these cosines is a series of impulses. The convolution of a triangular pulse and a series of impulses will yield a series of triangular pulses. It should be noted that the Fourier transform of sinc^2, an evenly symmetric function, is a real valued function, and hence does not alter the phase of the spectrum.

It was shown earlier that the far-field interference pattern generated by the example cantilever array will consist of 9 spatial harmonic functions. Thus, the amplitude spectrum of the Fourier transform of this intensity pattern will consist of 9 triangular pulses. The 1^{st}, 3^{rd}, 5^{th}, 7^{th} and 9^{th} of these pulses will be due to the spatial harmonic functions generated by S_{fm}. The phase terms corresponding to these peaks will give the composite phases Ψ. From these phase terms, the deflection t can be calculated as determined above.

5.4.1 Verification of the analysis

The above analysis can be verified using a simulation of the example array of cantilevers which has 5 fixed and 5 moving cantilevers. Figure 5.6(a) shows the intensity

pattern for the cantilever array when the deflection $t = 0$, and Figure 5.6(b) shows the amplitude spectrum of its Fourier transform. Recalling that the amplitude spectrum of a Fourier transform is symmetric about the y-axis and that the central peak corresponds to the DC value, Figure 5.6(b) clearly shows the 9 different spatial frequency components on either side of the DC value. The 1^{st}, 3^{rd}, 5^{th}, 7^{th} and 9^{th} peaks on either side of the central peak correspond to cosines having spatial frequencies of a/λ, $3a/\lambda$, $5a/\lambda$, $7a/\lambda$ and $9a/\lambda$, as generated by S_{fm}.

Figure 5.6(c) shows the phase spectrum (argument) of the Fourier transform of the interference pattern. The phase terms corresponding to the spatial frequencies where the 1^{st}, 3^{rd}, 5^{th}, 7^{th} and 9^{th} peaks of the amplitude spectrum are observed, are all found to be zero. This is expected, since the deflection is zero.

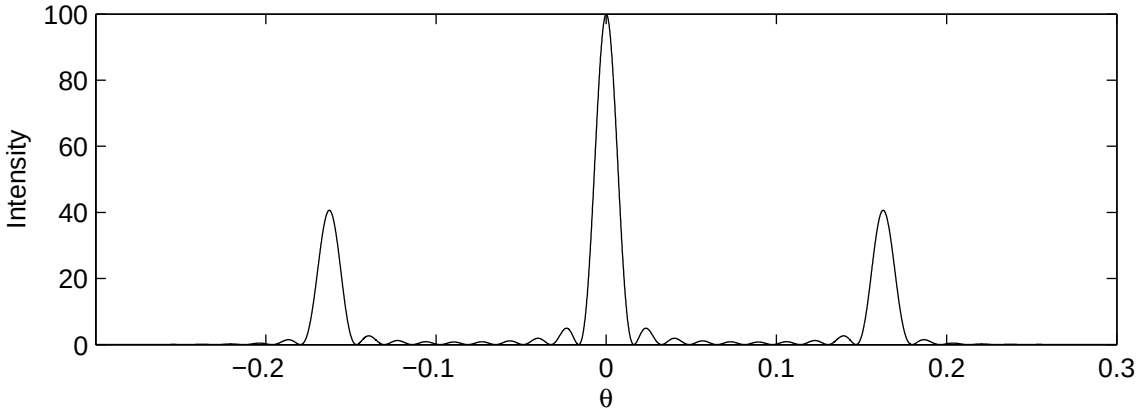

(a) Intensity pattern

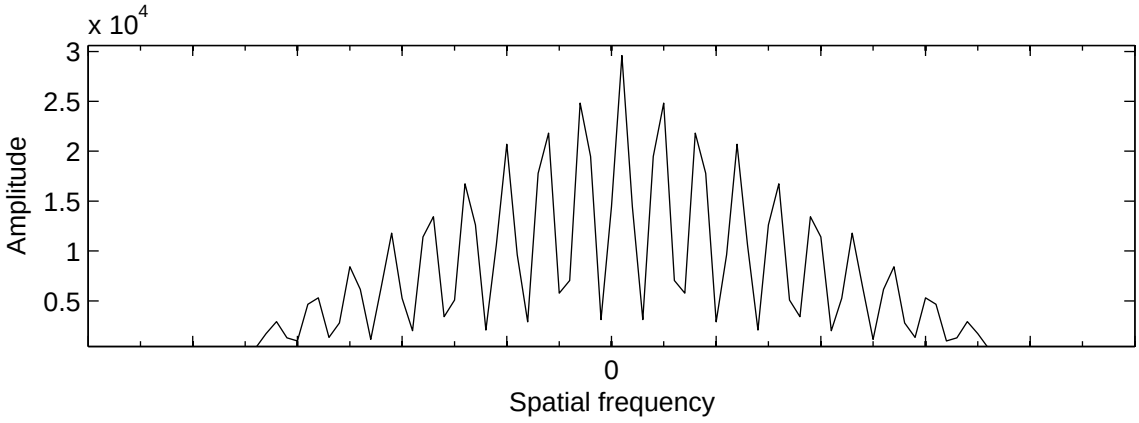

(b) Amplitude spectrum

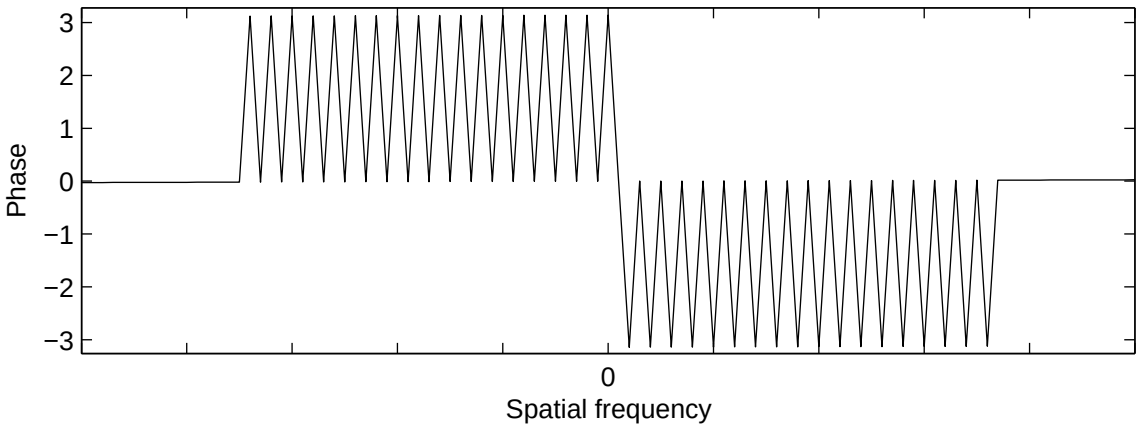

(c) Phase spectrum

Figure 5.6: (a) Intensity pattern, (b) amplitude spectrum and (c) phase spectrum of the example regular array when deflection $t = 0$.

Figure 5.7 plots the variation of the observed phases corresponding to the spatial frequencies a/λ, $3a/\lambda$, $5a/\lambda$, $7a/\lambda$ and $9a/\lambda$ as the deflection is increased from 0 nm to 650 nm. All 5 phase terms are cyclic over a deflection range of 325 nm, which is half the wavelength of the optical beam, a result that was predicted earlier. Figure 5.8 shows the variation of the constituent phase terms ϕ extracted from Figure 5.7 using the formulas of Table 5.2. It clearly shows 4 phase terms, varying between $\pm\pi/2$, being cyclic over a deflection range of 162.5 nm, or $\lambda/4$. The phase of the cosine having a spatial frequency of $9a/\lambda$ is cyclic over $\lambda/2$, and varies between $\pm\pi$. These results validate the theoretical predictions established earlier.

Therefore, deflections up to $\lambda/4$ can be measured using the phase of any one of the spatial cosines having frequencies of a/λ, $3a/\lambda$, $5a/\lambda$ and $7a/\lambda$ while deflections up to $\lambda/2$ can be measured using the spatial cosine with a frequency of $9a/\lambda$.

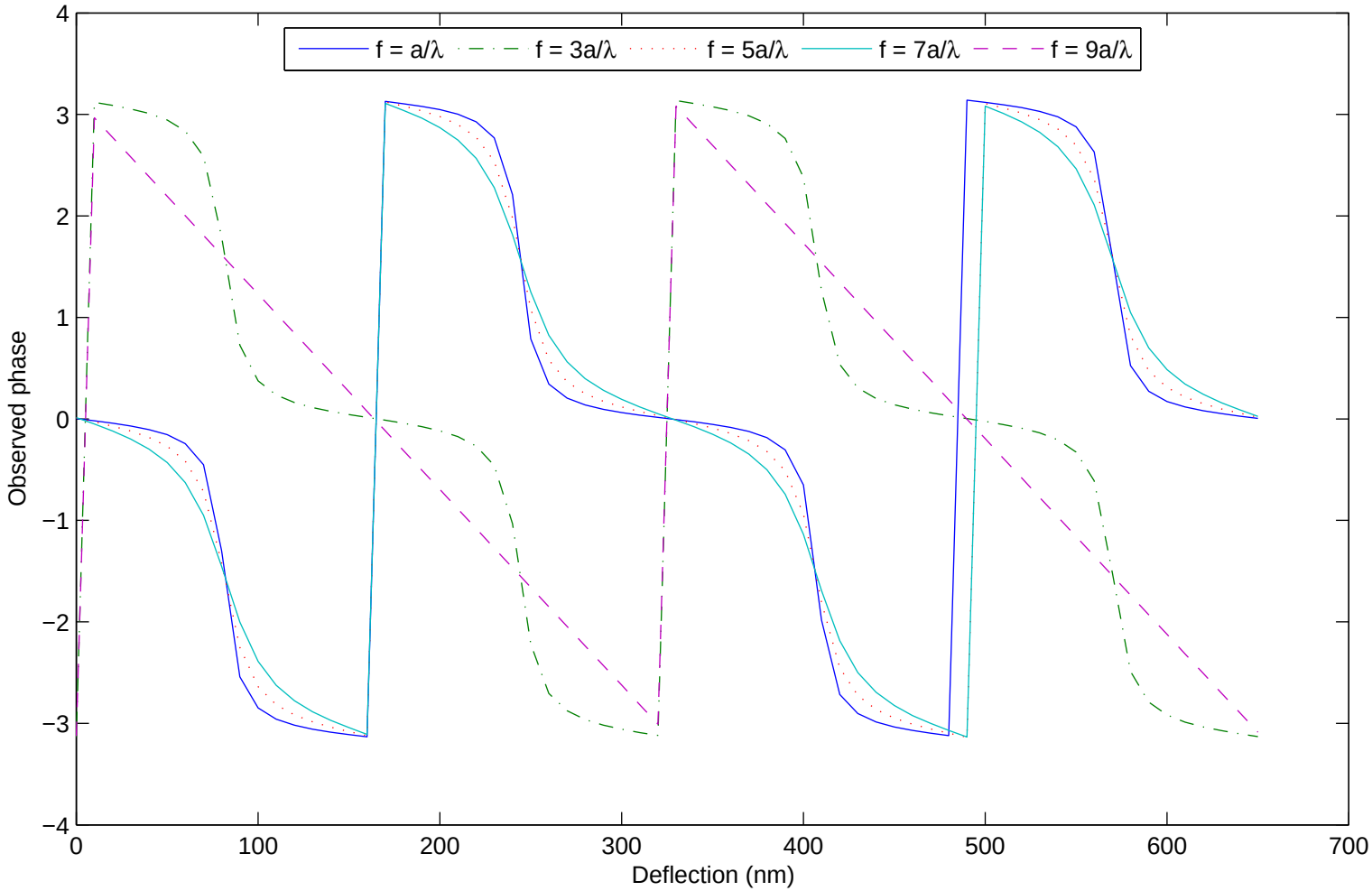

Figure 5.7: Variation of the phase terms observed from the Fourier transform of the intensity pattern of a regular array, with deflection.

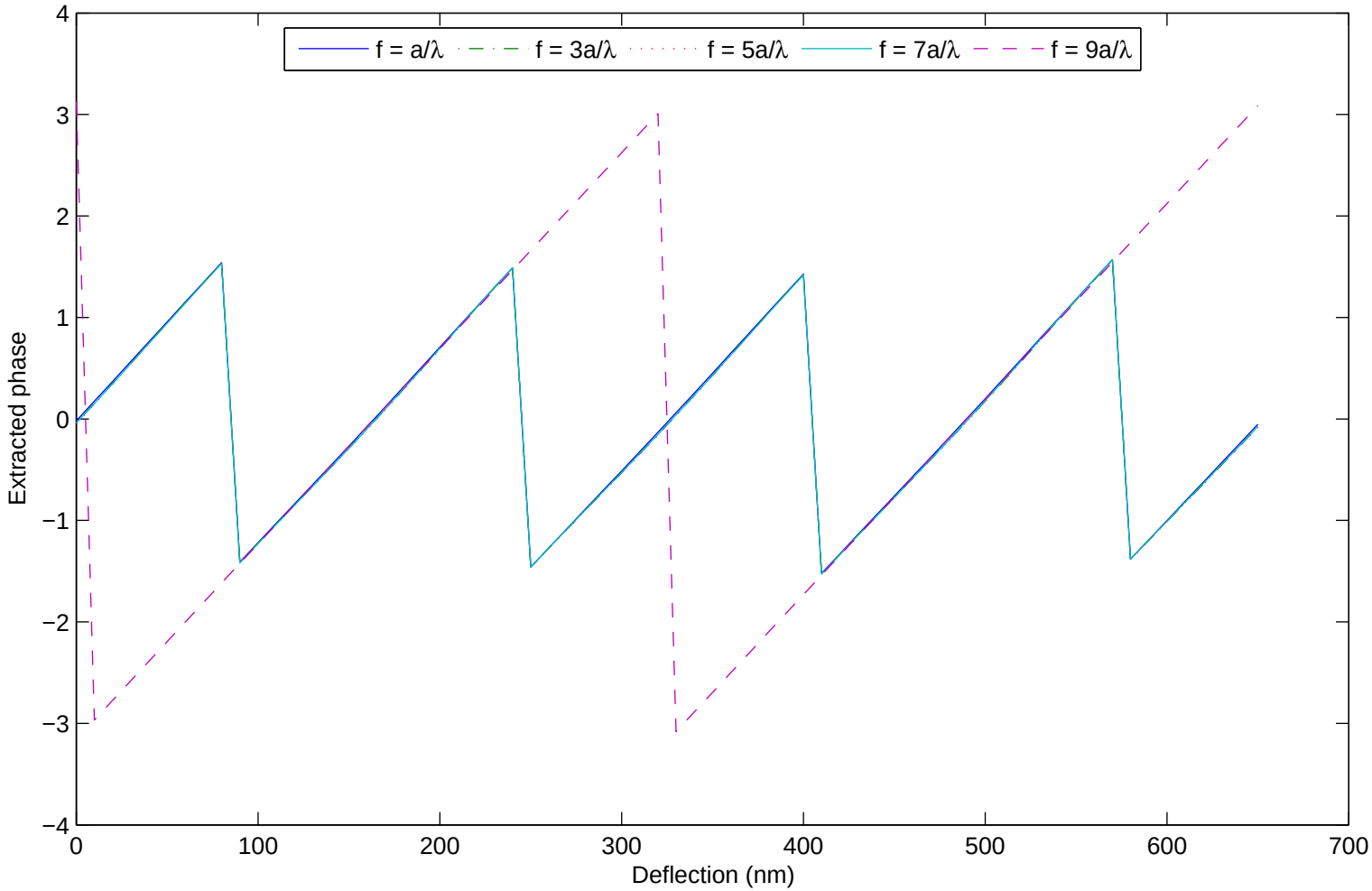

Figure 5.8: Variation of the constituent phase terms ϕ extracted from the observed phases, with deflection.

5.4.2 Enabling direct measurement of phases from the FT

It can be seen from Table 5.1(b) that since there is only a single instance of $|f-m| = 9$, there is only a single harmonic function having a spatial frequency of $9a/\lambda$, which enables its phase to be directly obtained from the Fourier transform. Now, if the values of f and m in Table 5.1 can be arranged in such a manner that there are several $(f-m)$ values appearing only once in the table, and are not obtained by any combination of $(f-f)$ or $(m-m)$, then the phases of spatial harmonic functions corresponding to those unique $(f-m)$ values can be directly obtained from the Fourier transform. Since phase calculations using tangent functions are avoided, this will result in these harmonic functions to have a period of $\lambda/2$ instead of $\lambda/4$.

One possible set of f and m values that meets this condition, and all the corresponding $(f-m)$ values are given in Table 5.3. Possible $(f-f)$ values are 3, 4, 7, 8,

Table 5.3: Values of $(f-m)$ for an irregular array

m \ f	0	3	7	11	15	19
2	-2	-1	5	9	13	17
6	-6	-3	1	5	9	13
10	-10	-7	3	1	5	9
14	-14	-11	-7	-3	1	5
18	-18	-15	-11	-7	-3	1

11, 12, 15, 16 and 19, while possible $(m-m)$ values are 4, 8, 12 and 16. Altogether, there are 19 different spatial frequencies. It is seen that 2, 6, 10, 14 and 18 appear only once in the table, and are not obtained with any other combination of $(f-f)$ or $(m-m)$ values. Thus, there is only one spatial harmonic function of each of the spatial frequencies $2a/\lambda$, $6a/\lambda$, $10a/\lambda$, $14a/\lambda$ and $18a/\lambda$. The phase terms of

these harmonic functions can be directly obtained from the Fourier transform of the far-field intensity pattern.

Referring back to the theoretical derivations, it is recalled that f and m values determine the placement of the cantilevers. The values of f and m given in Table 5.3 infer that the cantilevers of the array are no longer regularly placed. The fixed cantilevers are now placed at locations $x = 0$, $x = 3a$, $x = 7a$, $x = 11a$, $x = 15a$ and $x = 19a$, where a is some constant. The moving cantilevers are placed at $x = 2a$, $x = 6a$, $x = 10a$ $x = 14a$ and $x = 18a$. A cross-sectional view of this irregular array of cantilevers is shown in Figure 5.9.

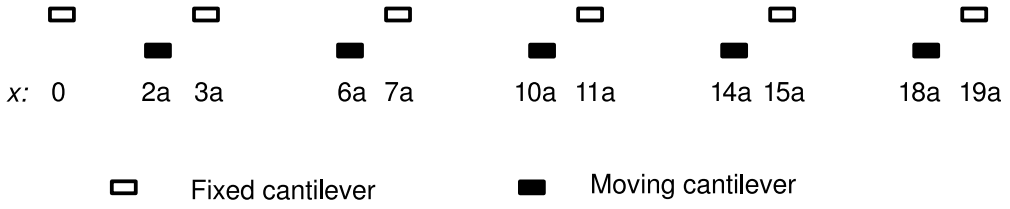

Figure 5.9: Cross-sectional view of an array of irregularly placed cantilevers.

Figure 5.10 is a plot of the variations of the observed phases of the harmonic functions having spatial frequencies of $2a/\lambda$, $6a/\lambda$, $10a/\lambda$, $14a/\lambda$ and $18a/\lambda$, with deflection, for the irregularly placed array. It is clearly seen that each phase is cyclic over a deflection range of 325 nm, corresponding to $\lambda/2$.

Thus, when using this irregular array, any of the phase terms can be used to measure deflections up to $\lambda/2$, or all of the phase terms can be used to determine the average deflection.

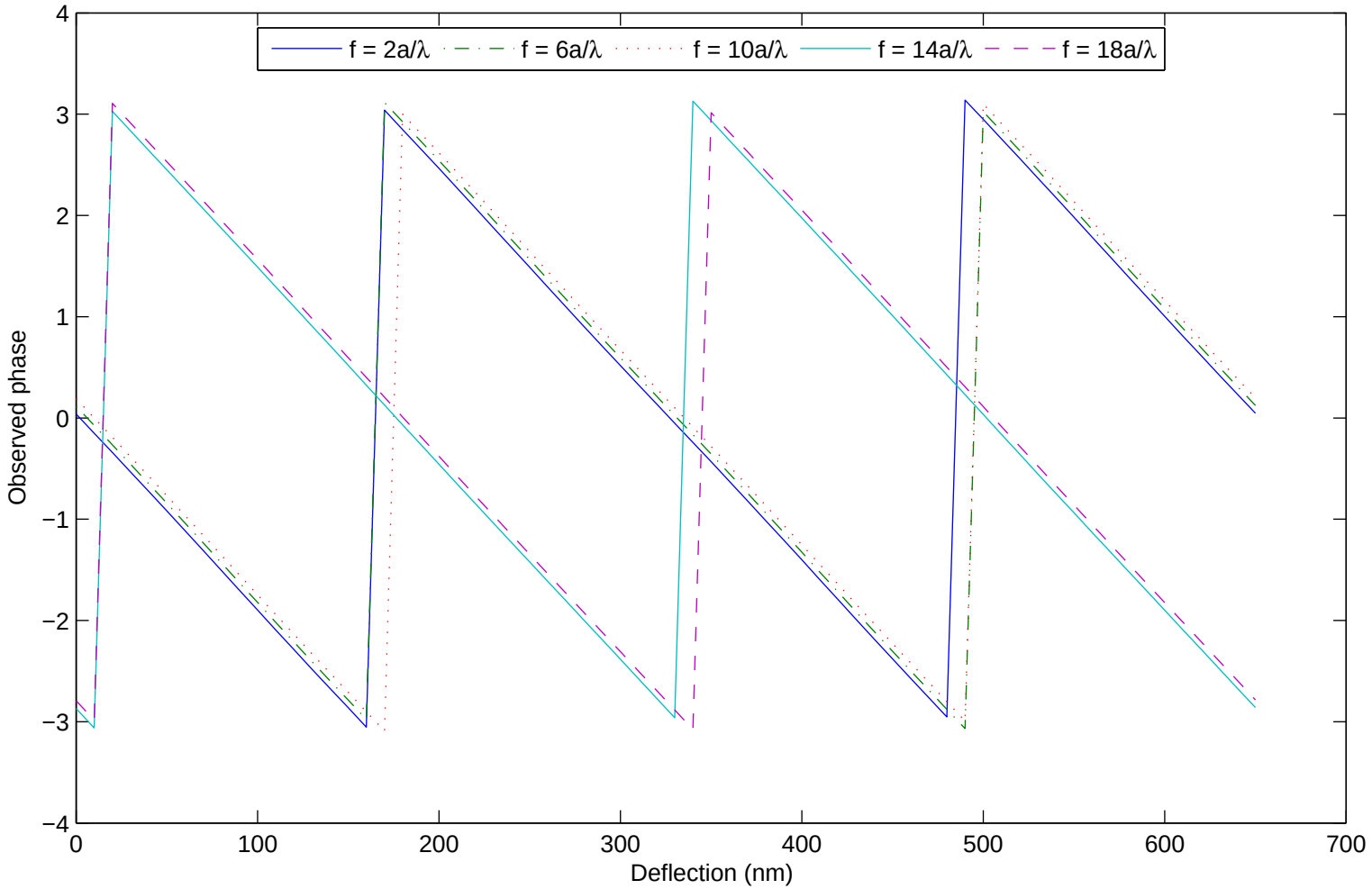

Figure 5.10: Variation of the phase terms obtained directly from the Fourier transform of the intensity pattern of an irregular array, with deflection.

5.5 Extending the measurement range beyond $\lambda/2$

It was noted in Figure 5.10 of the previous section that the phase terms of the spatial cosines having frequencies of $2a/\lambda$, $6a/\lambda$, $10a/\lambda$, $14a/\lambda$ and $18a/\lambda$ were cyclic over a deflection range of $\lambda/2$. However, suppose each spatial cosine of S_{fm} is made to have a different phase for the same deflection. Then, although the individual curves will still be cyclic over a short region, the range over which all phase terms repeat their values simultaneously is greatly enhanced. Refer Figure 5.11, which shows two phase–deflection curves. One curve is cyclic over 650 nm, while the other is cyclic over $650 \times 1.5 = 975$ nm. The 2 •'s in Figure 5.11 show two phase terms at a deflection of 175 nm. The same pair of phases is repeated only at a deflection of 2125 nm, shown by 2 ×'s in Figure 5.11, giving a range of 1950 nm, which is greater than the period of either curve. Thus if two spatial cosines can be made to have different phases for a given deflection, the measurement range can be extended further.

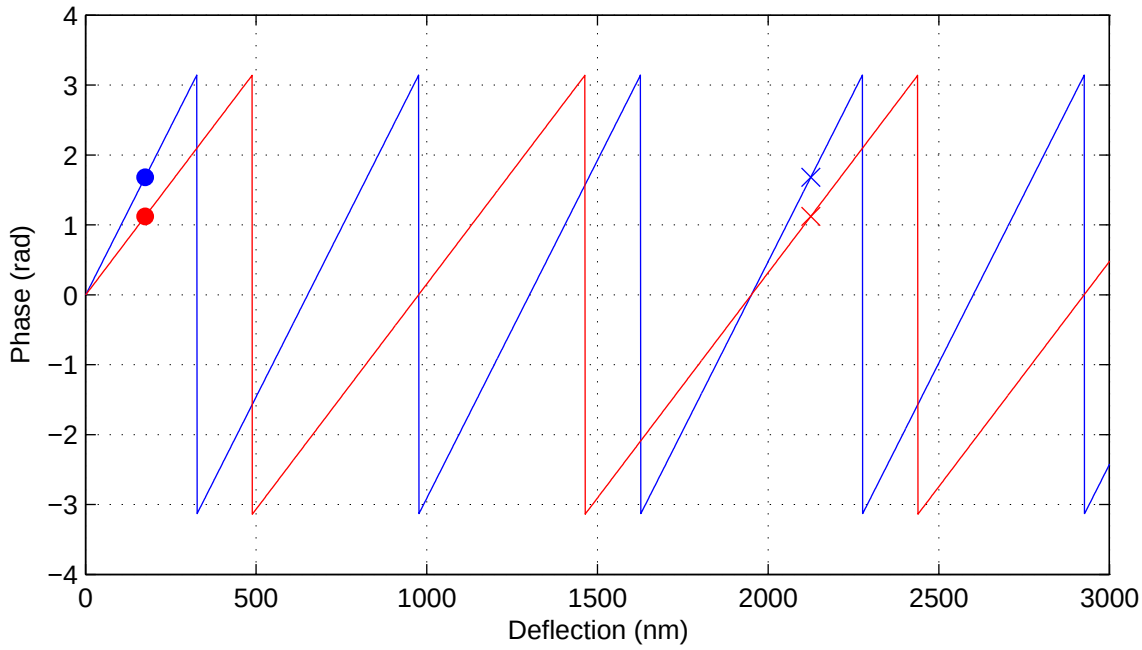

Figure 5.11: Variation of phase with deflection, for two phases having different periods.

Referring to Equation (5.22), it can be noted that the phase terms $\phi = kt(1+\cos\theta)$ of the spatial cosines are determined by the deflections t of the cantilevers. Now, if different cantilevers can be made to have different deflections for a given stimulus, the spatial cosines will have distinct phase terms. Then, if the relationships between the deflections of each cantilever is known, it will be possible to measure deflections much greater than $\lambda/2$.

Cantilevers with different deflections for the same stimulus can be achieved by making their lengths L different. However, then the free-ends of the cantilevers will no longer be aligned, preventing a proper diffraction grating from being achieved. Alternatively, the thicknesses h of the individual cantilevers can be varied. However, this significantly complicates the fabrication of the cantilever array. The use of perforated cantilevers provides an easy way of achieving an array of cantilevers with different deflections for a given stimulus. Cantilevers with identical overall dimensions and similar resonant frequencies can be made to have different deflections for a given stimulus, as demonstrated in Chapter 3.

Suppose the moving cantilevers of an irregularly spaced cantilever array are made to have different deflections for a given stimulus. Then from Equation (5.19), S_{fm} can be expressed as follows

$$S_{\text{fm}} = 2 \sum_{f \text{ fixed}} \sum_{m \text{ moving}} \cos\left\{2\pi \cdot \left(\frac{x_f - x_m}{\lambda}\right) \cdot \sin\theta + 2\pi \cdot t_m \cdot \left(\frac{1+\cos\theta}{\lambda}\right)\right\} \tag{5.29}$$

where x_f and x_m denote the locations of the fixed and moving cantilevers respectively. It can thus be seen that the deflection t_m of each cantilever gives rise to a unique phase term $\phi_m = 2\pi \cdot t_m \cdot (1+\cos\theta)/\lambda$. It can also be seen that there can be spatial harmonic functions having the same phase ϕ_m, but having different spatial frequencies depending upon the specific value of $(x_f - x_m)$. Recall that the requirement is to be able to measure all phase terms ϕ_m directly from the FT. From the earlier analysis, this requires that, for each value of m, there be at least one unique $(x_f - x_m)$ value not obtained with any other combination of $(x_f - x_f)$, $(x_m - x_m)$

or $(x_f - x_m)$.

Referring back to Table 5.3, it is seen that the f and m values used in the table meet this condition. Therefore, by placing cantilevers at locations shown in Figure 5.9, and by making the deflections of the cantilevers different to each other, the deflection measurement range can be extended beyond $\lambda/2$.

Consider an array of N moving cantilevers that have different deflections. Let their deflections be $(p_1/q_1)t$, $(p_2/q_2)t, \ldots, (p_N/q_N)t$, where the p's and q's are integers, and let all fractions be in the simplest form. For small angles of θ, the phases corresponding to these deflections can be obtained from Equation (5.19):

$$\frac{4\pi}{\lambda}\frac{p_1}{q_1}t \qquad \frac{4\pi}{\lambda}\frac{p_2}{q_2}t \qquad \ldots \qquad \frac{4\pi}{\lambda}\frac{p_N}{q_N}t$$

It was seen earlier that the phase terms are cyclic with deflection over a period of $\lambda/2$. Now suppose t increases by $n\lambda/2$, where n is an integer. Then, the phases become

$$\frac{4\pi}{\lambda}\frac{p_1}{q_1}(t + n\lambda/2) \qquad \frac{4\pi}{\lambda}\frac{p_2}{q_2}(t + n\lambda/2) \qquad \ldots \qquad \frac{4\pi}{\lambda}\frac{p_N}{q_N}(t + n\lambda/2)$$

which simplify to

$$2n\pi\frac{p_1}{q_1} + \frac{4\pi}{\lambda}\frac{p_1}{q_1}t \qquad 2n\pi\frac{p_2}{q_2} + \frac{4\pi}{\lambda}\frac{p_2}{q_2}t \qquad \ldots \qquad 2n\pi\frac{p_N}{q_N} + \frac{4\pi}{\lambda}\frac{p_N}{q_N}t$$

For each of these phase terms to be equal to their original respective phases, every np_i/q_i term must be an integer. The smallest n that satisfies this condition is the lowest common denominator (LCD) of $q_1,\ q_2, \ldots, q_N$. Thus, all phase terms will be cyclic with deflection over a period $L\lambda/2$, where L is the lowest common denominator of the deflection multiplication quotients p_i/q_i.

As an example, consider an array of 5 cantilevers, having deflections of t, $1.1t$, $1.2t$, $1.3t$ and $1.4t$. These deflections can be expressed using rational numbers as t, $11t/10$, $6t/5$, $13t/10$ and $7t/5$. The LCD of these numbers is 10. Hence, all the phase terms will be cyclic over a period of $10\lambda/2$. This is a 20-fold increase of the measurement range when compared with standard interferometric measurement systems reported in the literature.

5.6 Spacing of microcantilevers in the array

It was noted earlier that the frequencies of the spatial harmonic functions are given by terms of the form $(x_p - x_q)/\lambda$, where x_p and x_q denote the locations of the cantilevers. It was also shown earlier that the amplitude spectrum of the Fourier transform of the intensity pattern is a series of triangular pulses. Now, for these pulses to be easily identified by an automated system, the peaks should be clearly distinguishable as shown in Figure 5.12(a). If the pulses overlap, however, there will be a smoothing effect and the peaks will be less distinguishable, as shown in Figure 5.12(b).

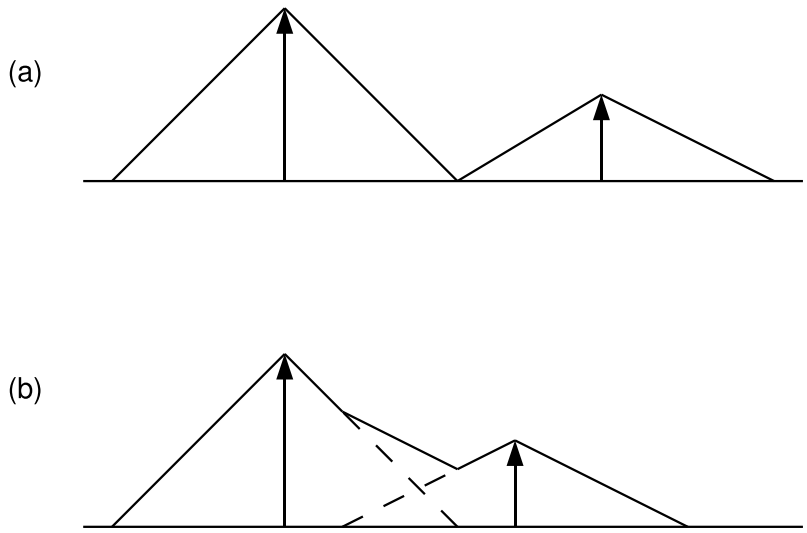

Figure 5.12: (a) Non-overlapping pulses are clearly distinguishable, while (b) overlapping pulses have an effect of smoothing out the peaks.

At a minimum, the triangular pulses can just touch each other, as in Figure 5.12(a). In this case, the separation between the peaks is equal to the width of the triangular pulses. The width of the triangular pulse can be derived from the diffraction envelope E_s^2 obtained from Equation (5.2).

$$E_s^2 = \text{sinc}^2\left(\frac{1}{2}kb\sin\theta\right) \tag{5.30}$$

The Fourier transform of this function can be obtained using standard FT tables and is found to be a triangular pulse of width $2b/\lambda$. Thus, for two consecutive pulses to be non-overlapping, the pulse separation should be greater than $2b/\lambda$. Referring to the spatial harmonic functions given by Equations (5.18)–(5.20) note that the spatial frequencies are given by terms of the form $(x_p - x_q)/\lambda$. Then the difference between two adjacent frequencies is given by

$$\begin{aligned}\Delta f &= \left(\frac{x_{p+1} - x_q}{\lambda}\right) - \left(\frac{x_p - x_q}{\lambda}\right) \\ &= \frac{x_{p+1} - x_p}{\lambda}\end{aligned}$$

Thus, for the triangular pulses to be non-overlapping,

$$\begin{aligned}\frac{x_{p+1} - x_p}{\lambda} &\geq \frac{2b}{\lambda} \\ x_{p+1} - x_p &\geq 2b \qquad (5.31)\end{aligned}$$

Thus, for the pulses in the amplitude spectrum of the FT to be non-overlapping, the spacing between any two adjacent cantilevers should be at least twice the width of the cantilevers.

The effect of pulse separation is shown in Figure 5.13, which shows the amplitude spectrum of the FT of the intensity pattern of different cantilever arrangements. In Figure 5.13(a), the cantilevers are placed at intervals $x_p - x_q = 1.25b$, and the peaks are indistinguishable. Figure 5.13(b) is plotted with $x_p - x_q = 2b$, where the peaks are just distinguishable. In Figure 5.13(c), $x_p - x_q = 4b$ and the peaks are well separated.

In the previous section, the minimum separation between two cantilevers was denoted by a. Therefore, the values of a should be selected such that $a \geq 2b$.

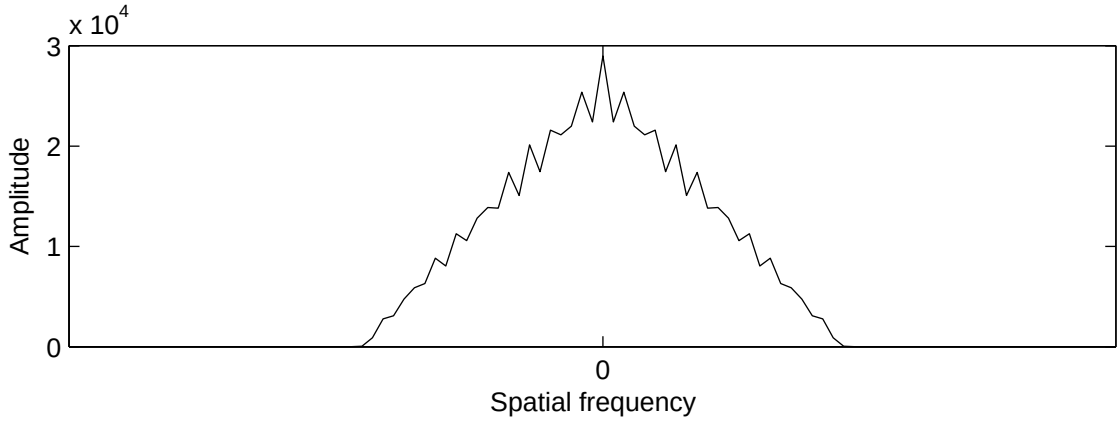

(a) $x_p - x_q = 1.25b$

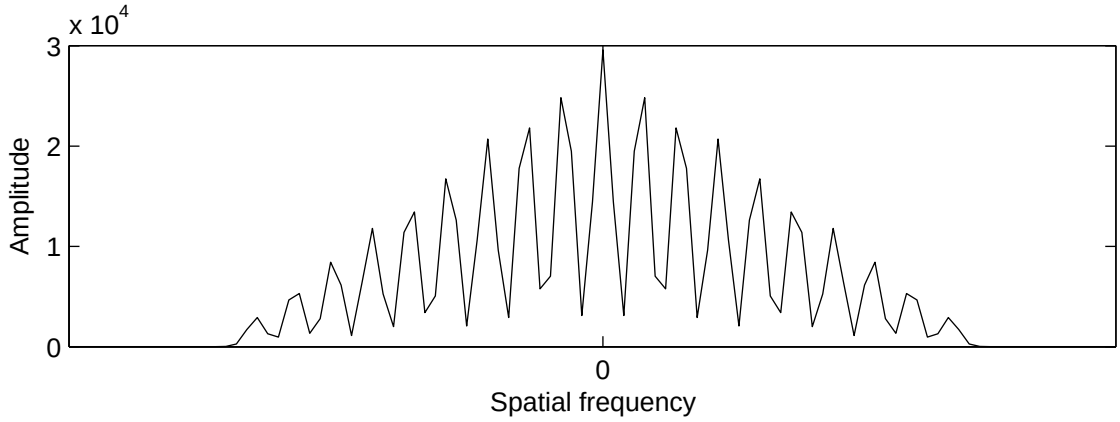

(b) $x_p - x_q = 2b$

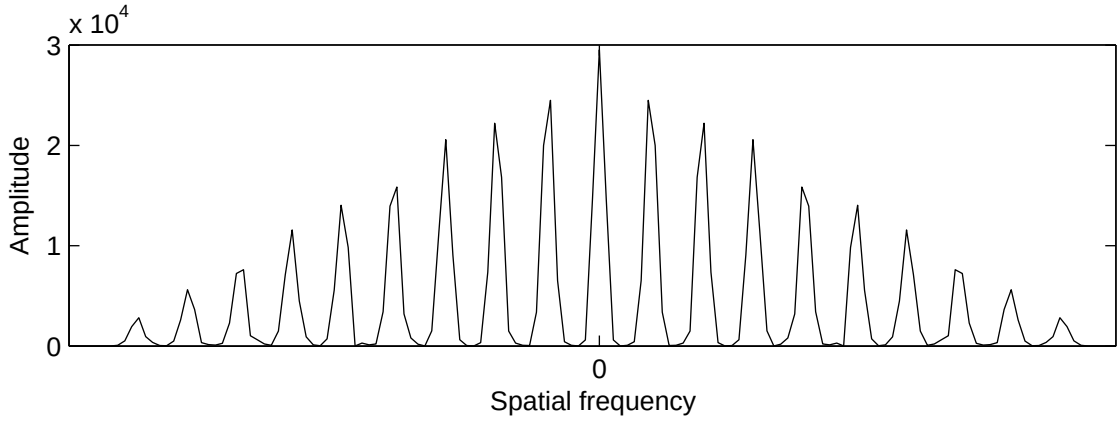

(c) $x_p - x_q = 4b$

Figure 5.13: Simulated amplitude spectra obtained from the FT of the intensity pattern for different values of cantilever separations ($x_p - x_q$).

5.7 Requirements of the optical detector

To implement the measurement technique proposed in this thesis on an electronic system, the optical diffraction pattern has to be captured by an image sensor and converted into digital data. The Discrete Fourier Transform of the interference pattern can then be calculated, from which the phases of the spatial cosines can be extracted.

In order to avoid measurement errors due to aliasing, the interference pattern must be sampled at sufficiently close intervals. This requires that the sensor have an adequate pixel resolution. The resolution of the measurements are determined by the resolution of the analog to digital converter (ADC) of the image sensor. Finally, the image sensor should be large enough to capture the entire intensity pattern. The minimum requirements of these sensor parameters are determined in this section.

5.7.1 Pixel resolution

Consider the spatial harmonic functions given by $\cos\{2\pi\cdot(x_p-x_q)/\lambda\cdot\sin\theta+\phi\}$, where the spatial frequency of the harmonic function is $(x_p - x_q)/\lambda$. Suppose the largest $(x_p - x_q)$ value is $\Delta x_{\max}$. Then the largest spatial frequency of this array will be $\Delta x_{\max}/\lambda$. The Sampling Theorem dictates that the sampling frequency be at least twice as large as the largest frequency component of the signal. Thus the required minimum sampling frequency becomes $2\Delta x_{\max}/\lambda$. Suppose the photodetector is placed at a distance D away from the cantilever plane. The sampling frequency then translates to a minimum theoretical sampling interval d_s of

$$d_s = D\lambda/(2\Delta x_{\max}) \tag{5.32}$$

The sampling interval of a photodetector is determined by the spacing between the pixels of the sensor. Therefore, the pixel spacing of the photodetector should be smaller than the value given by Equation (5.32). As an example, for the array used earlier $\Delta x_{\max} = 19a$. Assuming $D = 10$ mm, $\lambda = 650$ nm and the minimum spacing

between cantilevers $a = 8$ μm, Equation (5.32) gives the required pixel spacing as 21 μm. In practice, however, it is desirable to use a sensor with even more closely spaced pixels and sample at closer intervals than the theoretical minimum determined above.

5.7.2 Resolution of the ADC

The measurement resolution of standard interferometric arrangements is determined by the resolution of the ADC. If the ADC has n bits, the intensity pattern is quantized into 2^n discrete values. Noting that the intensity of a diffraction order varies between its maximum and minimum within a deflection range of $\lambda/4$, the theoretical measurement resolution of a standard interferometric system is $\lambda/(4 \cdot 2^n)$.

Even in the irregular cantilever array method proposed in this thesis, the spatial harmonic functions are cyclic over at least a deflection range of $\lambda/4$. An n-bit ADC will quantize these functions into 2^n discrete values. Therefore, when using an n-bit ADC, the theoretical measurement resolution is given by

$$t_{\min} = \frac{\lambda}{2^{n+2}} \tag{5.33}$$

As an example, if a 10-bit ADC is used with an optical source having $\lambda = 650$ nm, the measurement resolution is 0.159 nm.

5.7.3 Size of the sensor

Sufficient information for the measurement of phase information is contained within the main lobe of the diffraction envelope. Thus the image sensor should be large enough to capture the entire central lobe of the diffraction envelope. The diffraction envelope E_s^2 of the far-field intensity pattern is obtained from Equation (5.2). The minima of the diffraction envelope can be found from $\sin(0.5kb\sin\theta) = 0$ where b is the width of a cantilever [5]. From this, the locations of the first minima are found at $\theta = \pm\lambda/b$, which define the central lobe of the diffraction envelope. Assuming a

sensor at a distance D away from the cantilever plane, the required sensor size S_r is then obtained as

$$S_r = 2\lambda D/b \tag{5.34}$$

As an example, if $b = 4$ μm, $D = 10$ mm and $\lambda = 650$ nm, Equation (5.34) gives the required sensor size as 3.25 mm.

5.8 Alignment of the optical sensor

The deflection measurement technique presented above requires the accurate measurement of phase terms, through the Fourier transformation of the intensity pattern. When a signal is sampled, its phase is calculated from the midpoint of the data stream. Consider Figure 5.14 which shows a cosine wave. Suppose the wave is sampled in the interval AB as shown in Figure 5.14. Then, the sampled values are symmetric about the midpoint C of the data series, and the phase will be calculated as zero. However, if the wave was sampled between the interval XY, the midpoint of the data series will be Z and the calculated phase will no longer be zero. Thus, the calculated phase of a spatial signal depends on the interval between which the signal is sampled.

Now consider the diffraction envelope E_s^2 given by Equation (5.2). It can be seen that the diffraction envelope is symmetric about its midpoint. For the phase terms to be correctly interpreted from the Fourier transforms, the image sensor must capture the interference pattern symmetrically with respect to the diffraction envelope. Consider the far-field interference pattern of a standard, regular array of cantilevers. Figure 5.15 shows the far-field optical intensity pattern as well as the diffraction envelope for deflections $t = 0$ and $t = \lambda/4$. It can be seen that the intensity pattern is also symmetric with respect to the midpoint of the diffraction envelope. Since the cantilever array is symmetrically placed and deflects symmetrically, the intensity pattern is also symmetric, irrespective of the deflection. Thus if the image sensor

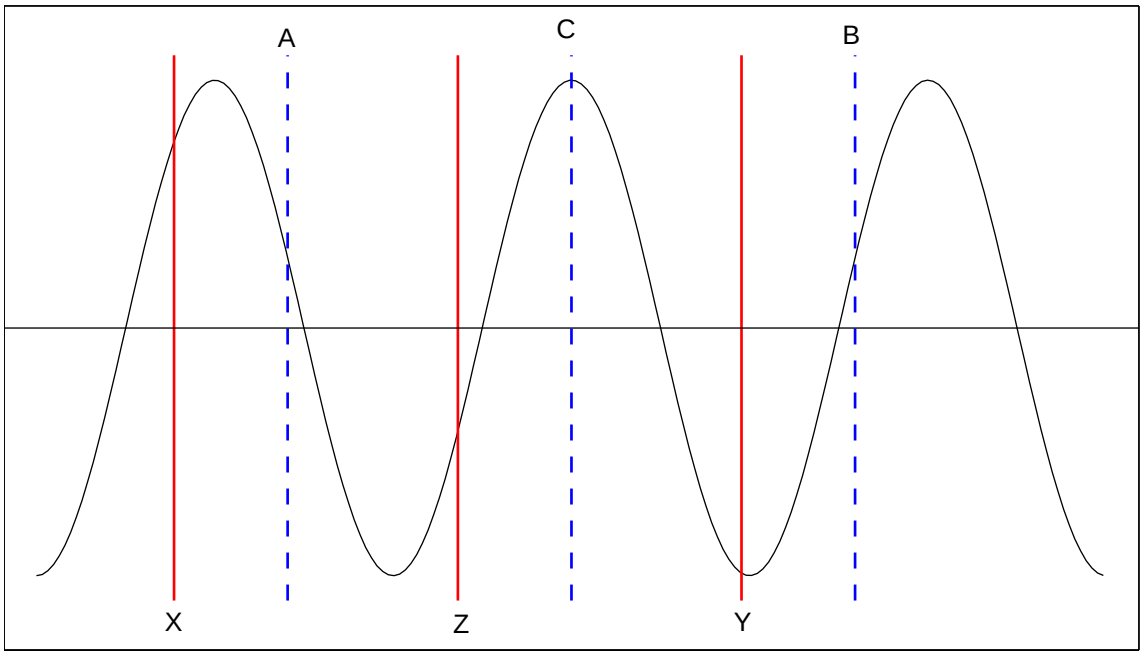

Figure 5.14: The measured phase depends on the interval over which the signal is sampled.

captures the entire diffraction pattern, the center of the envelope can be located from the intensity measurement. Then, the correct phase terms can be determined with respect to the calculated midpoint.

However, if an irregular array is used, the intensity pattern is asymmetric. Figure 5.16 plots the intensity pattern as well as the diffraction envelope for deflections $t = 0$ and $t = \lambda/4$. It is seen that the intensity pattern is not symmetric with respect to the midpoint of the diffraction envelope for non-zero deflections. Therefore it is not possible to locate the center of the diffraction envelope from the intensity measurements. Thus, to obtain the correct phase terms from the Fourier transform, the photodetector must be precisely aligned with respect to the diffraction envelope. This is difficult to achieve in a simple automated system. If the photodetector is not symmetrically placed, a phase error will be added to each measured spatial cosine term.

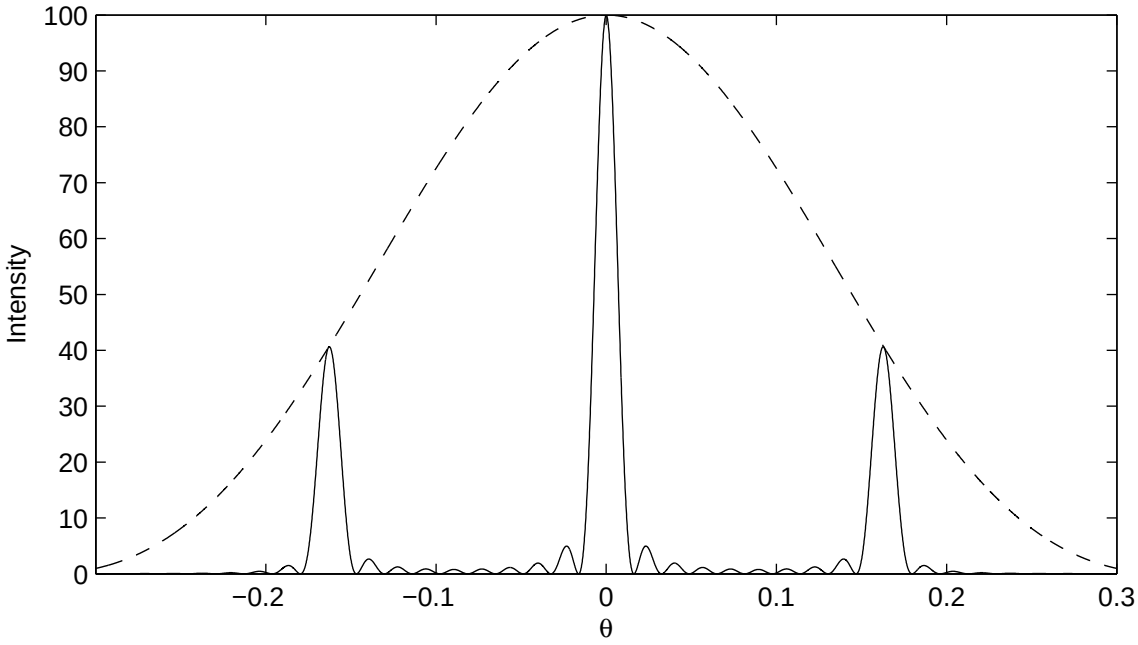

(a) $t = 0$

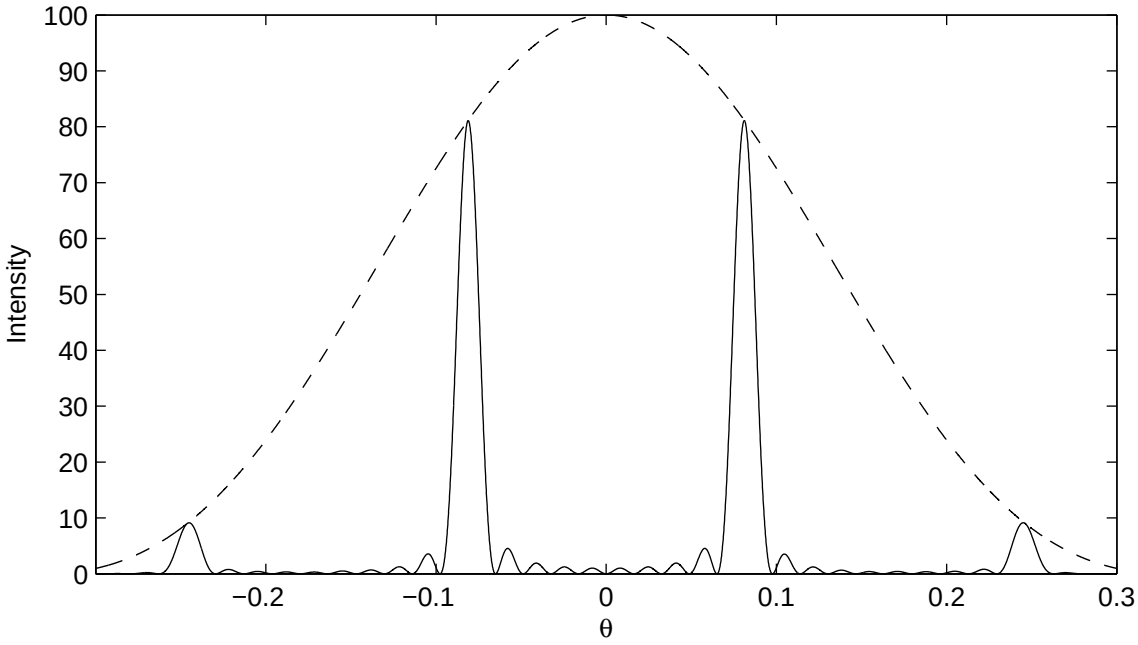

(b) $t = \lambda/4$

Figure 5.15: The diffraction envelope and the interference pattern of a symmetric array at (a) zero deflection and (b) at $t = \lambda/4$.

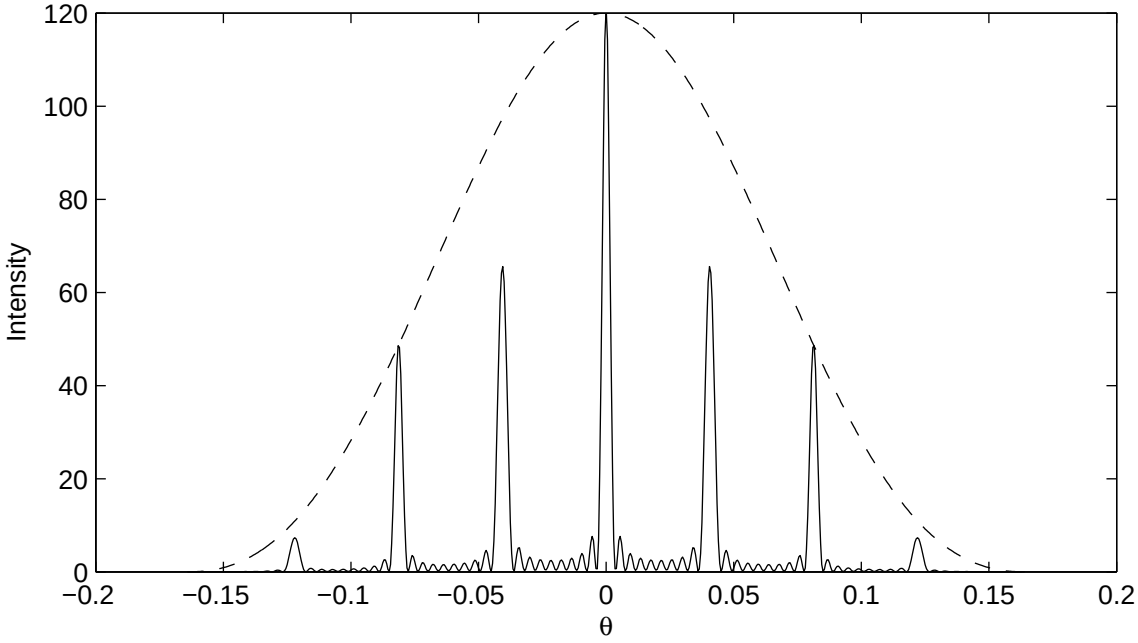

(a) $t = 0$

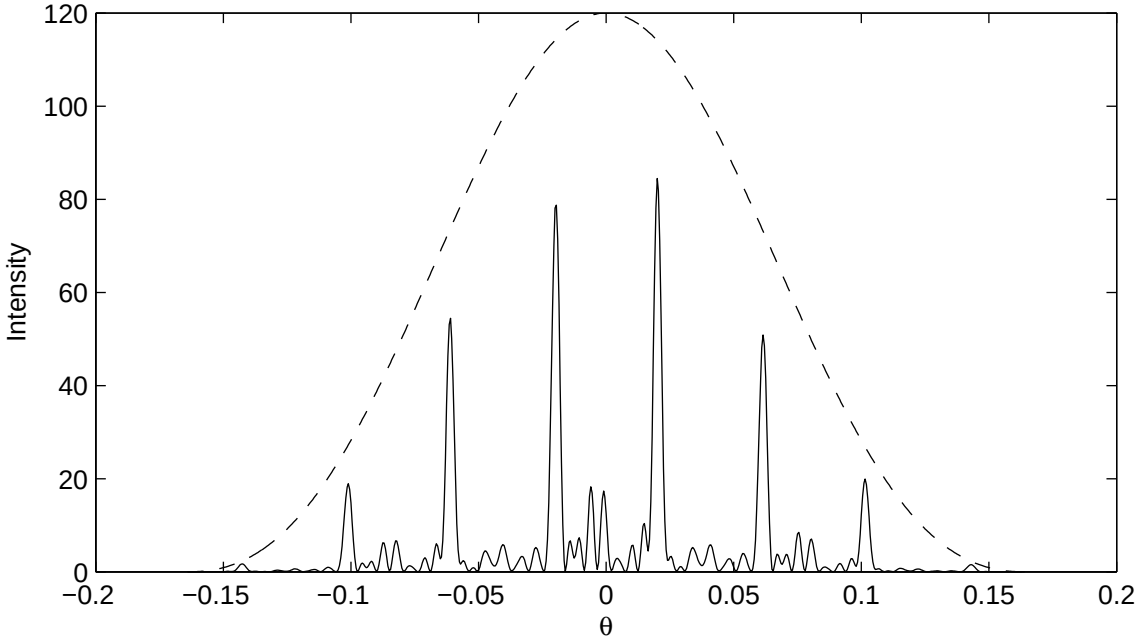

(b) $t = \lambda/4$

Figure 5.16: The diffraction envelope and the interference pattern of an irregularly spaced array at (a) zero deflection and (b) at $t = \lambda/4$.

Refer Figure 5.17 which shows two cosine waves $C1$ and $C2$, and let O denote the actual midpoint. Suppose the cosine $C1$ has a known phase. Now, if the signals are sampled between the interval AB, the measurement midpoint will be shifted by a distance δ to O', and both cosines will have phase errors. Since the phase of $C1$ is known, the phase error $\Delta\phi_1$ introduced to $C1$ due to misalignment can be calculated. Now, suppose the frequencies of $C1$ and $C2$ are f_1 and f_2 respectively. Then the phase error introduced to $C2$ due to misalignment can be calculated by

$$\Delta\phi_2 = \frac{f_2}{f_1}\phi_1 \tag{5.35}$$

Thus, if the phase of one cosine and the relative frequencies of the signal are known, the measurement phase errors of any number of other cosines can be calculated.

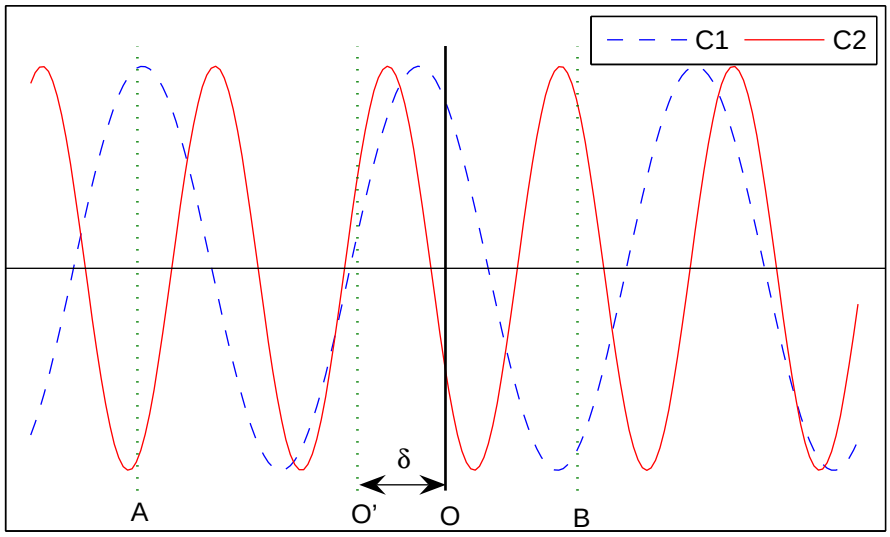

Figure 5.17: Phase errors of two cosines due to misalignment.

Referring to Figure 5.17, it can be seen that misalignments of up to one wavelength of the lowest frequency wave can be corrected using this method.

Now, in the far-field intensity pattern, spatial harmonic functions generated by S_{ff} are known to have zero phase, as seen from Equation (5.18). The relative frequencies

of the spatial harmonic functions depend only on the placement of the cantilevers in the array as seen from Equations (5.18)–(5.20), and these values are also known. Thus, if the phase of a cosine generated by S_{ff} can be measured, the phase errors of all other measurements can be corrected, eliminating the need for alignment.

Suppose the spatial frequency of such a cosine is $\Delta x_p/\lambda$. Its wavelength at a distance D gives the maximum correctable misalignment error ϵ

$$\epsilon = D\lambda/\Delta x_p \tag{5.36}$$

It immediately follows from Equation (5.36) that low spatial frequencies allow larger misalignment errors to be corrected.

Referring back to Table 5.3, the $(f - f)$ values generated by S_{fm} were shown to be 3, 4, 7, 8, 11, 12, 15, 16 and 19. Of these values, 19 is obtained only once, and is not obtained with any other combination of $(f - m)$ values nor $(m - m)$ values. Thus, the spatial harmonic function having a frequency of $19a/\lambda$ can be used to correct the phase errors due to misalignment of the photodetector with respect to the far-field intensity pattern. When the photodetector is placed at a distance $D = 10$ mm, Equation (5.36) gives the correctable misalignment range as 0.04 mm.

If a spatial cosine of lower frequency can be used for alignment correction, this range can be improved. Further, recalling the principle of extending the deflection measurement range developed earlier, this misalignment correction range can be increased several-fold by using two spatial cosines for alignment correction calculations.

5.9 Principles

The above investigations have established a method by which an interferometric arrangement of cantilevers can be realised to measure deflections using a simple optical arrangement, over a range unconstrained by the wavelength of the optical source. The principles established in this Chapter are summarised below.

- The far-field intensity pattern of an array of cantilevers is composed of several spatial harmonic functions. The frequencies of these functions are determined by the locations of the cantilevers in the array, and the phases are determined by the deflections.

- The measurement range of standard interdigital interferometric methods is limited to $\lambda/4$. This can be extended to $\lambda/2$ if the phases of the spatial harmonic functions are extracted from a Fourier transform of the far-field intensity pattern.

- The measurement range limitation of $\lambda/2$ is due to the fact that all spatial harmonic functions are cyclic over that range. By making the cantilevers have different deflections for the same stimulus, the measurement range can be extended beyond $\lambda/2$.

- The measurement range is then given by $\lambda/2 \times$ (the LCD of the deflections).

- To be able to directly measure the phases from the Fourier transforms, the location of cantilevers should meet the following requirement. Let x_f denote the location of the f^{th} fixed cantilever, and let x_m denote the location of the m^{th} moving cantilever. Then for every m, there should be at least one unique $(x_f - x_m)$ value not obtained with any other combination of $(x_f - x_f)$, $(x_m - x_m)$ or $(x_f - x_m)$ values.

- To correct phase errors due to misalignment of the optical sensor, there should be at least one unique $(x_f - x_f)$ value, not obtained with any other combination of $(x_f - x_m)$, $(x_m - x_m)$ or $(x_f - x_m)$ values. Lower $(x_f - x_f)$ values allow larger misalignments to be corrected.

- By using more than one unique $(x_f - x_f)$ which are not integer multiples of each other for misalignment correction, the misalignment correction range can be increased to (lowest unique $x_f - x_f$ value) $\times$ (LCD of the different unique $x_f - x_f$ values).

- To make the amplitude peaks of the Fourier transform clearly distinguishable, the minimum distance between two cantilevers should be at least twice as great as the width of each cantilever.

In the following chapter, these principles are used to demonstrate the performance of this novel technique.

5.10 Summary

In this Chapter, the theory behind the use of an interferometric array of cantilevers as a means of deflection measuring technique was reviewed. The interference pattern was shown to be a sum of spatial harmonic functions. Using this analysis, the limitation of the measurement range of standard interferometric measurements was highlighted, and the reason for this limitation was analysed. A novel technique that overcomes the limitation of a small measurement range was presented. The dimensions and the required placement of cantilevers in the array were established. The requirements of the optical sensor were investigated. A technique to eliminate the alignment requirement of the optical sensor was also presented.

References

[1] S. Manalis, S. Minne, A. Atalar, and C. Quate, "Interdigital cantilevers for atomic force microscopy," *Applied Physics Letters*, vol. 69, no. 25, pp. 3944–3946, 1996.

[2] G. Yaralioglu, A. Atalar, S. Manalis, and C. Quate, "Analysis and design of an interdigital cantilever as a displacement sensor," *Journal of Applied Physics*, vol. 83, no. 12, pp. 7405–7415, 1998.

[3] D. Rafaja, V. Valvoda, J. Kub, K. Temst, M. J. Van Bael, and Y. Bruynseraede, "Long-range periodicity and disorder in two-dimensional arrays of metallic dots

studied by x-ray diffraction," *Physical Review B*, vol. 61, no. 23, pp. 16144 LP – 16153, 2000.

[4] R. J. Bell, *Introductory Fourier Transform Spectroscopy*. New York: Academic Press, 1972.

[5] E. Hecht, *Schaum's Outline of Theory and Problems of Optics*. New York: McGraw-Hill, 1975.

[6] B. E. A. Saleh and M. C. Teich, *Fundamentals of Photonics*. Wiley series in pure and applied optics, New York: Wiley, 1991.

[7] E. B. Cooper, E. R. Post, S. Griffith, J. Levitan, S. R. Manalis, M. A. Schmidt, and C. F. Quate, "High-resolution micromachined interferometric accelerometer," *Applied Physics Letters*, vol. 76, no. 22, pp. 3316–3318, 2000.

[8] T. Thundat, E. Finot, Z. Hu, R. Ritchie, G. Wu, and A. Majumdar, "Chemical sensing in Fourier space," *Applied Physics Letters*, vol. 77, no. 24, pp. 4061–4063, 2000.

[9] T. Sulchek, R. Hsieh, S. Minne, C. Quate, and S. Manalis, "Interdigital cantilever as a biological sensor," *Proceedings of the 2001 1st IEEE Conference on Nanotechnology. IEEE-NANO 2001 (Cat. No.01EX516)*, pp. 562–566, 2001.

Chapter 6

System Design for Implementing the Measurement Method

6.1 Introduction

The previous Chapter established the principles by which an irregularly spaced array of cantilevers can be used in a manner that overcomes the $\lambda/4$ measurement range limitation and the alignment requirements of standard interferometric methods. In this Chapter, a cantilever array is designed using these principles to be compatible with a commercially available, example image sensor. This array and the measurement system is then simulated and shown to have the large measurement range, resolution and alignment correction capabilities predicted in the previous Chapter.

6.2 Functional description

Figure 6.1 shows a functional block diagram of an implementation of a deflection measurement system using an irregularly spaced cantilever array. The cantilevers in the array are placed irregularly, according to the placement principles established earlier. The moving cantilevers are each perforated to have different deflections for

a given stimulus.

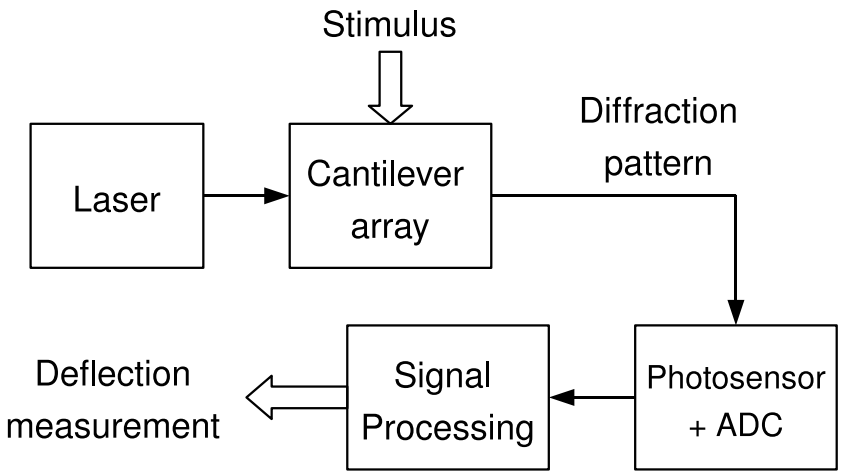

Figure 6.1: Functional block diagram of a deflection measurement system using an irregularly spaced cantilever array.

A collimated laser is focused onto the cantilever array, which diffracts the beam and generates a far-field interference pattern. A photosensor placed in the far-field digitizes the intensity pattern, and converts it to an electrical signal. A signal processing unit computes the Fourier transform of the output of the sensor array. An alignment-correction algorithm eliminates misalignment errors. Phase terms of the spatial harmonic functions obtained from the FT are then used to calculate the deflection.

For the purpose of demonstrating the performance of the system, the Micron Technology MT9D131 CMOS Digital Image Sensor [1], a commercially available sensor, was selected. This sensor has 2.8 μm$\times$2.8 μm pixels, the active sensor size is 4.73 mm$\times$3.52 mm, and has a 10-bit ADC. The sensor array has 1600×1200 pixels, giving the pixel spacing along the longer side of the array as 2.96 μm.

In the following sections, a cantilever array is designed such that this image sensor can be used in a measurement system. It is further assumed that deflections up to 3000 nm are required to be measured.

6.3 Design of the interferometric cantilever array

This section determines the locations of the cantilevers in the array, the widths of the cantilevers and the perforation parameters required to obtain the different deflection values.

6.3.1 Placement of cantilevers in the array

A possible set of f and m values that meet the placement conditions established in the previous Chapter are shown in Table 6.1(a)–(c). It can be seen from these tables that the values 1, 5, 9, 13 and 17 are unique to Table 6.1(a), and occur only once within Table 6.1(a). Hence the phases of the spatial harmonics having frequencies a/λ, $5a/\lambda$, $9a/\lambda$, $13a/\lambda$ and $17a/\lambda$ can be used to correct misalignment errors. It was noted in the previous Chapter that the harmonic function with the lowest frequency provides the largest error-correction range. Thus the phase of the cosine having a spatial frequency a/λ will have the largest alignment error correction capability.

Further, it can be noted that the $(f - m)$ values 3, 7, 11, 15 and 19 occur only once in the tables. Thus, the phase terms of the spatial harmonic functions having frequencies of $3a/\lambda$, $7a/\lambda$, $11a/\lambda$, $15a/\lambda$ and $19a/\lambda$ can be used to calculate deflection.

6.3.2 The minimum distance between cantilevers

The example image sensor has pixels at intervals of 2.96 μm. Assume that the sensor is placed at a distance $D = 10$ mm away from the cantilever plane. Then from Equation (5.32), the largest allowable distance between cantilevers is found to be $\Delta x_{\max} = 1.1$ mm. Referring to to Tables 6.1, it is seen that the maximum distance between 2 cantilevers is $19a$, where a is the minimum separation between 2 cantilevers. Thus, the largest allowable value is $a = 61$ μm. Selecting lower values

for a will improve the sampling accuracy of the system. As an example if $a = 6$ μm is selected, the intensity pattern will be sampled at a spatial frequency 10 times greater than the Nyquist limit.

Table 6.1: Values of $(f - f)$, $(m - m)$ and $(f - m)$ for an irregular array.

(a) All possible $(f - f)$ values

f \ f	0	1	5	9	13	17
0	–	1	5	9	13	17
1	–	–	4	8	12	16
5	–	–	–	4	8	12
9	–	–	–	–	4	8
13	–	–	–	–	–	4
17	–	–	–	–	–	–

(b) All possible $(m - m)$ values

m \ m	3	7	11	15	19
3	–	4	8	12	16
7	–	–	4	8	12
11	–	–	–	4	8
15	–	–	–	–	4
19	–	–	–	–	–

(c) All possible $(f - m)$ values

m \ f	0	1	5	9	13	17
3	-3	-2	2	6	10	14
7	-7	-6	-2	2	6	10
11	-11	-10	-6	-2	2	6
15	-15	-14	-10	-6	-2	2
19	-19	-18	-14	-10	-6	-2

6.3.3 Cantilever width

The example image sensor has a maximum active sensor size of 4.73 mm. Suppose the sensor is placed at a distance $D = 10$ mm away from the cantilever plane. Then the cantilever width can be obtained from Equation (5.34) as $b = 2.74$ μm. If cantilevers having this width are used, the main lobe of the diffraction envelope spans the entire length of the sensor, requiring precise alignment. Therefore, the widths of the cantilevers should be made larger than this, such that the diffraction envelope is smaller than the sensor length. The sensor can then be roughly placed to capture the entire central lobe of the diffraction envelope, and misalignment errors can be corrected using the method described in the previous Chapter.

Referring to Table 6.1, it can be seen that the spatial harmonic function having a frequency of a/λ can be used to correct alignment errors. Referring to Equation (5.36), it can be seen that this arrangement can correct alignment errors of up to ± 0.542 mm. Now, if the cantilever width is selected as $b = 3$ μm, the diffraction envelope will span 4.33 mm, according to Equation (5.34). Since the sensor size is 4.73 mm, this leaves a tolerance of ± 0.2 mm. As alignment errors of up to ± 0.542 mm can be corrected by this system, accurate deflection measurements can be taken as long as the entire central diffraction lobe falls on the image sensor.

6.3.4 Cantilevers with different deflections

It is required that deflections up to 3000 nm are able to be measured. A deflection of 3250 nm corresponds to 5λ. Since a phase-based interferometric arrangement can measure deflections up to $\lambda/2$ (ie. 325 nm), a system capable of measuring deflections up to 3250 nm requires that the cantilever deflection multipliers have a lowest common denominator of 10. An array of cantilevers having relative deflections of t, $1.1t$, $1.2t$, $1.3t$ and $1.4t$ is one possible solution. Using the analytical models developed in Chapter 3, a set of cantilevers having relative deflections of t, $1.1t$, $1.2t$, $1.3t$ and $1.4t$ can be designed. Perforations can be etched from the cantilevers to

change the relative deflections using standard photolithographic techniques. Since it is difficult to have different perforation depths in different cantilevers of the array, the perforation depth factor γ is kept constant. All other perforation parameters can be easily defined using an etch mask. Table 6.2 lists one possible set of perforation values to achieve this set of deflections. Note that while the moving cantilevers have different deflections, all cantilevers have similar resonant frequencies. It was highlighted in the Literature Review that the resonant frequency is directly related to the noise characteristics of cantilevers. Hence, each of these cantilevers will have similar noise characteristics.

Table 6.2: A possible set of perforation parameters to achieve a 10-fold deflection measurement range improvement. Perforation parameters are given as fractions of the cantilever dimensions, according to the notations of Chapter 3.

Rel. defl^n	Location (α)	Width (β)	Depth (γ)	Length (η)	Rel. f_0
1	–	–	–	–	1
1.1	0.2	1.0	0.25	0.1	0.95
1.2	0.2	1.0	0.25	0.2	0.92
1.3	0.2	1.0	0.25	0.3	0.92
1.4	0.2	1.0	0.25	0.8	1.04

6.3.5 Summary of cantilever array details

The moving cantilevers should have perforations with parameters given in Table 6.2. A schematic diagram of the cantilever array is shown in Figure 6.2. The locations of the cantilevers are also shown, in terms of the minimum separation a. The unmodified side of the cantilever array is illuminated by a collimated laser to avoid diffraction from the perforations. The photosensor should be placed to capture the

resulting interference pattern.

Number of fixed cantilevers	6
Number of moving cantilevers	5
Width of each cantilever (b)	3 μm
Minimum spacing between cantilevers (a)	6 μm
Locations of fixed cantilevers (x_{f})	0, 6, 30, 54, 78, 102 μm
Locations of moving cantilevers (x_{m})	18, 42, 66, 90, 114 μm

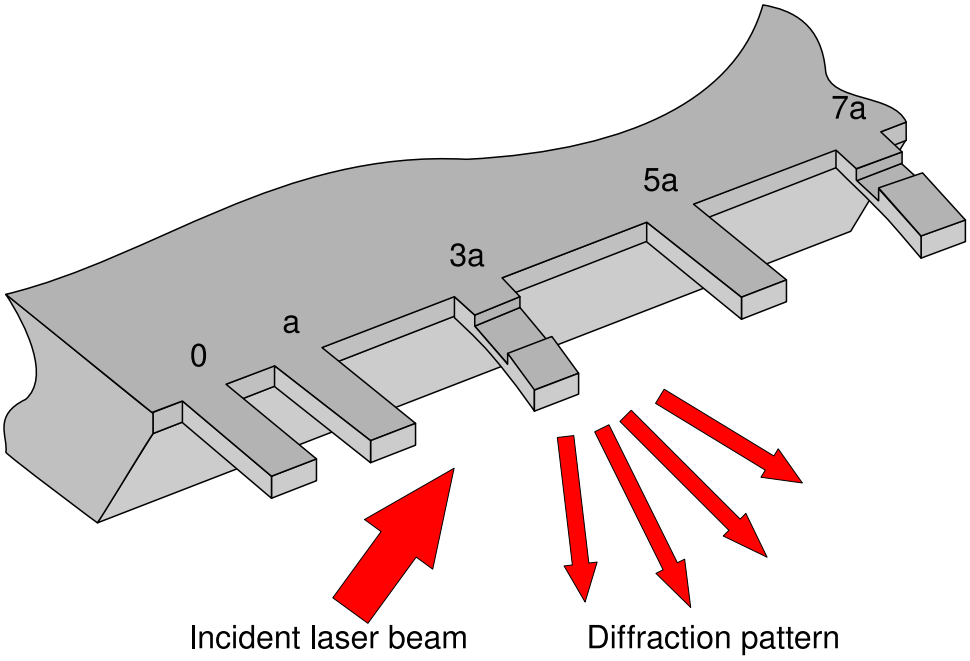

Figure 6.2: A schematic diagram of the cantilever array.

6.4 Algorithm for calculating the deflection

The image sensor will provide a digitised version of the far-field optical intensity pattern. This section lists the signal processing algorithm for calculating the deflection from this data.

For each deflection value within the measurement range, a unique combination of phase terms will be obtained from the FT of the intensity pattern. In order to determine the deflection from these phase terms, it is convenient to have a look-up table having all the phase terms for all deflections. A second such look-up table is required for the correction of alignment errors. Using these two tables, the deflection can be derived by a simple signal processing algorithm such as the one presented below.

- Compute the FFT of the digitized intensity pattern. Identify the peaks of the amplitude spectrum. Note the locations of the alignment-correction frequencies and the measurement frequencies on the spectrum.
- Using the phase values of the alignment-correction frequencies and the alignment-correction lookup table, compute the misalignment of the sensor.
- Using the locations of the cantilevers in the array, compute the phase errors introduced into the measurement cosines due to misalignment.
- Obtain the phase terms of the measurement frequencies from the FT. Remove the misalignment phase errors using the values computed earlier.
- Take the first corrected phase term. Cycle through the row of the lookup table corresponding to this spatial frequency, and note the possible deflection values corresponding to this phase. There can be several candidate deflection values.
- Repeat this procedure for all phase terms.

- Now, each measured phase term will have a set of possible deflection values. From these candidate deflection values, pick the deflection that is common to all phase terms. This is the desired deflection value of the cantilever array.

A *Matlab*® implementation of this algorithm was developed to validate the design and the underlying principles. The scripts are given in Appendix B. Results are presented in the next section.

6.5 Results

A cantilever array having the parameters designed above was simulated using *Matlab*. Figure 6.3(a) shows the far-field intensity pattern when the cantilever deflection $t = 0$. Figure 6.3(b) shows the amplitude spectrum of the FT of the interference pattern. This spectrum has 19 clearly distinguishable peaks on either side of the DC value, corresponding to the 19 spatial frequencies of the interference pattern. Figure 6.3(c) shows the calculated phase spectrum of the FT. The phase terms corresponding to all amplitude peaks are found to be zero.

Figure 6.4 is plotted when the deflection is 100 nm. The phases corresponding to the 3^{rd}, 7^{th}, 11^{th}, 15^{th} and 19^{th} amplitude peaks are non-zero, and contain the information to calculate the deflection.

Using these *Matlab* simulations, the performance of the system is verified in the following subsections. The measurement resolution is determined. Then it is shown that measurements can be taken up to deflections of 5λ, and that alignment errors can be corrected.

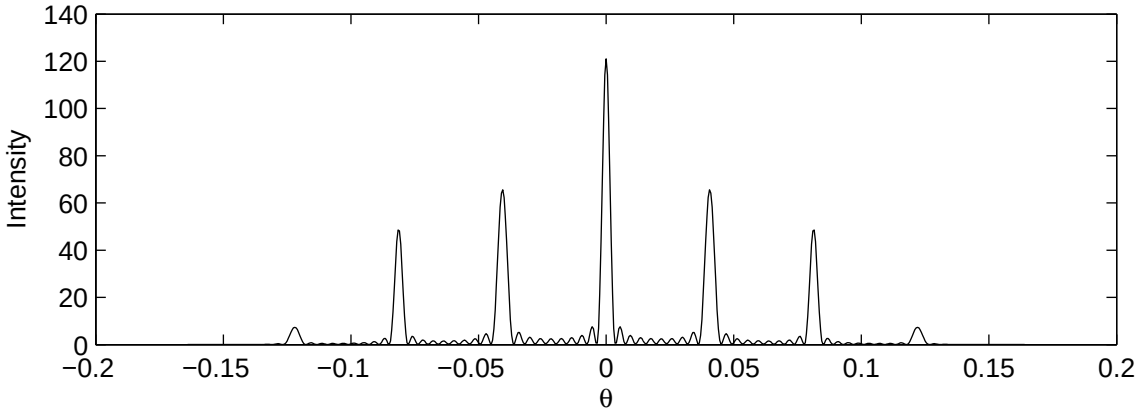

(a) Interference pattern

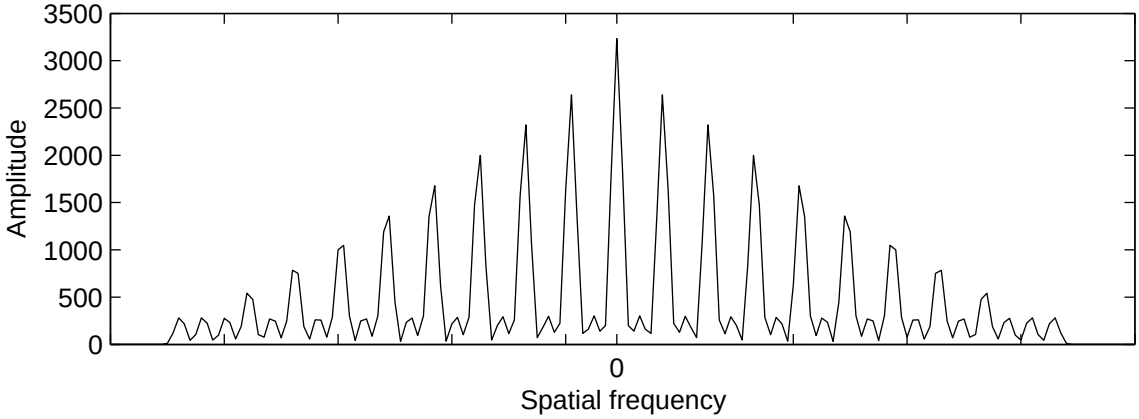

(b) Amplitude spectrum

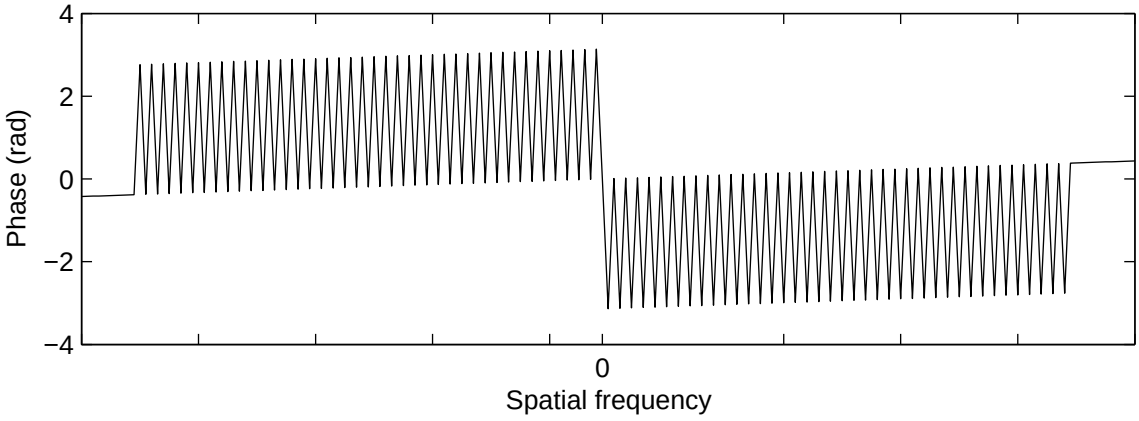

(c) Phase spectrum

Figure 6.3: Simulated (a) interference pattern, (b) amplitude spectrum and the (c) phase spectrum of the novel detection method when deflection $t = 0$ nm.

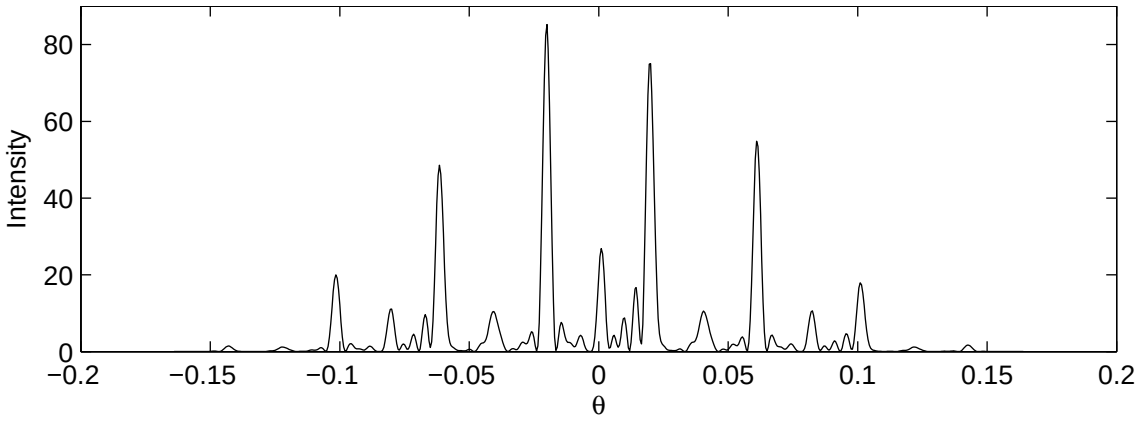

(a) Interference pattern

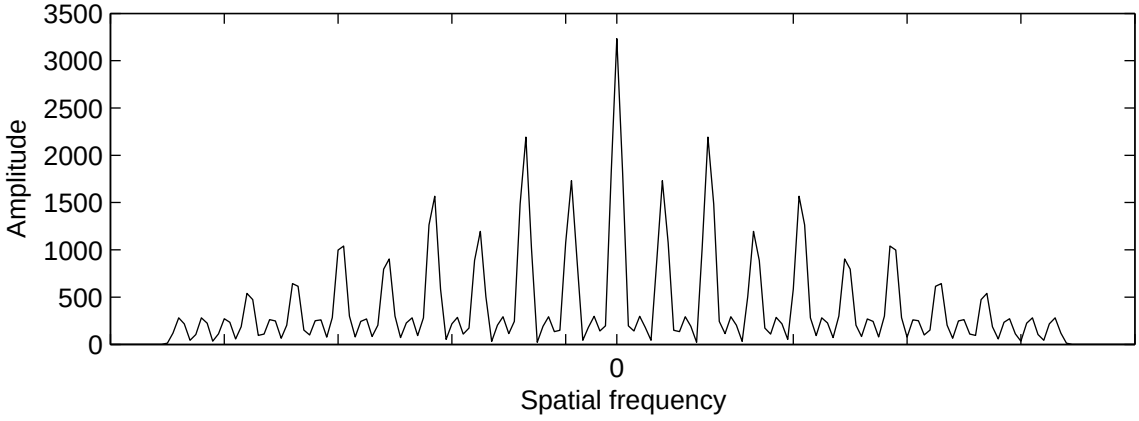

(b) Amplitude spectrum

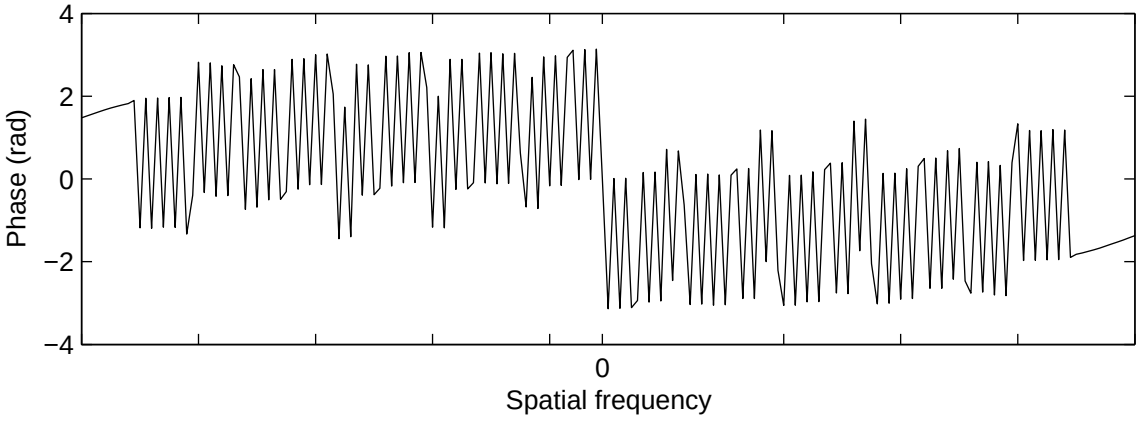

(c) Phase spectrum

Figure 6.4: Simulated (a) interference pattern, (b) amplitude spectrum and the (c) phase spectrum of the novel detection method when deflection $t = 100$ nm.

6.5.1 Measurement resolution

In order to determine the resolution of the system, the intensity patterns for deflections in the range 0–10 nm were simulated, in steps of 0.01 nm. Then, the phase terms of the FT of the intensity patterns were used to calculate the deflections. The difference between the actual deflection and the calculated deflection is shown in Figure 6.5.

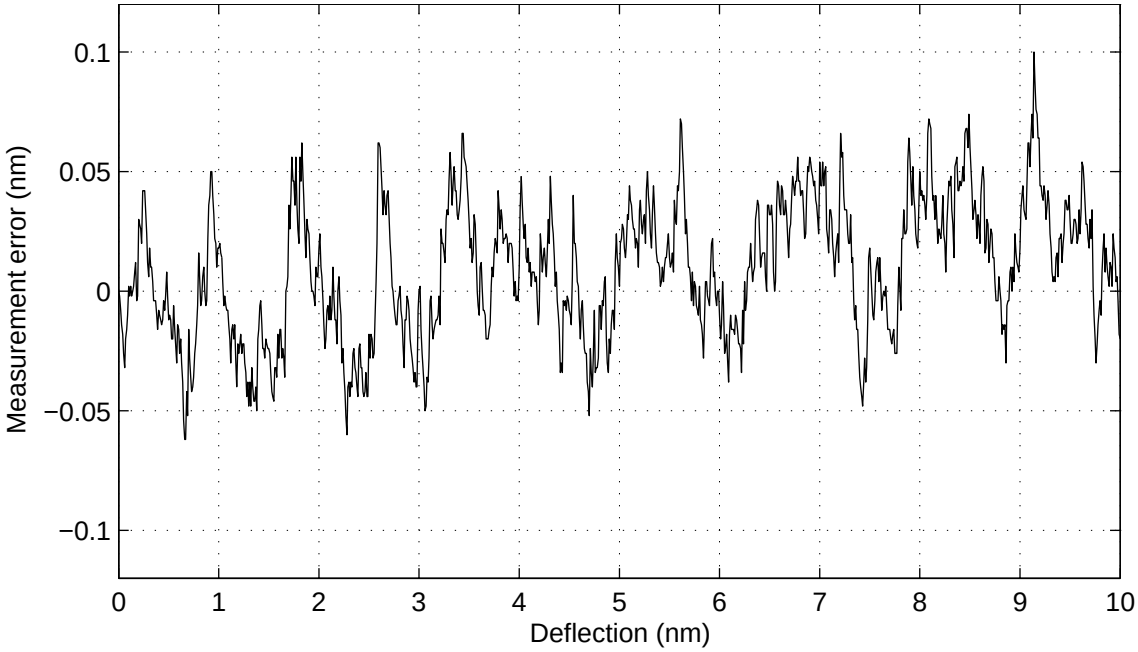

Figure 6.5: Calculated measurement error at each deflection value in the range 0–10 nm.

It can be seen that the largest measurement error is 0.10 nm. The resolution being twice the maximum error, the measurement resolution of the irregularly spaced cantilever array is then found to be 0.20 nm. This compares with a theoretical resolution of 0.159 nm for a standard interferometric array using a photosensor having an identical ADC resolution of 10-bits. This discrepancy is mainly due to the limitations of the signal processing code used in the simulations. A simple signal processing algorithm was implementation to demonstrate the concepts, but it lacks the precision required to obtain high resolutions measurements.

6.5.2 Measurement range

The variation of the phases of the spatial harmonic functions having frequencies $3a/\lambda$, $7a/\lambda$, $11a/\lambda$, $15a/\lambda$ and $19a/\lambda$ with deflection are shown in Figure 6.6. Deflection values were systematically varied from 0 through 3500 nm in steps of 10 nm, and the phase terms were calculated at each deflection value.

It is clearly seen that the five phase terms have different periods. In the deflection range 0–3250 nm, each deflection value gives a unique set of phase terms. Figures 6.7(a) and 6.7(b) are extracted from Figure 6.6 for the deflection ranges 0–250 nm and 3250–3500 nm respectively. It can be clearly seen that the phase patterns of both Figures 6.7(a) and 6.7(b) are identical, which shows that all phase terms are repeated after 3250 nm. These three figures demonstrate that unique phase patterns are obtained for a deflection range of 3250 nm, which corresponds to 5λ. Any deflection within this range can be distinctly measured, with sub-nanometric resolution, using the phase terms.

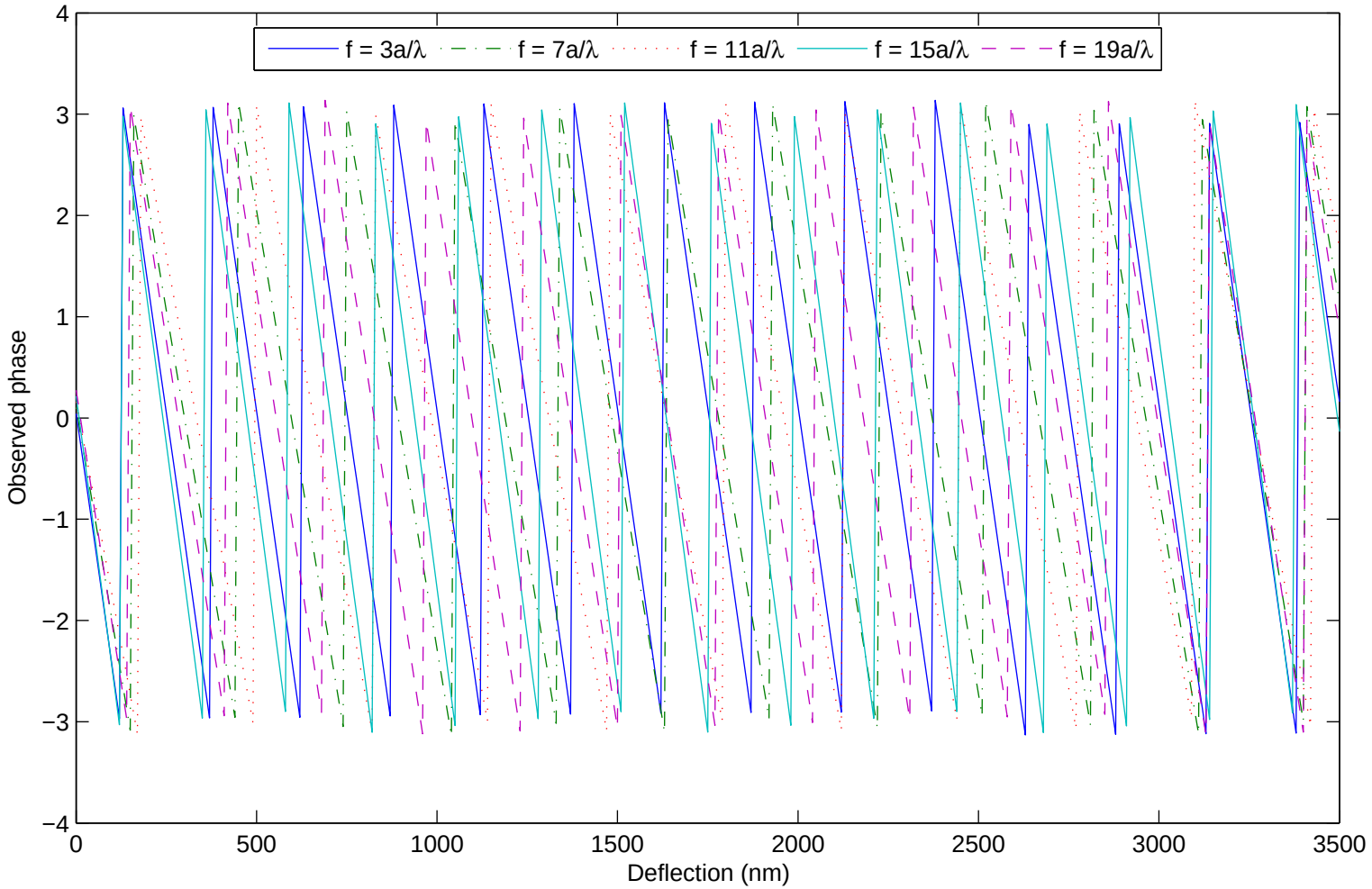

Figure 6.6: Variation of the phases of spatial cosines having frequencies of $3a/\lambda$, $7a/\lambda$, $11a/\lambda$, $15a/\lambda$ and $19a/\lambda$, with deflections between 0–3500 nm.

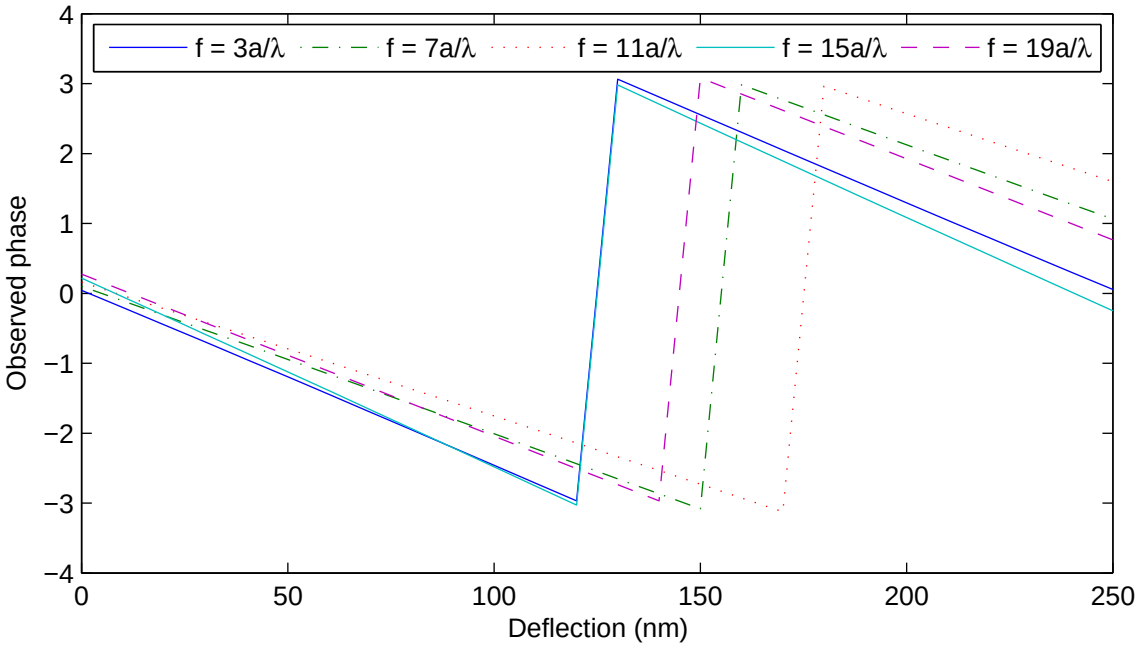

(a) Deflection range 0–250 nm

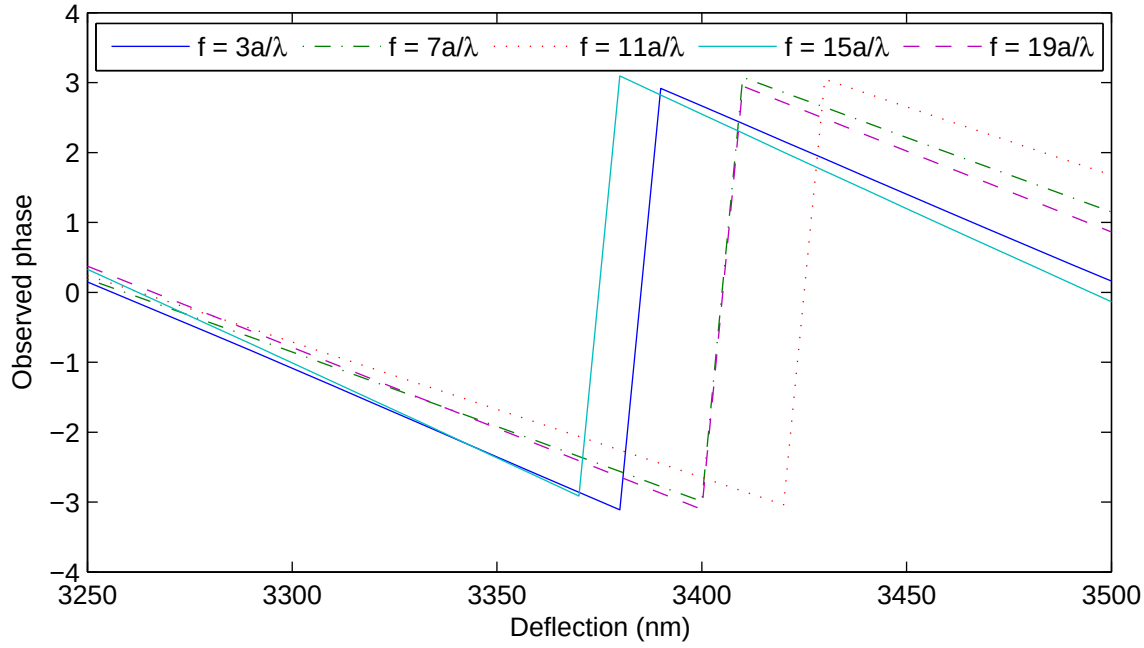

(b) Deflection range 3250–3500 nm

Figure 6.7: All phase variation patterns are repeated after a deflection of 3250 nm.

As an example, consider a nominal deflection of $t = 3000$ nm. The spatial frequencies of the harmonic functions of interest are given in the first column of Table 6.3, and the phase terms of these harmonic functions obtained from the FT are shown in the second column. Candidate deflection values obtained from the data table corresponding to Figure 6.6 are shown in the last column. As can be seen from Table 6.3, the only deflection value common to all phase terms is 3000 nm. Hence, this is the base deflection of the cantilever array. Note that this value is much greater than the maximum measurable deflection of 162.5 nm of a regular array of cantilevers.

Table 6.3: Measured phase values and candidate deflection values, when t=3000 nm.

Spatial frequency	Measured phase	Candidate deflection values
$3a/\lambda$	0.1405	500, 750, 1000, 1250, 1500, 1750, 2000, 2250, 2500, 2750, 3000, 3250, 3500
$7a/\lambda$	-0.7690	340, 630, 930, 1520, 1820, 2110, 2410, 2700, 3000, 3300
$11a/\lambda$	-1.1985	400, 720, 1050, 1370, 1700, 2020, 2350, 2670, 3000, 3330
$15a/\lambda$	0.7986	440, 910, 1140, 1370, 1840, 2070, 2300, 2770, 3000, 3230
$19a/\lambda$	-0.1178	290, 560, 830, 1100, 1370, 1640, 2190, 2460, 2730, 3000, 3270

Using the *Matlab* script given in Appendix B, it was verified that deflection values up to 3250 nm could be calculated, as predicted, using this method. Deflections beyond this range cause ambiguities, which is consistent with the theory established

in this thesis.

6.5.3 Misalignment correction

In the simulations conducted so far, it was assumed that the sensor was perfectly aligned with the diffraction envelope. In this section, the sampling range has been shifted to simulate a misaligned image sensor. At each misaligned value, the phase of the alignment-correction cosine having a frequency of a/λ was calculated. This is plotted in Figure 6.8. It can be seen that the phase varies linearly with misalignment,

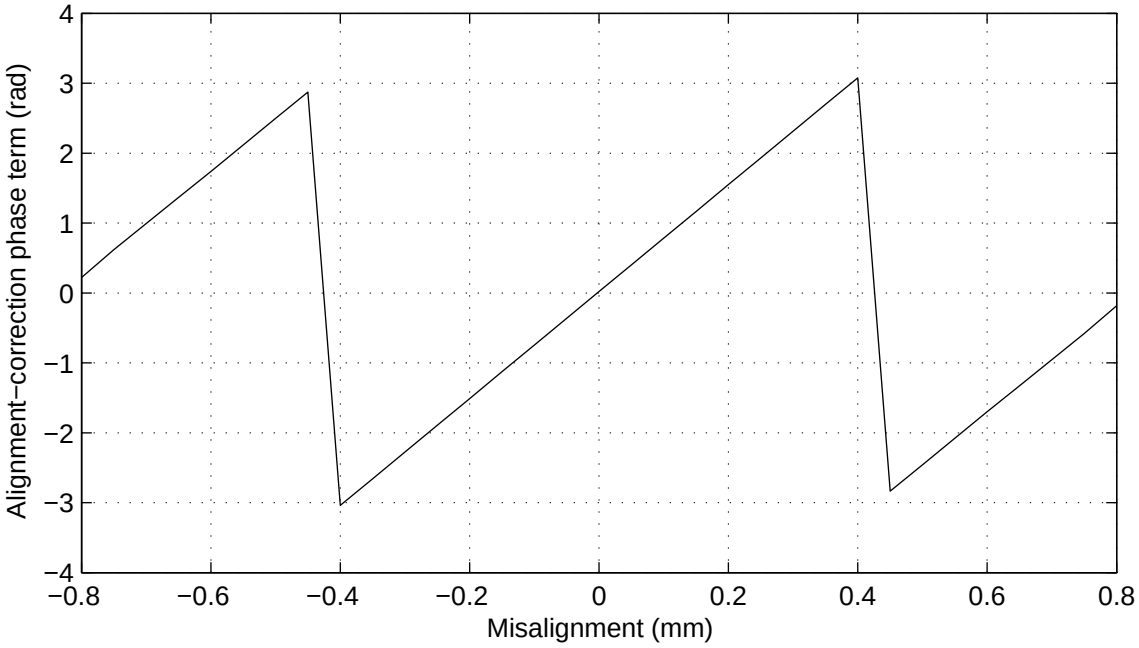

Figure 6.8: Variation of the phase of the alignment-correction cosine, with misalignment.

and that unique phase terms are observed within a misalignment range of ± 0.42 mm. Hence, misalignments of up to 0.84 mm can be corrected using this method.

It was noted earlier that the diffraction envelope will span 4.33 mm, while the length of the sensor is 4.73 mm. Thus, sensor can be misaligned by ± 0.2 mm with respect to the diffraction envelope, and still capture the entire central lobe of the diffraction envelope. It was seen above that misalignment errors of up to ± 0.42 mm can be

corrected. Therefore, provided the entire central lobe is captured by the image sensor, any alignment error can be corrected.

6.6 The effect of noise on measurements

The simulations of this Chapter assumed noise-free conditions. In practice, however, cantilever noise, laser diode noise, photodetector noise and electronic circuit noise is encountered which adversely affects the resolution of the measurement. The effects of random noise sources such as thermal-induced vibrations of the cantilevers are eliminated when the average deflection of several cantilevers is considered. The practical resolution of the measurement system is limited by the noise power of the implemented opto-electronic system.

6.7 Summary

In this Chapter, an example array of cantilevers was designed using the principles established in the previous Chapter. The system was designed to measure deflections of up to 3250 nm, considering a commercially available image sensor. The placement of cantilevers was determined in terms of the minimum separation a between cantilevers. Then, using the pixel dimensions, the numerical value of the minimum separation a between cantilevers was determined. Using the size of the image sensor, the width of the cantilevers was obtained. Finally, perforation parameters were determined to obtain an array of cantilevers that have different deflections for a given stimulus, yet similar resonant frequencies.

This array and the measurement system was then simulated. It was demonstrated that deflections up to 3250 nm were measurable as predicted, with a resolution of 0.2 nm. Misalignment errors up to ± 0.42 mm were shown to be correctable using the methods established earlier. Thus the principles of the measurement method established in Chapter 5 have been demonstrated to be valid.

References

[1] "CMOS Image Sensor : MT9D131C12STC."
http://www.micron.com/products/partdetail?part=MT9D131C12STC, December 2007.

Chapter 7

Conclusions

This thesis investigated the problem of enhancing the deflection sensitivity and measuring the deflection of microcantilevers for sensor elements. It was shown that if the deflection of a microcantilever was increased by increasing the length or by decreasing the thickness, its resonant frequency decreased. Since a lower resonant frequency results in a lower noise immunity, this method is not suitable for sensor elements.

This problem of an inverse relationship between the deflection and the resonant frequency of microcantilevers was investigated in Chapter 3. It was shown that the deflection and the resonant frequency of cantilevers can be simultaneously increased by creating perforations on the cantilever in a manner that reduces its mass by a larger fraction than the reduction of the spring constant of the cantilever.

Analytical models were developed to describe the dynamics of perforated microcantilevers. The moment–area method was used to develop an analytical model to describe the surface-stress-induced deflection of microcantilevers. Deflection values obtained from this model were within 6 % of the simulated deflection values obtained using *ANSYS*, which showed the validity of the models as well as the modelling technique. An analytical model to describe the resonant frequency was developed using the Rayleigh–Ritz method. Resonant frequencies obtained using this model were

within 4 % of the simulated values obtained using *ANSYS*.

The variations of deflection and resonant frequency of cantilevers with perforation parameters were characterised using these models. It was established that the deflection and resonant frequency can be selectively controlled using perforations, enabling cantilevers to be realised with larger deflections as well as higher resonant frequencies compared with standard rectangular cantilevers. Since larger resonant frequencies give a larger noise immunity, the cantilevers can be made more sensitive to smaller measurands. This enables the measurement technique to be simplified, since large deflections can be measured in less noise-controlled environments.

This analysis was then extended to determine the optimal profile of a cantilever that combined increased deflection with increased noise immunity. It was established that cantilevers with triangular profiles have a larger deflection–resonant frequency product when compared with standard rectangular cantilevers. These results were compared with values obtained from models available in the literature, as well as with simulations using *ANSYS*, which showed good agreement. The triangular-profiled cantilevers were shown to have a sensitivity to dimensional variations comparable to prismatic cantilevers, and to be relatively insensitive to smoothing effects of fabrication.

An important contribution of the thesis was the investigation of measuring the deflection of an array of cantilevers using the interdigital interferometric method. A novel mathematical approach was proposed that decomposed the far-field diffraction pattern into the sum of several spatial harmonic functions. The relationships between the parameters of the cantilever array, the cantilever deflections and the spatial harmonic functions which define the optical intensity pattern were established. The frequencies of these spatial harmonic functions were shown to be determined by the distances between each cantilever of the array, while the phase terms were shown to be dependent on the amount of deflection.

Using this representation of the diffraction pattern, the reason for the usual limitation of the measurement range to a quarter of the wavelength λ of the optical

source was identified. It was shown that instead of measuring the optical intensities of the diffraction orders, calculating the phases of the spatial harmonic functions from the Fourier transformation of the far-field diffraction pattern can extend the measurement range to $\lambda/2$.

It was further established that by making each moving cantilever of the array to have a different deflection for a given stimulus, the measurement range can be increased independent of the half-wavelength limitation. The principles of designing a cantilever array to enable this enhancement were established.

A key result of this thesis was the establishment of a principle to correct the errors induced by misalignment of the image sensor with respect to the diffraction envelope of the interference pattern. It was shown that the cantilever array can be designed to correct for large misalignments. Since the requirement of precise optical alignment is eliminated, the proposed method is well suited for automated systems to measure the deflection of cantilevers.

Practical design considerations of the cantilever array and the image sensor were investigated and the principles for determining the cantilever width and the locations of individual cantilevers were established. The requirements of the photo sensor, namely, the maximum allowable pixel spacing, the size of the image sensor and the resolution of the Analog to Digital Converter (ADC) for a given measurement resolution were also determined.

Using the principles established in the thesis, an example design of an array of cantilevers was presented. Using the specifications of a standard image sensor and assuming the wavelength of the laser to be 650 nm, the performance of this system was simulated on *Matlab*. Using a basic signal processing algorithm, a measurement resolution of 0.2 nm was demonstrated using a 10-bit ADC, which compares with the theoretical resolution of 0.159 nm of a standard interferometric deflection measurement technique using a photodiode of identical resolution. Deflections of up to 3250 nm was shown to be measurable from this array, compared with 162.5 nm for a standard interferometric measurement technique.

This thesis has established and proven the principles by which microcantilevers with higher deflections combined with higher noise immunity can be achieved, and how deflections of up to several micrometers can be measured with sub-nanometric resolution, using a simple optical technique. Thus the work of this thesis has overcome some of the limitations which prevent the achievement of a MEMS microcantilever-based, rapid diagnostic device.

Appendix A

Analytical Modelling

The complete mathematical derivations of the analytical models presented in this thesis are given in this Appendix. The background theories used in the derivations are also included.

A.1 Model of a perforated microcantilever

The cantilever is of length L, width b and thickness h. All perforations are cuboidal and are assumed to be geometrically identical. Their length, width and depth are parametrically defined by ηL, $\beta' b$ and γh respectively. The separation between perforations is denoted by λL and the distance to the first perforation from the fixed end is αL. Figure A.1 shows a sketch of a beam with an array of such perforations.

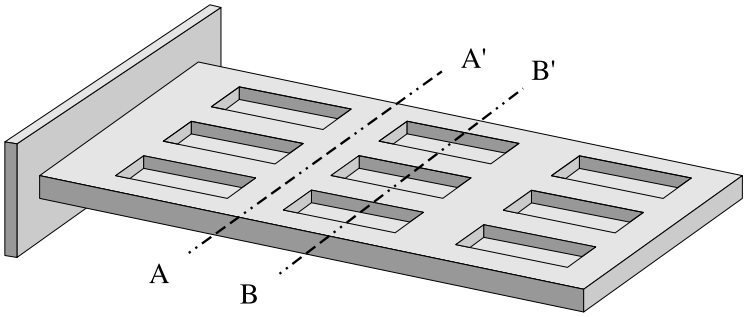

Figure A.1: A rectangular microcantilever with 9 cuboidal perforations.

A.2 Models for cantilever deflection

A.2.1 Moment–Area method

The moment–area method is a semi-graphical approach that can be used to calculate the deflection of cantilever beams [1, 2, 3]. This method is particularly useful when the beam is non-prismatic and is used here to develop analytical models for the deflection of perforated cantilevers.

When loads are applied to cantilevers, internal shear forces and bending-moments develop in the beam. These forces and moments, in general, vary from point to point along the axis of the cantilever. A moment diagram is a plot of the bending-moment M along the length of the cantilever. An example is shown in Figure A.2(b).

An M/EI curve (Figure A.2(c)) is obtained by dividing the internal moment M at every point along the cantilever length by the flexural rigidity EI at that point. E is the Young's modulus of the material and I is the moment of area of the cross-section at that point, and is computed about the neutral axis of that cross-section.

The deflection t of a point P on the microcantilever with respect to a point Q is given by [1, 2, 3]:

$$t_{P/Q} = \overline{x} \int_{P}^{Q} \frac{M}{EI} \, \mathrm{d}x \tag{A.1}$$

The area under the M/EI diagram between points P and Q (the shaded area in

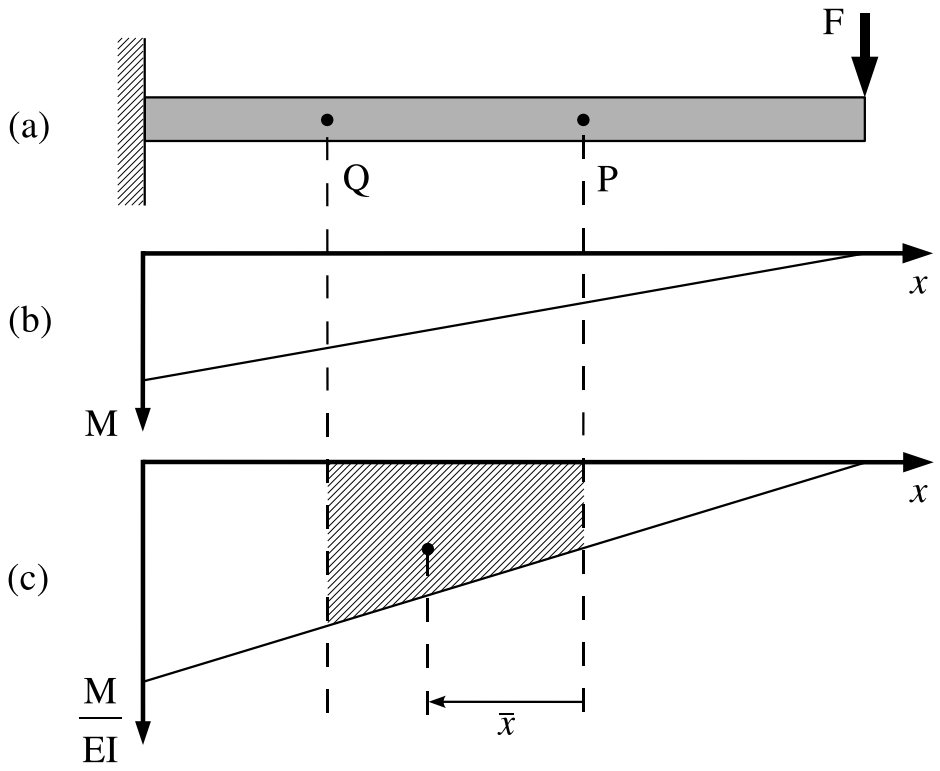

Figure A.2: (a) A cantilever with a point load at the free end, (b) the bending-moment diagram and (c) the resulting M/EI diagram.

Figure A.2(c)) represents the integral. $\overline{x}$ is the distance from point P to the centroid of the area under the M/EI diagram between P and Q.

When point P is at the free end and point Q is at the fixed end, Equation (A.1) gives the tip deflection of the microcantilever. Then, $\overline{x}$ is the distance from the free end to the centroid of the M/EI diagram and the integral represents the entire area under the M/EI diagram. This technique is used as the basis to formulate analytical models for the deflection of perforated microcantilevers.

Sign convention

In this thesis, the following sign convention is used for moments [1]:
the moment is considered to be positive if it causes a compression in the top fibres of the segment

Neutral axis

The moment–area method requires the determination of the moment of area of cross-sections, calculated about the neutral axis of that cross-section. Thus the neutral axis of cross-sections of the cantilever needs to be determined. It is shown in standard mechanics texts that the neutral axis of a cantilever is also its centroidal axis. The centroid $\overline{y}$ of an area A is defined by

$$\overline{y} = \frac{\int_A y \mathrm{d}A}{\int_A \mathrm{d}A} \tag{A.2}$$

If a composite area can be divided into several simpler shapes whose centroids are known,the centroid of the composite area can be determined from

$$\overline{y} = \frac{\sum \overline{y}_i A_i}{\sum A_i} \tag{A.3}$$

where $\overline{y}_i$ is the centroidal distance of the i^{th} composite part calculated about the same axis using Equation (A.2), and A_i is the area of the i^{th} composite part.

Consider a perforated cantilever as shown in Figure A.1. Cross-sections at unperforated segments of the beam (such as on AA') will be rectangular in shape. If the thickness of the cantilever is h, the centroidal axis of cross-sections at unperforated segments will be located at a depth of $h/2$.

A cross-section of a perforated segment (such as on BB') is shown in Figure A.3. Such a cross-section can be considered as a composite of several rectangular areas. Calculations can be simplified by assuming the composite area to be constructed by *removing* small rectangular areas from the larger rectangular area.

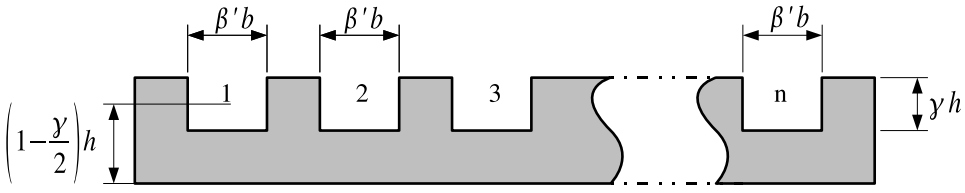

Figure A.3: Cross-section of a cantilever with n perforations.

Let there be n perforations across the cantilever width, each $\beta' b$ wide and γh deep, as shown in Figure A.3. The centroids of perforations are at a distance $(1 - \frac{\gamma}{2}h)$ from the unperforated surface. The distance to the centroid of the perforated cross-section from the unmodified surface (bottom surface) can be determined using Equation (A.3) as follows.

$$\begin{aligned}\overline{y} &= \frac{\sum \overline{y}_i A_i}{\sum A_i} \\ &= \frac{\frac{h}{2} \cdot bh - n \cdot \left(1 - \frac{\gamma}{2}\right) h \cdot \beta' b \gamma h}{bh - n \cdot \beta' b \gamma h} \\ &= h \frac{\left(\frac{1}{2} - n\beta' \cdot \gamma(1 - \frac{\gamma}{2})\right)}{1 - n\beta' \cdot \gamma}\end{aligned} \tag{A.4}$$

If we consider a cross-section with a single perforation of width $n\beta' b$, Equation (A.4) remains unchanged. Thus the centroid of a section with n identical perforations each of width $\beta' b$, is at the same depth as the centroid of a section with a single perforation of width $n\beta' b$.

In sections of the cantilever without any perforations, $\beta' = 0$ and $\gamma = 0$, and as expected, $\overline{y} = h/2$.

Moment of area

The moment of area I of an area A is given by the standard equation

$$I = \int_A y^2 \mathrm{d}A \tag{A.5}$$

It can be easily shown using this definition that the moment of area of a rectangle of width b and height h about its neutral axis is given by $\frac{1}{12} bh^3$.

Suppose the moment of area (MOA) of a shape about its neutral axis is given by I_0. Then its MOA about an axis Z parallel to the neutral axis can be determined using the parallel axis theorem:

$$I_Z = I_0 + Ad^2 \tag{A.6}$$

where d is the distance between the neutral axis and the Z axis, and A is the area.

If an area is a composite of several simpler parts, its moment of area is the algebraic sum of the MOA's of the composite parts, where all MOA's are taken about the same axis:

$$I_{\text{composite}} = \sum_i I_i \tag{A.7}$$

Refer Figure A.1 again that shows a perforated cantilever. Cross-sections at unperforated segments are rectangular in shape. Thus the moment of area of an unperforated cross-section about its neutral axis is $\frac{1}{12}bh^3$.

A cross-section at a perforated segment was shown in Figure A.3. The neutral axis of this cross-section was determined above and is given by Equation (A.4). For the moment–area method, MOA's of perforated sections should be taken about this axis.

A perforated cross-section can be considered as a composite shape constructed by removing small rectangular areas from the larger rectangular area. Using the parallel axis theorem, the MOA's of the composite parts about the neutral axis of the cross-section can be determined.

The MOA of an unperforated section about the neutral axis $\overline{y}$ given by Equation (A.4) can be obtained using the parallel axis theorem:

$$I_{u,\overline{y}} = \frac{1}{12}bh^3 + bh\left[\frac{h}{2} - h\frac{\left(\frac{1}{2} - n\beta'\gamma\left(1 - \frac{\gamma}{2}\right)\right)}{(1 - n\beta'\gamma)}\right]^2$$

This can be simplified to

$$I_{u,\overline{y}} = \frac{1}{12}bh^3\left[1 + 3\left(\frac{n\beta'\gamma\,(1-\gamma)}{1 - n\beta'\gamma}\right)^2\right] \tag{A.8}$$

Similarly, using the parallel axis theorem for cavities

$$\begin{aligned} I_{c,\overline{y}} &= \frac{1}{12}(\beta' b)(\gamma h)^3 + (\beta' b \cdot \gamma h)\left[h(1 - \frac{\gamma}{2}) - h\frac{\left(\frac{1}{2} - n\beta'\gamma\left(1 - \frac{\gamma}{2}\right)\right)}{(1 - n\beta'\gamma)}\right]^2 \\ &= \frac{1}{12}bh^3 \cdot \beta'\gamma\left[\frac{\gamma^2(1 - n\beta'\gamma)^2 + 3(1-\gamma)^2}{(1 - n\beta'\gamma)^2}\right] \end{aligned} \tag{A.9}$$

Now, the moment of area of the perforated cross-section about its neutral axis $I_p, \overline{y}$ can be obtained from the algebraic sum of the composite parts, as in Equation (A.7)

$$\begin{aligned} I_{p,\overline{y}} &= \sum_i I_{i,\overline{y}} \\ &= I_{u,\overline{y}} - n \cdot I_{c,\overline{y}} \qquad \text{(A.10)} \\ &= \frac{1}{12} bh^3 \left[1 + 3 \left(\frac{n\beta'\gamma\,(1-\gamma)}{1 - n\beta'\gamma} \right)^2 \right] \\ &\quad - n \cdot \frac{1}{12} bh^3 \beta'\gamma \left[\frac{\gamma^2 (1 - n\beta'\gamma)^2 + 3(1-\gamma)^2}{(1 - n\beta'\gamma)^2} \right] \\ I_{p,\overline{y}} &= \frac{1}{12} bh^3 \left[\frac{1 - 4n\beta'\gamma + 6n\beta'\gamma^2 - 4n\beta'\gamma^3 + n^2\beta'^2\gamma^4}{1 - n\beta'\gamma} \right] \qquad \text{(A.11)} \end{aligned}$$

If we consider a cross-section with a single perforation of width $n\beta' b$, Equation (A.11) remains unchanged. Thus the MOA of a section with n identical perforations each of width $\beta' b$, is the same as the MOA of a section with a single perforation of width $n\beta' b$.

It was shown earlier that the centroid of a cross-section with n identical perforations of width $\beta' b$, is at the same location as the centroid of a section that has a single perforation of width $n\beta' b$. Thus for the moment–area method, n perforations along the cross-section of the cantilever can be replaced by a single equivalent perforation. Therefore, an array of perforations on the cantilever can be modelled by a single line of equivalent perforations along the length of the cantilever. This equivalent model is used to represent perforations from this point onwards. Refer Figure A.4. The cumulative width of the individual perforations, $n\beta'$, is denoted by β.

Centroid and moment of area of the reduced model

The centroid of a perforated section was given above in Equation (A.4). The centroid of the reduced model can be obtained by substituting $n = 1$ and $\beta = n\beta'$.

$$\overline{y} = h \frac{\left(\frac{1}{2} - \beta\gamma(1 - \frac{\gamma}{2})\right)}{1 - \beta\gamma} \qquad \text{(A.12)}$$

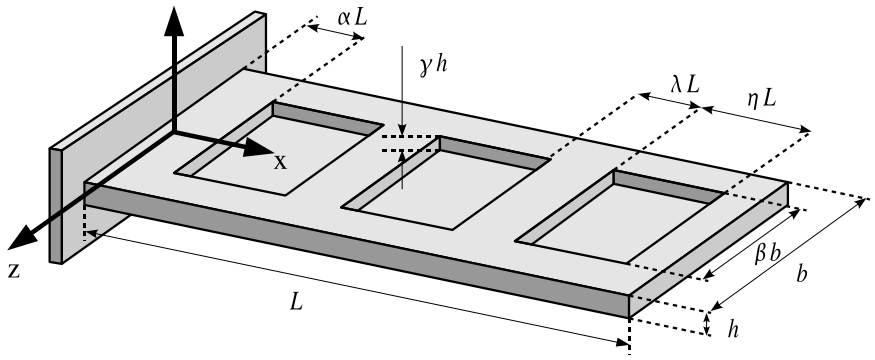

Figure A.4: Reduced model of a perforated microcantilever.

Similarly, substituting $n = 1$ and $\beta = n\beta'$ in Equation (A.11), the moment of area of a perforated cross-section of the reduced model is obtained.

$$I_{p,\overline{y}} = \frac{1}{12}bh^3\left[\frac{1 - 4\beta\gamma + 6\beta\gamma^2 - 4\beta\gamma^3 + \beta^2\gamma^4}{1 - \beta\gamma}\right] \tag{A.13}$$

The term $\frac{1}{12}bh^3$ is the moment of area of a uniform rectangular section taken about its neutral axis. Thus, the above expression for the moment of area of a perforated section can be expressed as

$$I_{p,\overline{y}} = \chi \cdot I_{u,0} \tag{A.14a}$$

where,

$$\chi = \frac{1 - 4\beta\gamma + 6\beta\gamma^2 - 4\beta\gamma^3 + \beta^2\gamma^4}{1 - \beta\gamma} \tag{A.14b}$$

A three-dimensional plot of the MOA factor χ versus the perforation width and depth factors is shown in Figure A.5. It can be seen from this Figure that the χ of a perforated section is less than 1 for every β and γ. Thus the moment of area of a perforated section is smaller than that of an unperforated section, for every value of β and γ.

A.2.2 Model for deflection with a point load

Figure A.6(a) shows a perforated cantilever with a point load F applied at its free end. The bending-moment diagram of an end-loaded cantilever is independent of

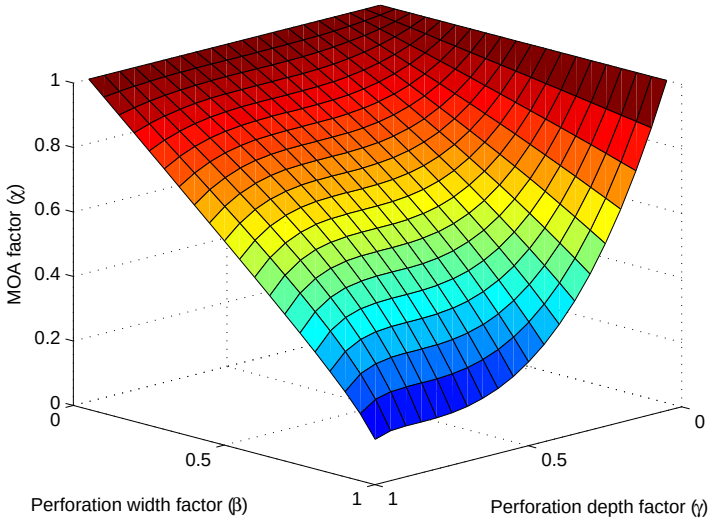

Figure A.5: Variation of moment of area χ factor with perforation width and depth.

the physical structure of the cantilever, and takes the shape given in Figure A.2(b) above. However, the M/EI diagram will be different to that of a uniform beam (shown in Figure A.2(c)), due to the perforations in the cantilever. The Young's modulus E of the material is assumed to be constant throughout the cantilever. It was shown in the previous section that the moment of area of a perforated section is smaller than that of a non-perforated section. Thus the flexural rigidity EI of a perforated section will be smaller than that of a non-perforated section. The M/EI diagram of Figure A.6(b) is obtained by dividing the bending-moment by the flexural rigidity at each point along the perforated cantilever.

To simplify calculations, the M/EI diagram can be divided into simpler shapes with known centroids. If these sections are numbered $A_1, A_2 \ldots A_N$ and the centroidal distances are given by $\overline{x}_1, \overline{x}_2 \ldots \overline{x}_N$, then the deflection is given by [2]

$$t_{P/Q} = A_1\overline{x}_1 + A_2\overline{x}_2 + \ldots + A_N\overline{x}_N \tag{A.15}$$

The M/EI diagram for the perforated cantilever can be divided into several triangular areas (refer Figure A.6(b)). Let the perforations be numbered $1, 2 \ldots N$ starting

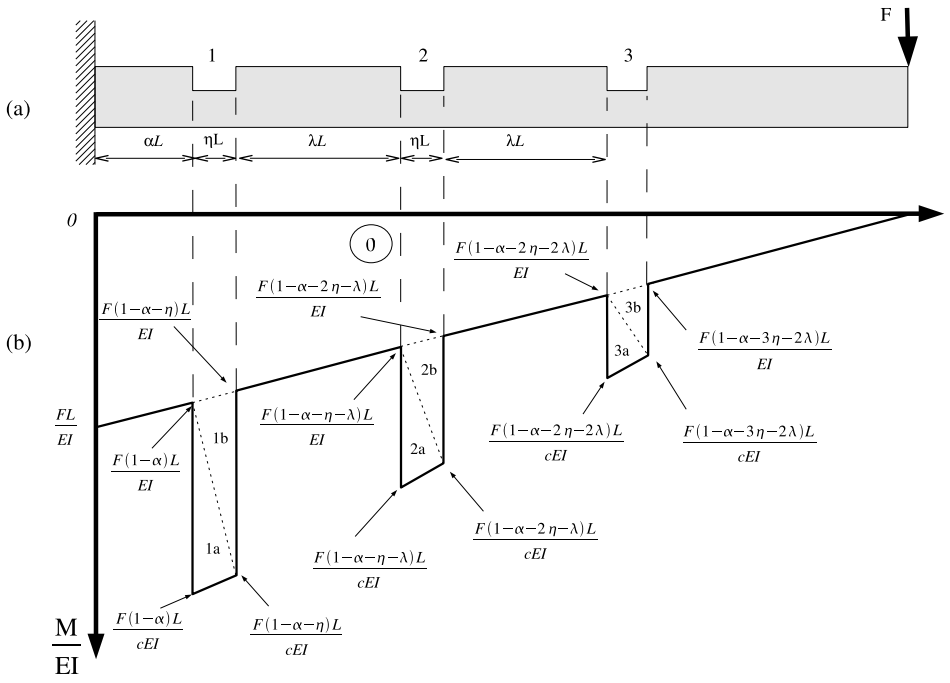

Figure A.6: (a) An end loaded perforated cantilever and (b) the resulting M/EI diagram.

from the fixed end. The triangular areas are labelled $0, 1a, 1b, 2a, 2b, \ldots Na$ and Nb, as shown in Figure A.6*b*.

The area of triangle 0 is given by

$$A_0 = \frac{1}{2}\frac{FL^2}{EI}$$

and the distance to its centroid from the free end is

$$\overline{x}_0 = \frac{2}{3}L$$

The areas of the triangles corresponding to the perforations can be determined as follows.

$$\begin{aligned} A_{1a} &= \frac{1}{2}\eta L\left[\frac{F(1-\alpha)L}{EI}\left(\frac{1}{\chi}-1\right)\right] \\ &= \frac{1}{2}\frac{FL^2}{EI}\left[(1-\alpha)\left(\frac{1-\chi}{\chi}\right)\eta\right] \end{aligned}$$

$$
\begin{aligned}
A_{2a} &= \frac{1}{2}\eta L\left[\frac{F(1-\alpha-\eta-\lambda)L}{EI}\left(\frac{1}{\chi}-1\right)\right] \\
&= \frac{1}{2}\frac{FL^2}{EI}\left[(1-\alpha-\eta-\lambda)\left(\frac{1-\chi}{\chi}\right)\eta\right] \\
A_{3a} &= \frac{1}{2}\eta L\left[\frac{F(1-\alpha-2\eta-2\lambda)L}{EI}\left(\frac{1}{\chi}-1\right)\right] \\
&= \frac{1}{2}\frac{FL^2}{EI}\left[(1-\alpha-2\eta-2\lambda)\left(\frac{1-\chi}{\chi}\right)\eta\right] \\
&\vdots
\end{aligned}
$$

By following this pattern, the area of triangle ia is given by

$$
A_{ia} = \frac{1}{2}\frac{FL^2}{EI}\left[\Big(1-\alpha-(i-1)\eta-(i-1)\lambda\Big)\left(\frac{1-\chi}{\chi}\right)\eta\right] \tag{A.16}
$$

In a similar manner,

$$
\begin{aligned}
A_{1b} &= \frac{1}{2}\eta L\left[\frac{F(1-\alpha-\eta)L}{EI}\left(\frac{1}{\chi}-1\right)\right] \\
&= \frac{1}{2}\frac{FL^2}{EI}\left[(1-\alpha-\eta)\left(\frac{1-\chi}{\chi}\right)\eta\right] \\
A_{2b} &= \frac{1}{2}\eta L\left[\frac{F(1-\alpha-2\eta-\lambda)L}{EI}\left(\frac{1}{\chi}-1\right)\right] \\
&= \frac{1}{2}\frac{FL^2}{EI}\left[(1-\alpha-2\eta-\lambda)\left(\frac{1-\chi}{\chi}\right)\eta\right] \\
A_{3b} &= \frac{1}{2}\eta L\left[\frac{F(1-\alpha-3\eta-2\lambda)L}{EI}\left(\frac{1}{\chi}-1\right)\right] \\
&= \frac{1}{2}\frac{FL^2}{EI}\left[(1-\alpha-3\eta-2\lambda)\left(\frac{1-\chi}{\chi}\right)\eta\right] \\
&\vdots
\end{aligned}
$$

By following this pattern, the area of triangle ib is given by

$$
A_{ib} = \frac{1}{2}\frac{FL^2}{EI}\left[\Big(1-\alpha-i\eta-(i-1)\lambda\Big)\left(\frac{1-\chi}{\chi}\right)\eta\right] \tag{A.17}
$$

The distances to the centroids of the triangles from the free end can be obtained as

follows.

$$\begin{aligned}
\overline{x}_{1a} &= \left(1-\alpha-\frac{1}{3}\eta\right)L \\
\overline{x}_{2a} &= \left(1-\alpha-\lambda-\eta-\frac{1}{3}\eta\right)L \\
&= \left(1-\alpha-\lambda-\frac{4}{3}\eta\right)L \\
\overline{x}_{3a} &= \left(1-\alpha-2\lambda-2\eta-\frac{1}{3}\eta\right)L \\
&= \left(1-\alpha-2\lambda-\frac{7}{3}\eta\right)L \\
&\vdots
\end{aligned}$$

By following this pattern, the distance to the centroid of triangle ia is given by

$$\overline{x}_{ia} = \left(1-\alpha-(i-1)\lambda-\frac{(3i-2)}{3}\eta\right)L \tag{A.18}$$

Similarly,

$$\begin{aligned}
\overline{x}_{1b} &= \left(1-\alpha-\frac{2}{3}\eta\right)L \\
\overline{x}_{2b} &= \left(1-\alpha-\lambda-\eta-\frac{1}{3}\eta\right)L \\
&= \left(1-\alpha-\lambda-\frac{5}{3}\eta\right)L \\
\overline{x}_{3b} &= \left(1-\alpha-2\lambda-2\eta-\frac{1}{3}\eta\right)L \\
&= \left(1-\alpha-2\lambda-\frac{8}{3}\eta\right)L \\
&\vdots
\end{aligned}$$

Following the pattern, the distance to the centroid of triangle ib is given by

$$\overline{x}_{ib} = \left(1-\alpha-(i-1)\lambda-\frac{(3i-1)}{3}\eta\right)L \tag{A.19}$$

Now the deflection of the perforated microcantilever due to a point load at the free end can be determined:

$$t_{\text{pl}} = A_0\overline{x}_0 + \sum_{i=1}^{N} A_{ia}\cdot\overline{x}_{ia} + \sum_{i=1}^{N} A_{ib}\cdot\overline{x}_{ib}$$

After some careful simplifications, the following expression can be obtained :

$$t_{\mathrm{pl}} = \frac{FL^3}{3EI}\Bigg[1 + \frac{N\eta}{2}\left(\frac{1-\chi}{\chi}\right)\Big\{2N^2(\eta+\lambda)^2 + 3N(\eta+\lambda)\lambda + 6\big(1-\alpha-N\left(\eta+\lambda\right)\big)(1-\alpha+\lambda) + \lambda(\lambda-\eta)\Big\}\Bigg] \tag{A.20}$$

The deflection of a uniform cantilever with a point load applied at the free end is given by $t_{\mathrm{pl,u}} = \frac{FL^3}{3EI}$. Therefore, the deflection of a perforated microcantilever with a point load at the free end can be expressed as follows:

$$t_{\mathrm{pl}} = \psi_{\mathrm{pl,N}} \cdot t_{\mathrm{pl,u}} \tag{A.21a}$$

where,

$$\psi_{\mathrm{pl,N}} = \Bigg[1 + \frac{N\eta}{2}\left(\frac{1-\chi}{\chi}\right)\Big\{2N^2(\eta+\lambda)^2 + 3N(\eta+\lambda)\lambda + 6\big(1-\alpha-N\left(\eta+\lambda\right)\big)(1-\alpha+\lambda) + \lambda(\lambda-\eta)\Big\}\Bigg] \tag{A.21b}$$

If there are no perforations, $N = 0$. In that case $\psi_{\mathrm{pl,N}} = 1$, and the deflection equals that of a uniform cantilever.

Cantilever with a single perforation

If the cantilever has only a single perforation, $N = 1$. Then the above model reduces to

$$t_{\mathrm{pl}} = \psi_{\mathrm{pl}} \cdot t_{\mathrm{pl,u}} \tag{A.22a}$$

where,

$$\psi_{\mathrm{pl}} = 1 + 3\eta\left(\frac{1-\chi}{\chi}\right)\left\{(1-\alpha)^2 + \eta\left(\frac{1}{3}\eta + \alpha - 1\right)\right\} \tag{A.22b}$$

A.2.3 Model for deflection with surface stress

In this section, analytical expressions are developed to describe the deflection of perforated microcantilevers that have a differential surface stress between its top and bottom faces. To keep the surface stress acting on a uniform surface, the stress is assumed to develop on the unmodified face of the cantilever.

The surface stress σ is a force per unit length, with units Nm^{-1}. Suppose a uniform surface stress σ acts on one face of a microcantilever. Then the resultant tangential force in the axial direction due to the surface stress is $\sigma \cdot b$, where b is the width of the cantilever. Refer Figure A.7. If the neutral axis at a cross-section of the microcantilever is at a depth of $\overline{y}$, this tangential force can be translated into an equivalent concentrated axial force σb acting along the neutral axis of the beam, and a moment $M = \sigma b \overline{y}$. This bending-moment can be used in the moment–area method to derive an expression for the deflection of perforated microcantilevers.

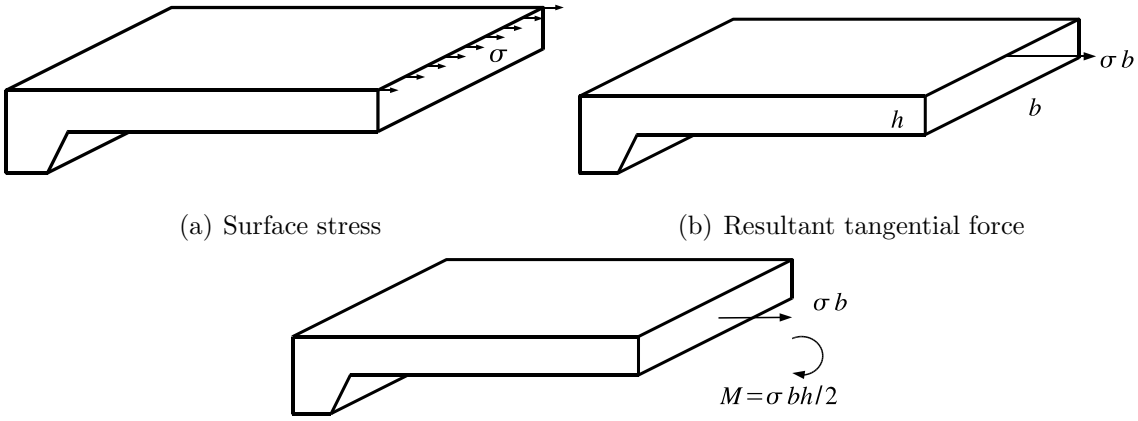

(a) Surface stress

(b) Resultant tangential force

(c) Equivalent axial force and moment

Figure A.7: Modelling surface stress. (a) The surface stress σ is a force per unit length. (b) The resultant tangential force, that can be translated into (c) an equivalent axial force and a moment.

When a uniform microcantilever is considered, $\overline{y} = h/2$, and the moment is given by $M = \sigma bh/2$ [4, 5, 6].

When a perforated microcantilever is considered, the location of the neutral axis at perforated sections will be different to that at unperforated sections. The distance to the neutral axis from the unmodified face at any cross-section along the beam can be obtained from Equation (A.12), and the moment can then be determined:

$$\begin{aligned} M &= \sigma b \overline{y} \\ &= \sigma b \cdot \frac{h\left(\frac{1}{2} - \beta\gamma(1 - \frac{\gamma}{2})\right)}{1 - \beta\gamma} \end{aligned} \tag{A.23}$$

For any value of β and γ between 0 and 1, $\overline{y}$ is always less than or equal to $h/2$. Thus the moment at perforated sections of the microcantilever is always less than the moment at unperforated sections. See Figure A.9(b).

Using the moment of area from Equation (A.14b), the expression for M/EI of a perforated section can be obtained:

$$\begin{aligned} \left(\frac{M}{EI}\right)_c &= \frac{\Delta\sigma b\overline{y}}{E\chi I} \\ &= \frac{\Delta\sigma bh}{EI}\left(\frac{\frac{1}{2} - \beta\gamma(1 - \frac{\gamma}{2})}{1 - \beta\gamma}\right)\left(\frac{1 - \beta\gamma}{1 - 4\beta\gamma + 6\beta\gamma^2 - 4\beta\gamma^3 + \beta^2\gamma^4}\right) \\ &= \frac{\Delta\sigma bh}{EI}\frac{\left(\frac{1}{2} - \beta\gamma(1 - \frac{\gamma}{2})\right)}{(1 - 4\beta\gamma + 6\beta\gamma^2 - 4\beta\gamma^3 + \beta^2\gamma^4)} \end{aligned} \tag{A.24}$$

At unperforated sections,

$$\left(\frac{M}{EI}\right)_u = \frac{\Delta\sigma bh}{2EI} \tag{A.25}$$

which leads to the result

$$\left(\frac{M}{EI}\right)_c = \left(\frac{M}{EI}\right)_u \cdot \frac{\left(1 - \beta\gamma(2 - \gamma)\right)}{(1 - 4\beta\gamma + 6\beta\gamma^2 - 4\beta\gamma^3 + \beta^2\gamma^4)} \tag{A.26}$$

Now, let $f(\beta, \gamma) = \dfrac{\left(1 - \beta\gamma(2 - \gamma)\right)}{(1 - 4\beta\gamma + 6\beta\gamma^2 - 4\beta\gamma^3 + \beta^2\gamma^4)}$

A 3-dimensional plot of $f(\beta, \gamma)$ versus β and γ is shown in Figure A.8. As can

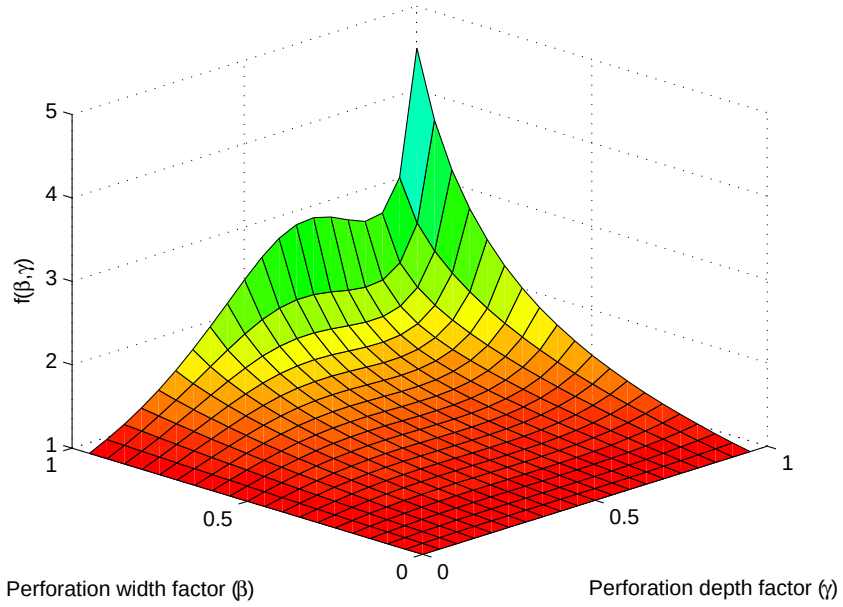

Figure A.8: Variation of $f(\beta, \gamma)$ with β and γ.

be seen from the plot, $f(\beta, \gamma)$ is always greater than or equal to 1. Referring to Equation (A.26), it can be deduced that for every value of β and γ, M/EI of perforated sections is greater than the M/EI of unperforated sections. Thus the M/EI diagram of a perforated microcantilever with a surface stress acting on it takes the form shown in Figure A.9(c).

The M/EI diagram of Figure A.9(c) can be divided into sections 0,1,2 and 3 as shown. The areas of sections 1,2 and 3 are identical. The areas of each section are as follows:

$$A_0 = \frac{\Delta\sigma bh}{2EI} \cdot L$$

$$\begin{aligned} A_1 = A_2 = \ldots = A_N &= \frac{\Delta\sigma bh}{2EI}\left[\frac{2\overline{y}}{\chi} - 1\right] \cdot \eta L \\ &= \frac{\Delta\sigma bh}{2EI}\beta\gamma\left(\frac{2 - 5\gamma + 4\gamma^2 - \beta\gamma^3}{1 - 4\beta\gamma + 6\beta\gamma^2 - 4\beta\gamma^3 + \beta^2\gamma^4}\right) \end{aligned}$$

The distances to the centroids of the sections from the free end are given by:

$$\overline{x}_0 = \frac{L}{2}$$

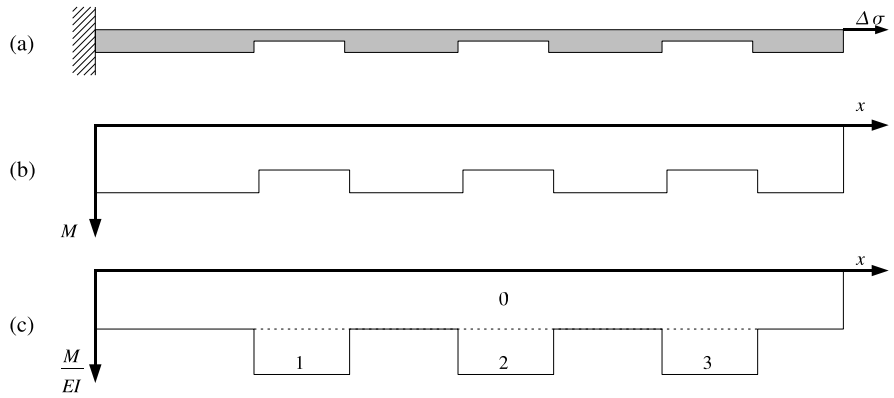

Figure A.9: (a) Microcantilever with a surface stress acting on its top face, (b) its moment diagram and (c) the resulting M/EI diagram.

$$\overline{x}_1 = \left(1 - \alpha - \frac{\eta}{2}\right) L$$
$$\overline{x}_2 = \left(1 - \alpha - \frac{3\eta}{2} - \lambda\right) L$$
$$\overline{x}_3 = \left(1 - \alpha - \frac{5\eta}{2} - 2\lambda\right) L$$
$$\vdots$$

Following the pattern,

$$\overline{x}_N = \left(1 - \alpha - \frac{(2N-1)\eta}{2} - (N-1)\lambda\right) L$$

The deflection of the microcantilever is then given by

$$t_{\text{ss}} = A_0\overline{x}_0 + A_1\overline{x}_1 + A_2\overline{x}_2 \cdots + A_N\overline{x}_N$$

Substituting expressions for areas and centroids and simplifying gives

$$t_{\text{ss}} = \frac{\Delta\sigma b h L^2}{4EI}\left[1 + N\eta\beta\gamma\Big(2(1-\alpha) - \lambda(N-1) - N\eta\Big)\right.$$
$$\left.\left(\frac{2 - 5\gamma + 4\gamma^2 - \beta\gamma^3}{1 - 4\beta\gamma + 6\beta\gamma^2 - 4\beta\gamma^3 + \beta^2\gamma^4}\right)\right]$$

The stresses considered so far have been unidirectional, acting along the length of the cantilever. However, when a surface stress develops on a cantilever due to receptor-analyte bindings, the stress is biaxial. When biaxial stresses are considered, the Young's Modulus E is replaced by $E/(1-\nu)$ [4]. Substituting this equivalent Young's modulus and using $I = \frac{1}{12}bh^3$,

$$t_{\text{ss}} = \frac{3(1-\nu)\Delta\sigma L^2}{Eh^2}\left[1 + N\eta\beta\gamma\Big(2(1-\alpha) - \lambda(N-1) - N\eta\Big) \left(\frac{2-5\gamma+4\gamma^2-\beta\gamma^3}{1-4\beta\gamma+6\beta\gamma^2-4\beta\gamma^3+\beta^2\gamma^4}\right)\right] \tag{A.27}$$

The cantilever can be reduced to an unperforated beam by making at least one perforation parameter (ie, β, γ, η or N) zero. This gives the deflection of an unperforated microcantilever:

$$t_{\text{ss,u}} = \frac{3(1-\nu)\Delta\sigma L^2}{Eh^2}$$

This is the equation commonly referred to as Stoney's Equation in the literature. Combining with Equation (A.27), this gives

$$t_{\text{ss}} = \psi_{\text{ss,N}} \cdot t_{\text{ss,u}}$$

where

$$\psi_{\text{ss,N}} = \left[1+N\eta\beta\gamma\Big(2(1-\alpha)-\lambda(N-1)-N\eta\Big)\left(\frac{2-5\gamma+4\gamma^2-\beta\gamma^3}{1-4\beta\gamma+6\beta\gamma^2-4\beta\gamma^3+\beta^2\gamma^4}\right)\right] \tag{A.28}$$

Cantilever with a single perforation

If the cantilever has only a single perforation, $N = 1$. Then the above model reduces to

$$t_{\text{ss}} = \psi_{\text{ss}} \cdot t_{\text{ss,u}} \tag{A.29a}$$

where,

$$\psi_{\text{ss}} = \left[1 + \eta\beta\gamma\Big(2(1-\alpha) - \eta\Big)\left(\frac{2-5\gamma+4\gamma^2-\beta\gamma^3}{1-4\beta\gamma+6\beta\gamma^2-4\beta\gamma^3+\beta^2\gamma^4}\right)\right] \tag{A.29b}$$

A.3 Analytical models for resonant frequency

The Rayleigh–Ritz method [7, 8, 9] can be used to obtain an approximate solution for the resonant frequency of structures with complex geometries. This method is based upon the principle of conservation of energy, and is an extension of Rayleigh's method.

A.3.1 Rayleigh–Ritz method

The deflection curve Y of a cantilever beam can be expressed by the general form [10]

$$Y = a_1\varphi_1(x) + a_2\varphi_2(x) + a_3\varphi_3(x) + \cdots \tag{A.30}$$

where x is measured from the fixed end of the microcantilever beam, and $\varphi_1(x), \varphi_2(x), \ldots$ are functions satisfying the boundary conditions. The maximum potential energy V and the maximum kinetic energy T of a vibrating beam can be obtained from the deflection curve Y using the following expressions [10]

$$V = \frac{1}{2}\int_0^L EI\left(\frac{\mathrm{d}^2Y}{\mathrm{d}x^2}\right)^2 \mathrm{d}x \tag{A.31}$$

$$T = \frac{\omega^2}{2}\int_0^L A\rho Y^2 \mathrm{d}x \tag{A.32}$$

where A is the cross-sectional area of the cantilever, ρ is the density of the material and ω is the angular natural frequency of vibration. As before, E is the Young's modulus, I is the moment of area, and L is the length of the cantilever. By the principle of conservation of energy, the maximum potential energy should be equal to the maximum kinetic energy. Thus by equating the above two expressions, the

resonant frequency can be obtained:

$$\omega^2 = \frac{\int_0^L EI \left(\frac{\mathrm{d}^2 Y}{\mathrm{d}x^2}\right)^2 \mathrm{d}x}{\int_0^L A\rho Y^2 \mathrm{d}x} \tag{A.33}$$

$$\omega = \sqrt{\frac{\int_0^L EI \left(\frac{\mathrm{d}^2 Y}{\mathrm{d}x^2}\right)^2 \mathrm{d}x}{\int_0^L A\rho Y^2 \mathrm{d}x}} \tag{A.34}$$

Substituting $f = \frac{1}{2\pi}\omega$,

$$f = \frac{1}{2\pi}\sqrt{\frac{\int_0^L EI \left(\frac{\mathrm{d}^2 Y}{\mathrm{d}x^2}\right)^2 \mathrm{d}x}{\int_0^L A\rho Y^2 \mathrm{d}x}} \tag{A.35}$$

This is the Rayleigh–Ritz method for determining the resonant frequency, and is applied below to perforated microcantilevers.

A.3.2 Model for resonant frequency

For a microcantilever, the boundary conditions are that the deflection at the fixed end, deflection gradient of the fixed end, the bending-moment at the free end and the shear force at the free end are all equal to zero [10]. If x is measured from the fixed end, these boundary conditions can be expressed as [8]:

$$\begin{aligned} (Y)_{x=0} &= 0 & \left(\frac{\mathrm{d}Y}{\mathrm{d}x}\right)_{x=0} &= 0 \\ \left(EI\,\frac{\mathrm{d}^2 Y}{\mathrm{d}x^2}\right)_{x=L} &= 0 & \frac{\mathrm{d}}{\mathrm{d}x}\left(EI\,\frac{\mathrm{d}^2 Y}{\mathrm{d}x^2}\right)_{x=L} &= 0 \end{aligned} \tag{A.36}$$

These boundary conditions are independent of the shape and structure of the microcantilever, and hold true for both uniform and perforated beams. The simplest expression for Y that satisfies all of these conditions was found to be

$$Y = \frac{x^4}{L^4} - \frac{4x^3}{L^3} + \frac{6x^2}{L^2} \tag{A.37}$$

Suppose a cantilever with an array of perforations as in section A.1 is considered. As demonstrated in section A.2.1, the moment of area of a cross-section with n

perforations of width $\beta' b$ each is equal to the MOA of a cross-section with a single perforation of width $n\beta' b$. The area of a cross-section with multiple perforations is equal to the cross-sectional area of the equivalent shape with a single perforation. Therefore, a single line of perforations along the length of the cantilever can be used with the Rayleigh–Ritz method as well to represent an array of perforations. This reduced model of perforation is shown in Figure A.4.

The Young's modulus and the density of the material were assumed to be constant throughout the beam. The moment of area I and the cross-sectional area A vary along the length of the beam due to the perforations. Using equations (A.35) and (A.37), the resonant frequency of a perforated microcantilever can be derived.

The cantilever can be divided into separate sections, as shown in Figure A.10. The values of distance x, moments of area, and cross-sectional areas of each section are presented in Table A.1.

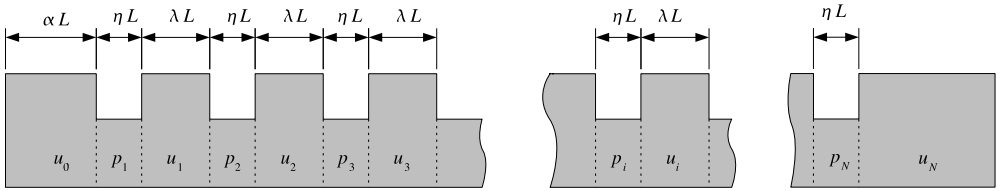

Figure A.10: Microcantilever with multiple perforations, divided into separate sections.

Table A.1: Parameters to calculate the resonant frequency of a perforated cantilever.

sec$^{\underline{n}}$	u_0	p_1	u_1	p_2	u_2	p_3	u_3	...	p_i	u_i	...	u_N
left	0	α	$\alpha+\eta$	$\alpha+\eta+\lambda$	$\alpha+2\eta+\lambda$	$\alpha+2\eta+2\lambda$	$\alpha+3\eta+2\lambda$	...	$\alpha+(i-1)(\eta+\lambda)$	$\alpha+i\eta+(i-1)\lambda$		$\alpha+N\eta+(N-1)\lambda$
right	α	$\alpha+\eta$	$\alpha+\eta+\lambda$	$\alpha+2\eta+\lambda$	$\alpha+2\eta+2\lambda$	$\alpha+3\eta+2\lambda$	$\alpha+3\eta+3\lambda$	...	$\alpha+i\eta+(i-1)\lambda$	$\alpha+i(\eta+\lambda)$		1
MOA	I	χI	I	χI	I	χI	I		χI	I		I
Area	bh	$(1-\beta\gamma)bh$	bh	$(1-\beta\gamma)bh$	bh	$(1-\beta\gamma)bh$	bh		$(1-\beta\gamma)bh$	bh		bh

Equation (A.33) can be written in the following alternate form:

$$\begin{aligned}\omega^2 &= \frac{\int_0^L EI\left(\frac{\mathrm{d}^2Y}{\mathrm{d}x^2}\right)^2 \mathrm{d}x}{\int_0^L A\rho Y^2 \mathrm{d}x} \\ &= \frac{E}{\rho}\frac{\int_0^L I\left(\frac{\mathrm{d}^2Y}{\mathrm{d}x^2}\right)^2 \mathrm{d}x}{\int_0^L AY^2 \mathrm{d}x} \\ &= \frac{E}{\rho}\frac{\text{Numerator}}{\text{Denominator}}\end{aligned} \tag{A.38}$$

The *Numerator* and *Denominator* parts are considered separately below.

$$\begin{aligned}\text{Num} &= \int_0^L I\left(\frac{\mathrm{d}^2Y}{\mathrm{d}x^2}\right)^2 \mathrm{d}x \\ &= \int_0^{\alpha L} I\left(\frac{\mathrm{d}^2Y}{\mathrm{d}x^2}\right)^2 \mathrm{d}x + \int_{\alpha L}^{(\alpha+\eta)L} \chi I\left(\frac{\mathrm{d}^2Y}{\mathrm{d}x^2}\right)^2 \mathrm{d}x + \int_{(\alpha+\eta)L}^{(\alpha+\eta+\lambda)L} I\left(\frac{\mathrm{d}^2Y}{\mathrm{d}x^2}\right)^2 \mathrm{d}x \\ &\quad + \int_{(\alpha+\eta+\lambda)L}^{(\alpha+2\eta+\lambda)L} \chi I\left(\frac{\mathrm{d}^2Y}{\mathrm{d}x^2}\right)^2 \mathrm{d}x + \int_{(\alpha+2\eta+\lambda)L}^{(\alpha+2\eta+2\lambda)L} I\left(\frac{\mathrm{d}^2Y}{\mathrm{d}x^2}\right)^2 \mathrm{d}x + \ldots\end{aligned}$$

Using the expression for the deflection curve Y given above in Equation (A.37), the following is obtained.

$$\begin{aligned}Y &= \frac{x^4}{L^4} - \frac{4x^3}{L^3} + \frac{6x^2}{L^2} \\ \frac{\mathrm{d}Y}{\mathrm{d}x} &= \frac{4x^3}{L^4} - \frac{12x^2}{L^3} + \frac{12x}{L^2} \\ \frac{\mathrm{d}^2Y}{\mathrm{d}x^2} &= \frac{12x^2}{L^4} - \frac{24x}{L^3} + \frac{12}{L^2} \\ \left(\frac{\mathrm{d}^2Y}{\mathrm{d}x^2}\right)^2 &= \frac{144x^4}{L^8} - \frac{576x^3}{L^7} + \frac{864x^2}{L^6} - \frac{576x}{L^5} + \frac{144}{L^4} \\ \int\left(\frac{\mathrm{d}^2Y}{\mathrm{d}x^2}\right)^2 \mathrm{d}x &= \frac{144x^5}{5L^8} - \frac{144x^4}{L^7} + \frac{288x^3}{L^6} - \frac{288x^2}{L^5} + \frac{144x}{L^4} \\ &= 144\left[\frac{x^5}{5L^8} - \frac{x^4}{L^7} + \frac{2x^3}{L^6} - \frac{2x^2}{L^5} + \frac{x}{L^4}\right]\end{aligned} \tag{A.39}$$

Using the result of (A.39) and the limits from Table A.1,

$$
\begin{aligned}
\text{Num} = 144I &\left[\frac{x^5}{5L^8} - \frac{x^4}{L^7} + \frac{2x^3}{L^6} - \frac{2x^2}{L^5} + \frac{x}{L^4}\right]_0^{\alpha L} \\
&+ 144\chi I \left[\frac{x^5}{5L^8} - \frac{x^4}{L^7} + \frac{2x^3}{L^6} - \frac{2x^2}{L^5} + \frac{x}{L^4}\right]_{\alpha L}^{(\alpha+\eta)L} \\
&+ 144I \left[\frac{x^5}{5L^8} - \frac{x^4}{L^7} + \frac{2x^3}{L^6} - \frac{2x^2}{L^5} + \frac{x}{L^4}\right]_{(\alpha+\eta)L}^{(\alpha+\eta+\lambda)L} \\
&+ 144\chi I \left[\frac{x^5}{5L^8} - \frac{x^4}{L^7} + \frac{2x^3}{L^6} - \frac{2x^2}{L^5} + \frac{x}{L^4}\right]_{(\alpha+\eta+\lambda)L}^{(\alpha+2\eta+\lambda)L} \\
&+ 144I \left[\frac{x^5}{5L^8} - \frac{x^4}{L^7} + \frac{2x^3}{L^6} - \frac{2x^2}{L^5} + \frac{x}{L^4}\right]_{(\alpha+2\eta+\lambda)L}^{(\alpha+2\eta+2\lambda)L} \\
&+ 144\chi I \left[\frac{x^5}{5L^8} - \frac{x^4}{L^7} + \frac{2x^3}{L^6} - \frac{2x^2}{L^5} + \frac{x}{L^4}\right]_{(\alpha+2\eta+2\lambda)L}^{(\alpha+3\eta+2\lambda)L} \\
&+ 144I \left[\frac{x^5}{5L^8} - \frac{x^4}{L^7} + \frac{2x^3}{L^6} - \frac{2x^2}{L^5} + \frac{x}{L^4}\right]_{(\alpha+3\eta+2\lambda)L}^{(\alpha+3\eta+3\lambda)L} \\
&\vdots \\
&+ 144\chi I \left[\frac{x^5}{5L^8} - \frac{x^4}{L^7} + \frac{2x^3}{L^6} - \frac{2x^2}{L^5} + \frac{x}{L^4}\right]_{(\alpha+(i-1)(\eta+\lambda))L}^{(\alpha+i\eta+(i-1)\lambda)L} \\
&+ 144I \left[\frac{x^5}{5L^8} - \frac{x^4}{L^7} + \frac{2x^3}{L^6} - \frac{2x^2}{L^5} + \frac{x}{L^4}\right]_{(\alpha+i\eta+(i-1)\lambda)L}^{(\alpha+i(\eta+\lambda))L} \\
&\vdots \\
&+ 144I \left[\frac{x^5}{5L^8} - \frac{x^4}{L^7} + \frac{2x^3}{L^6} - \frac{2x^2}{L^5} + \frac{x}{L^4}\right]_{(\alpha+N\eta+(N-1)\lambda)L}^{L}
\end{aligned}
$$

This equation can be simplified and rearranged as

$$\begin{aligned}\text{Num} = \frac{144I}{5L^3}\Bigg[1 + 5(1-\chi)\Bigg\{\Bigg(\frac{1}{5}\alpha^5 - \alpha^4 + 2\alpha^3 - 2\alpha^2 + \alpha\Bigg) \\ + \frac{1}{5}\sum_{i=1}^{N-1}\big(\alpha + i(\eta+\lambda)\big)^5 - \sum_{i=1}^{N-1}\big(\alpha + i(\eta+\lambda)\big)^4 \\ + 2\sum_{i=1}^{N-1}\big(\alpha + i(\eta+\lambda)\big)^3 - 2\sum_{i=1}^{N-1}\big(\alpha + i(\eta+\lambda)\big)^2 \\ + \sum_{i=1}^{N-1}\big(\alpha + i(\eta+\lambda)\big)\Bigg\} - 5(1-\chi)\Bigg\{\frac{1}{5}\sum_{i=1}^{N}\big((\alpha-\lambda) + i(\eta+\lambda)\big)^5 \\ - \sum_{i=1}^{N}\big((\alpha-\lambda) + i(\eta+\lambda)\big)^4 + 2\sum_{i=1}^{N}\big((\alpha-\lambda) + i(\eta+\lambda)\big)^3 \\ -2\sum_{i=1}^{N}\big((\alpha-\lambda) + i(\eta+\lambda)\big)^2 + \sum_{i=1}^{N}\big((\alpha-\lambda) + i(\eta+\lambda)\big)\Bigg\}\Bigg]\end{aligned} \tag{A.40}$$

The expression for the *Denominator* is derived next.

$$\begin{aligned}\text{Den} &= \int_0^L AY^2\mathrm{d}x \\ &= \int_0^{\alpha L} bhY^2\mathrm{d}x + \int_{\alpha L}^{(\alpha+\eta)L}(1-\beta\gamma)bhY^2\mathrm{d}x + \int_{(\alpha+\eta)L}^{(\alpha+\eta+\lambda)L} bhY^2\mathrm{d}x \\ &\quad + \int_{(\alpha+\eta+\lambda)L}^{(\alpha+2\eta+\lambda)L}(1-\beta\gamma)bhY^2\mathrm{d}x + \int_{(\alpha+2\eta+\lambda)L}^{(\alpha+2\eta+2\lambda)L} bhY^2\mathrm{d}x + \ldots\end{aligned}$$

Using the expression for Y from Equation (A.37) above, the following can be obtained:

$$\begin{aligned}Y &= \frac{x^4}{L^4} - \frac{4x^3}{L^3} + \frac{6x^2}{L^2} \\ Y^2 &= \frac{x^8}{L^8} - \frac{8x^7}{L^7} + \frac{28x^6}{L^6} - \frac{48x^5}{L^5} + \frac{36x^4}{L^4} \\ \int Y^2\mathrm{d}x &= \frac{x^9}{9L^8} - \frac{x^8}{L^7} + \frac{4x^7}{L^6} - \frac{8x^6}{L^5} + \frac{36x^5}{5L^4}\end{aligned} \tag{A.41}$$

Using the result of (A.41) and the limits from Table A.1,

$$
\begin{aligned}
\text{Den} = {} & bh\left[\frac{x^9}{9L^8}-\frac{x^8}{L^7}+\frac{4x^7}{L^6}-\frac{8x^6}{L^5}+\frac{36x^5}{5L^4}\right]_0^{\alpha L} \\
& +(1-\beta\gamma)bh\left[\frac{x^9}{9L^8}-\frac{x^8}{L^7}+\frac{4x^7}{L^6}-\frac{8x^6}{L^5}+\frac{36x^5}{5L^4}\right]_{\alpha L}^{(\alpha+\eta)L} \\
& +bh\left[\frac{x^9}{9L^8}-\frac{x^8}{L^7}+\frac{4x^7}{L^6}-\frac{8x^6}{L^5}+\frac{36x^5}{5L^4}\right]_{(\alpha+\eta)L}^{(\alpha+\eta+\lambda)L} \\
& +(1-\beta\gamma)bh\left[\frac{x^9}{9L^8}-\frac{x^8}{L^7}+\frac{4x^7}{L^6}-\frac{8x^6}{L^5}+\frac{36x^5}{5L^4}\right]_{(\alpha+\eta+\lambda)L}^{(\alpha+2\eta+\lambda)L} \\
& +bh\left[\frac{x^9}{9L^8}-\frac{x^8}{L^7}+\frac{4x^7}{L^6}-\frac{8x^6}{L^5}+\frac{36x^5}{5L^4}\right]_{(\alpha+2\eta+\lambda)L}^{(\alpha+2\eta+2\lambda)L} \\
& +(1-\beta\gamma)bh\left[\frac{x^9}{9L^8}-\frac{x^8}{L^7}+\frac{4x^7}{L^6}-\frac{8x^6}{L^5}+\frac{36x^5}{5L^4}\right]_{(\alpha+2\eta+2\lambda)L}^{(\alpha+3\eta+2\lambda)L} \\
& +bh\left[\frac{x^9}{9L^8}-\frac{x^8}{L^7}+\frac{4x^7}{L^6}-\frac{8x^6}{L^5}+\frac{36x^5}{5L^4}\right]_{(\alpha+3\eta+2\lambda)L}^{(\alpha+3\eta+3\lambda)L} \\
& \vdots \\
& +(1-\beta\gamma)bh\left[\frac{x^9}{9L^8}-\frac{x^8}{L^7}+\frac{4x^7}{L^6}-\frac{8x^6}{L^5}+\frac{36x^5}{5L^4}\right]_{(\alpha+(i-1)(\eta+\lambda))L}^{(\alpha+i\eta+(i-1)\lambda)L} \\
& +bh\left[\frac{x^9}{9L^8}-\frac{x^8}{L^7}+\frac{4x^7}{L^6}-\frac{8x^6}{L^5}+\frac{36x^5}{5L^4}\right]_{(\alpha+i\eta+(i-1)\lambda)L}^{(\alpha+i(\eta+\lambda))L} \\
& \vdots \\
& +bh\left[\frac{x^9}{9L^8}-\frac{x^8}{L^7}+\frac{4x^7}{L^6}-\frac{8x^6}{L^5}+\frac{36x^5}{5L^4}\right]_{(\alpha+N\eta+(N-1)\lambda)L}^{L}
\end{aligned}
$$

This expression can be simplified and rearranged as

$$\begin{aligned}\text{Den} = \frac{104bh}{45L}\Bigg[1 + \frac{45\beta\gamma}{104}\Bigg\{\Bigg(\frac{1}{9}\alpha^9 - \alpha^8 + 4\alpha^7 - 8\alpha^6 + \frac{36}{5}\alpha^5\Bigg) \\ + \frac{1}{9}\sum_{i=1}^{N-1}\big(\alpha + i(\eta+\lambda)\big)^9 - \sum_{i=1}^{N-1}\big(\alpha + i(\eta+\lambda)\big)^8 \\ + 4\sum_{i=1}^{N-1}\big(\alpha + i(\eta+\lambda)\big)^7 - 8\sum_{i=1}^{N-1}\big(\alpha + i(\eta+\lambda)\big)^6 \\ + \frac{36}{5}\sum_{i=1}^{N-1}\big(\alpha + i(\eta+\lambda)\big)^5\Bigg\} - \frac{45\beta\gamma}{104}\Bigg\{\frac{1}{9}\sum_{i=1}^{N}\big(\alpha - \lambda + i(\eta+\lambda)\big)^9 \\ - \sum_{i=1}^{N}\big(\alpha - \lambda + i(\eta+\lambda)\big)^8 + 4\sum_{i=1}^{N}\big(\alpha - \lambda + i(\eta+\lambda)\big)^7 \\ -8\sum_{i=1}^{N}\big(\alpha - \lambda + i(\eta+\lambda)\big)^6 + \frac{36}{5}\sum_{i=1}^{N}\big(\alpha - \lambda + i(\eta+\lambda)\big)^5\Bigg\}\Bigg]\end{aligned} \tag{A.42}$$

Now, substituting the expressions for the *Numerator* given by (A.40) and the *Denominator* given by (A.42) in Equation (A.38), the resonant frequency of the perforated microcantilever can be determined. Due to the complexity of the problem and the large amount of terms involved, a simple expression for the resonant frequency could not be obtained. However, these equations can be easily solved using mathematical analysis software such as *Matlab*. The terms of Equations (A.40) and (A.42) were coded into a *Matlab* script, and were solved to obtain the resonant frequency of a perforated cantilever. The solution contained over one hundred terms, and it is not presented here. Numerical values can be easily assigned to the parameters in *Matlab*, and numerical solutions to the resonant frequency can be obtained. The *Matlab* script used to obtain the resonant frequency of perforated cantilevers is given in Appendix B.

The simplest form of the deflection curve generally gives the resonance frequency of the fundamental mode of vibration. Even with the simplest expression for Y, analytical expressions for resonant frequency are complicated. Hence, it is not feasible to obtain models for resonant frequencies of higher modes using this approach, as the expressions then become even more complex.

Reduced model for a single perforation

When there is a single perforation, $N = 1$. In this case, a simpler analytical expression can be obtained for the resonant frequency.

$$f_0 = \frac{1}{2\pi}\sqrt{\frac{27E}{26\rho}} \cdot \frac{h}{L^2} \left[\frac{1-(1-\chi)\left[\{(\alpha+\eta)^5-\alpha^5\}-5\{(\alpha+\eta)^4-\alpha^4\}\right.}{1-\frac{45\beta\gamma}{104}\left[\frac{1}{9}\{(\alpha+\eta)^9-\alpha^9\}-\{(\alpha+\eta)^8-\alpha^8\}\right.} \right.$$
$$\left. \left. \frac{+10\{(\alpha+\eta)^3-\alpha^3\}-10\{(\alpha+\eta)^2-\alpha^2\}+5\eta\right]}{+4\{(\alpha+\eta)^7-\alpha^7\}-8\{(\alpha+\eta)^6-\alpha^6\}+\frac{36}{5}\{(\alpha+\eta)^5-\alpha^5\}\left.\right]} \right]^{1/2} \tag{A.43}$$

By making at least one dimension of the perforation (ie, β, γ or η) zero, the perforated cantilever is reduced to a uniform beam. By applying this condition to Equation (A.43), the expression for the resonant frequency of a uniform microcantilever $f_{0,\mathrm{u}}$ can be obtained.

$$f_{0,\mathrm{u}} = \frac{1}{2\pi}\sqrt{\frac{27E}{26\rho}} \cdot \frac{h}{L^2} \tag{A.44}$$

Equation (A.44) is consistent with the standard equations for the resonant frequency of rectangular cantilevers [7, 8, 9]. Thus, the resonant frequency of a microcantilever with a single perforation can be expressed as follows:

$$f_0 = f_{0,\mathrm{u}} \cdot \sqrt{\psi_{\mathrm{f}}} \tag{A.45a}$$

where ψ_{f} is given by

$$\psi_{\mathrm{f}} = \left[\frac{1-(1-\chi)\left[\{(\alpha+\eta)^5-\alpha^5\}-5\{(\alpha+\eta)^4-\alpha^4\}\right.}{1-\frac{45\beta\gamma}{104}\left[\frac{1}{9}\{(\alpha+\eta)^9-\alpha^9\}-\{(\alpha+\eta)^8-\alpha^8\}\right.} \right.$$
$$\left. \left. \frac{+10\{(\alpha+\eta)^3-\alpha^3\}-10\{(\alpha+\eta)^2-\alpha^2\}+5\eta\right]}{+4\{(\alpha+\eta)^7-\alpha^7\}-8\{(\alpha+\eta)^6-\alpha^6\}+\frac{36}{5}\{(\alpha+\eta)^5-\alpha^5\}\left.\right]} \right] \tag{A.45b}$$

The moment of area factor χ is given by Equation (A.14b)

$$\chi = \frac{1-4\beta\gamma+6\beta\gamma^2-4\beta\gamma^3+\beta^2\gamma^4}{1-\beta\gamma}$$

A.4 Deflection of tapering cantilevers

The general profile of a tapering cantilever can be expressed by the polynomial function

$$h(x) = h_b + (h_a - h_b)(x/L)^n \tag{A.46}$$

where h_a and h_b are the thicknesses of the fixed and free ends respectively, x is measured from the free end, L is the length of the cantilever and n is the order of the polynomial. Refer Figure A.11.

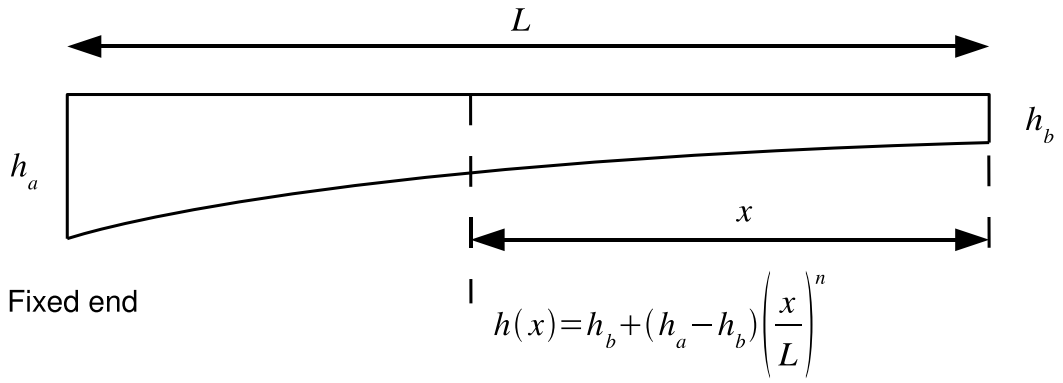

Figure A.11: The general form of a tapering cantilever.

A.4.1 Trapezoidal cantilevers

A trapezoidal cantilever is obtained by substituting $n = 1$ in Equation (A.46). Note that the cross-section at any point along a trapezoidal cantilever is rectangular. Therefore, the bending-moment at any point x can be obtained by $M = \sigma b h(x)/2$, and the moment of area can be determined from $\frac{1}{12} b[h(x)]^3$. Using the expression for $h(x)$ given in Equation (A.46) and substituting $n = 1$, the following are obtained.

$$M = \frac{\sigma b}{2}\left[h_b + \left(\frac{h_a - h_b}{L}\right)x\right] \tag{A.47}$$

$$I = \frac{1}{12}\, b\left[h_b + \left(\frac{h_a - h_b}{L}\right)x\right]^3 \tag{A.48}$$

Referring to Equation A.1 the deflection is given by

$$\begin{aligned} t &= \overline{x} \int_0^L \frac{M}{EI}\, \mathrm{d}x \\ &= \frac{\int_0^L \frac{M}{EI} x\, \mathrm{d}x}{\int_0^L \frac{M}{EI}\, \mathrm{d}x} \cdot \int_0^L \frac{M}{EI}\, \mathrm{d}x \\ &= \int_0^L \frac{M}{EI} x\, \mathrm{d}x \end{aligned} \tag{A.49}$$

Substituting the expressions for M and I,

$$t = \int_0^L \frac{\frac{\sigma b}{2}\left[h_b + \left(\frac{h_a - h_b}{L}\right) x\right]}{\frac{Eb}{12}\left[h_b + \left(\frac{h_a - h_b}{L}\right) x\right]^3}\, x\, \mathrm{d}x \tag{A.50}$$

This integration can be evaluated by substituting $u = h_b + \left(\frac{h_a - h_b}{L}\right) x$. Substituting $E/(1-\nu)$ for the Young's modulus to account for biaxial stresses as discussed above, the expression for the deflection of a trapezoidal cantilever due to a surface stress can be determined:

$$t = \frac{6\sigma(1-\nu)L^2}{E(h_a - h_b)^2}\left[\ln\left(\frac{h_a}{h_b}\right) + \frac{h_b}{h_a} - 1\right] \tag{A.51}$$

A.4.2 Quadratic (x^2 type) cantilevers

A quadratic cantilever profile is obtained by substituting $n = 2$ in Equation (A.46). The bending-moment and moment of area are then given by the following expressions.

$$M = \frac{\sigma b}{2}\left[h_b + \left(\frac{h_a - h_b}{L^2}\right) x^2\right] \tag{A.52}$$

$$I = \frac{1}{12}\, b\left[h_b + \left(\frac{h_a - h_b}{L^2}\right) x^2\right]^3 \tag{A.53}$$

By substituting M and I in Equation (A.49), the deflection can be obtained.

$$t = \int_0^L \frac{M}{EI} x \, \mathrm{d}x$$

$$t = \int_0^L \frac{\frac{\sigma b}{2}\left[h_b + \left(\frac{h_a - h_b}{L^2}\right) x^2\right]}{\frac{Eb}{12}\left[h_b + \left(\frac{h_a - h_b}{L^2}\right) x^2\right]^3} \, x \, \mathrm{d}x \tag{A.54}$$

This integration too can be evaluated by substituting $u = h_b + \left(\frac{h_a - h_b}{L}\right) x$. Substituting $E = E/(1-\nu)$, the deflection of a quadratic cantilever due to a surface stress can be determined:

$$t = \frac{3(1-\nu)\sigma L^2}{E(h_a - h_b)} \left[\frac{1}{h_b} - \frac{1}{h_a}\right] \tag{A.55}$$

A.5 Resonant frequency of a trapezoidal beam

The deflection curve given by Equation (A.37) used to determine the resonant frequency of perforated beams can be used in this case as well. Since this deflection curve assumes x to be measured from the fixed end, the expression for the profile of tapering cantilevers given by Equation (A.46) should be modified to

$$h(x) = h_a - \left(\frac{h_a - h_b}{L}\right) x \tag{A.56}$$

Then cross-sectional area A and the moment of area I at any point x along the cantilever is given by

$$A = b\left[h_a - \left(\frac{h_a - h_b}{L}\right) x\right] \tag{A.57}$$

$$I = \frac{1}{12} \, b\left[h_a - \left(\frac{h_a - h_b}{L}\right) x\right]^3 \tag{A.58}$$

Similar to earlier derivations, the *Numerator* and *Denominator* parts of Equation (A.38) are considered separately.

$$\begin{aligned}\text{Num} &= \int_0^L I \left(\frac{\mathrm{d}^2 Y}{\mathrm{d}x^2}\right)^2 \mathrm{d}x \\ &= \int_0^L \frac{1}{12}\, b \left[h_a - \left(\frac{h_a - h_b}{L}\right) x\right]^3 \left[\frac{12x^2}{L^4} - \frac{24x}{L^3} + \frac{12}{L^2}\right]^2 \mathrm{d}x \end{aligned} \tag{A.59}$$

This can be solved using a mathematical software tool such as *Maple* to give

$$\text{Num} = \frac{3b}{70}\left[\frac{35h_a^3 + 15h_a^2 h_b + 5h_a h_b^2 + h_b^3}{L^3}\right] \tag{A.60}$$

The *Denominator* is derived next.

$$\begin{aligned}\text{Den} &= \int_0^L AY^2 \,\mathrm{d}x \\ &= \int_0^L b \left[h_a - \left(\frac{h_a - h_b}{L}\right) x\right] \left[\frac{x^4}{L^4} - \frac{4x^3}{L^3} + \frac{6x^2}{L^2}\right]^2 \mathrm{d}x \end{aligned} \tag{A.61}$$

which can be solved to give

$$\text{Den} = \frac{8bL}{315}(18h_a + 73h_b) \tag{A.62}$$

Substituting *Num* and *Den* in Equation (A.38), and using $f = \frac{1}{2\pi}\omega$, the resonant frequency of a trapezoidal cantilever can be obtained.

$$f_0 = \frac{1}{2\pi}\sqrt{\frac{E}{\rho}} \cdot \frac{1}{L^2}\left[\frac{27}{16} \cdot \frac{35h_a^3 + 15h_a^2 h_b + 5h_a h_b^2 + h_b^3}{18h_a + 73h_b}\right] \tag{A.63}$$

References

[1] R. C. Hibbeler, *Mechanics of Materials*. New York, Toronto: Macmillan College Pub : Maxwell Macmillan International; Maxwell Macmillan Canada, 2nd ed., 1994.

[2] F. P. Beer, E. R. Johnston, and J. T. DeWolf, *Mechanics of Materials*. New York: McGraw-Hill, 2nd ed., 1992.

[3] J. M. Gere and S. P. Timoshenko, *Mechanics of Materials*. London: Chapman and Hall, 3rd SI ed., 1991.

[4] G. Chen, T. Thundat, E. Wachter, and R. Warmack, "Adsorption-induced surface stress and its effects on resonance frequency of microcantilevers," *Journal of Applied Physics*, vol. 77, no. 8, pp. 3618–3622, 1995.

[5] Y. Zhang, Q. Ren, and Y.-P. Zhao, "Modelling analysis of surface stress on a rectangular cantilever beam," *Journal of Physics D: Applied Physics*, vol. 37, no. 15, pp. 2140–2145, 2004.

[6] T. Miyatani and M. Fujihira, "Calibration of surface stress measurements with atomic force microscopy," *Journal of Applied Physics*, vol. 81, no. 11, pp. 7099–7115, 1997.

[7] E. Volterra and E. C. Zachmanoglou, *Dynamics of Vibrations*. Ohio: Charles E Merrill, 1965.

[8] W. Weaver, S. Timoshenko, and D. H. Young, *Vibration Problems in Engineering*. New York: Wiley, 5th ed., 1990.

[9] W. T. Thomson, M. D. Dahleh, and A. V. Bourmistrova, *Theory of Vibration with Applications*. MIET2124 (Reserve), Upper Saddle River, N.J.: Prentice Hall, 5th ed., 1998.

[10] S. Timoshenko, *Vibration Problems in Engineering*. N.Y: Van Nostrand, 2nd ed., 1937.

Appendix B

Software Scripts

This appendix lists some of the software scripts written to investigate the theories developed in this thesis

B.1 Matlab script to determine f_0

```
% Script to calculate Resonant Frequency of a Microcantilever
% with multiple perforations.
% Refer my thesis for derivation and explanation of model.
% Sanchitha Fernando

%clear variables in memory:
clear;

%Define symbols:
syms E r_ L b h;                % Material & Mechanical properties
syms N a_ b_ g_ e_ l_;          % N, alpha, beta, gamma, eta, lambda
syms k;                         % subscript for summation
```

```
%Basic Calculations:
I=1/12*b*h^3;                  % Moment of Area of a uniform beam
c = (1-4*b_*g_^3-4*b_*g_+b_^2*g_^4+6*b_*g_^2)/(1-b_*g_);    %MOA c-factor

p = a_ + k*(e_ + l_); q = a_ - l_ + k*(e_ + l_);

N1 = 1; N2 = 0.2*a_^5 - a_^4 + 2*a_^3 - 2*a_^2 + a_;

N3 = 0.2*symsum( p^5, k , 1, (N-1) );          %sum p^5 from 1 to (N-1)
N4 = -symsum( p^4, k , 1, (N-1) ); N5 = 2*symsum( p^3, k , 1,
(N-1) ); N6 = -2*symsum( p^2, k , 1, (N-1) ); N7 = symsum( p, k ,
1, (N-1) );

N8 = 0.2*symsum( q^5, k , 1, N ); N9 = -symsum( q^4, k , 1, N );
N10 = 2*symsum( q^3, k , 1, N ); N11 = -2*symsum( q^2, k , 1, N );
N12 = symsum( q, k , 1, N );

Num = 144*I/5/L^3*( N1 + 5*(1-c)*((N2+N3+N4+N5+N6+N7)
-(N8+N9+N10+N11+N12)) );

D1 = 1; D2 = 1/9*a_^9 - a_^8 + 4*a_^7 - 8*a_^6 + 36/5*a_^5;

D3 = 1/9*symsum( p^9, k , 1, (N-1) );          % sum p^9 from 1 to (N-1)
D4 = -symsum( p^8, k , 1, (N-1) );             % etc ...
D5 = 4*symsum( p^7, k , 1, (N-1) ); D6 = -8*symsum( p^6, k , 1,
(N-1) ); D7 = 36/5*symsum( p^5, k , 1, (N-1) );

D8 = 1/9*symsum( q^9, k , 1, N );              % sum q^9 from 1 to (N-1)
D9 = -symsum( q^8, k , 1, N );                 % etc ...
```

```
D10= 4*symsum( q^7, k , 1, N ); D11= -8*symsum( q^6, k , 1, N );
D12= 36/5*symsum( q^5, k , 1, N );

Den = 104/45*b*h*L*( D1+ 45/104*b_*g_*( (D2+D3+D4+D5+D6+D7) -
(D8+D9+D10+D11+D12) ));

f0 = 1/2/pi*sqrt(E/r_*(Num/Den));


%Initial values for mechanical & material properties:
%(can be over-ridden by specifying new values at the command line)
E  = 165e9;          %Youngs's Modulus
r_ = 2330;           %density
L  = 100e-6;         %length
b  = 20e-6;          %width
h  = 2e-6;           %thickness
```

B.2 Simulating an interferometric cantilever array

B.2.1 Simulate the diffraction pattern

```
% This script generates the far-field diffraction pattern
%
% Sanchitha, 21.01.2008

% Define constants
lambda = 650e-9;    % wavelength
```

```
k = 2*pi/lambda;    % wave number
a = 6e-6;           % interdigital spacing
b = 3e-6;           % width of digit
N = 5;              % Number of moving digits (= fixed digits)


% As per the pixels of photosensor used in the thesis, sampling should be
% at 0.00028 rad intervals. Here I use 0.0005, a rate worse than the
% sensor. The envelope is bound by +/-0.2166, & I use 0.217 ... actually,
% the sensor can cover +/-2.365 mm
theta=-0.217:0.0005:0.217;          % range of angles - for 1 diff envelope

% Introduce misalignment error:
theta = theta + MISALIGN;

% t = 10e-9;         % deflection : input at command prompt

mults = [1.3 1.1 1 1.4 1.2];   % vector of deflection multiples
tv = t*mults;

% Better system with wider alignment correction range
f = [0 1 5 9 13 17];        % fixed finger locations
m = [3 7 11 15 19];         % moving finger locations


% fixed - fixed Even terms
clear I; row=1; for r=2:N+1
    for s=1:r-1
        I(row,:) = 2*cos((p(r)-p(s))*k*a*sin(theta));
```

```
        row = row+1;
    end
end

% add each column, & add N+1 to it
Iee = sum(I) + N+1;

% Moving - Moving terms
clear I; row=1; for r=2:N
    for s=1:r-1
        I(row,:) = 2*cos((q(r)-q(s))*k*a*sin(theta) ...
            - k*(tv(r)-tv(s))*(1+cos(theta)));
        row = row+1;
    end
end

Ioo = sum(I) + N;

% Fixed - Moving terms
clear I; row=1; for r=1:N+1
    for s=1:N
        I(row,:) = 2*cos((p(r)-q(s))*k*a*sin(theta) ...
          + k*tv(s)*(1+cos(theta)));
        row = row+1;
    end
end

Ieo = sum(I);
```

```
% Diffraction term
Id = (sin(0.5*k*b*sin(theta))./(0.5*k*b*sin(theta))).^2; Id(
(length(Id)+1)/2 ) = 1;



I = Iee + Ioo + Ieo; I = I.*Id; S = fft(I);
% figure(1); plot(theta, I, theta, 121*Id); %xlim([0 400]);
% figure(2); plot(abs(S)); xlim([0 200])
% figure(3); plot(angle(S)); %xlim([0 120])
```

B.2.2 Calculated deflection

```
% This script attempts to determine the deflection from a measurement of
% intensity patterns

% Sanchitha 21.01.2007

% Generate look-up tables using "GenLookUp.m" before running this script



% obtain interference pattern:
SCRIPT_Interference;
J = round(I/121*1024);  % Round-off values to fit a 10-bit ADC
S = fft(J);

% phase readings: There'll be N readings, where N=no. of moving fingers
PhaseReadings = angle(S(POS));

% Misalignment correction (uses just one reading, for convenience) :
```

```
% Aligned = mean(Alignment(1,:));    % average ideal value when aligned
% MisAlign = angle(S(AlPos(1))) - Aligned;
% PhaseErrors = [3 7 11 15 19]*MisAlign;
% PhaseErrors = PhaseErrors - floor(PhaseErrors/2/pi)*2*pi;
        % Scale errors to range (0,2pi)
% PhaseReadings = PhaseReadings - PhaseErrors;
%
% for ss=1:N
%     if (PhaseReadings(ss) > pi)
%         PhaseReadings(ss) = 2*pi - PhaseReadings(ss);
%     elseif (PhaseReadings(ss) < -pi)
%         PhaseReadings(ss) = 2*pi + PhaseReadings(ss);
%     end
% end

% vector to store the possible readings:
Possible = zeros(N,1);

Elems = zeros(1,N); % no of matching elements for each phase reading..

% Pick the candidates
% If we have callibrated in steps of 1nm, angular resolution =
% 2*pi*(1nm)/(325nm)= 0.0193 rad. So, "error" = +/- 0.01 is sufficient
MaxErr = 0.1; %0.01; % radians
c=1;        %counter

X = length(LookUp);
Err_prev = 10;  % to make the 1st Err_this smaller than Err_prev
```

```
for ss=1:N   %cycle through all phase readings
    % Now using the ss-th phase reading ...
    for rr=1:X   %X = no. of points on the FFT
        % Now testing the rr-th FFT point
        % Error of this point:
        Err_this = abs(PhaseReadings(ss) - LookUp(ss,rr) );
        if ( Err_this <= MaxErr)     %Is this is a candidate point?
            % Yes, this is a candidate point
            % was the previous value also stored?
            if ( (c>1) && (LookUp(N+1,rr) - Possible(ss,c-1) < 10 ) )
                % Yes,  previous value was also stored
                % Is this point better than the previous point?
                if (Err_this < Err_prev)
                    % yes better, so replace with this one.
                    Possible(ss,c-1) = LookUp(N+1,rr);
                end
            else
                % No, previous point not stored
                Possible(ss,c)= LookUp(N+1,rr);
                c=c+1;
            end
            % This point become previous point for the next cycle
            Err_prev = Err_this;
        end
    end
    Elems(ss) = c-1;
    c=1;
end
```

```
% Now scan through the Possible readings and pick readings common to two
% adjacent rows. Store in "Common"
c = 1; Common = 0; for uu=1:N-1
    c=1;
    for ss=1:Elems(uu)
        for rr=1:Elems(uu+1)
            if ( abs(Possible(uu,ss) - Possible(uu+1,rr)) < 3)
                Common(uu,c) = 0.5*(Possible(uu,ss) + Possible(uu+1,rr));
                c = c+1;
            end
        end
    end
end

% Take average reading:
AvgDef = mean(Possible);
```